

High Precision Muon Lifetime Measurement with the FAST Experiment

THÈSE

présentée à la Faculté des sciences de l'Université de Genève
pour obtenir le grade de Docteur ès sciences, mention physique

par

Maria Chiara CASELLA

d'Italie

Thèse N° 3879



**Doctorat ès sciences
mention physique**

Thèse de *Madame Maria Chiara CASELLA*

intitulée

**" High Precision Muon Lifetime Measurement with
the FAST Experiment "**

La Faculté des sciences, sur le préavis de Messieurs M. POHL, professeur ordinaire et directeur de thèse (Département de physique nucléaire et corpusculaire), A. BLONDEL, professeur ordinaire (Département de physique nucléaire et corpusculaire), J.-J. BLAISING, docteur (CERN – Conseil Européen pour la Recherche Nucléaire – Division PH – Genève, Suisse) et F. NAVARRIA, professeur (Università e Istituto Nazionale di Fisica Nucleare di Bologna – Bologna, Italia), autorise l'impression de la présente thèse, sans exprimer d'opinion sur les propositions qui y sont énoncées.

Genève, le 31 juillet 2007

Thèse - 3879 -



Le Doyen, Jean-Marc TRISCONE

Contents

Introduction	vii
1 Theoretical motivations	1
1.1 The muon: Who ordered that?	1
1.2 The Standard Model	3
1.2.1 A few observations	5
1.3 The Lagrangian for the Standard Model in the Electroweak Sector . .	6
1.3.1 Gauge term in the Standard Model Lagrangian	6
1.3.2 Scalar term in the Standard Model Lagrangian	7
1.3.3 Fermionic term in the Standard Model Lagrangian	8
1.4 Parameters and Predictions of the EW Standard Model	10
1.5 The Fermi Coupling Constant and the Muon Lifetime	14
1.5.1 Experimental Uncertainty on G_F	16
1.5.2 Residual Theoretical Uncertainty on G_F	17
1.6 Weak Corrections on G_F	18
1.7 G_F in the Analysis of Electroweak Data	19
1.8 Improved G_F accuracy: Which Impact?	20
2 Current Experimental Status of the Muon Lifetime τ_μ	27
2.1 Concept of Muon Lifetime Experiments	28
2.2 Toward High Precision τ_μ experiments	29
2.3 Present High Precision τ_μ experiments	30
2.3.1 Status of the FAST experiment	30
2.3.2 The RIKEN-RAL experiment	30
2.3.3 The MuLan experiment	31
3 The FAST Experiment	33
3.1 General Concept of the Experiment	33
3.2 The DC π^+ Beam	37
3.2.1 The PSI Accelerator Facility	37
3.2.2 The π M1 Beam Line at PSI	37

3.2.3	The Level 1 (LV1) Trigger	38
3.3	The FAST Target	40
3.3.1	The Scintillator Target	40
3.3.2	Why “FAST”?	42
3.3.3	The LED Mask	44
3.3.4	The Photomultipliers (PSPM’s)	44
3.3.5	The Wedge and the Collimator	45
3.3.6	The Hodoscope z -Counter	45
3.3.7	The Magnetic Field	47
3.3.8	Final Configuration of the FAST target	47
3.4	Analogue Readout Electronics	49
3.4.1	Preamplifiers	49
3.4.2	Discriminators	50
3.4.3	Matching between Preamplifiers and Discriminators	51
3.5	Target Mapping and Cabling	52
3.6	The Data Acquisition (DAQ) System	52
3.6.1	Precise Time Measurement	52
3.6.2	The DAQ Architecture	55
3.6.3	DAQ Rate Performances	57
3.6.4	Future Upgrade in the DAQ Architecture	57
3.7	The Level 2 (LV2) Trigger	58
3.7.1	Electronics for the LV2 Trigger System	62
3.7.2	Operational Working Conditions for the LV2	64
3.8	FAST Slow Control	65
4	Commissioning and Performance of the FAST Detector	69
4.1	Light Yield in Scintillator and Pulse Height	70
4.2	Discriminators Thresholds Settings	72
4.3	High Voltage (HV) Settings	73
4.4	Beam Particles Range	77
4.4.1	Pion Range	78
4.4.2	Pion and Muon Range Comparison	79
4.5	Timing Considerations	79
4.5.1	Time Equivalence of one TDC tickmark	80
4.5.2	Zero Time ($t = 0$) Convention	81
4.6	Calibration Runs with Electrons: Efficiency and Time Resolution	81
4.6.1	Efficiency for MIP’s	83
4.6.2	Time Resolution	86
4.7	Pion Runs: Nominal Running Conditions	87
4.8	Global Time Distribution	88

4.9	Pixel Occupancy and Beam Profiles	90
4.10	TDC's and Event Builder	91
4.11	LV2 Trigger: Commissioning Activities and Efficiency	95
5	Muon Lifetime Analysis	99
5.1	Run 2006: Data Sample	99
5.1.1	Sub-samples	100
5.2	The Analysis Code: from Raw Data to Histograms	101
5.2.1	Event Reading and Event Structure	101
5.2.2	Event Processing: Selection Cuts and Positron ID	101
5.2.3	Lifetime Histograms	103
5.2.4	Control Histograms	106
5.2.5	FAST: An Online Analysis Experiment	106
5.3	Muon Lifetime Measurement: Fit Strategy	106
5.4	A Simple Fitting Function	108
5.5	Background Description, $B(t_{rel})$	110
5.6	Fit for the Negative Times Region	113
5.6.1	Period Determination	115
5.7	Muon Lifetime Fit on Separated Subsamples	116
5.7.1	Best Fitting Interval	118
5.8	Muon Lifetime Fit on the Full Sample	120
5.8.1	Fast Fourier Transform of the Residuals	122
5.8.2	Added structures in the data	124
5.9	Improved Fitting Function	127
5.9.1	Muon Lifetime Fit on the Full Sample with the Improved Fitting Function	129
5.10	Rebin Method	131
5.10.1	Muon Lifetime Fit on the Full Sample with the Rebin Method	134
5.11	Measurement of the Muon Lifetime: Conclusion	136
6	Study of the Systematic Uncertainty	139
6.1	Systematics Related to the Geometry	139
6.1.1	Lifetime vs Pion Position (x_π and y_π)	140
6.1.2	Lifetime vs Position inside the PSPM	141
6.1.3	Lifetime vs Target Geometry: PSPM, Chip, and TDC Structures	142
6.1.4	Geometrical Systematics: Summary	143
6.2	Systematics Related to μ SR Effect and Isotropy	146
6.2.1	μ SR: Possible Source of Systematic Error	146
6.2.2	μ SR Effects in the Lifetime Measurement	148
6.3	Systematics Related to the Fit Method	149

6.3.1	Lifetime vs Bin Width	151
6.3.2	Lifetime vs T_{RF} Value and Phase	152
6.3.3	Lifetime vs Bin Sharing Algorithm	153
6.3.4	Lifetime vs Integration Steps	153
6.3.5	T_{RF} and Number of Knots	153
6.3.6	Fit Method Systematics: Summary	154
6.4	Lifetime Estimator	155
6.5	Stability of the Measurement	156
6.5.1	Clock Stability	156
6.5.2	Beam Rate Dependence	156
6.6	Influence of the Time Smearing	157
6.7	Systematic Uncertainty: Summary	159
7	Conclusion	161
7.1	Future prospects for the FAST experiment	163
A	Additional Information about the Analysis	165
A.1	Numbering Schemes and Electron Patterns	165
A.2	Online and Offline Analysis	165
A.2.1	Monitoring Program	166
A.3	Blind Analysis	168
B	Résumé (French Summary)	177
B.1	Introduction	177
B.2	L'Expérience FAST	178
B.3	Échantillon de Données	181
B.4	La Méthode d'Ajustement	182
B.5	Résultat de l'Ajustement	183
B.6	Évaluation des Incertitudes Systématiques	184
B.7	Résultats et Conclusions	186
	Bibliography	189

Introduction

The Fermi coupling constant G_F plays a key role in the precision tests of the Standard Model of the electroweak interactions. Along with the electromagnetic coupling constant α and the Z boson mass M_Z , it is one of the best measured quantities of the electroweak physics and, as such, it is used as input in all calculations. G_F is one of the few quantities sensitive to the physics at very high energy scale, it is intimately related to the ρ parameter; it was indeed the value of G_F that provided some of the strongest constraints on the mass of the top quark, before its observation.

G_F is currently known to a precision of 9 ppm (part per million), dominated by the experimental uncertainty only. Although G_F is not at present the limiting factor in the electroweak fits, and it is not likely to become so before the uncertainties on other parameters (mainly the masses of the W and Higgs boson) are strongly improved, a reduction on its uncertainty of about one order of magnitude is experimentally feasible.

The most precise determination of G_F comes from the measurement of the positive muon lifetime τ_μ . Until recently, the accuracy in the derivation of G_F from τ_μ was limited by theoretical uncertainties. In 1999, second order QED corrections to the muon lifetime in the Fermi theory have been calculated, reducing to 0.3 ppm the theoretical error on G_F . With such a level of theoretical precision, an improved muon lifetime measurement will directly reduce the uncertainty on G_F .

The goal of the FAST experiment is a 1 ppm accuracy on the Fermi coupling constant. This will be achieved with a 2 ppm precision measurement of the positive muon lifetime. It will result in a one order of magnitude improvement in the world average. To meet the accuracy requirements, a large data sample of muon decay events of the order of a few 10^{11} must be acquired. The final data taking is foreseen for 2007 and 2008. A short run in 2006, in running conditions close to the ones foreseen for the final data taking, provided the first precise measurement of the positive muon lifetime with the FAST detector, to a precision comparable with the current world average.

The present work will describe the FAST experiment and the muon lifetime measurement obtained from the data sample of the 2006 run. In particular, it will be structured as follows.

Chapter 1 will provide the theoretical motivations behind a precise measurement of the muon lifetime. In particular, the role of G_F as a fundamental parameter in the general framework of the Standard Model will be described. Its connection with the muon lifetime will be also detailed.

Chapter 2 will summarize the present status of the experimental knowledge on the muon lifetime. A short overview of the past measurements and of the present experiments aiming to a precise determination of the muon lifetime will be given.

The FAST experiment will be described in Chapter 3. The general experimental concept, and the details of the several elements used to build up the setup of the experiment (the beam, the target, the readout electronics, the DAQ system, the trigger system) will be reported. Chapter 4 will complete the characterization of the detector, presenting some of the most relevant results about the commissioning activities performed on the detector in the past years.

Chapter 5 will be devoted to the muon lifetime analysis. The general tasks of the analysis program - from raw data to histograms - will be presented. The fit method applied to the decay time distribution for the run 2006 data sample will be described. The muon lifetime measurement thus obtained - within its statistical uncertainty - will be reported. Chapter 6, will complete the measurement, with the analysis of its systematical uncertainties.

Finally, Chapter 7 will conclude, comparing the measurement of the muon lifetime performed using the FAST detector with the other existing ones, and determining the new world average value for G_F . It will also briefly discuss the future prospects of the FAST experiment.

Chapter 1

Theoretical motivations

1.1 The muon: Who ordered that?

Since its discovery in cosmic rays in 1937, by Anderson and Neddermeyer [1] and by Street and Stevenson [2], the muon has played an important role in our understanding of nature. It was indeed the first particle to show evidence of the existence of different families, or generations, for elementary particles. And the study of its decay, together with nuclear beta decay, gave the clue for the establishment of the weak force as one of the four main interactions in nature.

Soon after its discovery, the muon, particle with an intermediate mass between the one of the proton and the one of the electron, called at that time *mesotron* or *mu meson*, was thought to be the Yukawa meson [3], the force carrier of the strong interaction. But it was later demonstrated, in 1947 (Conversi et al, [4]), that it could not be such a particle, because it did not interact through the strong force at all. The search for the Yukawa particle continued and a few months later Lattes, Muirhead, Occhialini and Powell [5] finally discovered a singly charged particle, now known as the pion, that fulfilled the Yukawa predictions, and that decayed into the already discovered muon. Figure 1.1 shows events similar to the typical ones that lead Powell and his collaborators to the discovery.

At that time - the late 1940's - the picture of "elementary" particle physics was quite simple, with the proton, the neutron and the electron being the "fundamental" constituents of matter, and the photon and the newly discovered pion the quanta of, respectively, the electromagnetic and strong interaction. The neutrino started also to appear in this scenario, with no experimental confirmation, but with a strong theoretical argument to its existence. The positron had been already discovered (Anderson, 1932 [6]), confirming Dirac's prediction of antimatter. But no explanation at all about the role of the muon could be found. Talking about the muon, Isidor I. Rabi said "*Who ordered that?*" indicating how puzzling was, at the time, the discovery

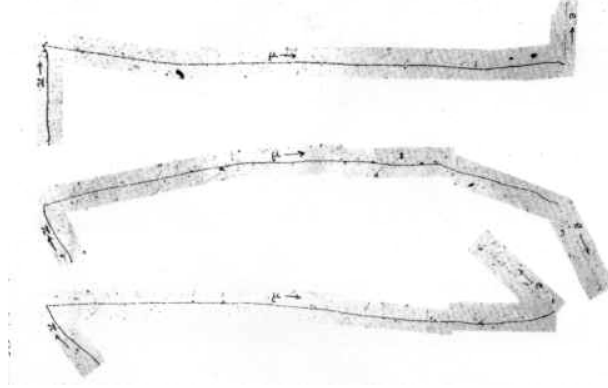


Figure 1.1: Some of the earliest pictures from photographic emulsions exposed to cosmic rays at high altitude, showing the decay sequence $\pi^+ \rightarrow \mu^+ \rightarrow e^+$. The pion decays into a muon (plus a neutrino, which is a neutral particle and leaves no track) and the muon decays into an electron (plus two neutrinos). Visible is the dense ionization of both pion and muon tracks near the end of the range, compared with the thin track of the relativistic electron. In the earliest Powell's pictures - the ones that led to the discovery of the pion [5] - the electron track was not visible, due to the low sensitivity of the photographic emulsion.

of a particle that could not fit into any established scheme. We can easily say now that the muon was only the first one of a long list of particles whose existence was not initially foreseen and was eventually responsible for big changes in the theoretical framework that physicists have built up to that moment. In some sense, for this reason, those times can be thought to be the beginning of modern particle physics: *“The muon was the unwelcome baby on the doorstep, signifying the end of days of innocence”* (M.Gell-Mann and E.P.Rosenbaum [7]).

When first accelerators became available, starting with the Ernest Lawrence's 184-inch cyclotron [8] in 1948, and the experiments moved from the cosmic rays domain in high mountain regions, to the controlled energy beams provided by accelerators, with higher and higher energies, an entire collection of new particles started to appear, and it took a long time, and a long, combined effort of many, until everything could be explained in a coherent and elegant way.

Now we know that the muon, together with other five leptons and six quarks, and their interactions mediated by the gauge bosons, is one of the fundamental constituents of matter, and perfectly sits in the frame of the so called Standard Model (SM), the theory which describes our actual knowledge of particle physics. A brief introduction to the Standard Model will be given in the next sections. After that, we will focus particularly on the muon interactions and lifetime.

1.2 The Standard Model

At present we base our understanding of physical phenomena on the existence of a few elementary - structureless and indivisible - particles¹ and four fundamental forces: the gravitational, the weak, the electromagnetic and the strong forces.

The fundamental particles are all fermions (spin 1/2 particles), classified in *leptons* (which interact through electromagnetic - if charged - and weak forces) and *quarks* (which interact through all three interactions: strong, electromagnetic and weak). There exist six leptons and six quarks, each one characterized by its *flavour*, divided into three generations. Differently from leptons, quarks - influenced by the strong force - carry *colour*, the strong charge. Leptons are colorless. Table 1.1 summarizes the 12 fundamental constituents of matter, together with their masses and electric charges. The “ordinary matter”, atoms and nuclei, is explained in terms of the leptons and quarks of the first generation only (e,u,d). Except for the masses of the involved particles, the second and third generations appear to be an identical replica of the first one. The reason why exactly three and only three families exist is still an open question that had found, so far, no answer. To complete the description of elementary constituents, one has to take into account also the antimatter: for each of the listed quarks and leptons there is a correspondent antiquark or antilepton, of identical mass and spin, but opposite charges.

LEPTONS			QUARKS		
flavour	Mass [Gev/c ²]	Q[e]	flavour	Mass [Gev/c ²]	Q[e]
ν_e (<i>neutrino el</i>)	$< 10^{-8}$	0	u (<i>up</i>)	0.003	2/3
e (<i>electron</i>)	0.511 10^{-3}	-1	d (<i>down</i>)	0.006	-1/3
ν_μ (<i>neutrino mu</i>)	< 0.0002	0	c (<i>charm</i>)	1.3	2/3
μ (<i>muon</i>)	0.106	-1	s (<i>strange</i>)	0.1	-1/3
ν_τ (<i>neutrino tau</i>)	< 0.02	0	t (<i>top</i>)	175	2/3
τ (<i>tau</i>)	1.7771	-1	b (<i>beauty</i>)	4.3	-1/3

Table 1.1: Leptons and quarks in the Standard Model [12].

In quantum field theory, fundamental interactions are described by the exchange of gauge vector bosons (spin 1 particles) among the interacting elementary fermions. So, for example, the electromagnetic attraction or repulsion of two charged particles

¹ History cautions that the list of elementary particles is dependent on experimental resolution. We should then specify that fundamental particles means structureless at the smallest distances currently probed by the highest energy accelerators (about 10^{-18} cm).

is explained in terms of an exchange of photons between the particles themselves, and the photon is said to be the quantum of the electromagnetic field or the gauge boson of the electromagnetic force (QED, *Quantum ElectroDynamics* is the quantum field theory describing this). The (eight) gluons are the strong force gauge bosons (and QCD, *Quantum ChromoDynamics* is the theory describing strong interactions among quarks). Finally, the two charged W^\pm and the neutral Z bosons are the carriers of the weak interactions (combined with QED this leads to the so called *electroweak theory*). Table 1.2 lists the vector bosons, together with their masses and electric charges.

Interaction	Gauge boson	Mass [GeV/ c^2]	Q [e]
Electromagnetic	photon (γ)	0	0
Weak	W^-	80.4	-1
	W^+	80.4	+1
	Z	91.187	0
Strong	gluon (g)	0	0

Table 1.2: Gauge vector bosons of the Standard Model [12].

One of the biggest achievements of modern particle physics is the understanding that interactions are prescribed by symmetries in the theory ([9, 10, 11]). In these terms the Standard Model is a gauge theory of quarks and leptons with strong, weak and electromagnetic interactions specified by local gauge symmetries on the group $SU(3)_c \times SU(2)_L \times U(1)_Y$. A locally gauge invariant theory would naturally include vector bosons as mediators of the interactions, and in particular an exact symmetry would necessarily imply *massless* vector bosons. This is the case for photons and gluons (QED and QCD), but cannot be true for the weak force carriers, W^\pm and Z . The existence of massive vector bosons can be accommodated - without destroying the gauge invariance - by the so called Higgs mechanism. It is a spontaneous breaking of the electroweak symmetry ($SU(2)_L \times U(1)_Y \rightarrow U(1)_{em}$), which leads to massive vector bosons for the electroweak force (actually three massive and one massless bosons, respectively W^+ , W^- , Z and γ), through the introduction of an additional massive scalar field, the Higgs boson (so far, not yet observed experimentally). The same Higgs mechanism may also be responsible for the fermion masses: once the Higgs scalar field is introduced in the theory, it is indeed possible to foresee interactions between the fermions and the scalar field (the Yukawa interactions), which, after symmetry breaking, lead to mass terms for the fermions. We should notice here that the masses of all the fermions, set by the Yukawa couplings, are arbitrary parameters of the Standard Model. Their values cannot be calculated or predicted by the theory. The same is true for the Higgs boson's mass itself. Some theoretical arguments and the

direct search for the Higgs bosons in e^+e^- collisions at LEP2, however, can constrain the Higgs mass, thus giving some indications about its most probable value. For the Standard Model Higgs: $144 \text{ GeV} \leq m_h < 1 \text{ TeV}$.

1.2.1 A few observations

Before developing the Lagrangian formalism for the Standard Model (next section), needed to identify which are the free parameters of the model, a few comments should conclude this concise presentation of the Standard Model.

First of all, the gravity has been deliberately totally disregarded, and in fact it does not play any role in the interactions of elementary particles. Also, among the fundamental forces, it is the only one that still cannot be described in terms of quantum field theory. The hypothetical - never observed - *graviton*, quantum of the gravitational force, would complete Table 1.2 of gauge vector bosons.

Almost the whole phenomenology of particle physics (excluding gravity) spanning many orders of magnitude in energy can be described with astonishing precision in the framework of the Standard Model. Starting from its original formulation, the electroweak theory first and the Standard Model later, have scored a number of great successes, both from the theoretical and experimental point of view. Examples are the prediction and subsequent observation of weak neutral currents, the prediction of the existence and the properties of the weak gauge bosons, the precise measurements of their parameters at the Z pole and incredibly precise measurements such as the determination of the anomalous magnetic moments of the electron and the muon. Despite this success, there are a lot of questions that still remain without answer and that make us believe that Standard Model is at least an incomplete theory. For example, the questions: which is the reason of the existence of three families of elementary particles, as it is observed, or why the masses are as they are, with such big differences among elementary constituents, cannot be answered in the frame of the Standard Model. The fact that neutrinos do have a mass, the nature of neutrinos (Dirac or Majorana), the matter-antimatter asymmetry, the existence of dark matter, the gravitational interaction are all subjects not included in the Standard Model. The Higgs boson, strongly needed by the theory to explain many phenomena, even if at the prize of introducing a large number of free parameters to be fixed by phenomenology, has not yet been observed, and may not exist.

The very near future of experimental particle physics, with the LHC exploring the TeV region, will finally find “something”, either the Higgs or its “substitute(s)”, whose existence is needed to solve unitarity problems and high energy divergences. Maybe it will confirm, maybe not, the Standard Model, and almost for sure it will reveal new physics beyond it (like e.g. supersymmetric particles, extra-dimensions) opening the doors for a completely new and exciting era in particle physics.

1.3 The Lagrangian for the Standard Model in the Electroweak Sector

Although the Standard Model includes both the Electroweak (EW) theory and QCD, from now on we will restrict our study to the EW sector only. Even if not specified anymore, in the following we will always assume the symmetry group to be $SU(2)_L \times U(1)_Y$ instead of $SU(3)_C \times SU(2)_L \times U(1)_Y$ and we will focus only on electroweak interactions between leptons and quarks. Also the interactions of the fermions and the gauge bosons with the Higgs must be considered. The Lagrangian formalism developed here and in the following parts will follow the treatment of [9].

The full Lagrangian for the Standard Model \mathcal{L}_{SM} in the electroweak sector consists of three parts:

$$\mathcal{L}_{SM} = \mathcal{L}_{gauge} + \mathcal{L}_{Higgs} + \mathcal{L}_{fermions} \quad (1.1)$$

The first one, the \mathcal{L}_{gauge} term, describes all the possible interactions among the gauge bosons themselves (explicitly: the vertexes ZWW , γWW , $ZZWW$, $\gamma\gamma WW$, γZWW , $WWWW$). The \mathcal{L}_{Higgs} term is a complex doublet scalar field Lagrangian with a self interacting potential (with a suitable choice of the potential to allow the symmetry breaking). As we will see later, this scalar term in \mathcal{L}_{SM} is responsible - after symmetry breaking - for the masses of the W^\pm , Z bosons and for the mass of the Higgs boson, for the self interactions of the Higgs boson and for the interactions between the Higgs and the gauge bosons (vertexes hWW or $hhZZ$, for example). The third term, $\mathcal{L}_{fermions}$, the one for quarks and leptons must include both the kinetic term (i.e. a free fermionic field Lagrangian) and the Yukawa term (i.e. interactions Higgs-fermions), which generates - after symmetry breaking - the mass terms for quarks and leptons.

1.3.1 Gauge term in the Standard Model Lagrangian

With g and A_μ^i ($i = 1, 2, 3$) respectively the gauge coupling constant and the three vector fields associated to the $SU(2)$ symmetry, g' and B_μ the gauge coupling constant and the one vector field of the $U(1)$ symmetry, the explicit gauge term for the Standard Model Lagrangian is

$$\mathcal{L}_{gauge} = -\frac{1}{4}F_{\mu\nu}^i F^{\mu\nu i} - \frac{1}{4}f_{\mu\nu} f^{\mu\nu}. \quad (1.2)$$

$F_{\mu\nu}^i$ and $f_{\mu\nu}$ are the gauge-field strength tensors for $SU(2)$ and $U(1)$ respectively:

$$F_{\mu\nu}^i = \partial_\mu A_\nu^i - \partial_\nu A_\mu^i + g\epsilon^{ijk} A_\mu^j A_\nu^k \quad (1.3)$$

$$f_{\mu\nu} = \partial_\mu B_\nu - \partial_\nu B_\mu \quad (1.4)$$

The \mathcal{L}_{gauge} term describes the motion of gauge bosons and their interactions. The coupling constants of weak and electromagnetic currents are defined and fixed in this sector. It is thus natural in the Standard Model to have universal couplings to all fermion generations.

1.3.2 Scalar term in the Standard Model Lagrangian

The scalar part of the Standard Model Lagrangian is explicitly written as follows:

$$\mathcal{L}_{Higgs} = |D_\mu \phi|^2 - V(\phi^\dagger \phi); \quad V(\phi^\dagger \phi) = -\mu^2 \phi^\dagger \phi + |\lambda|(\phi^\dagger \phi)^2 \quad (1.5)$$

D_μ is the covariant derivative (in $SU(2) \times U(1)$):

$$D_\mu = \partial_\mu + ig \frac{\sigma^i}{2} A_\mu^i + ig' Y B_\mu; \quad (1.6)$$

where σ_i ($i = 1, 2, 3$) are the Pauli matrices for the $SU(2)$ group, Y is the hypercharge operator. The μ and λ parameters contained in the scalar potential V are arbitrary parameters of the theory. For $\mu^2 > 0$, the Higgs field ϕ develops the following vacuum expectation value:

$$\langle \phi \rangle = \begin{pmatrix} 0 \\ v/\sqrt{2} \end{pmatrix} \quad (1.7)$$

where $v^2 = +\mu^2/\lambda$. The Higgs mass, extracted from \mathcal{L}_{Higgs} , developing around the vacuum expectation value $\phi = \frac{1}{\sqrt{2}} \begin{pmatrix} 0 \\ v + h \end{pmatrix}$, where h is the Higgs field, is given by $m_h^2 = 2\mu^2$.

After electroweak symmetry breaking, the $SU(2)$ and $U(1)$ gauge fields \vec{A}_μ , B_μ form the massless photon and the massive W^\pm , Z . At the tree level, their masses are simply expressed in terms of the coupling constants and the vacuum expectation value v :

$$M_W = \frac{gv}{2}; \quad M_Z = \frac{\sqrt{g^2 + g'^2} v}{2} \quad (1.8)$$

The coupling with the massless photon imposes a relation between the electric charge e and the coupling constants, which derives from the group structure:

$$e = \frac{gg'}{\sqrt{g^2 + g'^2}}, \quad (1.9)$$

which is needed to preserve the electromagnetic interactions in the theory.

It is convenient to introduce a weak mixing angle θ_W , the so called Weinberg angle, to parametrize the mixing of the neutral gauge bosons.

$$\cos \theta_W = \frac{g}{\sqrt{g^2 + g'^2}} \quad \sin \theta_W = \frac{g'}{\sqrt{g^2 + g'^2}} \quad (1.10)$$

One can now rewrite the covariant derivative 1.6 in terms of θ_W and the physical fields W_μ^+ , W_μ^- , Z_μ , A_μ , instead of the original gauge bosons fields \vec{A}_μ and B_μ

$$D_\mu = \partial_\mu - \frac{ig}{2\sqrt{2}}(W_\mu^+ \sigma^+ + W_\mu^- \sigma^-) - \frac{ig}{\cos \theta_W} Z_\mu (\sigma_3 - Q \sin^2 \theta_W) - ieQA_\mu \quad (1.11)$$

and also (from 1.9 and 1.10):

$$g = \frac{e}{\sin \theta_W} \quad (1.12)$$

The expression 1.11 for the covariant derivative leads immediately to the conclusion that the coupling of vector bosons is totally specified only by two parameters: e and $\sin^2 \theta_W$. Together with this, the masses of the vector bosons W^\pm, Z are not independent, but

$$M_W = M_Z \cos \theta_W. \quad (1.13)$$

In conclusion, the main information we can extract from Equations 1.8 to 1.13 is that the Standard Model in the gauge sector is fully described by three independent parameters only. They are usually identified with the following ones:

$$M_W ; e ; \sin^2 \theta_W \quad (1.14)$$

but any other set of parameters would be valid.

1.3.3 Fermionic term in the Standard Model Lagrangian

The fermionic term appearing in the Lagrangian must describe leptons, quarks and their couplings with the electroweak bosons W^\pm, Z, γ . Given that EW charged currents only couple with left handed particles, we need to introduce different representation for right and left handed fermions, which must be - respectively - singlets and doublets in $SU(2)$. For simplicity we will write here the Lagrangian only for the first family of particles, and in the limit of massless Dirac neutrinos. The leptons and quarks are respectively indicated by

$$L = \begin{pmatrix} \nu \\ e \end{pmatrix}_L ; \quad e_R \quad (1.15)$$

$$Q = \begin{pmatrix} u \\ d \end{pmatrix}_L ; \quad u_R ; \quad d_R. \quad (1.16)$$

The Lagrangian describing the weak interactions of leptons is

$$\mathcal{L}_{leptons} = i[\bar{L}\gamma^\mu D_\mu L + \bar{e}_R\gamma^\mu D_\mu e_R] \quad (1.17)$$

Rewriting the covariant derivatives of 1.17 in terms of the physical fields, as in 1.11, we obtain all the tree level leptonic interactions with the vector bosons (both charged and neutral currents: $W e \nu$, $Z \bar{l} l$, $\gamma e \bar{e}$ vertexes). No mass term for the leptons can be directly introduced in 1.17: the reason is that such a term, of the form $\bar{\psi} m \psi = (\bar{\psi}_L + \bar{\psi}_R)m(\psi_L + \psi_R) = m(\bar{\psi}_L\psi_R + \bar{\psi}_R\psi_L)$, would not respect the $SU(2)$ invariance of the Lagrangian, mixing singlets and doublets. However the same Higgs scalar field introduced to break the symmetry and give a mass to the vector bosons can be used to assign a mass also for the leptons. We can write a gauge invariant Yukawa term of interactions between leptons and the Higgs scalar ϕ as:

$$\mathcal{L}_{Yukawa-lept} = -\lambda_e[\bar{e}_R\phi^\dagger L + \bar{L}\phi e_R] \quad (1.18)$$

Substituting the vacuum expectation value for the Higgs field, i.e. $\phi = \frac{1}{\sqrt{2}} \begin{pmatrix} 0 \\ v + h \end{pmatrix}$, the Yukawa term becomes:

$$\mathcal{L}_{Yukawa-lept} = -\frac{\lambda_e v}{\sqrt{2}}(\bar{e}_R e_L + \bar{e}_L e_R) - \frac{\lambda_e h}{\sqrt{2}}(\bar{e}_R e_L + \bar{e}_L e_R) \quad (1.19)$$

The first term in this expression is the mass term for the electron: the mass $m_e = \frac{\lambda_e v}{\sqrt{2}}$ is proportional to the Yukawa coupling λ_e . The second term is the lepton-scalar coupling, which again is proportional to the mass of the lepton. All this is ruled by the parameter λ_e , which is an arbitrary constant.

The generalization to three families of leptons (L_l , l_R , with $l = e, \mu, \tau$) is straightforward, both for the kinetic part (from which we will extract all the interactions leptons-gauge bosons, obtaining e.g. not only $W e \nu_e$ but also $W \mu \nu_\mu$ and $W \tau \nu_\tau$) and for the Yukawa term (for which we have to introduce three separate couplings: $\lambda_e, \lambda_\mu, \lambda_\tau$).

As for the quarks, we can repeat (for one family) the same identical steps developed for the leptons, with the only difference that there are now two right handed singlets, instead of one. The kinetic part is then

$$\mathcal{L}_{quarks} = i[\bar{Q}\gamma^\mu D_\mu Q + \bar{u}_R\gamma^\mu D_\mu u_R + \bar{d}_R\gamma^\mu D_\mu d_R] \quad (1.20)$$

and the Yukawa term is

$$\mathcal{L}_{Yukawa-quark} = -\lambda_u[\bar{Q}\bar{\phi}u_R + \bar{u}_R\bar{\phi}^\dagger Q] - \lambda_d[\bar{Q}\bar{\phi}d_R + \bar{d}_R\bar{\phi}^\dagger Q]. \quad (1.21)$$

From the Yukawa term, after symmetry breaking, we obtain the masses for the u and d quarks: $m_u = \frac{\lambda_u v}{\sqrt{2}}$ and $m_d = \frac{\lambda_d v}{\sqrt{2}}$. Once again, each mass corresponds to an arbitrary coupling parameter and must therefore be specified by the experimentally measured value.

When we generalize to three families, in the case of quarks, the situation is complicated by the mixing among families: the “mass eigenstates” (corresponding to physical particles with a given mass) do not coincide with the “weak eigenstates” (which appear in the invariant Lagrangian). Usually the relation about the two eigenstates is expressed in term of a 3×3 unitary matrix, the CKM (Cabibbo, Kobayashi, Maskawa) matrix, whose nine entries can be parametrized in terms of three angles and one phase. The elements of the CKM matrix are observables and need to be determined experimentally.

A mixing matrix in the leptonic sector also exists. It is the MNS matrix (Maki, Nakagawa, Sakata), which accounts for neutrino oscillations. Four parameters, three mixing angles and one CP violating phase, are needed to describe the matrix (plus two additional phases, if the neutrinos are Majorana particles).

1.4 Parameters and Predictions of the EW Standard Model

The Standard Model, like indeed any other renormalizable theory, only becomes predictive when it is supplied with a sufficient number of experimental inputs, needed to fix the free parameters that appear in its Lagrangian.

The previous section has identified the free parameters for the Standard Model. They are:

- two coupling constants g and g' (or equivalently e and $\sin^2 \theta_W$);
- two parameters for the scalar potential μ and λ , from which we extract the vacuum expectation value v and the mass of the Higgs boson m_h ;
- nine Yukawa couplings, one for each flavour of (massive) fermions: $\lambda_e, \lambda_\mu, \lambda_\tau$ (or equivalently m_e, m_μ, m_τ) for leptons; $\lambda_u, \lambda_c, \lambda_t$ (or m_u, m_c, m_t) for u-type quarks; $\lambda_d, \lambda_s, \lambda_b$ (or m_d, m_s, m_b) for d-type quarks;
- four remaining parameters for the quark mass mixing (the CKM matrix);

1.4. PARAMETERS AND PREDICTIONS OF THE EW STANDARD MODEL 11

α^{-1}	$(137.03599911 \pm 0.00000046)$	0.003 ppm [12]
G_F	$(1.16637 \pm 0.00001) \times 10^{-5} \text{ GeV}^{-2}$	9 ppm [12]
M_Z	$(91.1876 \pm 0.0021) \text{ GeV}$	23 ppm [12]

Table 1.3: The three best measured quantities which provide the experimental inputs to the Standard Model (gauge sector).

- four remaining parameters for the neutrino mixing matrix (the MNS matrix).

Disregarding all the parameters associated with the fermion masses, where - as already pointed at - the Standard Model has no predictive power, and disregarding the Higgs mass and potential as well, only three free parameters remain in the gauge sector (see Eqn. 1.14), that have to be supplied to the theory as external inputs. In order for the subsequent theoretical predictions to be as accurate as possible, these inputs are chosen from the best measured quantities available. In the case of the Standard Model of the electroweak interactions (gauge sector) these are

$$\alpha ; G_F ; M_Z \quad (1.22)$$

α is the electromagnetic coupling constant, G_F is the Fermi coupling constant and M_Z is the mass of the Z boson. Their recognized best values, along with their absolute and relative errors are given in Table 1.3.

The set of three parameters identified in Eqn. 1.22 as the experimental inputs of the Standard Model is directly connected with the set of independent parameters derived from the theory in Eqn. 1.14. The relation among the different quantities is expressed by the following equations:

$$e^2 = 4\pi\alpha \quad (1.23)$$

$$\frac{G_F}{\sqrt{2}} = \frac{g^2}{8M_W^2} = \frac{e^2}{8 M_W^2 \sin^2 \theta_W} \quad (1.24)$$

$$M_Z^2 = \frac{M_W^2}{\cos^2 \theta_W} \quad (1.25)$$

These expressions are valid at the tree level only, i.e. at the lowest order in perturbation theory. They are substantially modified by higher order radiative corrections.

The fine structure constant α is experimentally determined from the e^\pm anomalous magnetic moment g and quantum Hall effects. Recently a new precise determination

of the fine structure constant from the electron g value, which constitutes a one order of magnitude improvement, has been reported [13]. In most electroweak renormalization schemes it is convenient to define a running α , dependent on the energy scale of the process. Couplings and masses must then be evolved or measured at the same energy scale to preserve the essence of Eqn. 1.23 to 1.25. Although $\alpha(0)$, at scale $q^2 = 0$, is precisely known experimentally (to the value quoted in Table 1.3) there are significant uncertainties on $\alpha(M_Z)$, of the order of hundreds ppm, mainly due to low energy hadronic contributions to the vacuum polarization [14].

The value of the Fermi coupling constant G_F is accurately determined from the muon lifetime (τ_μ) measurement. The value for G_F quoted in the above table already includes both experimental and theoretical contributions. It should be noticed, however, that the 9 ppm uncertainty on G_F is totally dominated by the experimental accuracy on τ_μ . The theoretical uncertainty on G_F , after $\mathcal{O}(\alpha^2)$ corrections to the muon decay process [17], is smaller than 0.3 ppm, and thus completely negligible when compared with the present experimental uncertainty.

The Z boson mass, M_Z , is determined from the Z -lineshape scan at LEP. It is unlikely that its precision could be significantly improved in the near future. Next generation colliders however (muon colliders, linear colliders) may well achieve a reduction by a further order of magnitude or more.

Over the past fifteen years, in essence due to the experiments carried out at the Z pole on the electron positron colliders SLC and LEP, several precision measurements (cross sections, forward-backward asymmetries, polarized asymmetries...) have tested the electroweak theory at the one per mille level. Figure 1.2 shows the comparison between different measurements and their expectations in the Standard Model, obtained from a global fit with a number of fixed initial parameters [14]. Also shown is the pull of each measurement, defined as the difference of measurement and expectation in units of the measurement uncertainty. With the inputs of Table 1.3, $\sin^2\theta_W$ and M_W , for example, can be calculated when values for m_t and m_h are given; conversely (as it is done at present) m_h can be constrained by the measured values of $\sin^2\theta_W$ and M_W .

The typical precisions obtained on the mass of the Z boson ($\sim 10^{-5}$) and on many observables related to its decay ($\sim 10^{-3}$) are so good that the tree level predictions of the theory are not sufficient anymore to describe the results: loop effects are visible and higher orders of perturbation theory are needed. As already observed, this is the case for the quoted value of G_F in Table 1.3. Such a level of precision was not predicted when LEP was started: in the mid-80's, just before the turn on of LEP, a CERN report [16] conservatively concluded that the error on M_Z would be ± 50 MeV, or 550 ppm, foreseeing a possible maximum improvement of a factor of 2-3 "with a determined effort". It was thus generally thought that M_Z would be the input parameter limiting the accuracy with which the theoretical predictions could

1.4. PARAMETERS AND PREDICTIONS OF THE EW STANDARD MODEL¹³



Figure 1.2: Precision electroweak measurements and the pulls they exert on a global fit to the Standard Model (Last update: Winter 2007). [15]

be made. The actual experimental progress was significantly underestimated and the uncertainty on M_Z now approaches that of G_F . The lesson that should be learnt is that it is extremely difficult to predict, even in the relatively short term, the rate of progress in the accuracy to which fundamental parameters will be determined. And it is therefore important to try to extract them to the limits that the current state of theory and experiment allows.

This is exactly the theoretical framework which provides the motivations for the FAST experiment. Its goal is an improvement by one order of magnitude in the precision of the Fermi coupling constant G_F , one of the fundamental parameters of the Standard Model that has to be fixed for it to become predictive. As it will be described below, an improved precision on G_F is experimentally achievable by a

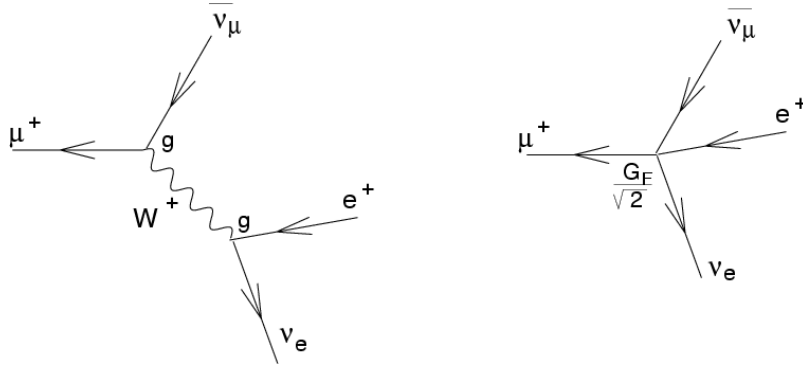


Figure 1.3: Left: Feynman diagram for the decay of the positive muon, at the lowest order of perturbation theory (i.e. $\mathcal{O}(g^2)$), showing the W propagator. Right: Four fermions contact interaction approximation of the positive muon decay. This approximation is valid at small energies ($q^2 \ll M_W$) only.

precise measurement of the positive muon lifetime τ_μ .

1.5 The Fermi Coupling Constant and the Muon Lifetime

The most precise measurement of the Fermi coupling constant G_F comes from the direct measurement of the muon lifetime τ_μ . Experimentally, in order to avoid uncertainties due to the capture of negative muons on target nuclei (forming muonic atoms), the *positive* muon lifetime is generally used to extract the value for G_F .

The muon decay is a purely leptonic process and therefore very clean, both experimentally and theoretically. It proceeds uniquely via the W boson exchange. Figure 1.3, left shows the Feynman diagram associated to the positive muon decay $\mu^+ \rightarrow e^+ \nu_e \bar{\nu}_\mu$, at the lowest order in perturbation theory. In the limit of momenta small compared to M_W the muon decay can very well be approximated - in the so called Fermi theory - by a four fermions contact interaction (Figure 1.3, right), where the decay amplitude is simply proportional to G_F .

At the tree level, G_F is related to the muon lifetime τ_μ by the following formula:

$$\frac{1}{\tau_\mu} = \Gamma_0 = \frac{G_F^2 m_\mu^5}{192\pi^3}, \quad (1.26)$$

which is derived from a standard application of the perturbation theory (lowest order) on the muon decay process [23].

The general expression relating G_F to τ_μ to the leading order in G_F and all orders in

α is:

$$\frac{1}{\tau_\mu} = \Gamma_\mu = \Gamma_0(1 + \Delta q), \quad (1.27)$$

where Γ_0 , from Eqn. 1.26, is the tree level muon decay width in the limit of vanishing electron mass and Δq encapsulates electron and neutrino mass terms and all higher order QED and QCD corrections. Δq can be expressed as a power series expansion in the renormalized electromagnetic coupling constant (α_r):

$$\Delta q = \sum_{i=0}^{\infty} \Delta q^{(i)}. \quad (1.28)$$

The index i gives the power of α_r that appears in $\Delta q^{(i)}$ (i.e. $\Delta q^{(i)} = \mathcal{O}(\alpha_r^i)$) [17, 18]. Assuming the electron neutrino is massless, and keeping the leading term in muon neutrino mass m_{ν_μ} only, it can be shown that

$$\Delta q^{(0)} = -8x - 12x^2 \ln(x) + 8x^3 - x^4 - 8y + \mathcal{O}(xy), \quad x = \frac{m_e^2}{m_\mu^2}, \quad y = \frac{m_{\nu_\mu}^2}{m_\mu^2} \quad (1.29)$$

which comes from phase space integration [20].

The $\mathcal{O}(\alpha_r)$ corrections in Δq (i.e. the 1-loop QED and QCD contributions: $\Delta q^{(1)}$), first obtained about 50 years ago [21, 22], are summarized in:

$$\Delta q^{(1)} = \left(\frac{\alpha_r}{\pi} \right) \left[\frac{25}{8} - 3\zeta(2) - (34 + 12 \ln(x))x + 96\zeta(2)x^{3/2} + \mathcal{O}(x \ln^2(x)) \right] \quad (1.30)$$

where ζ is the Riemann zeta function and x is defined in Eqn. 1.29.

Quite recently, complete 2-loop radiative corrections to the muon lifetime have been calculated [17, 18, 19]. The result:

$$\Delta q^{(2)} = \left(\frac{\alpha_r}{\pi} \right)^2 [6.700 \pm 0.002] \quad (1.31)$$

includes QED photonic corrections, with up to two virtual photons, as well as electron loops and $e^+ e^-$ pair production. Figure 1.4 collects a few examples of diagrams included in the calculation of these QED $\mathcal{O}(\alpha_r^2)$ corrections. Also muon loops in the photon vacuum polarization, as well as tau loops are included in Eqn. 1.31. Hadronic contributions - which constitute an independent subclass of 2-loop corrections, that cannot be evaluated using perturbative methods - are included as well [19]. The reported error in Eqn. 1.31 is a conservative estimate of the hadronic uncertainty.

The relative theoretical uncertainty in the determination of G_F - up to second order radiative corrections - is globally less than 0.3 ppm. The current best value of

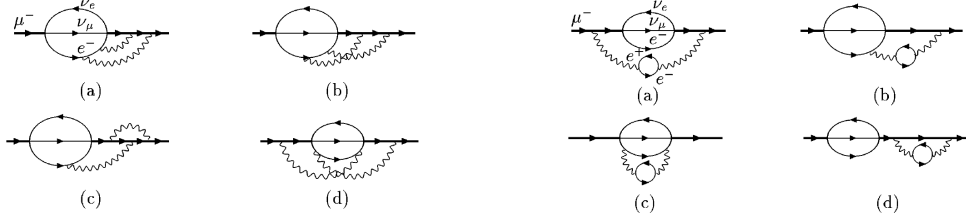


Figure 1.4: Examples of diagrams whose cuts give contribution to the 2-loop QED corrections to the muon decay. The 4 diagrams on the left are examples of photonic corrections, the 4 diagrams on the right are examples of diagrams containing an electron loop.

the muon lifetime $\tau_\mu = (2.19703 \pm 0.00004) \mu\text{s}$ [12], together with the expressions from Eqn. 1.27 to Eqn. 1.31, yield the actual best known value of G_F^2 :

$$G_F = (1.16637 \pm 0.00001) \times 10^{-5} \text{ GeV}^{-2}, \quad (1.32)$$

which corresponds to an uncertainty of 9 ppm, totally dominated by experimental errors.

Before the completion of 2-loop radiative corrections, when Eqn. 1.30 was the only contribution to the general uncertainty on G_F beyond tree level, the quoted error on G_F used to be $\frac{\delta G_F}{G_F} = 17$ ppm, of which 9 ppm was experimental and 15 ppm was theoretical. The latter was dominated by estimates of the uncalculated second order radiative corrections. Now that the theoretical uncertainty is so much reduced, further improvements on the knowledge of G_F have to come from the experimental side.

1.5.1 Experimental Uncertainty on G_F

On the experimental side, the accuracy of the known values for the muon lifetime τ_μ , the muon mass m_μ and the muon neutrino mass m_{ν_μ} can each exert a significant effect on the extracted value of G_F . From Equations 1.26 to 1.29, the change in G_F in response to changes in these quantities is given by, in linear approximation:

$$\frac{\delta G_F}{G_F} = -\frac{1}{2} \frac{\delta \tau_\mu}{\tau_\mu} - \frac{5}{2} \frac{\delta m_\mu}{m_\mu} + 4 \frac{m_{\nu_\mu}^2}{m_\mu^2}. \quad (1.33)$$

² The way used to extract G_F from the calculations is the same one adopted in [12], where $\alpha_r = \alpha_r(m_\mu)$ [$\alpha_r(m_\mu)^{-1} \sim 136$] and the hypothesis of massless neutrinos is used.

Table 1.4 lists the measured values of the quantities affecting $\delta G_F/G_F$, together with the contribution that each one gives to the global experimental uncertainty on G_F .

	measured value	relative precision	contribution to $\delta G_F/G_F$
τ_μ	$(2.19703 \pm 0.00004)\mu\text{s}$ [12]	18 ppm	9 ppm
m_μ	$(105.6583692 \pm 0.0000094)$ MeV [12]	0.09 ppm	0.2 ppm
m_{ν_μ}	< 0.19 MeV (90% C.L.) [12]	-	< 13 ppm
	$< 2 - 3$ eV (95% C.L.) [24]	-	0

Table 1.4: Summary of the contributions to the experimental uncertainty on G_F .

It is clear that the total uncertainty on G_F is dominated by the uncertainty on the muon lifetime τ_μ . A new generation of high precision muon lifetime experiments (at the Paul Scherrer Institute and at the Rutherford-Appleton Laboratory, see next chapter) plan to reduce it by about one order of magnitude, thus pushing the global uncertainty on G_F somewhere in the range from 0.5 to 1 ppm.

The precision on the m_{ν_μ} value, as reported in table 1.4, is to be understood as follows: setting its value to the current upper bound, as it is found from direct measurements [12] is indeed an overestimation of the actual neutrino mass. Complementary indirect informations on the neutrino mass, derived from analysis of cosmological data, especially anisotropies in the CMB and distribution of large scale structures, constrain the total neutrino mass, fixing an upper bound of a few eV only [24].³ The contribution on the experimental uncertainty on G_F due to m_{ν_μ} is then totally negligible.

1.5.2 Residual Theoretical Uncertainty on G_F

With the inclusion of 2-loop QED corrections in Δq , missing higher order corrections in the muon decay process, and consequently in G_F , are not expected to exceed a few tenths of a ppm. The main contributions to these residual theoretical uncertainties could come from the hadronic uncertainties and 3-loop QED corrections.

An additional uncertainty on the lifetime of positive muons and G_F can come from effects of materials, typically the formation of muonium $M = \mu^+e^-$ in the material where the μ^+ comes to rest. Detailed calculations from Czarnecki, Lepage and Marciano [25] show that the lifetimes of a muonium and a free μ^+ differ only

³ A unique cosmological upper bound on neutrino mass does not exist: the values depend on the assumed cosmological model. The quoted values of 2 to 3 eV in the table refer to CMB data only. More stringent values are derived combining CMB analysis with other cosmological data.

by time dilation effects which are $\sim 10^{-9}$ and so completely negligible for future 1 ppm muon lifetime experiments. A similar suppression is expected on other material effects on the μ^+ lifetime.

1.6 Weak Corrections on G_F

The radiative corrections to muon decay in the full Standard Model naturally factorize into two pieces [26]: one is the QED corrections term described above, absorbed - to a very high degree of accuracy - in the Δq term of Equation 1.27; the other contains purely weak corrections. The advantage in such a differentiation between QED and weak corrections on G_F is that, once the QED has been “isolated” as far as possible into Δq , we are left with a definition of G_F which possesses an enriched sample of weak sector physics, and plays an important role in the analysis of electroweak data. The importance of its role is enforced by the very high accuracy with which it can be measured.

The weak corrections to the muon lifetime may be encapsulated in a quantity Δr defined by the relation

$$\frac{G_F}{\sqrt{2}} = \frac{g^2}{8M_W^2}(1 + \Delta r). \quad (1.34)$$

Δr will be defined in such a way that Eqn. 1.27 is true exactly. In an analogous way to Δq , Δr can be expressed as a power series in α_r :

$$\Delta r = \sum_{i=0}^{\infty} \Delta r^{(i)}, \quad (1.35)$$

where, once again, the index i indicates the power of α_r that appears in $\Delta r^{(i)}$.

The weak corrections due to W propagator effects contribute at leading order with:

$$\Delta r^{(0)} = \frac{3m_\mu^2}{10M_W^2} + \mathcal{O}\left(\frac{m_e^2}{m_\mu^2}\right). \quad (1.36)$$

Such a contribution shifts the extracted value of G_F by 0.52 ppm. This has not been of any significance up to now, and thus it has not been included in the definition of G_F used to extract its value from τ_μ (Eqn. 1.32). As soon as improved accuracy measurements of G_F will be available, the finite range effects of the W boson will become visible. With a high accuracy level on G_F , one reaches the regime where the weak interaction can no longer be described by the contact term; for this reason it is often said that a high precision experiment on G_F can be considered like a high

energy experiment, performed in fact at a low scale.

The relevance of the weak corrections for G_F is that it is ultimately the knowledge of Δr , obtained from the extracted value of G_F (Eqn. 1.34), that provides access to the underlying structure of the theory, in particular in the Yukawa sector. The most striking example is the prediction of the top quark mass (m_t) from precision electroweak data. Δr is closely related to the ρ parameter

$$\rho = \frac{M_W^2}{M_Z^2 \cos^2 \theta_W} = 1 + \delta\rho, \quad (1.37)$$

introduced by Ross and Veltman [27] as a way of interrogating the mass generation sector of the theory. For classes of radiative corrections that occur only in the W and Z self energies:

$$\delta\rho = -\frac{\sin^2 \theta_W}{\cos^2 \theta_W} \Delta r. \quad (1.38)$$

And asymptotically $\delta\rho$ is quadratic in m_t :

$$\delta\rho \sim \left(\frac{\alpha}{4\pi}\right) \frac{3m_t^2}{4M_W^2 \sin^2 \theta_w}. \quad (1.39)$$

It was this quadratic m_t dependence in $\delta\rho$ to provide some of the strongest constraints in the prediction of the mass of the top quark, well before it was directly observed at Tevatron in 1994 [28].

1.7 G_F in the Analysis of Electroweak Data

On the level of realistic observables such as measured cross sections, ratios and asymmetries, the electroweak precision data from LEP, SLD and Tevatron, consist of over thousand measurements with partially correlated uncertainties. This large set of results is reduced to a more manageable set of 18 precision results, so called pseudo observables, on which global Standard Model analysis is performed (see Figure 1.2) [14], [29]. Within the framework of the Standard Model, each pseudo observable is calculated at the Z -pole as a function of a few free parameters not predicted by the theory, such as the coupling constants and the masses of fundamental fermions, W , Z and Higgs. Consistency of the Standard Model framework requires that all measurements are accommodated by the same values of these free Standard Model parameters. These measurements test successfully all aspects of the Standard Model, and many of them show large sensitivity to electroweak radiative corrections at loop level.

The five input parameters of the Standard Model relevant for the calculation of the Z -pole observables are the coupling constants of QED and QCD at the Z -pole, $\alpha_{em}(m_Z^2)$ and $\alpha_s(m_Z^2)$, and the masses of the Z boson, m_Z , top quark, m_t and Higgs boson, m_H . The masses of all fermions, with the exception of the top quark, are small compared to M_Z , and precisely enough measured to be considered fixed. The running electromagnetic coupling constant α_{em} is represented by the hadronic vacuum polarization $\Delta\alpha^{(5)}(m_Z^2)$, as this is the contribution with the largest uncertainty. The dependence on m_t and m_H enters through radiative corrections.

The Z boson mass and the Fermi coupling constant G_F are known to such a good precision that - in the analysis of the electroweak data - they “currently act as two fixed points of the Standard Model, around which all other quantities are forced to find their place” [14]. Formally, M_Z is treated as a free parameter of the theory. Its experimental accuracy, however, is sufficient to ensure that no Standard Model constraints can pull it appreciably. It could be taken as well as a fixed quantity.

Two famous examples of tests of the Standard Model and constraints that could be derived are given in Figures 1.5 and 1.6. The masses of the top quark and W boson can be predicted by evaluating couplings and their electroweak radiative corrections, as shown in Section 1.6. The resulting 68% C.L. contour curve in the (m_W, m_t) plane, from SLD and LEP1, is compared with the direct measurements of both quantities, at Tevatron and LEP2, in Figure 1.5. The two contours overlap, successfully testing the Standard Model at the level of electroweak radiative corrections. The diagonal band in Figure 1.5 shows the constraint between the two masses within the Standard Model, which depends on the mass of the Higgs boson, and to a small extent also on the hadronic vacuum polarization (small arrow labeled $\Delta\alpha$).

The best constraint on m_H , shown in Figure 1.6, is obtained by a global fit, analysing all data. The most probable value corresponds to the minimum of the χ^2 distribution. The pulls of the 18 measurements entering the fit was shown already in Figure 1.2. The single largest contribution to the χ^2 arises from the forward-backward asymmetries of the b quark. The theoretical uncertainty on the Standard Model calculations of the observables is visualized as the thickness of the blue band. It is dominated by theoretical uncertainty in the calculation of the electroweak mixing angle, where a complete 2-loop calculation is needed.

1.8 Improved G_F accuracy: Which Impact?

As described above, G_F is one input of the electroweak fits to the Standard Model, fixed to the value and the accuracy reported in Equation 1.32. To quantitatively assess the effects of an improved measurement of G_F , the electroweak fits are repeated, for different values of G_F . The original ZFITTER package [30, 15] used in the standard electroweak fits is slightly modified in this study [31] in order to include G_F as

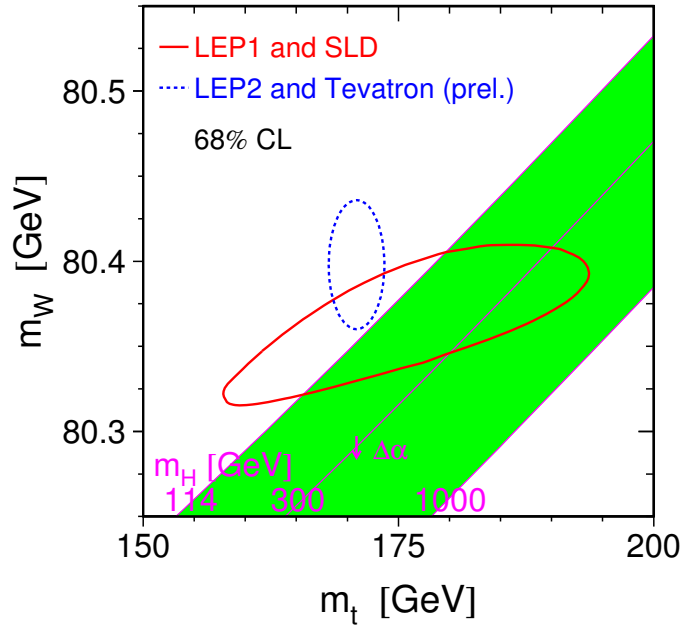


Figure 1.5: Contour curves of 68% C.L. in the (m_W, m_t) plane for the direct measurements (LEP2 and Tevatron) and the indirect determinations via couplings and radiative corrections (LEP1 and SLD). The band shows the correlation among the two masses expected in the Standard Model. The small arrow indicates the uncertainty due to the error on α .

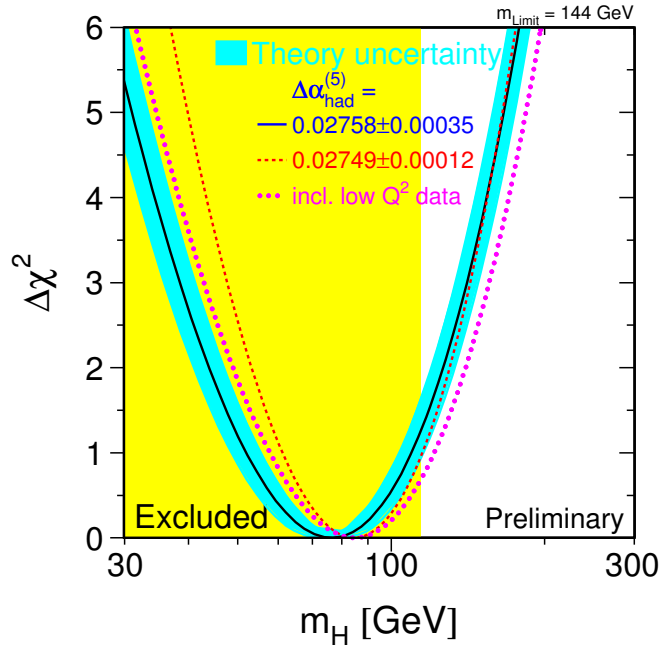


Figure 1.6: $\Delta\chi^2$ curve of the global fit of the Standard Model as a function of the Higgs mass m_H . The line is the result of the fit. The associated blue band is the estimate of the theoretical uncertainty. The vertical band shows the exclusion limit on $m_H < 144$ GeV, derived from the direct search at LEP2.

one additional input parameter. In addition, the suggested complete 2-loop fermionic corrections adopted in the latest version of the ZFITTER package cannot be used, because they are parametrized assuming a fixed value for G_F . The old default, corresponding to the sub-leading corrections has been used. The difference is anyhow negligible for the present study, as shown in Figure 1.7.

Figure 1.8 shows the most probable Higgs mass value derived from the fit, as a function of the G_F value. As shown, the current G_F accuracy accounts for an uncertainty of only a few hundreds of MeV on the prediction of the Higgs mass, to be compared with the one sigma uncertainty of about 30 GeV on the expected value from the global electroweak fit (Fig. 1.6).

The χ^2 of the custom global electroweak fit as a function of G_F is plotted in Figure 1.9. As a comparison, the current status scenario and other possible scenarios - based on arbitrary estimates of the precisions reachable at LHC and ILC for the parameters relevant for the fit - are plotted together. The increase in χ^2 , along with the reduced

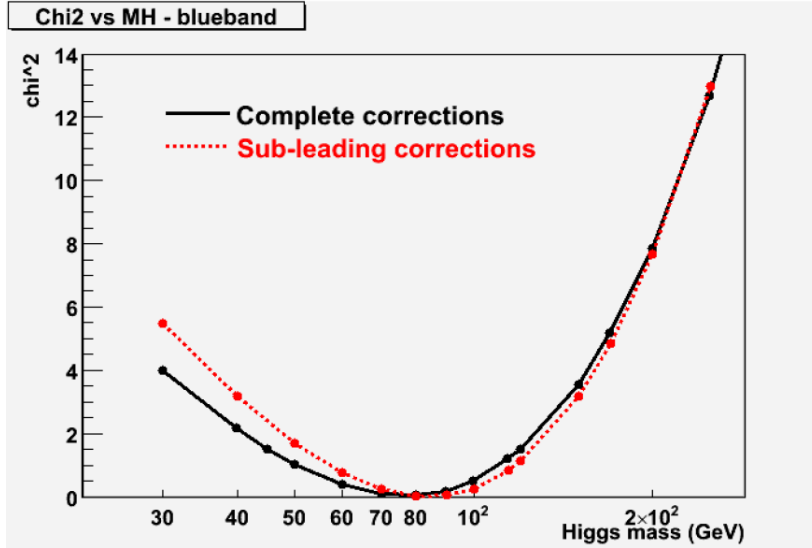


Figure 1.7: Equivalent of the “blue band” plot of Figure 1.6, obtained using the proposed fit for G_F analysis. The solid black curve contains the complete 2-loop fermionic corrections (standard EW fit); the dashed red line contains only the sub-leading corrections (modified EW fits, for G_F analysis).

errors on the other parameters is clear, but the effect is minimal.

Figure 1.10 shows by which factor the errors on the electroweak parameters have to be reduced so that they can constrain G_F at its current level of accuracy. A scale factor (from 1/5 to 1/1000) is applied on all the current error values, and the uncertainty on G_F is derived from the fit. One finds that a factor of 100 at least for the error on M_W is needed.

In conclusion, the current uncertainty on G_F is not at present the limiting factor in the electroweak fits. The relevance of one order of magnitude improvement in its value could start to play a role only when the precision on the other parameters, mainly m_W and m_H , will be at least two or three orders of magnitude better than the current values.

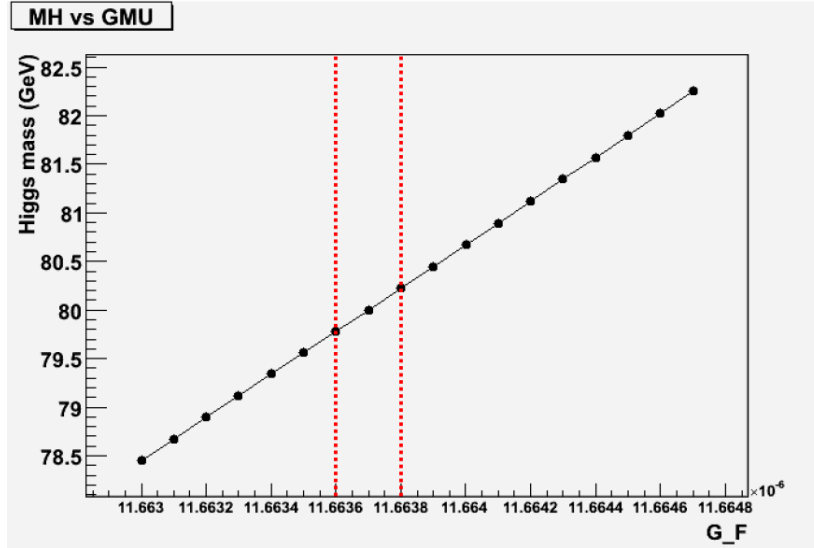


Figure 1.8: Predicted m_H value as a function of the input G_F value. G_F is changed in steps of $10^{-10} \text{ GeV}^{-2}$ (which is equivalent to one sigma in its current accuracy); the dashed vertical lines indicate the present known value for G_F , within the one sigma accuracy. (For readability, the W boson mass is artificially changed in the fits, to have a central m_H value of exactly 80 GeV.)

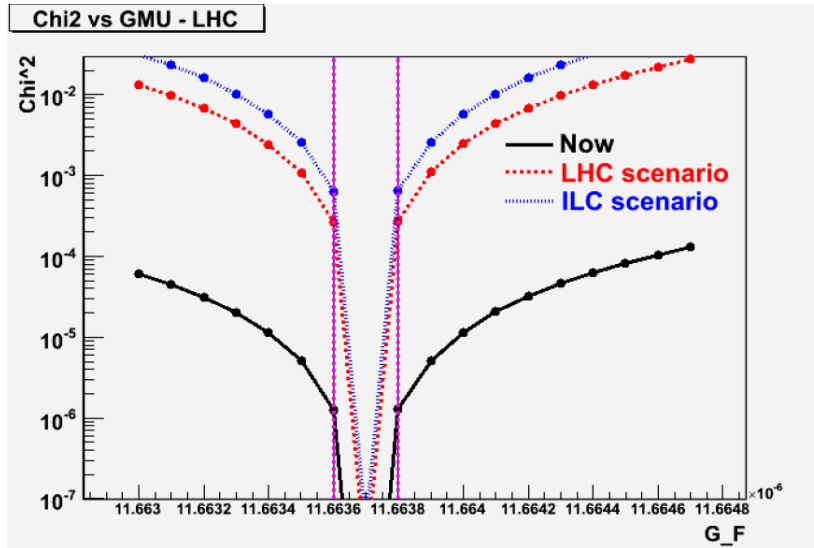


Figure 1.9: Variation of the χ^2 for electroweak global fit, as a function of the G_F value, both for the current scenario (black line), and for the projected accuracies expected at LHC and ILC times.

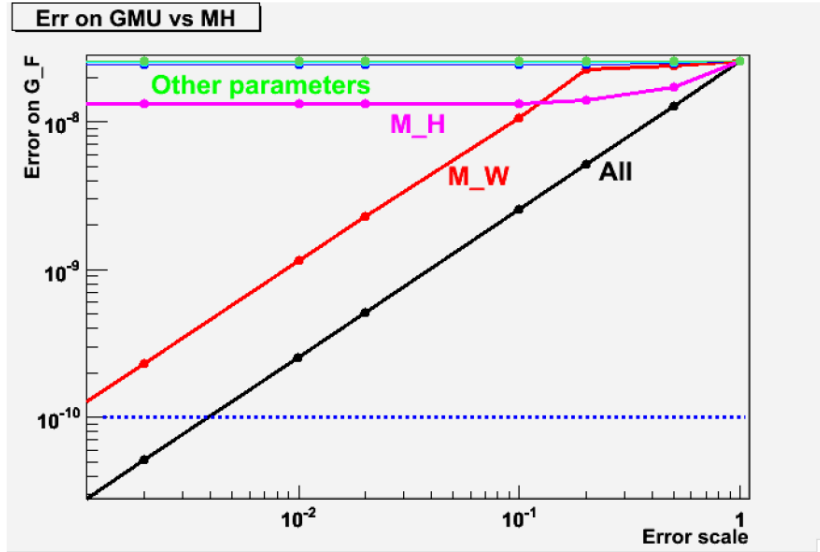


Figure 1.10: Derived uncertainty on G_F as a function of the error rescaling factors on the other parameters. The black line (All) is obtained by rescaling all parameters at the same time. The red and purple lines are obtained by rescaling only the errors on m_W and m_H , respectively. Rescaling of the other parameters gives negligible contributions. The dotted line represent the current level of accuracy on G_F : an improvement of two orders of magnitude in the uncertainty of the other parameters is needed before G_F can be constrained by the electroweak fits.

Chapter 2

Current Experimental Status of the Muon Lifetime τ_μ

The value of the positive muon lifetime τ_μ quoted in literature [12] is:

$$\tau_\mu = (2197.03 \pm 0.04) \text{ ns.} \quad (2.1)$$

It is determined as the weighted average of the results of four different experiments, performed more than twenty years ago. The references for these previous experiments are given in Table 2.1 and the results are summarized in Figure 2.1.

	ref.	year	measured value [ns]	
Bardin <i>et al</i>	[32]	1984	2197.078 ± 0.073	(33 ppm)
Giovanetti <i>et al</i>	[33]	1984	2196.95 ± 0.06	(27 ppm)
Balandin <i>et al</i>	[34]	1974	2197.11 ± 0.08	(36 ppm)
Duclos <i>et al</i>	[35]	1973	2197.3 ± 0.3	(136 ppm)
world average value			2197.03 ± 0.04	(18 ppm)

Table 2.1: Previous experiments of the positive muon lifetime

All the measurements listed above were essentially limited by their statistical errors, each one being based on a sample of about 10^9 muon decays. The FAST experiment, as indeed all the other new generation muon lifetime experiments aiming to a precision of a few parts per million (ppm) on τ_μ , needs to collect hundred times more data and to control its systematics in order to not compromise the statistical precision.

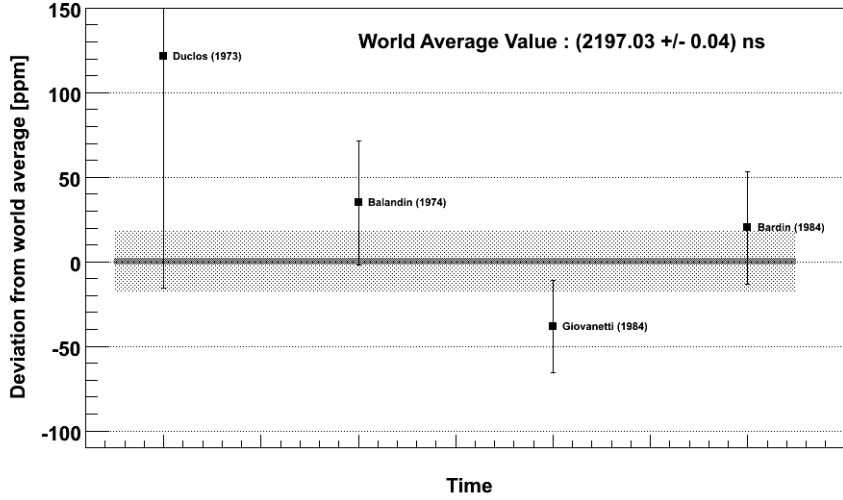


Figure 2.1: Dominant contributions to the current world average value of the positive muon lifetime. The plot shows the deviation from the quoted world average value (in ppm units) of each single measurement. The light grey band represents the world average value, within the one sigma deviation (corresponding to 18 ppm). The dark grey band would correspond to a 2 ppm precision measurement, needed to achieve a 1 ppm precision on G_F .

2.1 Concept of Muon Lifetime Experiments

Although each experiment adopts its own approach to the problem and uses different techniques and materials, the basic concept of muon lifetime experiments - both past and present - is common to all the experiments. Positive muons¹ are brought to rest in a target and decay within a few microseconds into one positron and two neutrinos ($\mu^+ \rightarrow e^+ \nu_e \bar{\nu}_\mu$). The two neutrinos from the decay escape unobserved, while the decay positron is observed by a detector system which surrounds, or coincides with the target where the muon was stopped. The time difference between the emerging positron and the stopping muon is recored for each event. A statistical sample of decay events N_{events} needs to be collected. Since for an exponential distribution the mean value is an estimator of lifetime τ_μ and RMS at the same time, the statistics immediately fixes the highest achievable precision in the measurement:

$$\frac{\sigma_{stat}}{\tau_\mu} = \frac{1}{\sqrt{N_{events}}} \quad (2.2)$$

¹ Positively charged muons are used for the lifetime measurements, to avoid any effect due to their capture by target nuclei.

Beside the statistical error σ_{stat} on the measurement of τ_μ , one has to include the systematics uncertainty σ_{syst} . This is intrinsically connected with the design of the experiments and the performance of each detector.

2.2 Toward High Precision τ_μ experiments

In the past experiments ([32]-[35]) the accuracy on τ_μ was limited statistically, since only a few muons, or even only one, were observed in a typical time window of about 20 μs , corresponding to about ten muon lifetimes. This was done to minimize count-loss effects, mainly due to pile-up signals, when two or more positrons passing through the same detector element within a short period are registered as one.

The TRIUMPH experiment [33], for example, used a DC beam of pions and muons, stopped in a water filled target. The decay positron was detected through its Cherenkov radiation by a pair of scintillator counters. The data were time intervals between electronic logic signals, started by a first beam trigger and consisting of a maximum of three signals from Cherenkov counters (π^+ , μ^+ , e^+) and a second beam trigger as a stop. If more than one additional beam trigger, other than the stop one, occurred within 20 μs the interval set was canceled.

The Saclay experiment [32], almost contemporary to the above mentioned one, used a totally different technique, with a pulsed π^+ beam stopped in a rapidly depolarizing sulfur target. Plastic scintillator telescopes, surrounding the target, allowed the detection of the positrons. A pulsed beam has the advantage that muons can be accumulated in bursts and the time distribution of the muon decay positrons can be measured after the burst, before the new one comes. In principle this method would allow simultaneous observation of more stopped muons at the same time. However only one muon decay per one time window was allowed to avoid distortions of the time spectrum, loosing the advantage of the pulsed beam.

The new generation τ_μ experiments, aiming at a much higher accuracy on τ_μ (few ppm) must abandon the “one decay per one time window” method, where each decay is measured individually in sequence. This method would not suffer of any pile-up effect, but - extended to a 10^{12} events collection - would require a large amount of beam time. Thus parallelization is needed, in the sense that several μ -decay events have to be handled in the same time window, with the consequent problems related to overlapping events.

In addition, new high precision muon lifetime experiments will be challenged not only by the need of a high statistical sample, but also by the requirement of keeping under control all systematic effects.

2.3 Present High Precision τ_μ experiments

At present, there exist three different experiments aiming at a high precision muon lifetime (and G_F) measurement:

- The FAST experiment [36, 37], which is performed at the Paul Scherrer Institute (PSI) accelerator facility, in Switzerland, on a DC pion beam.
- The MuLan experiment [38], performed on a pulsed muon beam, at PSI.
- The RIKEN-RAL experiment [39], at the Rutherford Appleton Laboratory in the UK, using a pulsed muon beam. It completed its foreseen data taking but has not yet published its final result.

In the following, we'll quote the experimental approach of the different experiments. We postpone the description of the experimental setup of the FAST experiment to the next chapter, only summarizing here its current status. From these concise descriptions it will be clear that the three experiments adopt very different approaches. This will result in different systematics related to the measurements. And it is indeed important for a new measurement - especially when it implies a one order of magnitude improvement with respect to the past value - to be validated by different experiments.

2.3.1 Status of the FAST experiment

The goal of the FAST experiment is a 1 ppm precision on the Fermi coupling constant G_F . This is equivalent to a 2 ppm precise measurement on the muon lifetime τ_μ .

FAST uses a DC π^+ beam on a target that is - at the same time - the stopping material for the π^+ and the consequent μ^+ , and the detector for the positron e^+ . It is essentially a “video camera” for the $\pi^+ \rightarrow \mu^+ \rightarrow e^+$ decays, which associates the members of each decay chain, while allowing multiple decays to occur in different portions of the target.

At present the experiment has not yet completed the final data taking (expected in 2007-2008). A first subsample of data, corresponding to a statistics comparable with the world average ($\sim 10^{10}$ events), has been collected during a few weeks run in December 2006, providing the first muon lifetime result of the FAST experiment, statistically competitive with the PDG accuracy.

2.3.2 The RIKEN-RAL experiment

A precise measurement of the positive muon lifetime was performed at the RIKEN-RAL muon facility. The experiment [39] developed the new method of a fast accumulation of muon events with a strong pulsed muon (μ^+) beam. Of the order of 10^4

muons per pulse are deposited in a thin paramagnetic holmium target, where muons are quickly depolarized and decay into positrons. The decay positrons are in turn observed by four multi-wire proportional chambers, providing a very high segmentation, needed to control pile-up effects, placed in two couples on the two sides of the target, thus covering only a part of the total solid angle.

A few 10^{10} muon decays have been accumulated. The first goal of the experiment is to improve the τ_μ accuracy at the level of 10 ppm. Data analysis, mainly focused on the systematics errors, is in progress and will be completed in the near future [40].

2.3.3 The MuLan experiment

The goal of the MuLan experiment [38] is a 1 ppm precision measurement of τ_μ , corresponding to a 0.5 ppm precision on G_F , resulting in the highest ever achieved precision.

The experiment plans to collect approximately 10^{12} muon decay events, taking advantage of a pulsed μ^+ source: during an accumulation period of a few μs a stream of a few tens of muons is stopped in a thin target; the muon beam is then switched off, and decay positrons are recorded by a surrounding segmented scintillator detector. This cycle has to be repeated until the final statistics is achieved. The time structured muon beam is created by means of a high frequency electrostatic kicker, on a continuous μ^+ beam at PSI. Each scintillator element is read by a photomultiplier whose signal is sampled by a waveform digitizer, providing informations about arrival time and energy deposition of the positrons. The main sources of systematic effects to be faced by the MuLan experiment are related to multi particle pile-up and muon spin rotation, since the μ^+ source is 100% polarized in the beam direction.

The MuLan experiment is running at present, it is supposed to complete the data acquisition in 2007. The analysis on a reduced set of data, collected in 2004, corresponding to a statistics comparable with the world average, has been recently finalized. The result has been submitted recently [41].

Chapter 3

The FAST Experiment

3.1 General Concept of the Experiment

The goal of the FAST experiment is a precise measurement of the muon lifetime τ_μ , to a precision equal to 2 ppm (i.e. ≤ 4 ps). After including all experimental and theoretical uncertainties this will correspond to a measurement of the Fermi coupling constant G_F to a precision of 1 ppm.

From the purely statistical point of view, 2.5×10^{11} μ -decay events are needed to achieve the expected precision. One single decay event must correspond to an observation period of approximately $20 \mu\text{s}$ i.e. about 10 muon lifetimes¹. The need of “parallelization” (i.e. treating more events in the same time window) has been already stressed in the previous chapter.

The approach of the FAST experiment is to use a continuous pion beam stopped inside a highly segmented plastic scintillator target, which serves at the same time both as stopping material for the pion (π^+) and the muon (μ^+) from its decay, and as detector for the positron (e^+) from the μ^+ decay.

The pion beam momentum has to be chosen so that each pion stops inside the target. The signature for a stopping pion is an almost straight track entering the target and ending with a large energy deposition (Bragg peak), corresponding to a large light pulse in the scintillator. The pion at rest decays into a muon in a few tens of ns ($\pi^+ \rightarrow \mu^+ \nu_\mu$; $\tau_\pi \sim 26$ ns [12]). The kinetic energy of the μ^+ is 4.1 MeV, which corresponds to a range in plastic scintillator of only about 1.5 mm. This makes that the $\pi^+ \rightarrow \mu^+$ decay has a distinctive signature as well: a second large pulse, due to the Bragg peak of the μ^+ , close in space and time to the one produced by the stopping pion. Finally the positron track from the μ^+ decay ($\mu^+ \rightarrow e^+ \bar{\nu}_\mu \nu_e$; $\tau_\mu \sim 2.197 \mu\text{s}$ [12]) is a minimum ionizing track (low pulses) emerging from the muon stop location.

¹This requirement is indeed an arbitrary choice, done to compromise between a reasonably short time of data taking and a sufficiently long interval to fully observe the decay.

The FAST experiment has to identify the full $\pi^+ \rightarrow \mu^+ \rightarrow e^+$ decay chain² and measure the time where the particles appear. In particular it has to measure the $t_e - t_\mu$ time difference for each event. The entire design of the experiment is based on the tracking capability of the detector. The FAST target (described later) is a high granularity scintillator block, composed of about 1500 small scintillator bars placed vertically with respect to the beam. Each bar constitutes a single target channel (one “pixel”) corresponding to one channel of the full readout chain. Each bar is connected to a multi anode photomultiplier, whose output is passed to the analogue readout modules (preamplifiers and discriminators), then read by the TDC’s and finally processed by the rest of the data acquisition system.

The way the parallelization is achieved in FAST is *geometrical*: with a DC beam and a tracking target, multiple asynchronous events can be handled simultaneously, provided they happen in different regions in the target. A uniform spread of the stopping points for pions in the target is needed. This is assured, as it will be shown later, by a wedge shaped degrader in front of the target, combined with a large beam profile.

Figure 3.1 shows a schematic view of the FAST target (both side and top view), including the wedge shaped beam degrader. Also the sketch of a typical $\pi^+ \rightarrow \mu^+ \rightarrow e^+$ event inside the target is drawn in the picture. Several events like the one shown will overlap in the target, at a rate determined by the beam rate, combined with the observation time window. As an example, in a 20 μs window, about 20 events would overlap in the target, at a beam rate of 1 MHz.

The design of the FAST experiment intends to reduce the systematic effects encountered in previous experiments. The pion beam provides an isotropic muon source, highly suppressing all the systematics originated by the muon spin rotation. The high granularity of the target, able to disentangle overlapping events especially at high rate, is mandatory. The symmetry and a large solid angular acceptance of the detector are important requirements as well. The imaging nature of the detector provides strong rejection of accidental backgrounds in the presence of high beam rate. Finally a DC beam minimizes the effects related to time dependent variations in the gain and detection efficiency of the detector.

When the experiment was designed, the choice was made to use high performance TDC’s to time stamp the pulses from the photomultipliers with essentially no conversion time. The advantage of this solution is a very good time resolution, together with high rate capability. Nevertheless, the price to pay is that no analogue information about the signal pulse heights can be retained. As it will be explained in the following, this implies a clever design of the discriminators, which have a double threshold, and so are able to discriminate between mip’s (i.e. the e^+ track) and stopping particles

² Here and in the following the notation $\pi^+ \rightarrow \mu^+ \rightarrow e^+$ will indicate the consecutive π^+ and μ^+ decays ($\pi^+ \rightarrow \mu^+ \nu_\mu$; $\mu^+ \rightarrow e^+ \bar{\nu}_\mu \nu_e$).

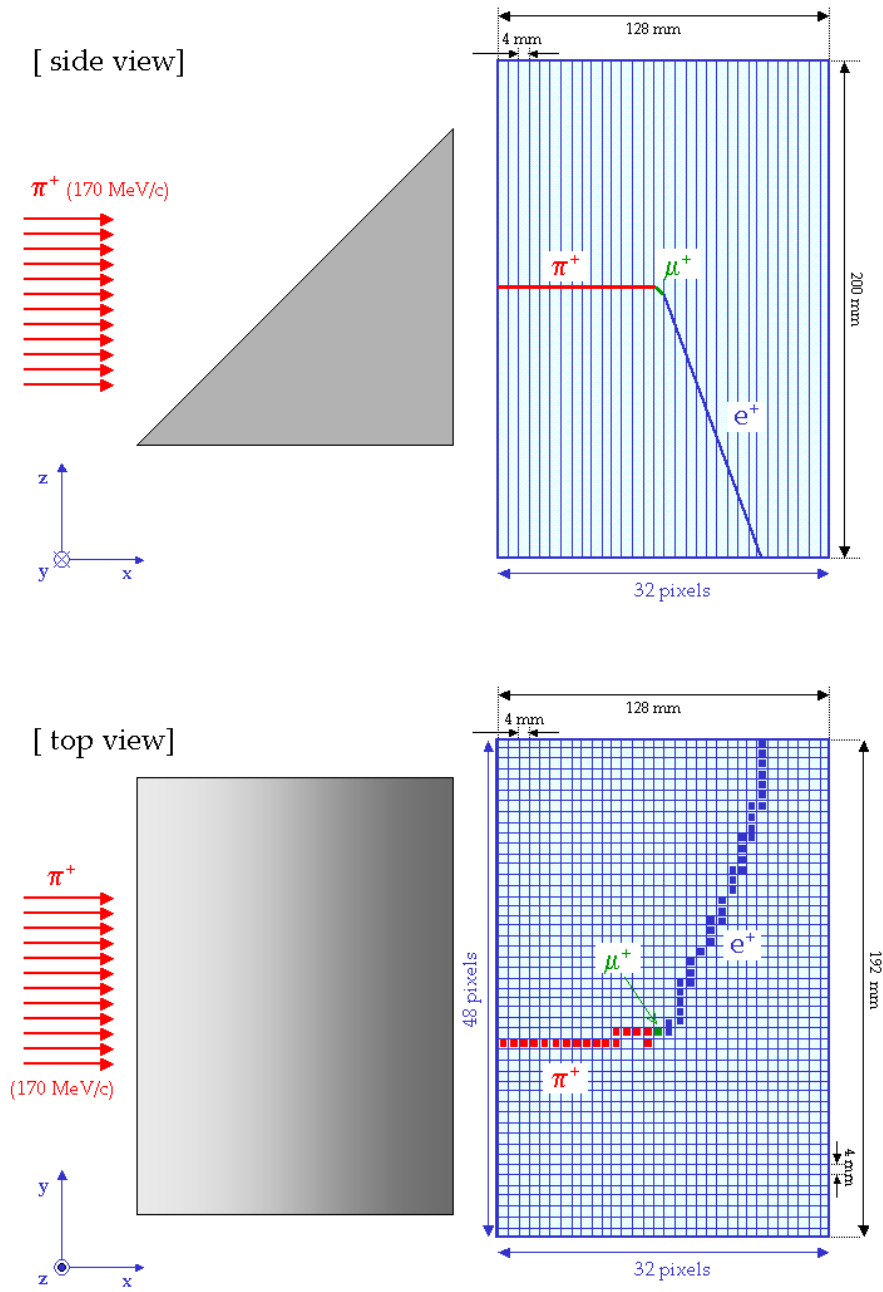


Figure 3.1: Schematic view of the FAST target, illustrating the general concept of the experiment. A pion is stopped in the target and the full $\pi^+ \rightarrow \mu^+ \rightarrow e^+$ chain is observed.

(i.e. π^+ and μ^+).

Both the detector and the readout, must be able to cope with a high intensity beam (up to about 1 MHz). This translates into a huge amount of data sent to the TDC's, to be processed by the DAQ chain (event builder, event analysis, storing) and the need of a data reduction system. The solution comes, once again, from the high granularity of the target. The information needed to measure τ_μ is spatially confined in a small region around the π^+ stopping point: the typical region of interest is a 7×7 or 5×5 pixels region around the π^+ stop. One needs to identify the π^+ stopping point for each event, and then apply a selective trigger which “activates” only a part of the DAQ. In practice, this is a selective trigger for the TDC's, so that - for each event - only the few TDC's interested by the event are read. The identification of the stopping pion location, together with the identification of the $\pi^+ \rightarrow \mu^+$ decay (i.e. the selection of good events) and the subsequent transmission of a selective trigger to the TDC's, is performed by means of a dedicated custom made circuitry, the so called Second Level (LV2) Trigger, whose logic and behavior will be detailed later in this chapter.

The present section provided an outline of the experimental concept of the FAST experiment, as well as a list of the main elements forming the experimental apparatus:

- the DC π^+ beam;
- the high granularity scintillator target, with its opto-electronics readout;
- the analogue readout chain, including preamplifiers and discriminators;
- the DAQ system, whose core are the time stamps of the analogue pulses by means of 16 TDC's;
- the LV2 trigger system.

The rest of this chapter will describe the design concept and the general characteristics of each of the above elements. The next chapter will complete the description of the FAST detector, with details about the detector performance.

The particles involved in the FAST experiment are *positively charged* pions, muons and positrons. Even when not specified, the positive charge of the particles will always be implicitly assumed in all the rest of this work. In particular, when “electrons” will be quoted, they mean indeed positrons.

3.2 The DC π^+ Beam

3.2.1 The PSI Accelerator Facility

The accelerator facility of the Paul Scherrer Institute (PSI) [42] - named after the Swiss physicist Paul Scherrer (1890-1969) and located in Villigen, Switzerland - is specialized in the production of extremely intense particle beams. The main accelerator is a separated sector cyclotron (the “Ring”) providing a high power proton beam at an energy of 590 MeV. Present beam currents are around 1.8 mA. The proton beam, not directly accessible by the experiments, is transported to two meson production target stations to generate secondary beams of pions and muons, which are available in several experimental areas. Table 3.1 lists the main properties of the PSI proton beam.

Ring proton beam at PSI	
Injection energy	72 MeV
Extraction energy	590 MeV
Beam current	ca. 1.8 mA DC
Accelerator RF frequency	50.63 MHz
Time between pulses	19.75 ns
Bunch width	ca. 1 ns

Table 3.1: Main characteristics of the PSI proton beam from the Ring cyclotron.

Behind the production targets, the beam is either stopped in a high power beam dump, or refocused on the target of a high flux spallation neutron source (SINQ). A few medical beam lines, for cancer treating proton therapy, are also active at PSI on dedicated areas.

3.2.2 The π M1 Beam Line at PSI

The π M1 beam line at PSI, where the FAST experiment is located, is a high resolution direct current pion beam line with a momentum range between 100 and 500 MeV/c. It is attached to the target station at an extraction angle of 22° . A momentum resolution of better than 0.1 % is achieved. The characteristics of the beam line are listed in Table 3.2.

For the FAST scopes, the beam has a momentum calibrated to 170 MeV/c, optimized for the pions to stop in the scintillator target material. It is operated in a

	π M1 beam line	FAST
Total path length	21 m	~ 24 m
Momentum range	100-500 MeV/c	170 MeV/c
Solid angle	6 msr	
Momentum resolution	0.1 %	
Spot size on target (FWHM)	15 mm horizontal	~ 10 cm
	10 mm vertical	~ 10 cm
Angular Divergence on target(FWHM)	35 mrad horizontal	
	75 mrad vertical	

Table 3.2: Characteristics of the π M1 beam line at PSI. The last column shows the specifics of the beam when operated to match the FAST requirements.

strongly defocused configuration - with an early focusing point - to provide a flat and wide distribution at the entrance to the target. The RMS spot size on target can be as big as many squared centimeters (order of 200 cm^2). Although the beam settings are tuned to optimize both the shape of the beam and its content in pions, a contamination of both muons and electron is still present. In the FAST beam tuning conditions the content of the beam has been directly measured (Figure 3.2) with the time of flight method: A first scintillator counter (BC1) is placed at the end of the last quadrupole of the beam line, another one (BC2) is in front of the FAST target location, about 4 m away from BC1. The start time is given by the RF cycle of the cyclotron, the stop time is given by a wide gate coincidence (20 ns) of the RF signal and the signal of the particle in both the scintillating counters. The measured TOF spectrum agrees well with the expected values. The pion beam content is approximately 55 % of the total.

3.2.3 The Level 1 (LV1) Trigger

The TOF spectrum of Figure 3.2 shows that we can efficiently separate the various particle components of the beam. In particular electrons are used for calibration purposes, while pions are selected for normal running.

A set of three scintillator beam counters is arranged along the beam line (see Figure 3.3):

- Beam Counter 1 (BC1): $30 \times 30 \text{ cm}^2$ wide, 0.5 cm thick ; located after the last quadrupole of the beam line.
- Beam Counter 2 (BC2): $16 \times 20 \text{ cm}^2$ wide (to match the size of the target), 1 cm thick ; located upstream of the target, very close to it.

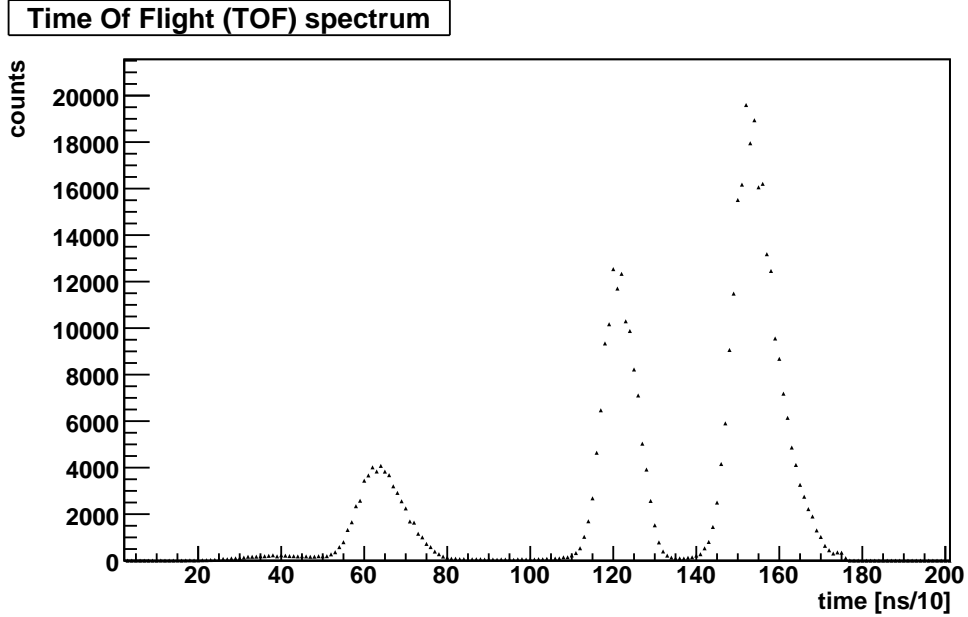


Figure 3.2: Time Of Flight (TOF) spectrum for the π M1 beam line, operated at momentum of 170 MeV/c in a defocused configuration. The clear separation between the different components of the beam (from left to right: muons, electrons, pions) is used to select pions for normal running and electrons for calibration tests.

- Beam Counter 3 (BC3): 30×30 cm² wide, 0.5 cm thick ; located downstream of the target.

A narrow gate coincidence (5 ns) between the RF signal and the beam counters BC1 and BC2 allows the selection of pions or electrons. When electrons are selected, the additional coincidence with BC3 is required to guarantee that the electron passed through the whole target.

The RF.BC1.BC2 coincidence (or RF.BC1.BC2.BC3 when electrons are selected) constitutes the nominal narrow³ beam trigger for FAST. For completeness we should add here that the z counter hodoscope (see Section 3.3.6) is also integrated in the beam trigger. The narrow beam trigger will be referred in the future as Level 1 (LV1) trigger. It has a fixed known delay of ~ 400 ns, with respect to the beam particle entering the target, due to cables length. It will be used as gate for the TDC and/or for the Level 2 Trigger System.

³ “Narrow” trigger means here selective trigger on one type of particles. It is to be considered opposite to the “wide” trigger - realized with a wide (20 ns) gate coincidence - where every beam particle (π^+ , μ^+ , e^+) entering the target provides a trigger.

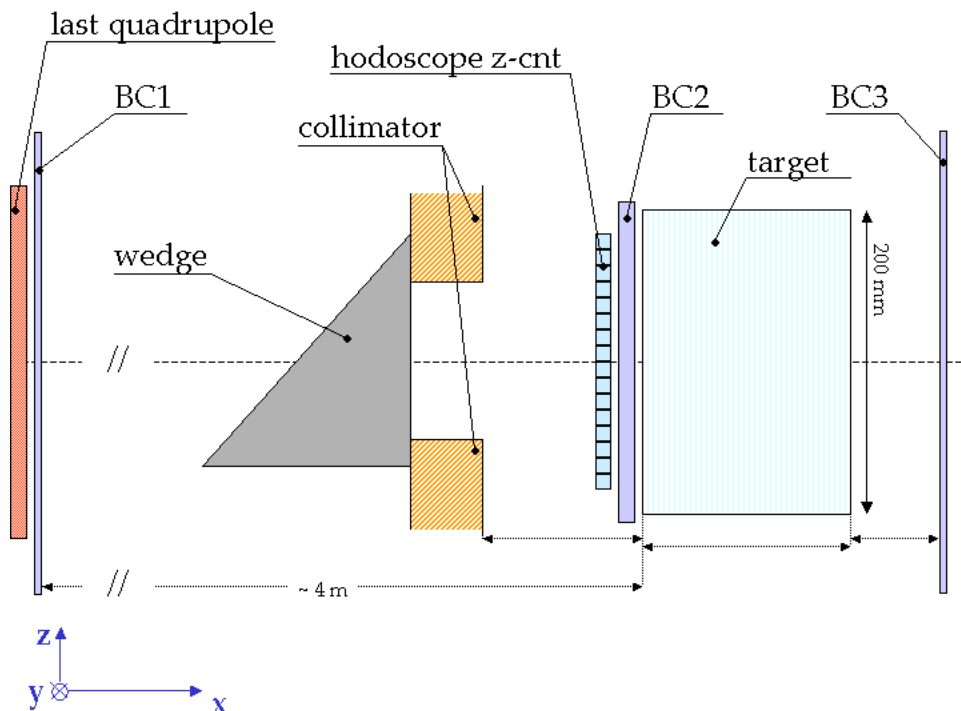


Figure 3.3: Side view of the beam line arrangement, from the last quadrupole of the π M1 beamline to the target. Incoming particles come from the left. The position of the three beam counters BC1,2,3 with respect to the target is shown. The role of the wedge, the collimator, and the hodoscope z counter drawn here is explained later in the text.

3.3 The FAST Target

3.3.1 The Scintillator Target

The FAST target is a high granularity scintillator target, built of 1536 scintillator bars (pixels), each of dimensions $4 \times 4 \times 200 \text{ mm}^3$, arranged vertically in a $32(x) \times 48(y)$ geometry⁴ for a total dimensions of $128(x) \times 192(y) \times 200(z) \text{ mm}^3$.

Each single pixel bar is cut from plates of solid plastic scintillator Bicron BC-400 (solid solution of organic scintillating molecules in a polymerized solvent) [43]. The scintillation emission of a typical plastic scintillator has a maximum around 400 nm (typical blue light). Plastic scintillators are characterized by a relatively large light output, typically 25-30% of NaI(Tl), and a short decay time, on the order of a

⁴The x, y, z reference convention used for FAST is the one shown in the sketches of Figures 3.1 and 3.3: the (x, y) plane is the horizontal plane, with x being the beam direction. z is the vertical direction.

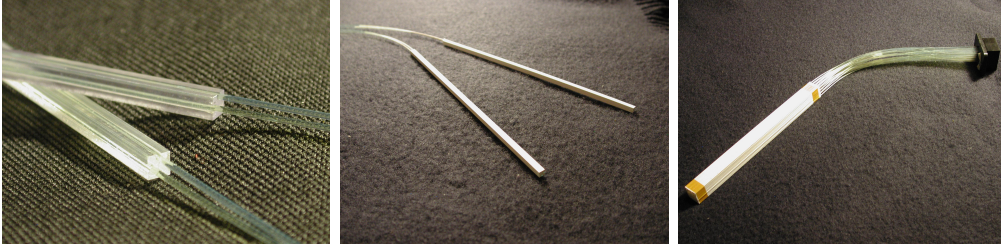


Figure 3.4: A few bars in different stages of their construction. Left: bare scintillator bars with the two grooves machined and the two wavelength shifting fibers inserted in the grooves. Center: two completed bars (fibers inserted and glued, bars painted). Right: group of 16 bars, arranged in a 4×4 geometry. The black mask visible at the end of the fibers is needed for the optical coupling with the photomultiplier.

nanosecond. This makes the material well suited for fast timing measurements.

The optical coupling between the scintillator bars and the photomultipliers, in charge of collecting the scintillation light and converting it to an analogue signal, is obtained by wavelength shifting fibers (WLSF), which absorb scintillation light and re-emit it near the wavelength of maximum response of the photomultiplier tubes. The re-emitted light is guided to the end of the fiber by total reflection. Several schemes concerning the number and diameter of the fibers have been tested. The adopted solution, which maximizes the light yield, minimizing at the same time the dead material, is to use two Bicon BCF-92 fibers [44] (1 mm diameter) inserted in each scintillator bar. They are fast blue to green shifters, characterized by a long attenuation length of more than 3.5 m. The peak in their emission spectrum corresponds to a wavelength of about 480 nm. To house the WLSF, two grooves are machined alongside each bar, on two adjacent sides. The two WLSF are then inserted and glued into the grooves with an optical cement (Bicon BC-600 [45]) specifically formulated for making optical joints with plastic scintillator. It has a refractive index ($n = 1.56$) very close to that of BC-400 plastic scintillator ($n_{scint} = 1.58$) and a very high transmission efficiency at the interesting wavelength: transmission $> 98\%$, for radiation of wavelengths above 400 nm, $> 95\%$ for wavelengths in 340 - 400 nm [44]. Each pixel, constituted by a scintillator bar with two WLSF inserted and glued in it, is finally uniformly painted with a white reflective diffusive paint (Bicon BC-620 [46]) to enhance photon collection and optically insulate each pixel from its neighbor channels. Figure 3.4 shows a few bars in different stages of their construction. After painting is applied, the final 1536 bars forming the target are bundled in 96 groups of 16 bars each in a 4×4 geometry (Figure 3.4, right), corresponding to a single photomultiplier tube. The wavelength shifting fibers of one bundle are inserted into a mask, which positions them with respect to the photocathode pads, and fixed by

glue. Figure 3.5 is a photograph of the target, assembled in its final geometry and housed in a special aluminum frame. The photomultipliers, each one reading one bundle, are mounted on the frame.

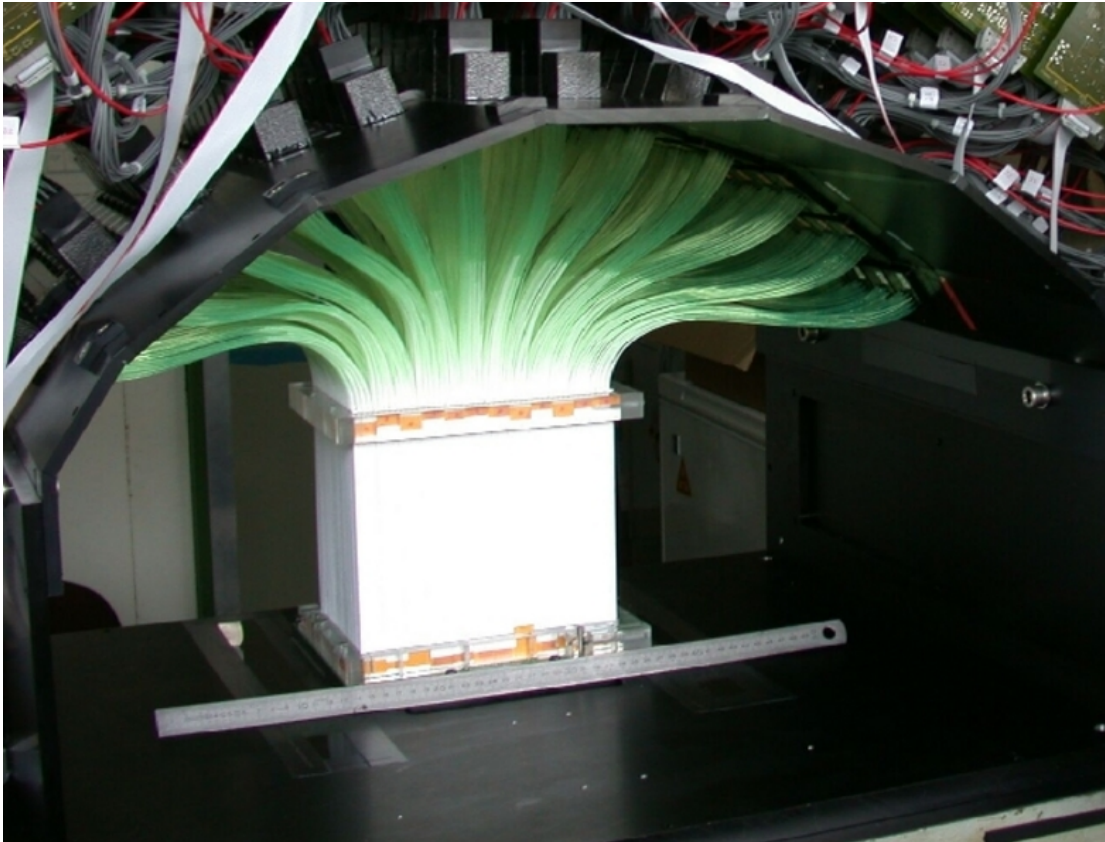


Figure 3.5: The FAST target: bars and fibers mounted in the final geometry. The scale in the photograph (50 cm long) gives an idea of the target dimensions. The black aluminum structure housing the target and the photomultipliers (on the top of it) is shown in the photograph.

Table 3.3 summarizes the materials adopted for the FAST target, together with their most relevant technical details, important for the detector concept.

3.3.2 Why “FAST”?

The original idea of the FAST target [36], when the experiment was proposed in 1998, was to have an active target built of scintillator fibers, instead of bars. This *Fiber Active Scintillator Target* (hence the name of the experiment) foresaw a parallel

Material	Technical Properties	
Scintillator		
BC-400[43]	refractive index	$n = 1.58$
	density	$\rho = 1.032 \text{ g/cm}^3$
	emission peak wavelength	$\sim 420 \text{ nm}$
	attenuation length	$\lambda_l = 160 \text{ cm}$
	decay time	$t = 2.4 \text{ ns}$
WLSF		
BCF-92[44]	diameter	$d = 1 \text{ mm}$
	attenuation length	$\lambda_l > 3.5 \text{ m}$
	absorption peak wavelength	$\sim 400 \text{ nm}$
	emission peak wavelength	$\sim 480 \text{ nm}$
Optical Cement		
BC-600[45]	refractive index	$n = 1.56$
	transmission	$> 98\%(\lambda > 400 \text{ nm})$
		$> 95\%(\lambda \in [340, 400] \text{ nm})$
Diffusive Paint		
BC-620[46]	reflectivity	$> 90\%(\lambda > 400 \text{ nm})$

Table 3.3: Materials adopted for the FAST target manufacturing, together with some of their technical specifications.

assembly of 0.5 mm diameter double cladded plastic scintillating fibers (Kuraray SCSF-78M), densely packed with a pitch of 0.51 mm. A group of 8×8 fibers ($4 \times 4 \text{ mm}^2$) formed the single target channel, one pixel. The manufacturing procedure with the original idea for the target was slow, manpower intensive, and rather costly. Finally the new way of building the target by means of plastic bars, instead of fibers turned out to be much more simple and efficient. The filling factor, i.e. the ratio of active scintillating material to passive material in a pixel is improved from 78.5 % in an all fibers construction to 87.5% for the current scheme. The improved attenuation length of the WLSF compared to the one of scintillating fibers is also a good advantage in terms of uniformity in the target response. The only potential draw-back is that the dead material (the two WLSF) is now concentrated in two places inside each pixel, instead of being distributed over its volume. Monte Carlo simulations have shown that this does not compromise the performance of the detector in terms of uniformity.

3.3.3 The LED Mask

At the base of the target a mask of 1536 light emitting diodes (LED) in a 1 : 1 correspondence to every bar of the target (within mechanical tolerance) allows illumination of single pixels in a controlled way, mainly for test purposes, target cabling control and channel integrity checks.

3.3.4 The Photomultipliers (PSPM's)

The opto-electronic readout of the FAST target is performed via Hamamatsu H6568-10 multianode position sensitive photomultipliers (PSPM) modules (Figure 3.6). The bare photomultiplier tube - without the base assembly - is the Hamamatsu R7600-00-M16 [47]. It is a 16 channels photomultiplier, with 4×4 pixels photocathode, each with a photosensitive area of $4 \times 4 \text{ mm}^2$. Metal mesh dynodes are powered by a built-in divider chain, which provides a gain above 10^6 and very sharp pulses, with a rise-time below 1 ns. The spectral response range is 300 nm - 650 nm, with a good uniformity of the quantum efficiency in the interesting wavelength region ($< 500 \text{ nm}$), Figure 3.7. The cross talk among the channels is below 1 %. Gain shifts between the 16 channels, up to 30%, are expected.

A total of 96 PSPM's is required to read out the 1536 target pixels. To match the PSPM granularity, the target pixels are bundled in groups of 4×4 bars. Each group of bars is connected to one PSPM via the special mask which houses the WLSF of one single bundle. To improve the optical coupling between the fibers and the photocathods, a thin layer of optical grease (Bicron BC-630) is put between the mask surface and the photocathode.



Figure 3.6: One of the photomultipliers adopted for FAST. The photocathode, with its 16 pixels (4×4), is visible in the front.

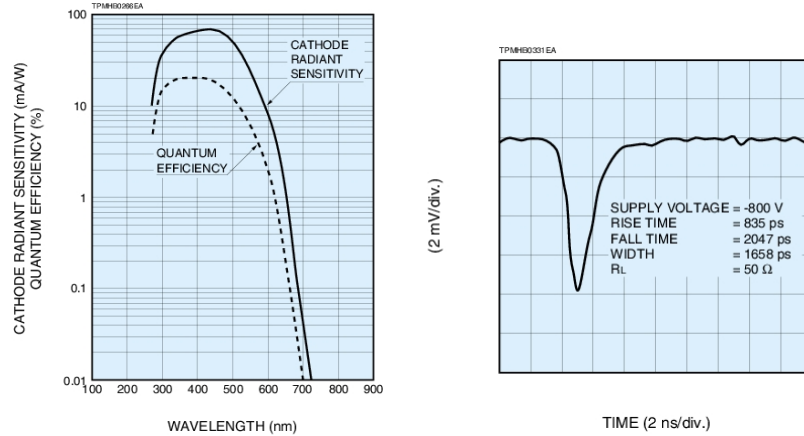


Figure 3.7: Typical spectral response (left) and time response (right) of the R7600-00-M16 tube in the H6568-10 assembly.

3.3.5 The Wedge and the Collimator

A uniform distribution of the pions stopping points inside the target is needed. This is achieved by the wide beam in the vertical (z, y) plane, and by a plexiglass wedge shape beam degrader in the beam x direction. The wedge provides a vertical gradient in the thickness of the absorber material, so that the pions entering the target penetrate different depths, depending on their vertical entry position. The shape and dimensions of the wedge are calculated computing the range of pions in plexiglass and scintillator, and combining this with the expected beam dimensions.

To cut the tails of the large beam distribution and also to restrict the fiducial volume for the stopping pions to the center of the target (to avoid efficiency loss or border effects due to pions too close to the limits of the target) a 5 cm thick copper collimator is placed between the wedge and the target (see Figure 3.3). Its aperture, centered with the target itself is $16(y) \times 10(z)$ cm². These are the final dimensions of the effective beam profile inside the target.

3.3.6 The Hodoscope z -Counter

The granularity of the FAST target allows the identification of the horizontal x and y positions of the particles, but is blind to the vertical z position. The z information is provided by the z -counter hodoscope, located immediately upstream of BC2 (see Figure 3.3). It is a horizontal hodoscope, built with the same material and technology than the target itself. It consists of 16 scintillator bars (of dimensions $10(x) \times 200(y) \times 10(z)$ mm³ each), piled horizontally one on top of the other, covering the central region of the target. The thickness of the bars assures a clear signature for the

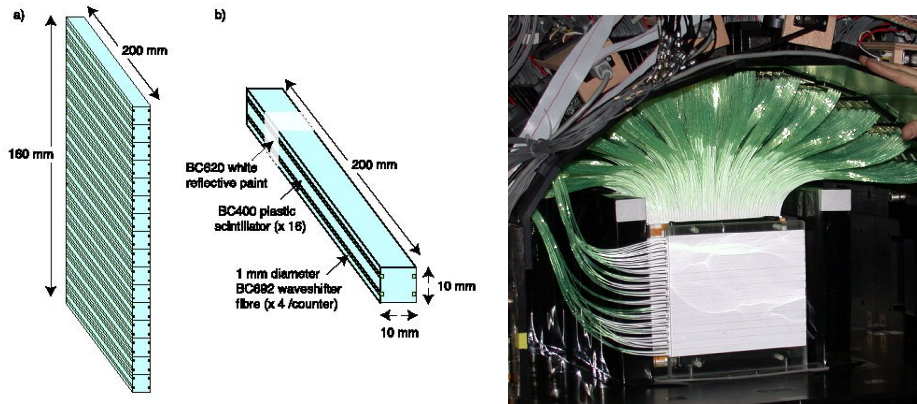


Figure 3.8: Left: Hodoscope z -counter design: assembly (a) and details of a single counter (b). Right: A picture of the z -counter hodoscope.

particles entering the detector, thus making available unambiguous information on their vertical position, with a 1 cm pitch. Two PSPM's are used to read the 16 channels of the hodoscope. Their signals are integrated into the full readout chain of FAST, so that a z -entry position of the beam particle is attached to every event. The scintillation light from each bar of the hodoscope is led to the PSPM's by four WLSF attached to each bar. Figure 3.8 shows a sketch and a picture of the z -counter hodoscope geometry.

The z -counter signals are included in the LV1 trigger. In particular the OR of the z -counters from bar 3 to 14 is used in coincidence with the RF, BC1 and BC2 signals to form LV1. The lower ($z = 1, 2$) and upper ($z = 15, 16$) part of the hodoscope are excluded from the trigger, because they correspond to the region of the target masked by the copper collimator.

In the original design of the FAST experiment [36] the measurement of the vertical position of the beam was not foreseen, but it turned out to be extremely useful, under different points of view. First of all, the z information integrated in the full read-out chain of FAST allows a fast direct measurement of the vertical beam profile. In addition, it is useful to suppress residual beam muons. Despite the fact that beam muons are already highly suppressed by the requirement of positive identification of the $\pi^+ \rightarrow \mu^+$ decay, a small contamination of muons remains. At a momentum of 170 MeV/c, the kinetic energy of the muons exceeds that of the pions by several MeV, resulting in a strong range separation between the two beam particles: muons travel about 8 cm – i.e. 20 pixels – deeper into the target. When the wedge is installed we cannot discriminate between pions that travel through a thin part of the wedge, and muons that travel through a thick part of it. However, with a z -counter tag, it is possible to resolve the $\pi^+(\mu^+)$ vertical position, and so to reject the beam muons by

a large factor. Finally, the existence of the z -counter tag for each muon decay event allows a study of the possible systematics related to the vertical position of the event in the target.

3.3.7 The Magnetic Field

To assess systematics due to residual muon spin rotation (μ SR) effects, a weak and homogeneous transverse magnetic field of about 80 G is constantly maintained in the target region. The problematics related to the μ SR effects, including the systematic uncertainty that derives, will be treated in Chapter 6. For the moment, it is important to underline the existence of a possible residual anisotropy in the detection efficiency for the electrons, which would mimic the effects of a polarized muon source, and the existence of a residual contamination of polarized beam muons. The latter is suppressed, at the first order, by the identification of the complete $\pi^+ \rightarrow \mu^+ \rightarrow e^+$ chain, and even further suppressed by the range requirements combined with the z -entry point information. In the presence of a magnetic field (and at least the Earth's magnetic field $B \sim 0.5$ G has always to be considered), the residual polarization effects combined with possible anisotropies, could result in a time dependent efficiency, affecting the muon lifetime slope, with a periodicity fixed by the precession frequency of the muon spin in the magnetic field. The role of a stronger local field in the target region is to accelerate the muon spin rotation, precessing the muons on a known and measurable timescale, short compared with the lifetime measurement interval ($20 \mu\text{s}$). A suitable field is 80 G, which produces a muon precession frequency f_μ (Hz) = 13.55×10^3 B(Gauss) = 1.1 MHz and a precession period $T_\mu = 0.92 \mu\text{s}$.

The magnetic field should be roughly homogeneous inside the target, and transverse with respect to the bar orientation. The photomultipliers have to be arranged accordingly. They have indeed a recommended orientation inside magnetic fields, where the dynodes gain is unaffected. The magnetic field is provided by a permanent magnet - designed and commissioned by the PSI magnet group [48] - consisting of two magnetized ferrite planes, placed on the two sides of the target. Each one of the two magnet planes is formed by several ferrite blocks, separately magnetized and then assembled to achieve a symmetrical array structure (Figure 3.9). Measurements of the magnetic fields produced by the two ferrite arrays show good performance, with a homogeneity in the target region inside the specified limits of $\pm 20\%$ (Figure 3.10).

3.3.8 Final Configuration of the FAST target

Figure 3.11 shows the FAST target in its final configuration, housed in the "mailbox" aluminum frame, which serves as a holding structure for the WLSF bundles and for the photomultipliers. In front of the target the wedge and the z -counter hodoscope



Figure 3.9: Left: An array of (not yet) magnetized ferrite blocks arranged on the aluminum plate support. The outer thick ring provides the main field, the inner thinner blocks improve homogeneity. Right: One of the two ferrite plane assemblies, ready for installation. (Dimensions: $30 \times 30 \text{ cm}^2$).

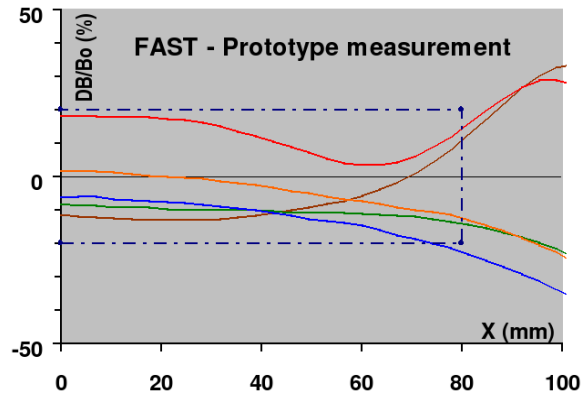


Figure 3.10: Homogeneity of the magnetic field, measured on five planes separated by 4 cm one to the other. The planes are chosen parallel to the target diagonal and then projected on the X-axis, which corresponds to the y direction in the FAST reference.

(partly hidden by the wedge itself) are visible. Between the hodoscope and the target there is the BC2 beam counter (not visible). The two vertical black blocks at the sides of the target are the two magnet plates: they are inserted in the target region from the bottom through two slits machined in the aluminum frame base. They are shown in the photograph already enclosed in their light shielding. The whole target area is light shielded with black plastic foils glued on the vertical planes (front and rear) of the target housing. The photomultipliers are mounted on the supporting structure. The cables visible at the top of the PSPM's location are the analogue signal cables entering the preamplifiers and their power supply. The two grey aluminum plates

at the two sides of the mailbox, as well as the wooden structures inserted among the photomultipliers, are the supports for ventilator units, needed to improve air circulation in the dense preamplifier cabling above the photomultipliers region.



Figure 3.11: The final FAST target, including the wedge, the z -counter hodoscope and the magnet plates on the two sides of the target.

3.4 Analogue Readout Electronics

The analogue front-end electronics for FAST is realized with custom made units of preamplifiers and discriminators, designed explicitly to match the FAST requirements. Both units have been designed and constructed at PSI.

3.4.1 Preamplifiers

The preamplifier unit is a custom made unit (Figure 3.12, left), built on a PCB card, with $16 \times 50\Omega$ analogue lemo inputs and $16 \times 50\Omega$ analogue outputs, mounted

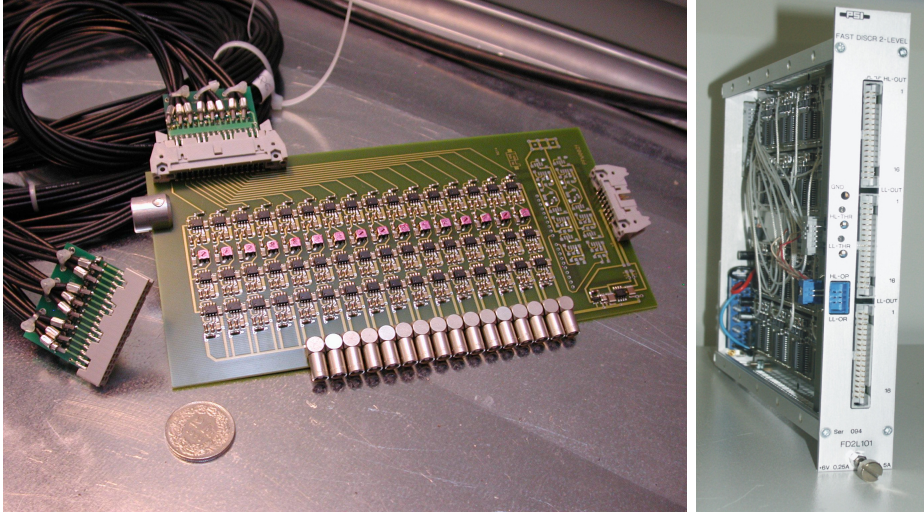


Figure 3.12: Photographs of the analogue FAST readout electronics components. On the left is a preamplifier unit, connected to the long 50Ω cable. The input signals for the preamplifier (through the 16 lemo connectors) are the raw pulses from the PSPM's. On the right is a discriminator: the input connector is on the rear panel, the output connectors (HL \times 16, LL \times 16, LL \times 16) are on the front panel. The 2 photographs do not have the same scale.

on a flat-cable connector. Each preamplifier unit receives the raw pulses from one photomultiplier and serves both as shaper and amplifier, with a gain of about a factor 5. It is powered by a low voltage (6 V, 1 A) standard NIM power supply.

The preamplifier design foresees as an option the possibility to install an analogue OR of all the 16 inputs. This feature is used only on the two z -counters preamplifiers, to provide the signal for the LV1 trigger formation.

The preamplifiers are mounted about 30 cm above the target (above the PSPM region) and densely packed in their frame structure.

3.4.2 Discriminators

The FAST discriminators are custom 16 channels NIM leading-edge discriminator units (Figure 3.12, right). They are dual threshold discriminators, with two independently adjustable thresholds, that will be referred to as LL (for the low level) and HL (for the high level). The discriminators receive as inputs the 16 analogue signals from the preamplifiers. They provide, as output, two identical LL signals and one HL signal for each of the 16 input channels. The LL(\times 2) and HL outputs have identical circuitry, with two independently adjustable thresholds (common to all 16 channels). The output pulses are standard differential ECL pulses, with a minimum width of

13 ns, which matches the TDC requirements. The output is triggered by any input pulse exceeding the threshold for at least 2 ns. The double hit resolution for the discriminator is about 13 to 15 ns. The discriminators work in “updating mode”, so that if two input signals are closer than the double hit resolution, the output is one single wider pulse. This feature is important to avoid generation of glitches, that would compromise the good functioning of the TDC’s. Every discriminator unit has two additional ECL LL-OR and HL-OR outputs, which are the logic OR of the 16 channels, both in LL and HL. With the present configuration of the experiment, the OR outputs of the discriminators are not used.

The thresholds for the discriminators are remotely adjustable (via Slow Control), in a range from 50 mV to 2 V. This design feature is useful for calibrations, for dedicated special runs (especially LV2 tests in HL mode), and it is needed to suppress the discriminators outputs during the TDC initialization phase (where the thresholds are set to the maximum allowed value).

With a proper choice of the two LL and HL thresholds, discriminators are sensitive to both mip’s (e^+ tracks) and stopping particles (π^+ close to its stopping point and $\pi^+ \rightarrow \mu^+$ decay). The LL outputs of the discriminators are the inputs for the TDC’s, which will have the full information (position and timing) for all the hits happening in the target. At this stage in the DAQ chain, there is no discrimination between a pion and an electron. The HL outputs of the discriminator are sent to the LV2 trigger – only element in FAST to have access to HL data – which computes the stopping π^+ and μ^+ coordinates and passes these informations to the TDC’s.

3.4.3 Matching between Preamplifiers and Discriminators

In the baseline design, the discriminators have a 50Ω input impedance. This imposes the use of 50Ω cables between the preamplifiers and the discriminators, as well as 50Ω matched output impedance for the preamplifiers. On the other hand, both preamplifiers and discriminators are designed - for simplicity and cost reasons - to use flat cable connectors, as output (for the preamplifier) and input (for the discriminator). Custom made bundles of 5 m long 16 coaxial lemo cables (50Ω) between preamplifiers and discriminators are used. The 16 cables are bundled together in a small PCB card with signals and grounds separately connected, and a flat cable connector mounted on it (Figure 3.12).

96 preamplifier units, coupled to 96 discriminators are needed. When the preamplifier is connected to the discriminator, it shows an additional negative offset of about 100 mV, due to a strong asymmetry in the power consumption of the discriminator. This offset is temperature dependent. Special care has been taken to keep the working temperature as stable as possible: the preamplifiers are constantly powered and several fans are added in the proximity of the preamplifiers to improve the air

circulation.

3.5 Target Mapping and Cabling

Figure 3.13 shows the schematics of the FAST target, including the mapping adopted for each of its channels. It is a modular mapping, repeated identically in all the different regions of the target. One tube corresponds to a 4×4 pixels region of the target, and it also corresponds to one preamplifier and one discriminator unit. The output signals of a group of 6 discriminators - corresponding to a rectangular 8×12 pixels region of the target - are sent to one TDC. The thick red lines in the picture are the TDC's borders. To cover the target with this mapping logic, 16 TDC's are needed.

3.6 The Data Acquisition (DAQ) System

The Data Acquisition System (DAQ) for FAST is in charge of the following tasks:

- Measure the timing of the raw pulses (outputs of the discriminators), corresponding to particles hits in the detector. A precise time measurement is needed. This is done by means of high performance CAEN V767 Time to Digital Converters (TDC's), clocked by an accurate frequency standard.
- Build the events, grouping together the single hits that are fragments of the same particle track, or the same time slots (Event Builder stage).
- Pass these events to the analysis stage, which has to recognize the particles in the $\pi^+ \rightarrow \mu^+ \rightarrow e^+$ chain and extract the muon lifetime value.

Given the high beam rate and the high target granularity, a huge amount of data is generated. A data reduction system (the LV2 trigger) has been developed, as it will be shown later.

This section will explain how the precise time measurement is obtained in FAST and how the DAQ system works, from the raw data up to the analysis stage. The details of the analysis procedure will be given in Chapter 5.

3.6.1 Precise Time Measurement

The requirements of a high precision time measurement and high rate capabilities for the FAST detector are met by 16 CAEN V767 Time to Digital Conversion (TDC) units, driven by a very precise and stable external clock.

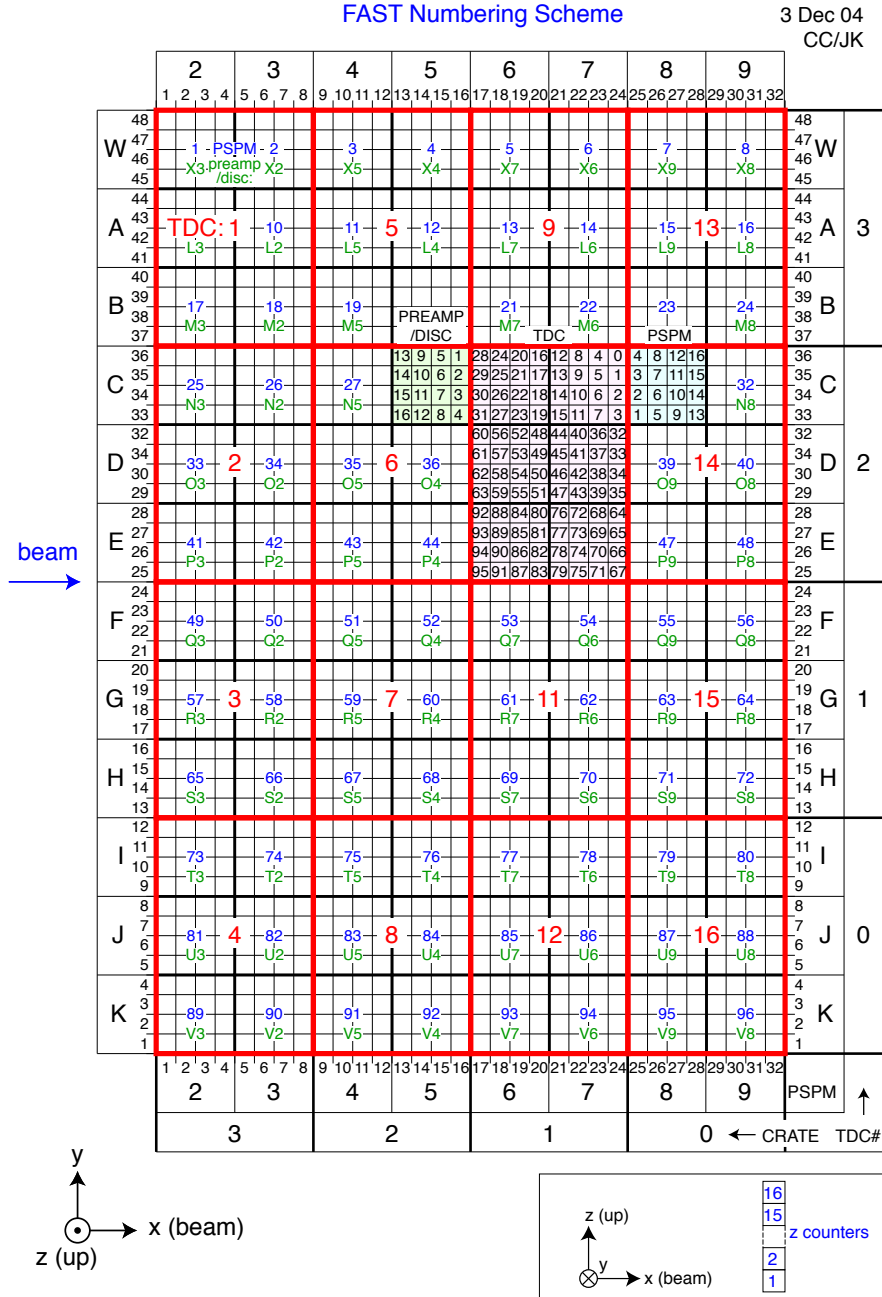


Figure 3.13: Scheme of the FAST target, where the photomultiplier (blue), preamplifier/discriminator (green) and TDC (red) structure and mapping is shown: each photomultiplier is connected to one preamplifier, which is in turn connected to one discriminator. Each TDC is receiving data from 6 different discriminators. At the bottom the numbering scheme for the z counters is also shown.

The CAEN V767 TDC units [49] are high performance TDC's, based on a custom 32-channels general purpose TDC chip developed by the CERN/ECP micro electronic group for high precision time measurements [50]. The CERN/ECP-MIC TDC chip provides a time stamp of each incoming hit, with zero conversion time. The typical bin size (1 TDC tickmark) is 0.78 ns at 40 MHz clock speed (1.04 ns at 30 MHz), with a 21 bit dynamic range. The most significant 16 bits are the "coarse" time counting, given by the counting of the clock cycles; the 5 less significant bits (32 TDC tickmarks) are generated by the TDC chip, through a Delay Locked Loop (DLL) and a Charge Integration Device. The two hits resolution on a single channel is 10 ns and the rate capability is up to 1 MHz/channel with all channels hit simultaneously. The CERN/ECP-MIC TDC chip has an internal circular hit buffer and the capability to retain only those hits within a software set time window. Both the width and the position of the time window relative to the trigger signal for the TDC's are programmable parameters. In our case the trigger is provided by the pion entering into the target and the time window is set to $[-10 \mu\text{s}, +20 \mu\text{s}]$ with respect to the trigger. This means that, together with the hits in the 20 μs time window needed to observe the μ -decay events, also the hits occurring in the target up to 10 μs before the arrival of the pion are recored. This negative time region provides the best way to estimate the level and the detailed structure of the background for the experiment.

Four CERN/ECP-MIC TDC chips are hosted in one CAEN V767 board, which manages the sharing of the informations from the chips and the dispatch of the control signals (like the trigger and the clock) to each chip. Beside the distribution of common control signals, the board is in charge of the VME interface of the TDC chips. It provides a local memory FIFO buffer, that can be readout via VME, in a completely independent way from the acquisition itself.

The TDC can be driven by an internal 40 MHz clock, or an external clock (maximum allowed frequency 45 MHz). The precision of the TDC clock determines the "coarse" time linearity of the TDC. The requirements for FAST are a high precision ($\Delta t \sim 0.1$ ps) and a high stability ($\frac{\Delta t}{t} < \frac{0.1 \text{ ps}}{2 \mu\text{s}} \Rightarrow \Delta t/t < 5 \times 10^{-8}$). These requirements are beyond the performance of temperature compensated crystal oscillators, like the ones internal to the CAEN V767 boards ($\Delta t/t \sim 10^{-6}$), and impose the use of a more precise external clock. At present, FAST adopts a 60 MHz rubidium atomic frequency standard (made by Quartzlock UK, Totnes England), prescaled by a factor two to 30 MHz, with a precision that largely exceeds the requirements ($\Delta t/t \sim 2 \times 10^{-10}$). A calibration and monitoring system, based on a pair of these clock units - one to provide the clock to the TDC's, the other to verify possible time drifts - is used to verify the stability of the time measurement and the full functionality of the system.⁵

⁵ The double Rb clock system as external clock to the TDC's and stability cross check device will be replaced in the future by a standard GPS 40 MHz clock - whose nominal stability already

Each CAEN V767 unit has a total of 128 independent Time to Digital Conversion channels. TDC channels are cabled such as to correspond to rectangular contiguous regions of target pixels (see Fig. 3.13). In particular, three of the four available chips in each TDC unit (96 channels) are devoted to the reading of the data hits from the target (LL hits from the discriminators). The remaining chip is filled by the so called “control words”, which include all the other needed information, like the triggers, the tags and the LV2 coordinates (see below). In total 16 TDC units are needed for the FAST readout, for a total of $128 \times 16 = 2048$ available channels (1536 of which are used for data, the rest for control words information).

3.6.2 The DAQ Architecture

Despite its small size, the FAST detector generates a very high data flow, due to the 1 MHz beam rate, combined with the target granularity. This sets severe constraints on the architecture of the data acquisition system. It must be able to sustain a high data throughput rate of 80 MB/sec (see later for the justification of this number). The incoming data must be read out by the TDC’s and transferred to the processor stage, where event reconstruction has to be performed *in real time*. Data have then to be analyzed *online*. A full online analysis is mandatory, because it is not feasible to store such a huge amount of data: assuming that all the data could be written on disks at the rate of 80 MB/sec, the required disk space would be of the order of 7 TB per day. Only the relevant histograms created by the online analysis code are stored on disks.

The architecture of the DAQ system is schematically illustrated in Figure 3.14. The 16 CAEN V767 TDC’s are accommodated in four VME crates. A VME-PCI interface (PVIC link, [51]) allows a CPU-less access to the VME bus by the dedicated DAQ PC’s (“daq0x” in figure) through their PCI bus. Four PVIC chains are used in total, each one linking one VME crate to the corresponding dual processor DAQ PC. The maximum nominal data rate extraction from every VME-PVIC chain is ~ 20 MB/sec. This limits the maximum data rate from the DAQ to 80 MB/sec.

Data are read out from the DAQ PC’s by means of a “collector” PC, which receives data and routes them toward the “event builder” PC’s, sending time-slices of the collected data in a round-robin fashion. Given the TDC’s reading structure, including the selective LV2 trigger that will be described below, an event builder procedure is needed. Each event can indeed be formed by parts obtained by different TDC’s (fragments of the event), and a priori it is not known how many TDC’s contain fragments of the same event. It cannot be assumed that the fragments are coming out of the TDC’s in a particular order and there is no event number provided by the

meets the FAST requirements - with the advantage of well reduced maintenance costs. The higher clock period would also correspond to an improved resolution.

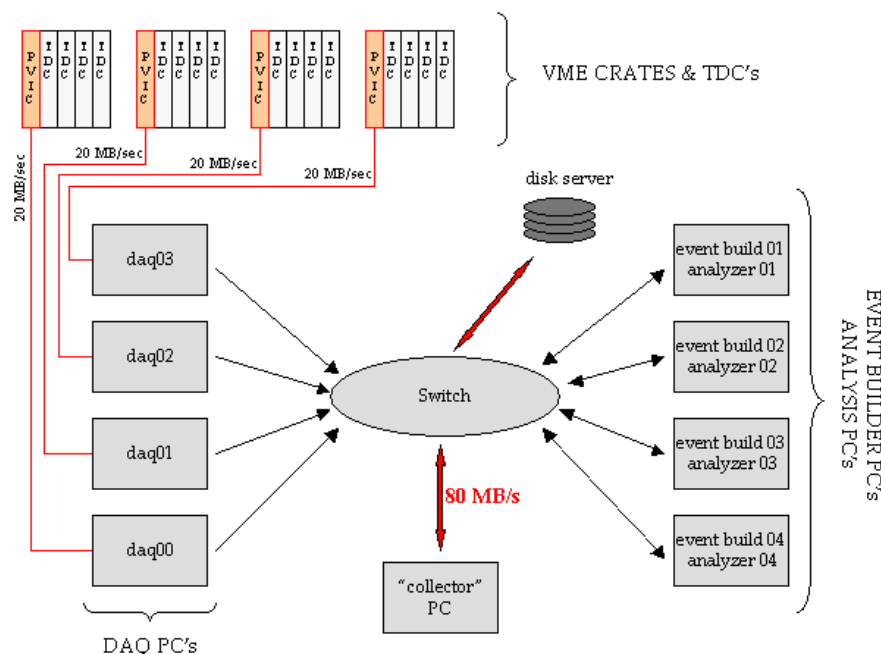


Figure 3.14: DAQ architecture design for 2006 data taking run, corresponding to a maximum achievable bandwidth of 80 MB/sec. The current scheme is proved to sustain a LV2 data rate of about 60 kHz, corresponding to a beam rate of about 350 kHz. An upgrade of the DAQ (with the doubling of the number of PVIC nodes, from 4 to 8) is foreseen for the 2007 run, where the maximum nominal allowed bandwidth will be 160 MB/sec.

TDC's. The reconstruction of the events is done on the basis of two control signals sent to dedicated channels simultaneously on all TDC's. They are two asynchronous clocks with a period of $18 \mu\text{s}$ ("TAG1" control word) and $19 \mu\text{s}$ ("TAG2" control word). The periods for the tag clocks are chosen such that at least one TAG1 and one TAG2 appear in the $30 \mu\text{s}$ time window. In 60 % of the cases, two TAG1 and TAG2 signals are contained. Their time difference (TAG1 – TAG2) constitutes the event number attached to every fragment, that permits to associate the fragments coming from different TDC's but forming the same event.

Once the event is completely built, it is passed to the analysis stage. The event builder PC's, four dual processor machines, also host the code running the full analysis, and producing all the data histograms. All histograms, together with a fraction

($\sim 1/100$) of the full events are stored on a RAID disk server, with 5 TB of maximum disk space.

The local area network uses a dedicated Gigabit switch/router. The data transfer protocol used both for DAQ and analysis PC's is based on UDT [52], a reliable high performance data transport protocol, with less overhead, compared to standard TCP/IP. It has the advantages of auto-tuning and auto-monitored mechanisms.

The current scheme (adopted for the data taking run of 2006) has been proven to sustain a TDC trigger rate up to 60 kHz, where saturation of the VME bandwidth starts to appear. When this happens, a BUSY signal feed-back provided by the TDC's is used to veto incoming new triggers, until the buffers are empty and ready again to acquire new data.

3.6.3 DAQ Rate Performances

With the present DAQ architecture design (Figure 3.14), the maximum achievable bandwidth corresponds to 80 MB/sec. As mentioned, bandwidth saturation is achieved at a trigger rate for the TDC's of about 60 kHz. Table 3.4 summarizes - in terms of rates (TDC trigger rate, LV1 rate, beam rate) - the best performances achievable by the present DAQ system. As it will be explained in the following section, the TDC trigger rate is the selective LV2 trigger rate; the corresponding LV1 trigger rate is the rate of pions in the target.

DAQ rate performances		Efficiency
bandwidth	80 MB/sec	
TDC trigger rate (LV2)	60 kHz	
LV1 trigger rate	160 kHz	LV2/LV1 = 0.37 (see § 4.11)
beam rate	300-350 kHz	LV1/beam \sim 0.55 (see Fig. 3.2)

Table 3.4: Best achievable performance of the DAQ system – in the design of Figure 3.14 – at its bandwidth limit.

With the rates quoted in the table, the required data taking period would be larger than a few months. An improvement by a factor 2 to 3 at least is thus required in the DAQ to be able to increase the beam rate in the running conditions, and consequently reduce the data taking period. The foreseen actions for the 2007 data taking are detailed below.

3.6.4 Future Upgrade in the DAQ Architecture

A significant hardware upgrade in the DAQ, consisting in doubling of the number of PVIC nodes, is foreseen for the 2007 data taking period. We presently use 4 VME

crates, with 4 TDC's per crate. The PVIC system will be doubled to run with 8 VME crates and only two TDC's per crate, read by 8 PVIC links. This upgrade will raise the data bandwidth limit from 80 to 160 MByte/s. Eight DAQ PC's will be needed, while four event builder and analyser PC's will be sufficient to manage the doubling of the PVIC nodes.

A different strategy to increase the allowed rate is a change in the operating mode of the TDC's. The TDC's are currently operated in the nominal *stop trigger matching* mode, where the TDC's measure the timing of the group of hit signals that reach the enabled channels within $-10 \mu\text{s}$ and $+20 \mu\text{s}$ of a given trigger. They can also be operated in the *continuous storage* mode, that ignores triggers (the concept of "event" becomes meaningless) and simply continuously time stamps all hits and streams them through the buffer. In the trigger matching mode, at high beam rates, when overlapping events start to appear geometrically close one to the other, the same hits can be read out several times, for every time window attached to a different LV1 trigger, generating additional data and occupying bandwidth. This would be avoided in the continuous storage mode, where every hit would be counted only once. The change from stop trigger matching to continuous mode for the TDC's would allow an increase in the maximum achievable rate, that has still to be quantified by measurements. A factor two in the final beam rate is expected. It will however involve a very substantial re-writing of the DAQ software and event building, since e.g. the trigger matching over the $30 \mu\text{s}$ window must then be done in the DAQ software.

For the incoming 2007 data taking period both lines of actions, double the hardware and continuous storage mode, will be tested.

3.7 The Level 2 (LV2) Trigger

The second level trigger system (LV2) is a crucial element in the FAST detector, mainly needed to reduce at an early stage the data bandwidth that has to be handled by the DAQ chain. The problematic is the following: at 1 MHz beam rate, the global data throughput from FAST – calculated via realistic simulations that include triggered events, spectator beam particles, overlapping TDC triggers and efficiencies [53] – is around 2300 MB/sec. This number largely exceeds the hardware bandwidth limitations of the data acquisition system (80 MB/sec at present; 160 MB/sec after the foreseen hardware upgrade). The need of a reduction in the data rate that accesses the DAQ is then evident. This task is performed by the LV2 trigger system, which serves as a *selective* trigger for the TDC's. At the same time, it performs an event selection, retaining only those events where the stopping π^+ and the subsequent $\pi^+ \rightarrow \mu^+$ decay are observed. All the other events, e.g. the ones where the μ^+ pulse is lost, because of the double hit resolution, are rejected. Beside this, the LV2 also provides the coordinates of the stopping particles, that help to correctly analyse the events

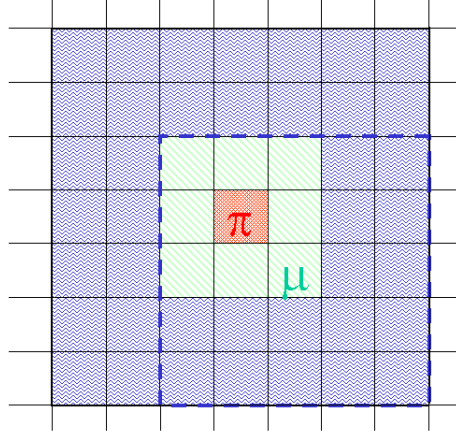


Figure 3.15: The superpixel logic: once the (x_π, y_π) coordinates for the stopping pion are defined, all the relevant time information for the event are confined in a 7×7 pixels region centered on (x_π, y_π) , the *superpixel*.

and identify the relevant hits of the $\pi^+ \rightarrow \mu^+ \rightarrow e^+$ chain among the data written to the TDC's.

The LV2 trigger system receives as inputs the HL data from the discriminators, corresponding to stopping π^+ and μ^+ , and is gated by the LV1 trigger signal, which indicates that a correct beam π^+ entered the target. The LV2 trigger provides as output a trigger only for the TDC's interested by the event, which contain the π^+ and μ^+ decays. This selective trigger for the TDC's will be referred to in the future as LV2 trigger (or simply LV2).

The LV2 trigger logic is based on the fact that each TDC (Fig. 3.13) covers a rectangular – 8×12 pixels – region of the target and that all the relevant time information for each event is confined in a small geometrical region of a few pixels centered around the pion stopping point. This is shown in Figure 3.15. Regardless of the beam rate, once the stopping pion coordinates (x_π, y_π) are identified, the muon, which has a range of ~ 1.5 mm, will be stopped in the same pixel as the pion or in a neighboring one, in the 3×3 pixels region surrounding (x_π, y_π) . The positron track emerges from the muon coordinates pixel (x_μ, y_μ) . Obviously, the bigger the region where one can look for the positron track, the better is the e^+ identification. But indeed a 5×5 pixels region surrounding (x_μ, y_μ) is enough to identify without ambiguity the e^+ track, because it always provides - apart from possible inefficiencies - at least two hits for the track. Finally, a 7×7 pixels region, centered on (x_π, y_π) is the minimum region which fully contains the event, without any loss of information. This region of interest for the event will be also referred to as *superpixel*, and it will

always be centered on the stopping pion coordinates (x_π, y_π) .

The LV2 trigger system operation can be separated into the following stages. For each event that is triggered by a LV1 trigger, the LV2 system has to perform the following operations :

- Localize the pion stopping point in the target and define its coordinates (x_π, y_π) .
- Look for the appearing muon in the 3×3 pixels region around (x_π, y_π) , in a time interval of about 100 ns after the pion has stopped. The muon coordinates (x_μ, y_μ) are then computed.
- Define the superpixel centered on (x_π, y_π) , and identify which are the TDC modules containing at least one pixel of the superpixel.
- Send the trigger signals only to those TDC's containing the superpixel: it can be only one, two or four (see Fig. 3.13). On average 2.4 TDC's, instead of 16, are triggered for each event.

When operated in its nominal conditions (see later), the LV2 does not send the triggers to the TDC's if the μ^+ has not been found. In this sense, it acts as an event selection tool.

- Send the coordinates of either the pion or the muon to the TDC that contains it.

The role of the LV2 trigger system as a data reduction system for FAST is explicitly shown in Figure 3.16, where two different real event displays corresponding to LV1 (left) and LV2 (right) triggered events are compared. In case a *global LV1 trigger* is used for the TDC's, the trigger is provided by a pion entering into the target and it is sent simultaneously to all 16 TDC's. All the hits happening in the target in the $[-10 \mu s, +20 \mu s]$ time window (w.r.t. the trigger) are recorded by the TDC's and sent to the subsequent DAQ stages. In the event shown (Figure 3.16, left), three decay events happen in the same TDC time window. However the trigger has been provided by one event only (the one with the most penetrating track, in black dots that represent the track for the pion which provides the LV1 signal) and the TDC time window has been set with respect to its timing. In the analysis, only the muon lifetime informations relative to this event will be retained. Only for this event we can unambiguously identify the time of the pion ($t=0$) and apply the rest of the analysis for the recognition of the muon and the electron. The other two events are background. Increasing the beam rate in such a configuration for the trigger would increase the accidental rate, without improving the rate of good events, i.e. $\pi^+ \rightarrow \mu^+ \rightarrow e^+$ chains, with π^+ in time with LV1. The situation is totally different when the *selective LV2 trigger* is used (Figure 3.16, right). As usual, a pion

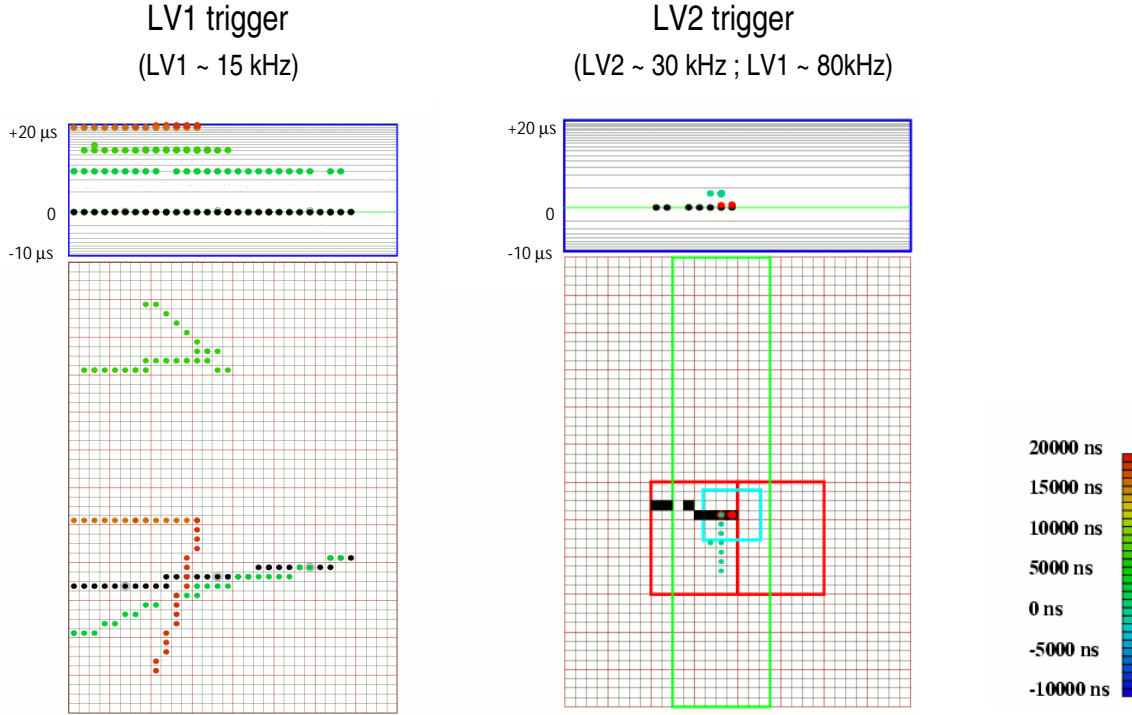


Figure 3.16: Typical event displays for two different events where the global LV1 (left) and the selective LV2 (right) trigger are used as triggers for the TDC's. The two pictures correspond to rates of beam pions (LV1) of 15 and 80 kHz respectively. The big rectangular box at the bottom of the pictures is the horizontal section of the target (beam is entering from the left). The coloured dots are the hits recorded by the TDC, in their global (x,y) coordinates. The colour shows the time attached to all the hits, according to the legend on the right. The smaller upper box of both the event displays is the time projection (in logarithmic scale) of the hits recorded in the target ($[-10 \mu\text{s}, +20 \mu\text{s}]$). The black dots or squares correspond to $t = 0$ and represent the pion track in time with the LV1. In the right event display (LV2 trigger), the red dots are the muon candidate hits; the thick red borders of TDC's regions identify the TDC's that have been triggered; the thick green band is the x region compatible with the z information, coming from the hodoscope z -counter.

track provides a LV1 trigger signal. This is used by the LV2 trigger system, which looks for the stopping pion coordinates (x_π, y_π) , verifies if the $\pi^+ \rightarrow \mu^+$ is observed,

identifies the TDC's containing the superpixel centered on (x_π, y_π) , and finally sends the trigger to these TDC's only (2, in the event shown in figure 3.16). There is no need to record all the other hits that are happening in the target at the same time: they would occupy bandwidth for the DAQ, without adding any further useful information. A big increase in the data taking rate is now allowed. The reason is twofold: first (evident already from the comparison in the events displays), is that the size of every LV2 event is reduced if compared with the typical LV1 event size; second, the parallelization can be effectively performed when LV2 is used: while a few TDC's are occupied for the 30 μ s time window by an event in a certain region of the detector, other events can occur and be observed elsewhere in the target. Of course, when the beam rate is further increased, geometrically overlapping events start to appear, and several background tracks can be found even in the few TDC's triggered by the LV2 trigger. The task of the analysis code will then be to apply the proper cuts and distinguish between the relevant particles tracks and the background hits.

3.7.1 Electronics for the LV2 Trigger System

The electronics for the LV2 trigger consists of 17 FPGA-based VME boards, including 16 "Box Processors" (BP) and one "Main Processor" (MP). All the boards are interconnected through a custom designed backplane and are located in a single VME 6U crate. The system has been entirely designed and developed at CIEMAT [54]. Figure 3.17 shows the architecture of the LV2 trigger system. Each box processor corresponds to one TDC region of 8×12 pixels. It receives as inputs the HL data coming from the same discriminators that provide the LL data to the corresponding TDC. The LV1 trigger and the RF clock are sent as input to the Main Processor, and then distributed to every Box Processor via the backplane. The BP's are in charge of the pion and muon identification, and the sending of the coordinates. All the rest (trigger definition, trigger dispatch, setting of different operating modes, sharing the informations among boxes) is managed by the Main Processor.

The first operation that LV2 has to perform is the pion identification. Every BP board latches all the HL hits from the corresponding discriminators in the time window $[t_0, t_0 + 15 \text{ ns}]$ (*first snapshot time window*), with t_0 the time of the LV1 trigger signal. The first snapshot hits correspond to the track of the incoming pion. They are accumulated by rows in the beam direction, and the projection of the track on the two axis, both parallel and orthogonal to the beam is computed. The LV2 algorithm for the definition of x_π is the following: at least 3 first snapshot hits are required in a row of the target; if this is the case, all the hits belonging to the detected row(s) above the 3-hits threshold, plus the hits of one row above and one row below, are projected on the x axis; a pion is found if this x -projection fulfills one of the following 3 patterns: 1xx1000; x1x1000; xx11000 (1 means a hit in that location, 0 means no hit, x

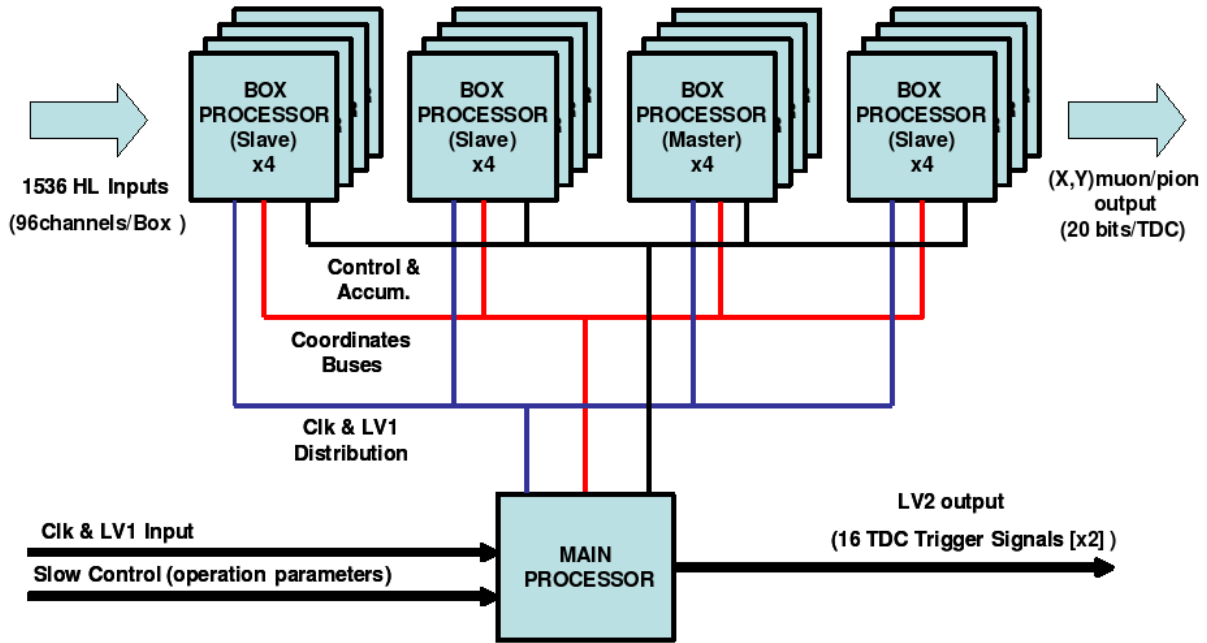


Figure 3.17: The LV2 Trigger system architecture, with 16 Box Processors (Masters and Slaves, where each Master controls the 4 modules in its row) and one Main Processor.

means that there can be a hit, but it is not a necessary requirement). In other words, the pion is the rightmost hit of the row cluster, in front of at least 3 empty pixels. To allow for possible inefficiencies and scatters, but to avoid the misidentification of the pion in an isolated pixel, at least one other hit in the 3 pixels before the stopping point is required. Given the geometry of the target and its mapping, where one row is shared by 4 BP's, the row accumulation procedure implies that one out of the 4 BP's serves as a master, collecting the sum from the other 3 boxes. The 16 BP boards are thus differently programmed, so to have 4 master boxes and 12 slave boxes. Once x_π is identified, the corresponding y_π is found by the BP that contains it.

Once the first snapshot operation is complete, and the stopping pion coordinates are identified, the system has to search for the presence of a HL hit from discriminator

in the neighborhood of the pion stopping point, inside the time window $[t_0 + 15 \text{ ns}, t_0 + 100 \text{ ns}]$ (*second snapshot time window*). This second snapshot period corresponds to the $\pi^+ \rightarrow \mu^+$ decay and represents the LV2 trigger itself (when used in the nominal working conditions of trigger on muon identification). Any BP can perform the muon identification and define the (x_μ, y_μ) coordinates.

Finally, when the first and second snapshots operations are completed, i.e. stopping π^+ and $\pi^+ \rightarrow \mu^+$ decay identified, the MP computes which are the TDC's containing the superpixel, and sends the trigger to those TDC's only. The outputs of the LV2 trigger system are 16 trigger signals at the front panel of the MP⁶, plus the (x, y) (pion or muon) coordinates, at the front panel of each BP board, sent from the BP to the corresponding TDC only. All signals are differential ECL standard.

The main characteristics of the LV2 design is the high rate capability. This imposes a low processing time for each event. The processing time for LV2 is 180 ns in the worst case. Moreover, with an appropriate input buffer to compensate the possibility of several LV1 signals in a short time, the electronics virtually turns into a dead-time-free system. The final limitation to the maximum rate that the LV2 can follow comes from the LV1 input pulse width, that must be a 50 ns pulse. If two events occur closer than 50 ns, the second one cannot be resolved by the LV2 system, and is lost. This restriction largely exceeds anyhow the needs of the FAST experiment: it would correspond to an average LV1 rate of 20 MHz.

3.7.2 Operational Working Conditions for the LV2

The LV2 system allows some flexibility in its operational working conditions, summarized in Table 3.5.

The standard way to operate the LV2 trigger system is to use it as described above, as a selective trigger for the TDC's. The trigger type, the size of the superpixel and the coordinates to be transmitted can be chosen. The trigger type can be selected between the "trigger on muons" (nominal), which provides a trigger to the TDC's only if a $\pi^+ \rightarrow \mu^+$ decay is found or the "trigger on pions", where only the stopping π^+ identification is required. The superpixel size can be selected between 7×7 (nominal) or 5×5 pixels. The smaller size superpixel is a more favorable choice in terms of data bandwidth and data reduction for the DAQ, corresponding to an average number of triggered TDC's equal to 1.8, but some e^+ events could be lost, especially when the muon does not happen in the same pixel as the pion. Finally one can also choose which coordinates, (x_π, y_π) or (x_μ, y_μ) , should be transmitted as added information to the TDC which contains them.

For calibration and commissioning, the LV2 trigger can be operated also in the so

⁶ The trigger outputs $[\times 16]$ is indeed doubled inside the MP: one is used as TDC trigger, the other is sent into a scaler to monitor the LV2 behavior and efficiency.

LV2 MODE	PARAMETERS	Options for Parameters
SELECTIVE TRG MODE ALL TDC's MODE	Trigger Type	on muons / on pions
	Superpixel Size	7 × 7 / 5 × 5
	Coords Transmission	($\mathbf{x}_\mu, \mathbf{y}_\mu$) / (x_π, y_π)
BYPASS MODE	-	-

Table 3.5: Operational working conditions for the LV2 trigger system. The bold face options correspond to the default LV2 settings used in nominal running conditions.

called “all TDC’s mode”, where the LV2 logic works as usual but the LV2 trigger is just used as a flag, and all 16 TDC’s are triggered at the same time.

Another possible way to operate the LV2 system is the “bypass mode”, where LV2 behaves simply as a transparent system, serving as a fan out of the LV1 trigger signal to all 16 TDC’s.

The different operational parameters are set in the LV2 with appropriate bit encoding masks, through the Slow Control system.

3.8 FAST Slow Control

The Slow Control System for the FAST experiment described above and summarized in Figure 3.18, is in charge of the monitoring and control of the proper functioning of the different elements of the chain and the settings of the adjustable parameters which determine the running conditions. The different tasks of the Slow Control are the following:

- Temperature readout: a few PT100 temperature sensors are placed in the most critical points (preamplifier region, LV2 crate) to constantly monitor their operation temperature. In case the temperature exceeds the preset limits, a warning message is sent via e-mail and/or SMS to the operators.
- Monitoring of the power status of all NIM crates, through the measurement of the low voltages for the preamplifiers and the discriminators. In case of problems, a warning message, which also localizes the failure, is sent.
- Setting and monitoring of the thresholds of the discriminators. The thresholds of the discriminators are remotely adjusted and constantly controlled by a DC

voltage. During the initialisation phase of the TDC's by the DAQ, all thresholds are raised to 2000 mV to avoid any signal on the input of the TDC's. During the running time the LL and HL thresholds are set, respectively, to 100 and 400 mV. They have to remain stable; if not, warning messages are sent.

- High Voltage (HV) for the PSPM's: the HV for the photomultipliers is provided by CAEN SY127 multichannel modules, controlled by the Slow Control program. One can set the HV separately for each tube. The HV is constantly monitored, and, in case of failures, warnings are sent.
- Definition of LV1 trigger options: narrow or wide trigger, and - if narrow - which type of particle.
- Definition of LV2 trigger options: different operational modes for LV2 trigger (Table 3.5) can be set.
- Register all rate information: scalers are integrated in the system, so that all the interesting rates can be acquired. Not only the beam and trigger rates (LV1 and LV2) are registered, but also the rates of events received, processed and analysed in the DAQ PC's.
- Data Base recording. All the informations about trigger rates from the scaler, output rates from the DAQ PC's and data taking conditions are registered on disk in data base files.

The Slow Control is realized by a LabView program, running on a dedicated PC. A variety of different standard interfaces to the control PC are combined, to accomplish the different tasks. A CAMAC interface is responsible for the trigger scalers acquisition and LV1 trigger modes setting; the PSI Midas Slow Control Bus (MSCB) system [55] manages the temperature readout, the thresholds settings (with analogue I/O cards in both cases) and the LV2 operational parameters settings (with a digital I/O card); the power status of all the crates is checked via a serial RS232 interface; a special CAEN interface card is in charge of the high voltage control for the photomultipliers. Finally, a TCP/IP standard interface for communications between the Slow Control PC and the DAQ PC's provides the information sharing: transmission of the DAQ rates to the scalers and actions to be taken by the Slow Control, driven by the DAQ, e.g. the raising of the thresholds during the initialisation of the TDC's.

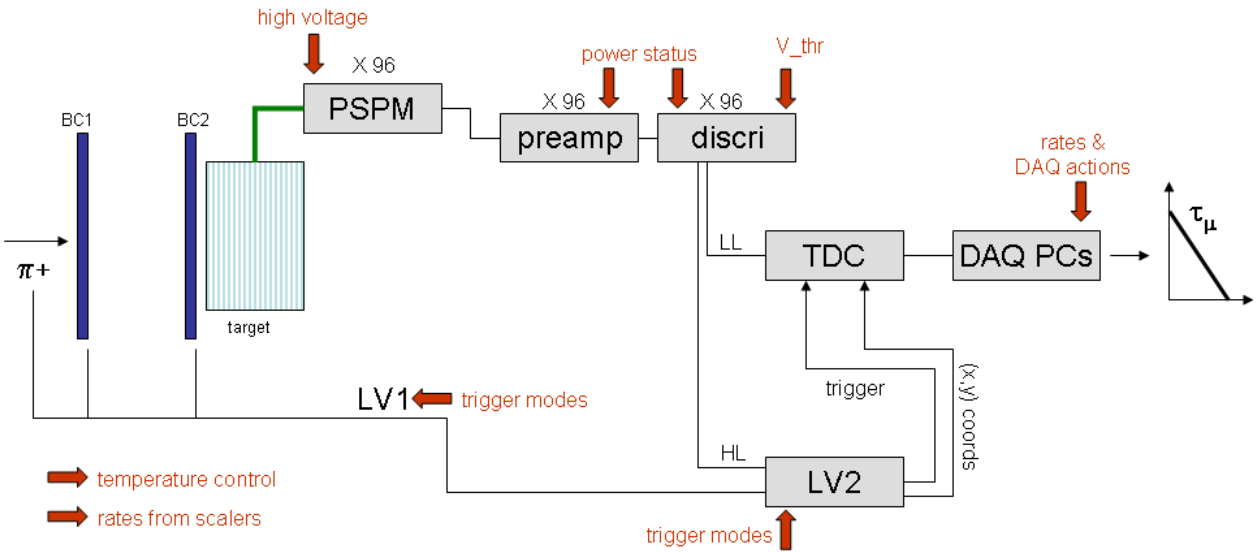


Figure 3.18: Schematics of the full FAST chain, from the raw pulses of the target to the muon lifetime result. The big red arrows indicate where in the chain and how the Slow Control system acts.

Chapter 4

Commissioning and Performance of the FAST Detector

The FAST target was completed by August 2003, although it was not fully equipped with the complete electronics, because only a part of the needed photomultipliers was available at that time. A first engineering run was performed at PSI by the end of 2003, with only part of the target readout system available.

In 2004 the full optoelectronic and analogue readout was completed; the magnet and the z -counter hodoscope were commissioned, and a first prototype for the LV2 system (involving only 1/4 of the final setup) was tested in a first testbeam phase.

In 2005 the fully operating LV2 system was commissioned and proved to meet the requirements. In parallel, the DAQ was constantly improved, both in terms of the maximum sustainable rate, and in terms of the event builder logic and efficiency (from fragments to correctly reconstructed events).

In 2006 the DAQ system was brought up to its maximum rate, and several issues previously encountered in the functioning of the TDC's – especially concerning the synchronization and managing of the 4 chips on the TDC CAEN boards – were fixed. A first data taking period of approximately 3 weeks at the end of 2006 allowed the collection of about 10^{10} muon lifetime good events. This constitutes the first high precision measurement of the muon lifetime with the FAST detector, to a statistical precision comparable with the world average.

In the present chapter we will report the main results obtained by the commissioning activities for the detector, spanning the engineering runs and the testbeams of the past four years, characterizing the target, the beam, the readout and DAQ chain. The aim will be both to show and justify the working conditions of the data taking, and to underline some of the aspects that have to be included in the systematics analysis of the measurement (Chapter 6). Unless differently stated, the results presented here are for the target in its final configuration and assembly. The labeling

and numbering notation is the one already adopted in Figure 3.13 of the previous chapter.

4.1 Light Yield in Scintillator and Pulse Height

Although the FAST detector does not foresee any pulse height measurement, a dedicated test with a standard Lecroy 2249 ADC (0.25 pC/ch) and a simple stand alone Camac based DAQ system was performed to measure the pulse heights of the typical signals for FAST [56].

The measurement was made on a single test bar of the target, adjusted to correspond to a pion stop pixel by 100 mm lucite preceding the target. Before being acquired by the ADC, the raw pulse from one channel of the photomultiplier is amplified, to simulate the FAST preamplifier. The gate for the ADC unit is the amplified signal from the target bar, discriminated via a Lecroy discriminator unit of tunable threshold (referred to, in this section, as V_{thr}^{ADC}), in coincidence with the selective LV1 trigger. The pulse height was measured at different V_{thr}^{ADC} values, from maximum to lower efficiencies, for electrons (Figure 4.1), for pions close to their stopping point, with 80 mm lucite preceding the target (Figure 4.2) and for pions at their stopping point, with 100 mm lucite (Figure 4.3). A direct measurement of the muon pulse height from $\pi^+ \rightarrow \mu^+$ decay was not performed, because of the difficulty in triggering the exact signal with the simple setup described. It should be noticed, however, that the pulse height of a stopping pion corresponds to an average distance in one single pixel bar of about 2 mm. This is very close to the muon range of ~ 1.5 mm for muons produced by the pion decay at rest, and makes that the muon pulse height closely coincides with the stopping pion pulse height.

The calibration of ADC channels in photoelectron (pe) units (16 ADC channels/pe) allows to interpret the results of Figures 4.1 to 4.3 in terms of the light yield from the typical signals recorded by the detector: electrons, pions close to the stopping point, stopping pions and muons from their decay. This information is used to fix the thresholds to be used for the FAST discriminators (LL V_{thr} and HL V_{thr}). Table 4.1 summarizes the typical light yield values. It also shows the correspondence between the thresholds settings for the FAST discriminators and the relative number of photoelectrons, calculated converting the used V_{thr}^{ADC} values to the effective V_{thr} values of the FAST discriminators. The optimal threshold values, which will be validated later in this chapter, are LL $V_{thr} = 100$ mV and HL $V_{thr} = 400$ mV.

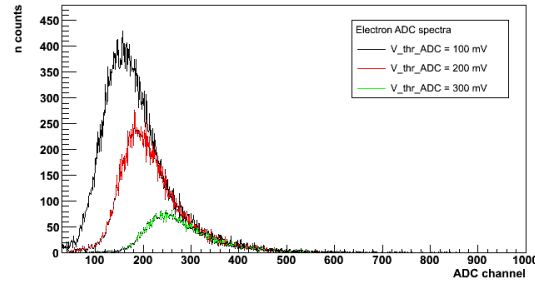


Figure 4.1: ADC pulse height measurement for electrons in a single test bar of the FAST target, at different threshold values in the discriminator. The counts are not pedestal subtracted. The pedestal for this and the following ADC data is at channel 41.

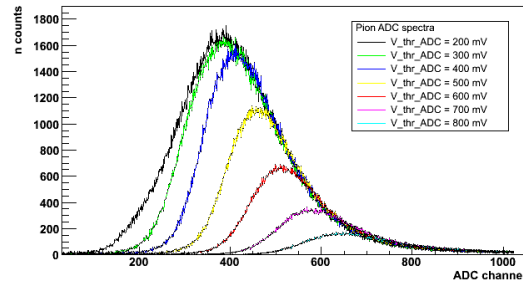


Figure 4.2: ADC pulse height spectra, not pedestal subtracted, with the pedestal in channel 41, for pions with 80 mm lucite preceding the target, i.e. pions with about 20 mm (5 pixels) range remaining.

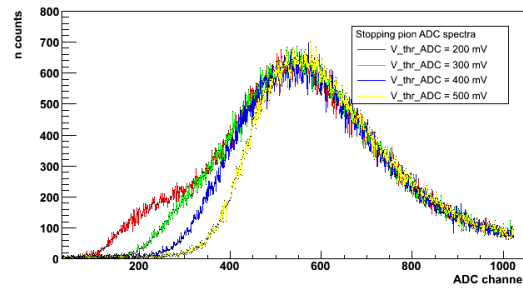


Figure 4.3: ADC pulse height spectra, not pedestal subtracted, with the pedestal in channel 41, for stopping pions (100 mm lucite). With very good approximation this also corresponds to the muon pulse height, from pion decay at rest.

Particle Type	Estimated Light Yield [pe]
electrons (i.e. mip's)	9
pions with 20 mm range	25
stopping pions	35
$\pi \rightarrow \mu$ decay	35
LL $V_{thr} = 100$ mV	~ 3
HL $V_{thr} = 400$ mV	~ 18

Table 4.1: Typical light yields (in photoelectron units) of the FAST target for the different types of signal occurring in the detector and chosen threshold values for the FAST discriminators, in photoelectrons.

4.2 Discriminators Thresholds Settings

The outputs of the double threshold (low level, LL and high level, HL) discriminators for FAST are inputs, respectively, to the TDC's (LL) and to the LV2 trigger system (HL), in charge of the pion and/or muon stopping point definition and location. The values of the two thresholds (LL V_{thr} and HL V_{thr}) are constrained, in both cases, by efficiency requirements on the detection of mip's and pions respectively. The LL threshold should be low enough to allow good efficiency in the detection of the decay electrons and minimum ionizing particles in general, rejecting at the same time the single photoelectron noise. The HL threshold should be high enough to record only pions and muons hits, suppressing the mip's signals while remaining fully efficient on pion tracks.

According to Table 4.1, LL $V_{thr} = 100$ mV, corresponding to a pulse height of about 3 photoelectrons, is good enough to detect the mip's. A higher value for the LL threshold would not be sufficiently efficient. This is shown in Figures 4.4 and 4.5, where the results from a threshold scan (from 100 mV to 700 mV) in terms of number of hits in electron tracks for dedicated electron runs are presented. It will be shown (Sections 4.3 and 4.6.1) that the final efficiency in the detection of mip's is fixed not only by the LL threshold settings, but also by the gain for the PSPM's. It is indeed the combined setting of the threshold and the high voltage values that fixes the working conditions of the detector.

As for the HL threshold, its ultimate tuning is done optimizing the LV2 efficiency for different HL threshold values. The optimal value in terms of the number of photoelectrons, efficiency on the pion tracks detection (Table 4.1), and mip's rejection (Figures 4.4 and 4.5), is HL $V_{thr} = 400$ mV. This same result will be confirmed by the LV2 commissioning tests, described in Section 4.11.

From now on, the nominal threshold settings for the FAST discriminators will be assumed to be: LL $V_{thr} = 100$ mV and HL $V_{thr} = 400$ mV.

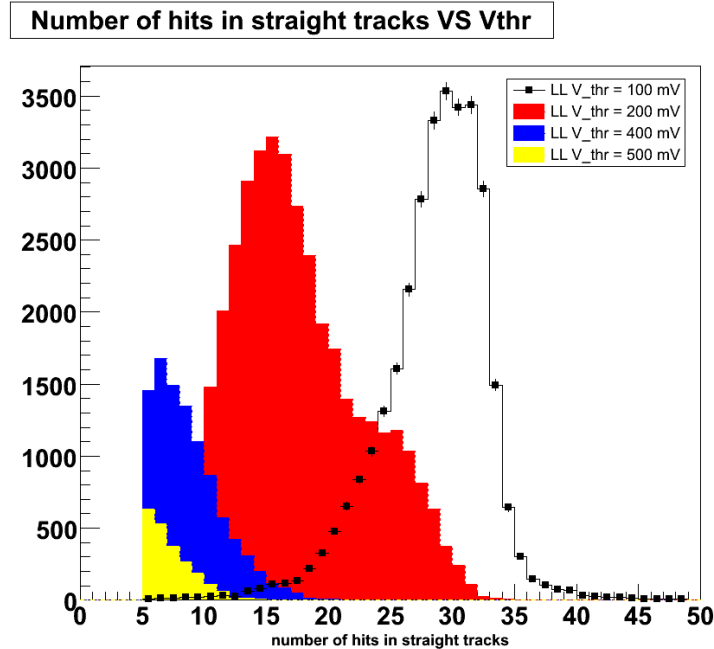


Figure 4.4: Number of hits observed for straight electron tracks, at different values of $LL V_{thr}$. A straight track is defined here as a track of electron hits in time with the trigger (minimum 5 hits are required), occupying at maximum 3 consecutive y rows of pixels. An ideal straight track (not divergent and fully efficient) should have 32 hits. Given that three rows are allowed, more than 32 hits in a track are possible. Threshold values higher than 100 mV are clearly inefficient.

4.3 High Voltage (HV) Settings

The values of high voltage (HV) for the power supply of the photomultipliers must be carefully tuned, to equalize the target and obtain a uniform response from it.

The need of a calibration for the high voltage values is twofold. First, all the tubes don't have exactly the same gain. Second, different preamplifiers present different baseline shifts (DC offsets of the order of 100 mV) when connected to the discriminators (see Section 3.4.3). A proper tuning of the high voltages of the tubes, i.e. of their gain, will automatically take care of any variation on the DC offset of the preamplifiers.

The best way to calibrate the high voltage of the tubes is to use straight electron tracks passing through the target and to measure, for each tube, the efficiency in the detection of the electrons as a function of the high voltage of the tube. The HV working points are then decided in terms of equal efficiencies for all the photomultipliers. Tubes have shown to be strongly affected by afterpulses when the running voltages

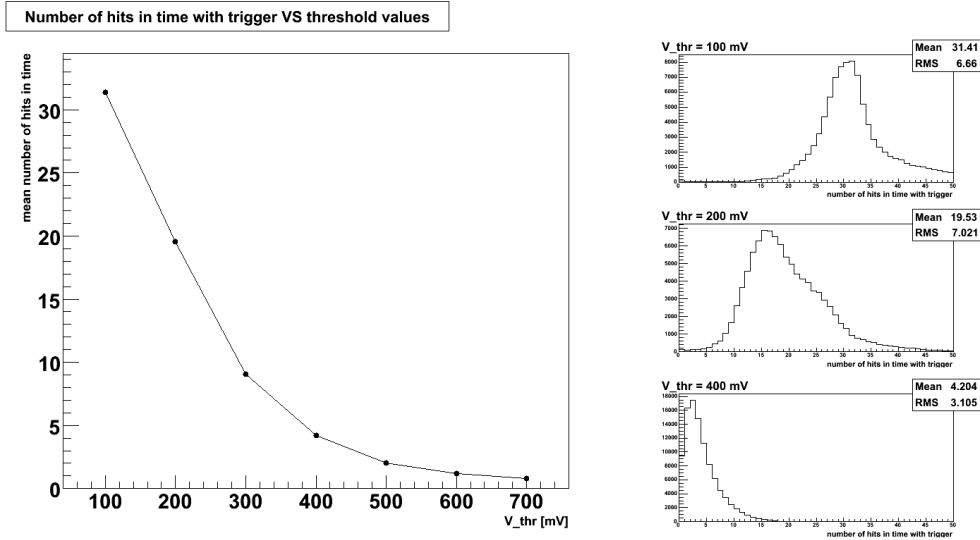


Figure 4.5: Number of hits in time with the trigger versus the LL V_{thr} values for electron runs at different thresholds. These plots here generalize the histograms in Figure 4.4, independently on any particular definition of straight track. The left plot is the mean number of hits in time vs the threshold values, for the full threshold scanning. On the right are three examples of the distributions of the number of hits at three different LL V_{thr} (100 mV, 200 mV, 400 mV).

are too high. The optimal high voltage working point should be the compromise between a high efficiency for the tube and a low afterpulsing probability.

Figure 4.6 shows the efficiency curves obtained for a set of representative tubes. Similar plots for every PSPM in the target have been produced. The HV for the tubes is varied from 700 V to 980 V (in the following steps: 700 V, 750 V, 775 V, 800 V, 825 V, 850 V, 875 V, 900 V, 925 V, 950 V, 980 V) and the efficiency for straight tracks (i.e. the number of hits recorded by each tube and belonging to the track, normalized to 4) is computed at each voltage point. The two slopes of the curves - the flat one of the plateau and the rising one - are fitted by two straight lines and their crossing point is computed. Such a procedure to build efficiency curves implies an a priori definition of straight tracks, independent on the tube for which the efficiency is calculated. This is achieved by the granularity of the target in 8×12 PSPM's units (Fig. 3.13), combined with an iterative procedure. One can separate the target in 8 columns of tubes, from column 2 (W2, A2, ... , K2) to column 9 (W9, A9, ... , K9) in the usual notation of Figure 3.13, and change simultaneously the voltages of the 12 tubes in each column, using the other parts of the target as telescope counters to define the track. The procedure is then iterated for all the columns.

To obtain straight electron tracks to extract the efficiency plots like in Figure

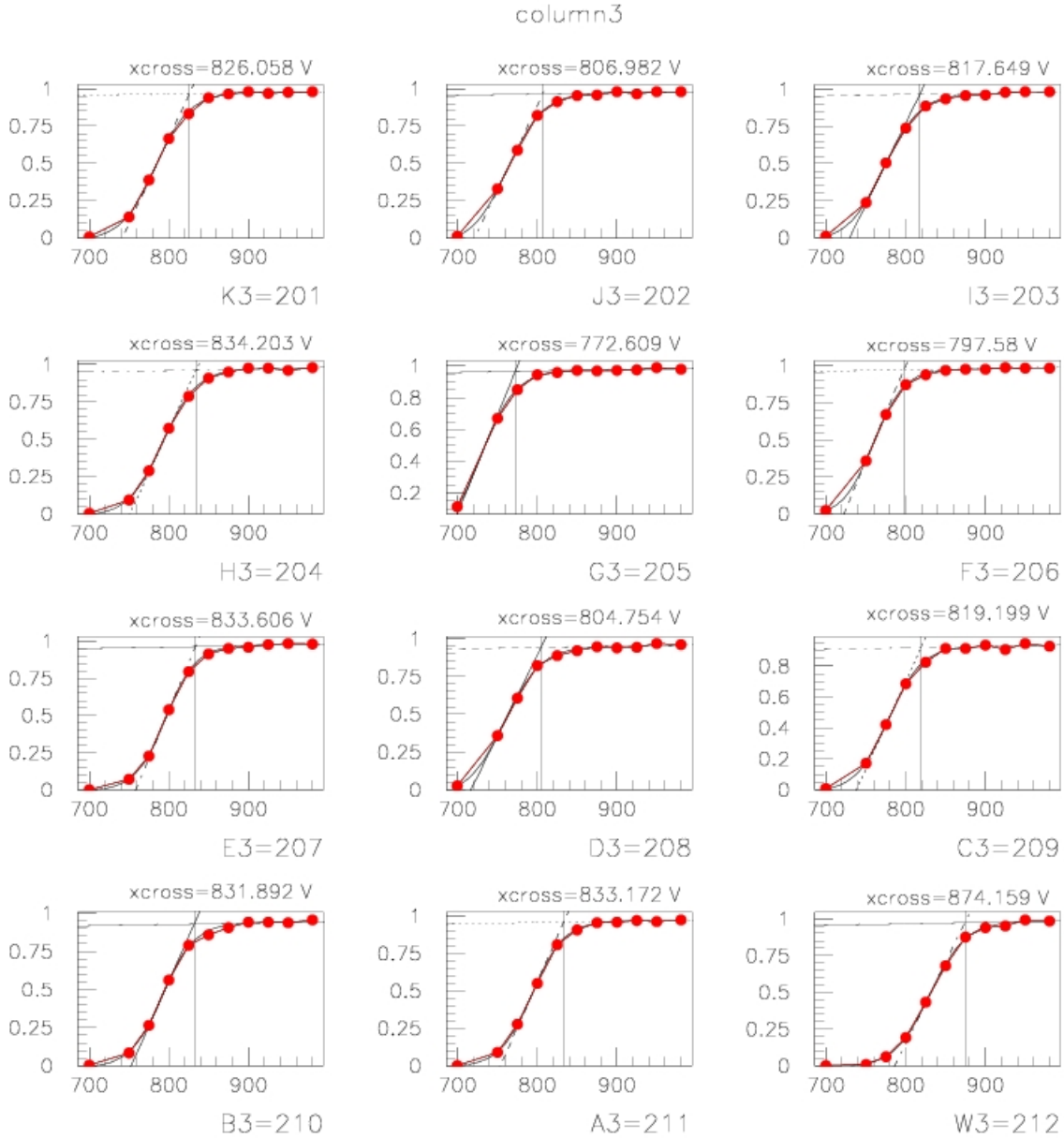


Figure 4.6: Efficiency for minimum ionizing particles as a function of the high voltage for a representative set of 12 PSPM's (K3, J3, I3... W3 in the notation of Figure 3.13). The “xcross” number at the top of each plot is the crossing point of the two linear fits of the flat and sloped lines.

4.6, a low rate LV1 trigger, timed for electrons, is used. BC3 is included in the trigger, to assure the particles are really minimum ionizing particles, passing through, and not stopping inside the detector; BC2, whose length does not cover the full target, is temporarily replaced by a horizontal “finger counter” that matches the target dimension; the wedge is removed. The 16 TDC’s are simultaneously triggered with the global LV1 signal thus obtained.

Once the efficiency plateau curves for the tubes are obtained, the “xcross” points give good estimates of the “knee” position where the tube passes from an inefficient response to a good efficiency. Several HV settings, with respect to the “xcross” point, have been tested:

- HV_{ref} (\sim knee value).
- $HV_{ref} - 10$ V.
- $HV_{ref} + 10$ V.
- $HV_{ref} + 20$ V.

The best compromise between efficiency and afterpulses is obtained fixing the working point of the tubes to the $HV_{ref} + 10$ V voltage values. Figure 4.7 shows the number of hits obtained in a straight track in the four different HV settings. In a perfectly efficient target, each track should have 32 hits: HV values close to the knee (HV_{ref}), or below ($HV_{ref} - 10$ V), would provide an inefficient response of the target; values above the knee ($HV_{ref} + 10$ V, $HV_{ref} + 20$ V) are good in terms of efficiency. Among the two settings, the first one provides better performances in terms of afterpulses and dirty tracks, without losing too much in efficiency.

From now on, these HV settings ($HV_{ref} + 10$ V) will be the nominal HV values for the FAST target. Table 4.2 lists the HV values for all the tubes in the FAST setup.

If a tube has to be replaced with a spare one, or its position in the target is changed, the calibration procedure for the HV tuning has to be redone on the new/moved tube. The tubes anyhow are quite reliable, and no need of change or replacement has been registered so far.

The HV tuning for the PSPM’s described here was done both without and with the magnetic field in the target region. The obtained values for the HV settings in the two cases are compatible, confirming that the magnetic field does not affect the performance of the PSPM’s.

High Voltage working conditions							
tube	voltage(V)	tube	voltage(V)	tube	voltage(V)	tube	voltage(V)
K2	825	K3	834	K4	813	K5	802
K6	878	K7	851	K8	800	K9	792
J2	864	J3	815	J4	837	J5	825
J6	844	J7	825	J8	879	J9	828
I2	828	I3	826	I4	838	I5	828
I6	869	I7	837	I8	829	I9	899
H2	829	H3	842	H4	793	H5	800
H6	896	H7	803	H8	868	H9	901
G2	833	G3	781	G4	865	G5	850
G6	911	G7	786	G8	854	G9	788
F2	885	F3	806	F4	860	F5	852
F6	810	F7	828	F8	807	F9	800
E2	836	E3	842	E4	832	E5	754
E6	834	E7	834	E8	880	E9	882
D2	804	D3	813	D4	853	D5	846
D6	879	D7	853	D8	811	D9	803
C2	861	C3	827	C4	836	C5	836
C6	848	C7	885	C8	809	C9	860
B2	802	B3	840	B4	814	B5	815
B6	809	B7	827	B8	816	B9	907
A2	808	A3	841	A4	858	A5	828
A6	898	A7	914	A8	867	A9	879
W2	806	W3	855	W4	842	W5	851
W6	817	W7	832	W8	837	W9	834

Table 4.2: High voltage values for the full set of PSPM's in FAST (with the notation of Figure 3.13 for the tubes position).

4.4 Beam Particles Range

To define the dimensions of the lucite wedge beam degrader and get a uniform distribution of the stopping pions in the target, the range of the pions in the scintillator has to be measured. Although we are interested in the pion content of the beam, the comparison in the ranges of beam pions and beam muons is also important, to be able to suppress the residual muon contamination.

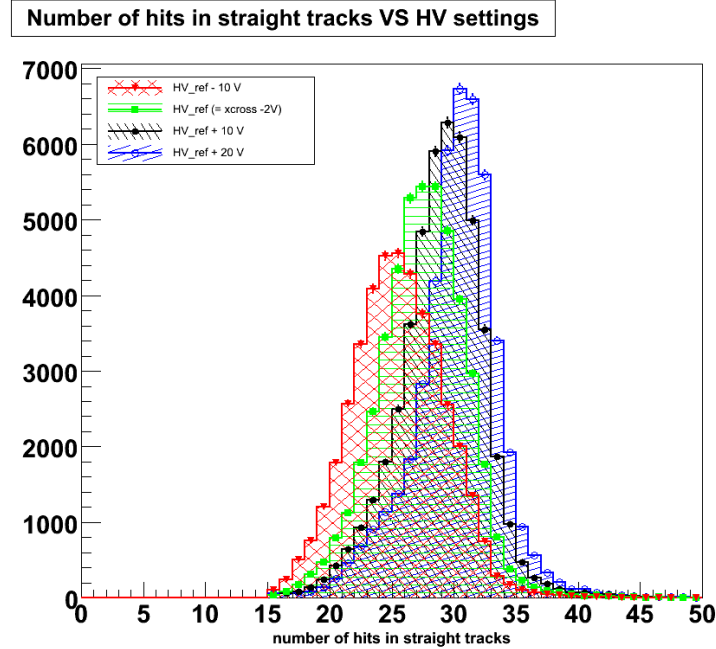


Figure 4.7: Number of hits observed in straight electron tracks for the FAST target with four different HV settings for the tubes. The nominal running conditions correspond to the setting $HV_{ref} + 10$ V. To obtain the present histograms, a straight track is defined as follows: a candidate straight track - in the y row - must contain at least 15 hits in time with the LV1 trigger ; the candidate is taken as a straight track if all its hits occupy at maximum three rows ($y-1$, y , $y+1$). Given that three rows are allowed in a track, more than 32 hits in a track are possible.

4.4.1 Pion Range

To measure the range of the pions at the momentum of 170 MeV/c in the scintillator target, several lucite plates (2 cm thick each) are added in front of the target and the mean position of the stopping pions is recorded as a function of the global lucite thickness (Figure 4.8). The result is that one pixel in the target (4 mm depth of scintillator, plus the paint and the fibers material) corresponds to $\frac{1}{0.2721} = 3.7$ mm of lucite. This results in a real target density very close to the one of lucite ($\rho_{lucite} = 1.19$ g cm⁻³), rather than the one of pure BC400 scintillator material ($\rho_{BC400} = 1.032$ g cm⁻³), because of the paint and the fibers. To obtain the optimal spread of pions, the wedge should be positioned in front of the target so to have a thickness of about 9 cm in the vertical middle point of the target.

As an example of the range measurement, Figure 4.9 shows the histograms relative to the penetration depth of the pions in the target, for a 80 mm thickness of lucite.

The range is extracted as the mean value of the stopping pion location, and is well consistent with the position at half height of the sigmoid function representing the penetration of pion tracks in the target.

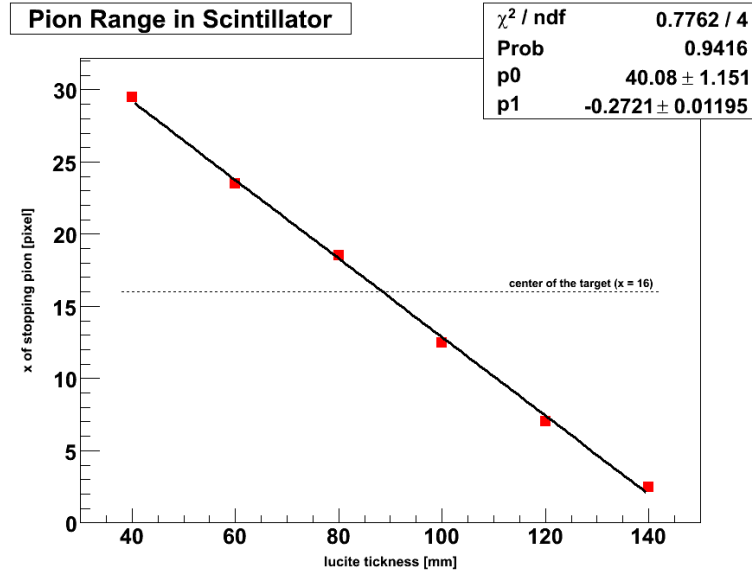


Figure 4.8: Penetration of the pions inside the target (in pixel units) as a function of the lucite absorber thickness.

4.4.2 Pion and Muon Range Comparison

A special run with a muon beam and a fixed amount of lucite (140 mm) was done to measure the penetration depth of beam muons, and compare it with the pions of Figure 4.8. Since the muons have the same momentum as the pions but a smaller mass ($m_\mu = 105$ MeV; $m_\pi = 140$ MeV), they have a higher kinetic energy and a lower $\frac{dE}{dx}$, and so penetrate a bigger depth. The measurement shows that, at the same lucite thickness, the beam muons penetrate about 20 pixels more than the pions. This difference is a very powerful tool to suppress the muon beam background in our data. Section 4.9 will show how this suppression can be achieved.

4.5 Timing Considerations

Before starting to describe the results obtained from several different data taking runs - both for nominal runs with pion beams, and for calibration runs with electrons - a few observations about the time conversion (from raw times in the TDC's to real time) and some timing reference conventions are added here.

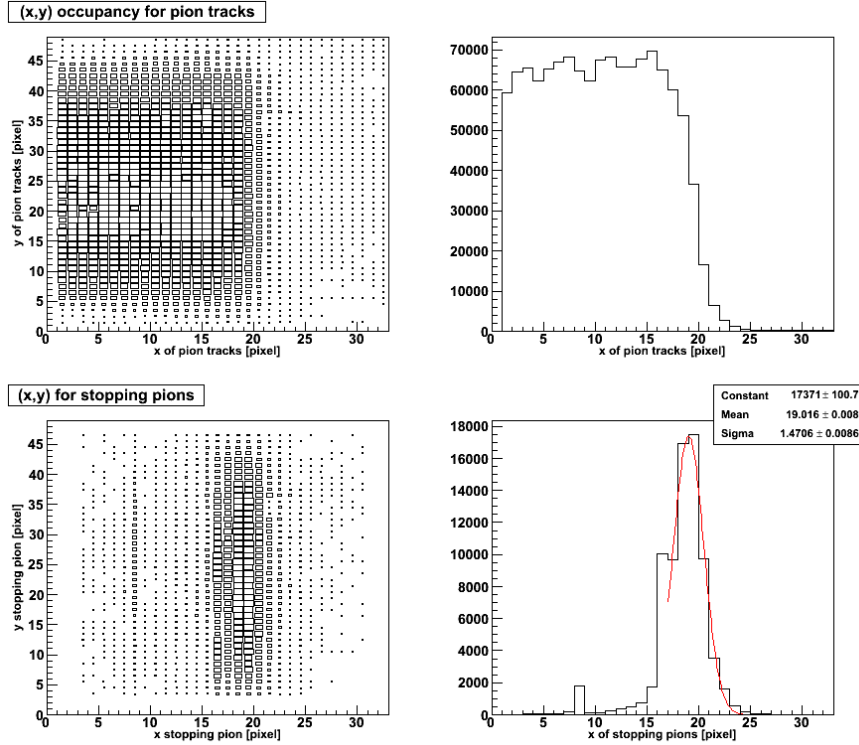


Figure 4.9: Example of the pion range measurement for a 80 mm thickness of lucite in front of the target. The top left bidimensional distribution is the (x,y) occupancy of the hits of the pion tracks (all hits in time with the trigger). Its projection on the x axis is the sigmoid function of the penetration depth of the pions (top, right plot). The bottom left plot is the (x,y) location of the stopping pions. The projection on the horizontal x axis (bottom, right plot) is the range measurement. The peaks at $x = 8$ and $x = 16$ (borders of TDC's) in the stopping pion position are due to not yet properly optimized event reconstruction, and so excluded in the gaussian peak.

4.5.1 Time Equivalence of one TDC tickmark

For any histogram or analysis process that will contain time information, the time has always to be considered in TDC tickmark units (ticks). If applied, the conversion to real time units (typically ns) will always be specified.

Each clock cycle of the TDC's is divided in 32 tickmarks (5 LSB, see Section 3.6.1). One TDC tickmark corresponds, in real time units, to:

$$1 \text{ tickmark} = \left[\left(\frac{1}{\text{clock [MHz]}} \right) / 32 \right] \times 1000 \text{ ns} \quad (4.1)$$

For a 30 MHz clock, we have: 1 tick = 1.0416667 ns. The high precision of the used clock justifies the many significant digits used for the conversion.

4.5.2 Zero Time ($t = 0$) Convention

The TDC time window is set with respect to the trigger signal sent into the TDC itself ($t = 0$, in the internal TDC timing reference). In our specific case the TDC window is chosen to be $[-10 \mu\text{s}, +20 \mu\text{s}]$ i.e. $[-9600, 19200]$ TDC ticks, or equivalently $[-300, 600]$ coarse TDC clock cycles.

It is convenient to set the zero time $t = 0$ for the hits to coincide with the time when the beam particles enter the target and provide the beam trigger. This would be the case if the trigger signals sent to the TDC's were perfectly in time with the beam particles. This condition however can never be produced, because the trigger is always delayed due to cable length, logic units and LV2 processing time. A different global time shift is then applied to the *raw* times of each TDC, so that the $t = 0$ time of the hits treated by the analysis coincides with the time when the beam particles enter into the target. The fact that a different shift is applied separately in each TDC allows a good time synchronization for the whole target, removing all the possible residual time differences due to the hardware.

The consequence of the time shift is a shift also in the effective time window of the TDC's (Figure 4.10). When LV1 is used as trigger, this shift corresponds to a few hundreds ns; the TDC window will be still referred to as $[-10 \mu\text{s}, +20 \mu\text{s}]$. When LV2 is the trigger for the TDC's, the trigger comes about $2 \mu\text{s}$ later than the pions in the target; the effective window will be referred to as $[-8 \mu\text{s}, +22 \mu\text{s}]$. In both cases, the quoted TDC window limits are just approximations of the real time windows.

For the following, time information will always be provided:

1. in TDC tickmark units (ticks)
2. referred to a $t = 0$ time that corresponds to the moment when the triggering beam particle enters into the target.

4.6 Calibration Runs with Electrons: Efficiency and Time Resolution

With the HV settings of Table 4.2 for the photomultipliers and the threshold settings described in Section 4.2, high performance of the target in terms of efficiency and uniformity are achieved. This is proved by short calibration electron runs (with straight tracks), mainly used to characterize the detection efficiency of the target and the time resolution of the full readout chain.

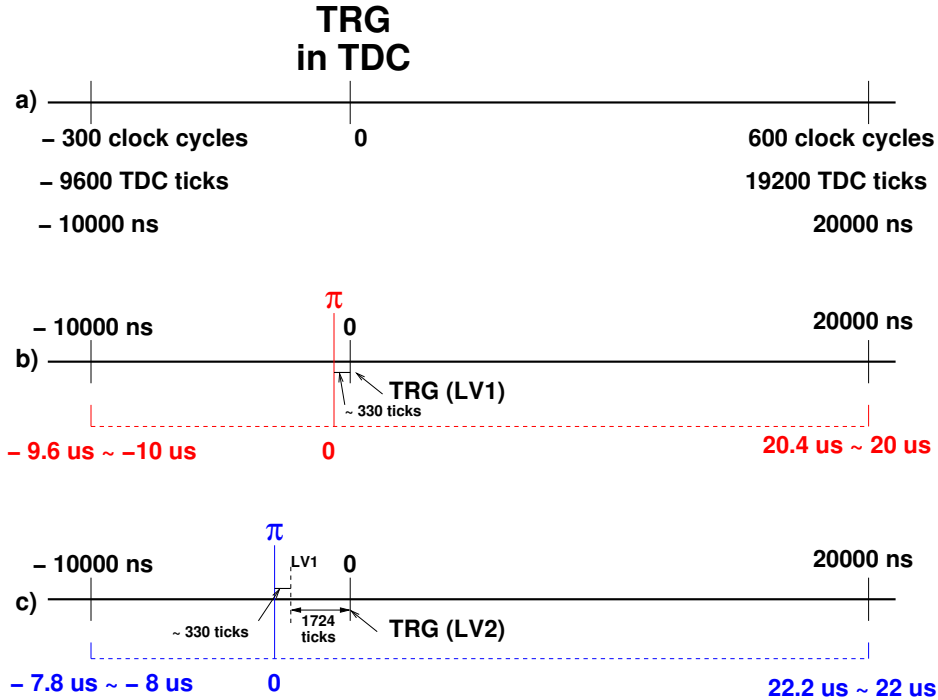


Figure 4.10: Sketch of the TDC time reference adopted. The top line (a) represents the internal timing reference of the TDC, in clock cycles, tickmarks and ns units. The zero time is given by the trigger. The two bottom lines, (b) when LV1 is used and (c) when LV2 is used, represent in color dashed lines the new reference time assumed w.r.t. the pion time (fixed as $t = 0$), compared to the TDC time scale (continuous black lines). The time window for the TDC, whose width and offset remain fixed w.r.t. to the trigger, is also shifted if referred to the new $t = 0$ time.

The general running conditions for an electron run are the following ones:

- Narrow coincidence beam trigger, timed on electrons.
- BC3 included in the beam trigger.
- Wedge removed.
- No collimator in place.
- LV1 trigger used for the TDC's.
- Nominal HV values for the tubes and threshold values for the discriminators.

The BC3 counter included in the trigger assures that the hits in time with the trigger signal (i.e. the electron tracks) correspond to minimum ionizing particles.

4.6.1 Efficiency for MIP's

Figure 4.11 shows the general pixel occupancy in a short electron run, showing the very good uniformity of the target and the equalization of the tubes achieved with the HV settings procedure. Also the good beam settings producing a wide and centered electron beam can be deduced (Figure 4.12).

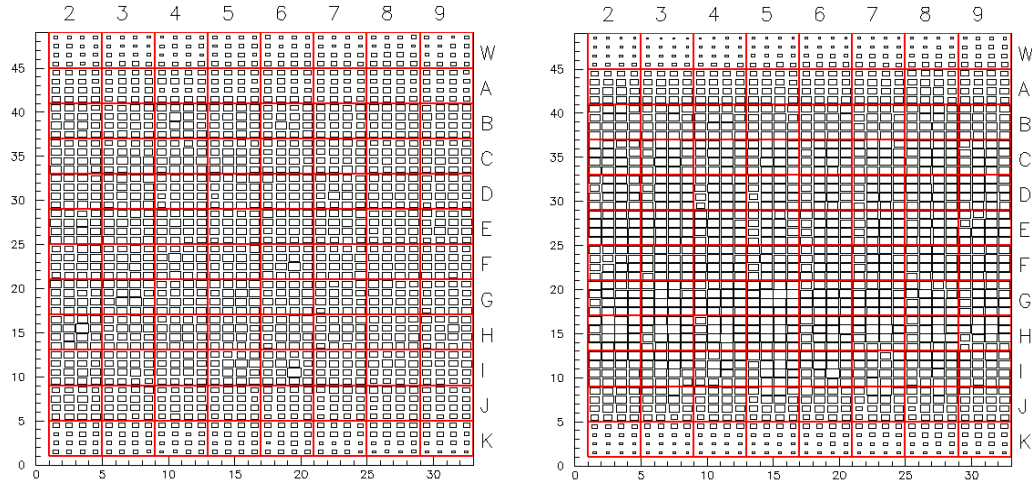


Figure 4.11: Global (x,y) occupancy of the target for a calibration electron run, in the nominal conditions of HV and threshold settings. On the left is the (x,y) occupancy for all the hits (at any time in the full TDC window $[-10 \mu\text{s}, +20 \mu\text{s}]$). On the right is shown the (x,y) occupancy for the hits in time with the trigger (i.e. the incoming electron tracks only). The projection of the right plot on the y axis (Figure 4.12) is the (horizontal) profile of the electron beam.

From such an electron run, where the beam tracks uniformly illuminate all the pixels (Figure 4.11, right) it is possible to measure the detection efficiency for mip's for each pixel of the target. The pixel efficiency is calculated as the ratio between the number of successes in a pixel (i.e. how many times there is a hit belonging to a straight track in that pixel) and the number of trials (i.e. the number of straight tracks that would include that pixel). This assumes a binomial distribution, i.e. a detection probability in the pixel equal for all the tracks. Given the poor number of straight tracks in the upper and lower rows of the target ($y \leq 4$ and $y \geq 45$), the pixels belonging to these rows have been excluded in the calculations of global pixel efficiencies. These calculations will then be referred to 80 over 96 tubes only, or equivalently 1280 over 1536 pixels. For efficiency calculations, a simple but restrictive definition of straight track is adopted: a straight track is a track which occupies one row only ($y_{min} = y_{max}$), with a minimum amount of 15 hits in time with the trigger,

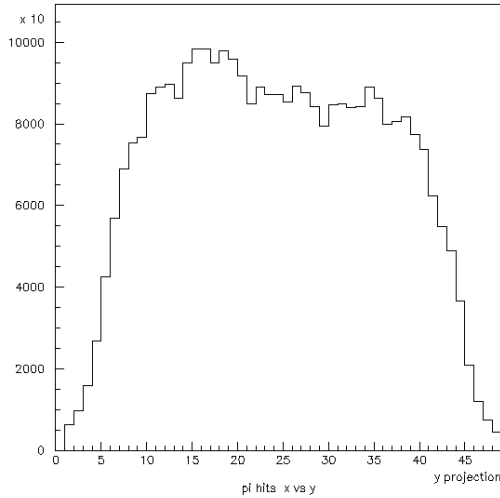


Figure 4.12: Electron beam profile in the y (horizontal) direction. Assuming the beam has no divergence, this plot can also be interpreted as the number of straight tracks as a function of their y coordinate.

and at least one hit in the first tube ($x_{min} \leq 4$) and in the last tube ($x_{max} \geq 29$).

The results about the detection efficiency for mip's are shown in the histograms of Figures 4.13 (single pixel efficiency) and 4.14 (average efficiencies, per tube and per position inside the tube). The average pixel efficiency for mip's (ϵ) is around 85%. The efficiency is high enough to conclude that the bias introduced by the track definition for the hits in the first and last columns of tubes ($x_{min} \leq 4$ and $x_{max} \geq 29$) is small. The probability P of having zero hits in these first and last tubes is indeed negligible:

$$P(0|4) = (1 - \epsilon)^4 \sim 5 \times 10^{-4}.$$

From the average efficiencies, per tube and position inside the tube (Fig. 4.14) we conclude that all the efficiencies stay in a range of about 10% around the value of the average pixel efficiency. As for the pixel position inside the tubes, strong differences in the efficiencies are registered, with the four central pixels more efficient than the others. This is due to systematic gain variations by up to 30 % between central and peripheral channels in the same PSPM. When the systematic uncertainty of the muon lifetime measurement will be treated (Chapter 6), the dependence of the muon lifetime versus the efficiency will be included. In particular the lifetime measured with tubes with different efficiencies and the lifetime measured in different pixel position inside each tube will be studied.

4.6. CALIBRATION RUNS WITH ELECTRONS: EFFICIENCY AND TIME RESOLUTION 85

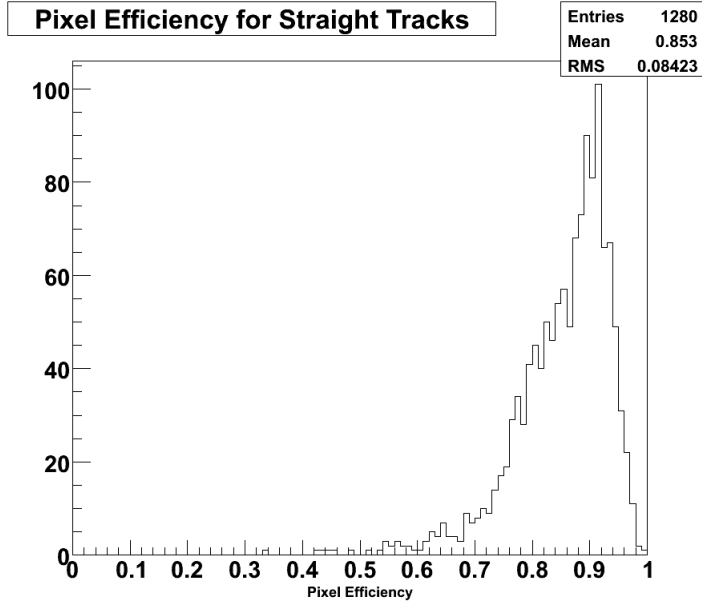


Figure 4.13: Pixel efficiency for mip’s detection for the FAST target, obtained from the straight tracks of a calibration electron run.

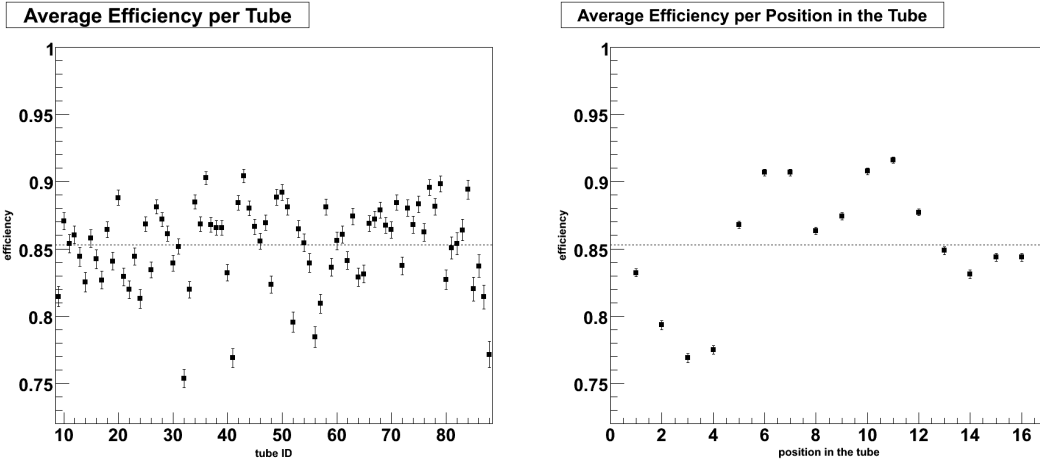


Figure 4.14: Left: Average pixel efficiency in each tube of the FAST target (only 80 of the 96 tubes are considered here). Right: Average pixel efficiency in every position (from 1 to 16) inside the tube. The dashed line in both plots represent the value of the average efficiency per pixel, extracted from Figure 4.13. The numbering scheme for the tubes and positions inside the tubes is the same one of Figure 3.13.

4.6.2 Time Resolution

One important information that can be extracted from runs with straight electron tracks is the time resolution of the full readout chain. For each straight track in the target, its average time (as the average of the timestamps of all the hits belonging to the track) is calculated. Then the difference between the average time of the track and the times of the hits is obtained, and used to fill the histogram of Figure 4.15. The result - as shown from the fit - is a nice gaussian shaped distribution. The sigma of the distribution, $\sigma = (0.994 \pm 0.001)$ TDC tick, is the time resolution of the full readout chain, which includes both the hardware resolution i.e. differences in cable lengths, and the software timing shift and adjustment needed to synchronize the zero time of each TDC with the particle tracks (as described in Section 4.5.2).

The important consequence of the result of Figure 4.15 is the definition of simultaneity in FAST: hits are considered simultaneous if they happen in a ± 3 TDC ticks window, corresponding to 3σ 's of the time resolution.

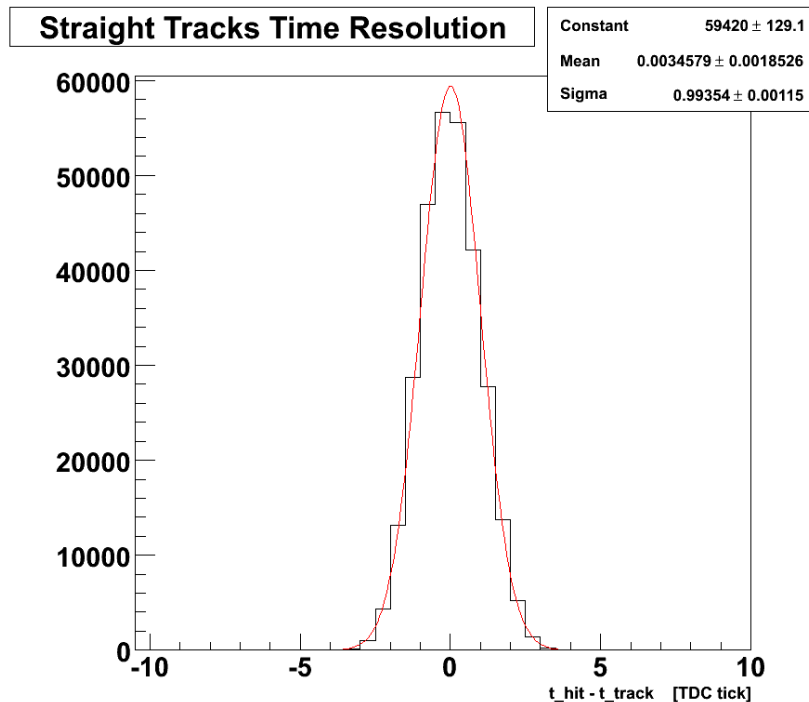


Figure 4.15: Time difference between the times of the hits of a straight track and the average time of the track itself, measured in TDC ticks. The time resolution of the full FAST readout chain is ~ 1 ns.

4.7 Pion Runs: Nominal Running Conditions

The FAST experiment, in its nominal conditions for muon lifetime measurement, runs with a pion beam. The running conditions are in general the following ones:

- Narrow LV1 beam trigger timed on pions.
- BC3 removed from the trigger.
- Wedge and collimator in place.
- Nominal HV values for the PSPM's (Table 4.2) and nominal threshold values for the discriminators (Section 4.2).
- As for the trigger of the TDC's, by default it is the selective LV2 trigger: trigger on muons, 7×7 superpixel, and muon coordinates transmission. During commissioning activities, however, the LV2 operational conditions can be changed, according to the needs. So for example, for the characterization of the pion beam profiles, the most convenient choice is to use the LV2 system in pion coordinates transmission; sometimes also the global, non selective, trigger is used. (See Table 3.5, Section 3.7.2, for the operating options of LV2).
- As for the beam rate, the goal has always been to run with the highest possible rate that the DAQ system could handle. In practice, a LV2 rate of about 15 kHz for the data collected during the 2005 beam tests (about 40 kHz of LV1 pion triggers, about 80 kHz of beam rate) and a LV2 rate between 30 kHz and 35 kHz for the nominal running conditions in 2006 run (i.e. about 80 kHz of LV1 triggers, 160 kHz of beam rate) have been used. From the point of view of the DAQ system, a LV2 rate of 60 kHz would have been achievable in 2006 (Section 3.6.3). It was however not feasible, due to a problem affecting the TDC's, that will be treated later in Section 4.10.
- For every beam rate (corresponding to different tunings of the settings of the beam line components) the beam position and profiles in the target have to be tuned, in order to have a wide and centered beam, both horizontally (y profile) and vertically (z profile).

The plots about time distribution and global target occupancy that will be presented in the remainder part of the present chapter refer to typical pion runs, in the running conditions listed above.

4.8 Global Time Distribution

Figure 4.16 shows the time distribution of all hits for a typical short run of 10^5 events with a pion beam (LV2 trigger rate ~ 30 kHz), both in the full time range and with a large binning (left histogram), and in a small time region around zero, with a fine binning (right histogram).

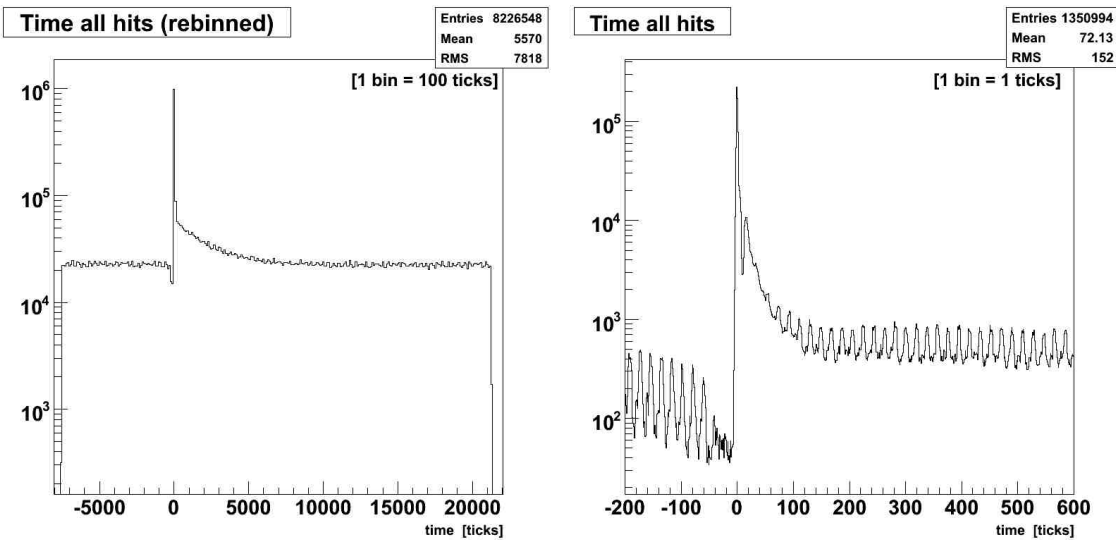


Figure 4.16: Time distribution for all the hits of all the events of a typical short pion run, corresponding to a total statistics of 10^5 events (with about 80 hits in average for each event). The histogram on the left is the global time distribution, in the full TDC time window (about $[-8 \mu\text{s}, +22 \mu\text{s}]$), with a large bin width (1 bin = 100 TDC ticks). The histogram on the right is a closer view (around $t = 0$) of the global time distribution, with the finest allowed bin size (1 bin = 1 TDC tick). The RF structure of the beam, the double hit resolution and the LV1 dead time (see text) are visible effects. The data correspond to a LV2 trigger rate of about 30 kHz, anyhow the shape and the characteristics of the time distribution are totally rate independent.

Several important informations are contained in these two plots:

- Three main time structures are recognized in the global time distribution (Fig. 4.16, left): a “peak” around zero, corresponding to the pions entering the target; a negative slope on the positive times region, which represents the muon decay times; and a almost flat accidental background distribution. A closer view around zero (Fig. 4.16, right) shows that the $t = 0$ peak has a step slope coming from the pion decays. A very simple exponential fit can be applied to verify this (Figure 4.17): although the fit quality is obviously very poor,

the values obtained from the slopes are compatible with the pion and muon lifetimes:

$$\begin{aligned}\tau_{\pi}^{fit} &= [28.3 \pm 1.3] \text{ ticks} \sim 29.5 \text{ ns}; \quad \tau_{\pi} = 26 \text{ ns} [12] \\ \tau_{\mu}^{fit} &= [2104.2 \pm 66] \text{ ticks} \sim 2192 \text{ ns}; \quad \tau_{\mu} = 2197.03 \text{ ns} [12]\end{aligned}$$

- The background is the combination of a flat accidental distribution and a periodic structure. This is the RF structure of the beam with a period of $T_{RF} = 19.75 \text{ ns}$. It is due to all beam particles which periodically flow into the target.
- When the LV2 is used as trigger for the TDC's, as it is the case for the data presented here, the full TDC window is $[-8 \mu\text{s}, +22 \mu\text{s}]$. This is in fact the range limit of the general time distribution (Fig. 4.16, left).
- The double hit resolution of the discriminators, i.e. the minimum time separation between two consecutive hits, is 15 ns. This explains the depletion region at early positive times, where no second hits can be recorded.
- The suppression of beam particles between -50 and 0 ticks is due to the 50 ns required separation between two LV1 (beam) triggers.

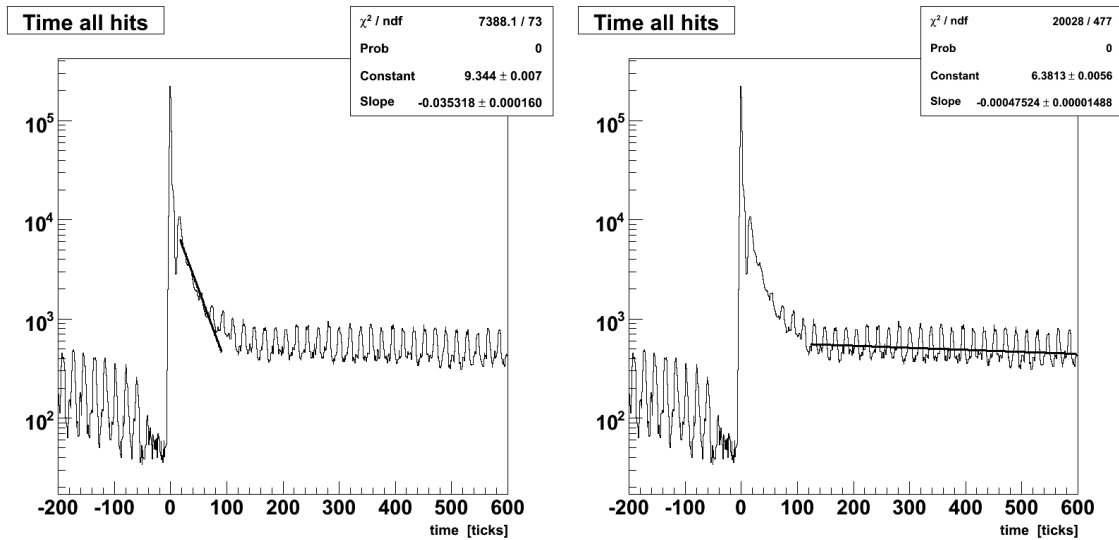


Figure 4.17: Simple exponential fits applied to the two time slopes of the general time distribution of a short pion run. The fitted slopes show that the two time structures come from pion (left) and muon (right) lifetimes.

4.9 Pixel Occupancy and Beam Profiles

Figure 4.11 showed the pixel occupancy for all hits from straight electron tracks in the target. The corresponding result when a pion beam (nominal condition, including the wedge beam degrader) is used, with the TDC's triggered by the global LV1 trigger at low rate (LV1 ~ 7 kHz), is shown in Figure 4.18. Although the electron beam remains the best tool to prove the uniformity achieved in the target, the overall occupancy with pion tracks and global LV1 trigger has the important feature of showing the effect of the wedge beam degrader which leads to a gradient in the occupancy of the hits, from left to right, along the pion penetration direction x .

When LV2 is used as trigger for the TDC's (Figure 4.19, left) the selective TDC readout pattern is visible. Very different occupancies in the TDC's are now allowed (Figure 4.19, right), because of the selective trigger which geometrically privileges the four middle TDC's. The effect of the wedge remains visible, in the global gradient in the (x,y) occupancy along the x direction, even if dominated by the discontinuity at the TDC's borders lines.

The selective LV2 trigger readout justifies non uniform global hits occupancies in the target. However the stopping pions distribution must be uniform. This is indeed the case, as shown in Figures 4.20 and 4.21, once the beam settings are properly tuned. The results reported in these figures refer to a pion run, chosen as example, at LV2 trigger rate of 15 kHz, with LV2 used in the pion coordinates transmission mode. The distributions of Figures 4.20 and 4.21 can be indeed generalized to any other trigger rate, provided that, for each different rate, the beam position and dimensions are tuned to have a centered, not divergent and wide enough beam. The three bidimensional histograms in the figures (xy , yz and xz planes) show the good uniformity in the stopping pion distributions, both in the horizontal and vertical planes. Indirectly (with the projection on the three x , y and z axis) they also describe the typical pion beam profiles characterizing the nominal data taking phases. These beam profiles are reported in Figure 4.23. Their shape corresponds to well tuned parameters for the beam settings.

Figure 4.21 shows the strong correlation - imposed by the wedge degrader - between the penetration depth of the pions x and their vertical entry position, z , recorded as a z -counter tag from the hodoscope. In Figure 4.22 the same (x,z) distribution obtained with a muon beam is shown. The run was a short test run with a muon beam, in not optimal conditions of event building, which explains the effect of enhancement on the border of the TDC's. The enhancement of the muon stopping points in the lower and deeper part of the target only (high x , low z coordinates) is clear. If compared with the same result for pions (Fig. 4.21), this confirms the conclusion of Section 4.4.2 from direct range measurement: the muons penetrate in the target about 20 pixels more than the pions. A proper cut applied on the x of the pion

stopping point, depending on its z -tag (expected $x(z)$ value ± 8 pixels) allows a very efficient reduction of the beam muons.

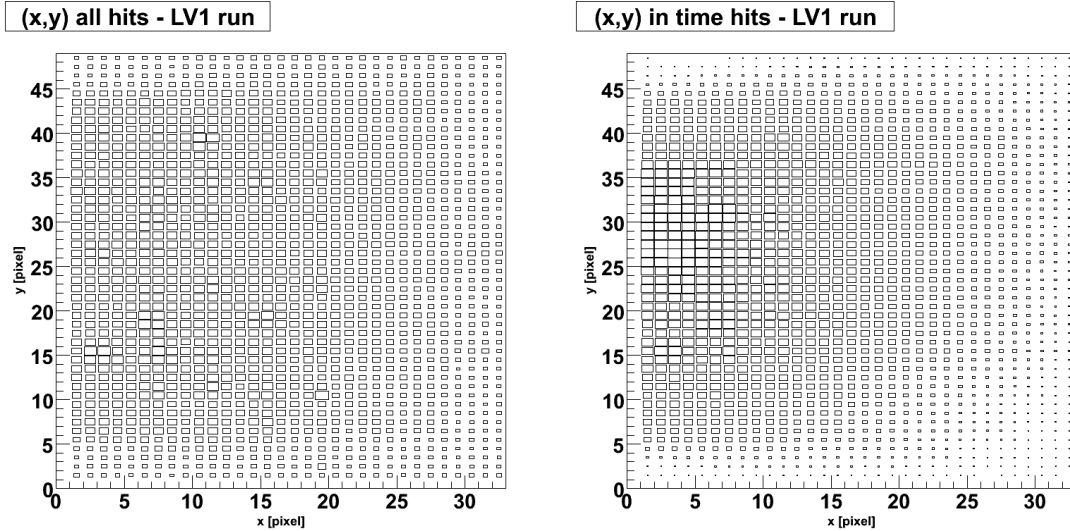


Figure 4.18: All hits (x,y) occupancy of the target for a low rate (LV1 rate = 7 kHz) pion beam run, when global LV1 trigger is used for the TDC's. On the left is the (x,y) occupancy for all the hits (at any time in the full TDC window); on the right is the (x,y) distribution of the hits belonging to the triggering pion tracks only (i.e. hits in time with the trigger).

4.10 TDC's and Event Builder

Special attention has been given to the optimization of the TDC's performance and the way the events are built, starting from the single TDC fragments.

The performance of the event building is summarized in Figure 4.24, where the number of TDC's per event is plotted: according to the superpixel logic, only 1 or 2 or 4 TDC's are allowed per event, with 2.4 in average. The obtained result is compatible with the expectations. The small number of events with 3 or more than 4 TDC's, corresponding to 1.5% of the total, are split and/or merged events, due to the finite size of the buffers adopted for the event building logic. Most of the wrongly built events are removed, however, in the analysis stage, by quality cut criteria.

From the hardware point of view, mandatory elements for properly working TDC's are:

- very well shaped input hits (data and control words) and control signals (trigger and clock);

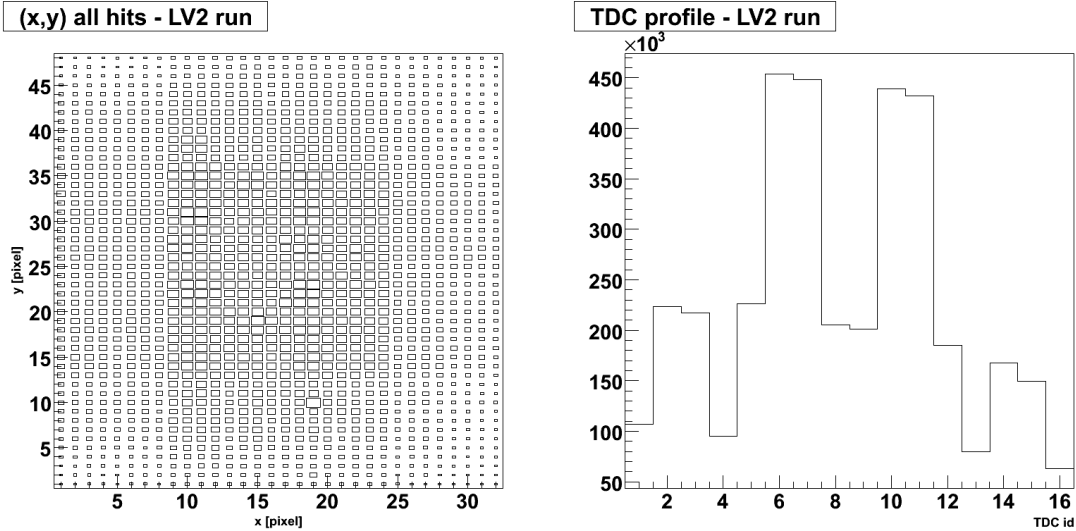


Figure 4.19: Left: Global (x,y) occupancy in the target, for all the hits at any time in the full TDC window, for a typical pion run with selective LV2 trigger (LV2 rate = 15 kHz). Right: Total TDC occupancy profile for the same pion run.

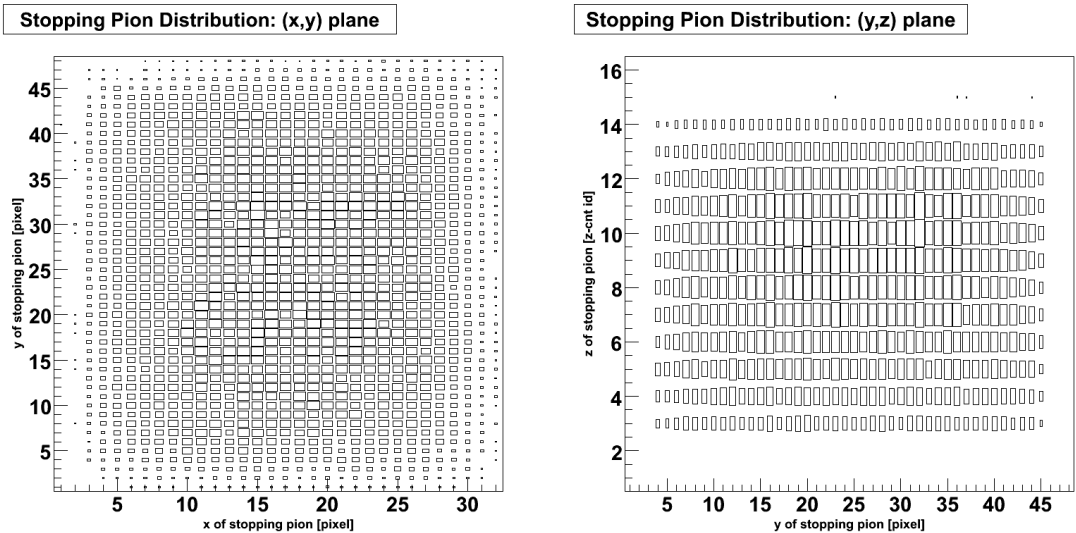


Figure 4.20: Distributions of the stopping pion points for a pion run with selective LV2 trigger (LV2 = 15 kHz). On the left is the stopping pion distribution in the horizontal (x,y) plane. On the right is the stopping pion distribution in the vertical (y,z) plane.

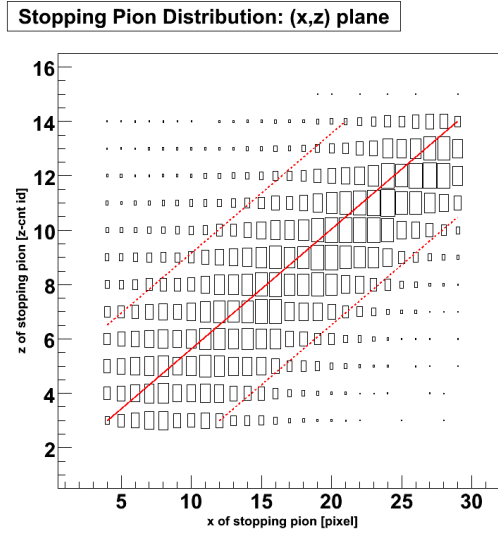


Figure 4.21: Distribution of the stopping pion points in the (x,z) plane, for the nominal LV2 trigger pion run (LV2 = 15 kHz). The analysed run is the same as in Figure 4.20. The diagonal band represents the expected xz occupancy for a pion beam: central xz value (straight line) $\pm 8 x$ pixels (dashed lines) around it.

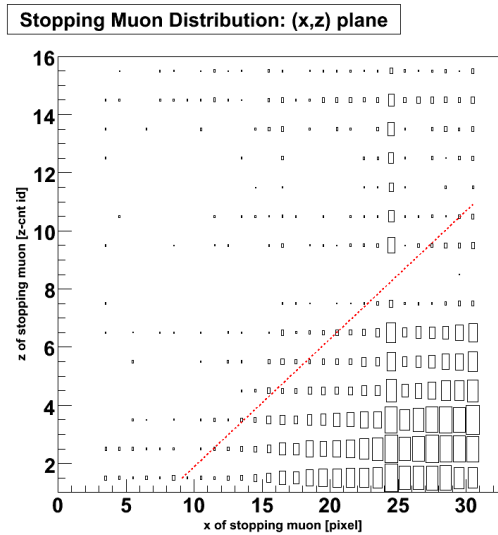


Figure 4.22: Distributions - in the vertical (x,z) plane - of the stopping points of the muons for a special dedicated run with a muon beam. The enhancement at $x = 24$ (on the TDC border) is due to bad performance of the event building in this run. The dashed diagonal line limits the region where pions stops are expected.

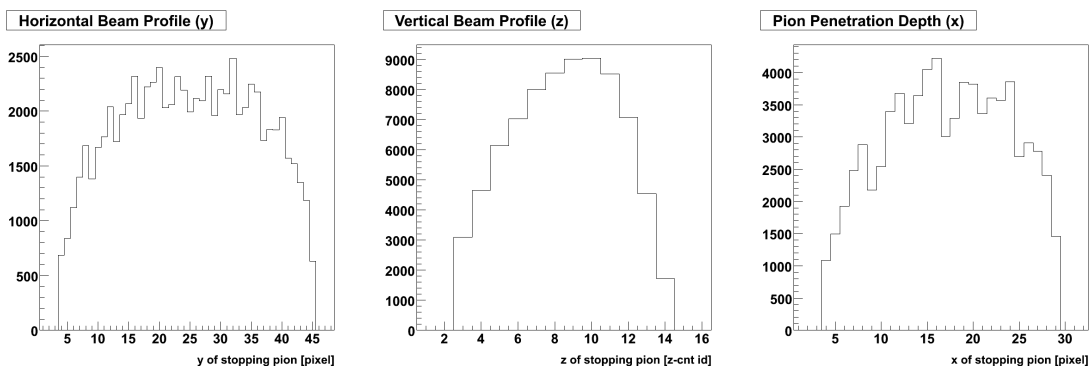


Figure 4.23: Pion beam profiles on the horizontal y direction (left histogram) and on the vertical z direction (middle histogram) at the target location. For completeness, also the x position (penetration depth) of the pions in the target is given (right histogram).

- full masking of all the hits during the initialization phase of the TDC's. This is achieved by setting - during the initialization - the discriminator thresholds to a very high value (to block all the target hits), and by blocking all the control words with a proper coincidence logic;
- the veto of any new trigger when the TDC's are in a busy status.

Beside this, TDC's performance is optimized by a careful tuning of the internal parameters which regulate the memory access and manage the internal buffers of the TDC's. When these conditions are met, the system is reliable and efficient, except for one single problem remaining in the TDC's functioning, the *time smearing* problem, that corresponds, to our present understanding, to a failure in the synchronization of the four chips belonging to the same TDC board.

The effect of the time smearing is shown in Figure 4.25, where the time distribution of all hits, when the problem occurs, is presented. Figure 4.25 should be compared with the typical time distribution of Figure 4.16. When the time smearing occurs, it is reliably detected online by counting hits in a narrow time window preceding the trigger time: whenever a significant number of hits is detected in this window, the run is aborted and the bad events discarded. The data affected by this problem are then excluded from the analysis, so they do not provide a bias in the measurement presented here. The influence of time smeared data on the muon lifetime analysis will be included in the systematic uncertainty study, Chapter 6, to account for possible failures in the rejection of bad data.

A side effect of the time smearing problem is the limitation of the usable LV2 rate well below the possible 60 kHz rate achievable by the DAQ hardware. At trigger rates

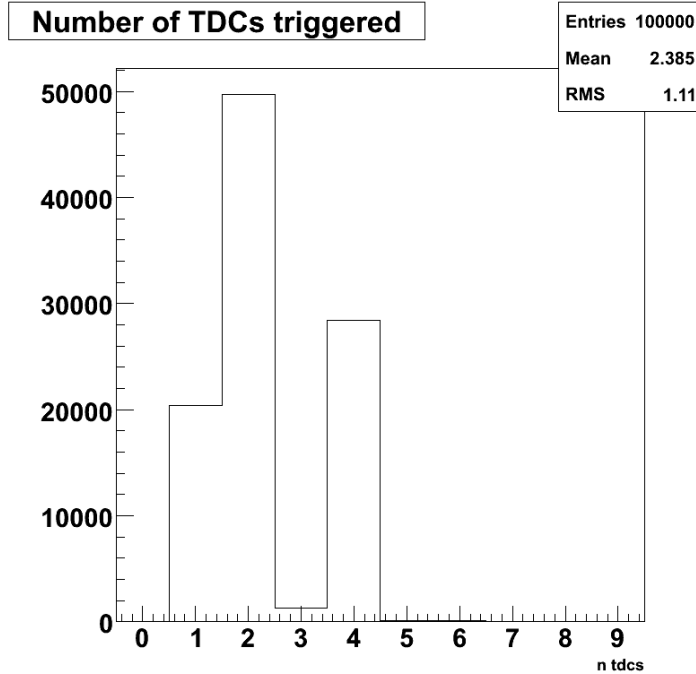


Figure 4.24: Number of triggered TDC's per event, in a typical selective LV2 run, with 7×7 superpixel dimension.

above 45 kHz, the data loss by this deformation effect becomes prohibitively large. Therefore data taking during 2006 was limited to a LV2 trigger rate of about 30 kHz.

4.11 LV2 Trigger: Commissioning Activities and Efficiency

The performance of the LV2 Trigger System is tested and optimized in a series of LV2 commissioning test runs. For these tests, the trigger for the TDC's is provided by the LV1 trigger, but the full informations from the LV2 (i.e. the coordinates of the stopping particle, and which TDC's would have been triggered if LV2 was acting as selective trigger) is also recorded in the TDC's. The LL V_{thr} value (for TDC input data) is set equal to the HL V_{thr} (for LV2 input data). With this, all the LV2 informations are available as data in the TDC's. A software emulator of the LV2, with an algorithm that reproduces the logic of the LV2 trigger in finding the pion and muon stopping point, is applied in an offline analysis. The comparison between the software algorithm and the LV2 hardware response checks the consistency of the LV2 outputs, both in the definition of the stopping particles and for what concerns the superpixel

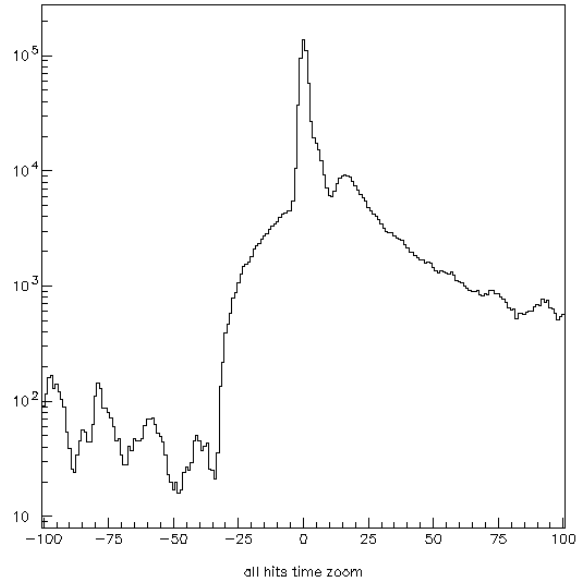


Figure 4.25: Anomalous time distribution of all the hits as recorded by the TDC's when the time smearing problem appears. The data shown here include only one TDC unit with the time smearing problem; the other TDC's are in this case unaffected.

logic, with the number and pattern of the activated TDC's. This is repeated for all the different LV2 operational working conditions. The same method also allows the fine time tuning of the first and second snapshot time windows, whose exact length has to be validated with data (see below) and finally defines the efficiencies for the LV2 trigger system. In addition, a scan of the LV2 performance at different values of HL V_{thr} , allows the determination of the HL threshold working point (see Section 4.2).

The efficiency for LV2 in its nominal operational conditions (trigger on muon, 7×7 superpixel, and muon coordinates transmission), is the ratio between the number of LV2 triggers (logical OR of the 16 output signals) and the number of LV1 triggers:

$$\epsilon_{LV2} = \frac{LV2 (OR \times 16)}{LV1}.$$

It corresponds to 37%, and it is independent on the beam LV1 rate. This efficiency is the result of the product of the efficiency in the pion detection and the efficiency in the muon detection.

The detection efficiency of the stopping π^+ is approximately 80% (Figure 4.26). It

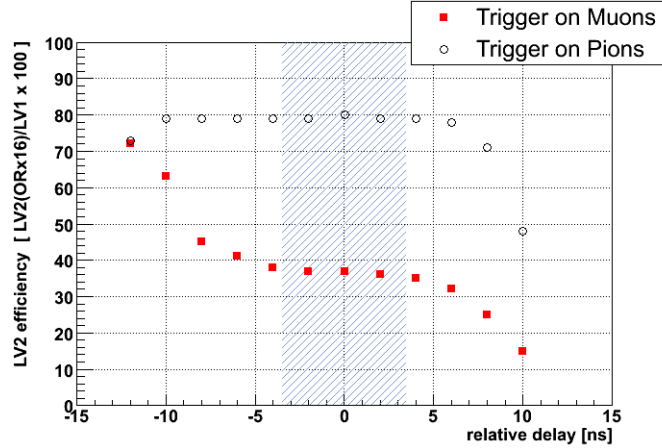


Figure 4.26: LV2 efficiency (for LV2 used both in muon trigger mode and in pion trigger mode) versus a global delay time of the LV2 window w.r.t. the data hits. In nominal conditions of trigger on muons, the operative region for the LV2 trigger system is provided by the flat region of constant efficiency (vertical band in the figure). The nominal LV2 efficiency is 37%: it is the result of the combined efficiency for pion and muon detection, and it is dominated by the double hit resolution.

includes both the efficiency of the LV2 algorithm in the detection of the pion stopping point, and the purity of the LV1 signal. The performance and reliability of the algorithm is tested using the software emulation, with LV2 used in pion trigger mode and pion coordinates transmission, showing an excellent agreement between the software emulation and the LV2 hardware, up to 95 %. The small (5%) discrepancy is due to unavoidable mismatch between the LL and HL outputs of the discriminators: the software and the hardware differ in fact mainly by 1 pixel only, explained with a single hit loss, either at LV2 or TDC input.

As for the detection of the muon from the pion decay, the efficiency is dominated by the double hit resolution. If the muon appears in the same pixel as the pion, it can be observed only if it happens at least 15 ns after the pion. Since τ_π is around 26 ns, the probability of muons before 15 ns is about 40%. This fraction of events is lost, unless the muon is in a pixel adjacent to the pion one. Since the sample is dominated by muons in the same pixel as the pions, this intrinsic inefficiency in the muon detection cannot be avoided. It is indeed the dominating factor in the final LV2 efficiency of 37% (Figure 4.26).

The LV2 global efficiency depends on the lengths and relative positions of the first snapshot (for the pion identification) and the second snapshot (for the muon finding). A too short first snapshot, for example, would result in anomalously high efficiency, because muons can be faked by pion hits; on the contrary, a too long first

snapshot would not be efficient enough for muons. The two windows are initially set respectively to $[0, +15 \text{ ns}]$ and $[+15 \text{ ns}, +100 \text{ ns}]$, but the actual working conditions have to be determined with data in the final setup. Figure 4.26 shows the fine time tuning for the 1st and 2nd snapshot positions. A global time shift is applied between the LV2 window and the LV1 signal, and the global LV2 efficiency is registered at every delay point. This defines a large working region for the LV2, with constant efficiency values. In the working region, corresponding to well tuned snapshots positions, the mean efficiency values for pion and muon detection from the LV2 are - as seen before - around 80% and 37%, respectively.

A scanning of the efficiency of the LV2 trigger system in the muon detection, as a function of different values of HL V_{thr} is shown in Figure 4.27. It confirms that 400 mV is the correct setting for the HL, and also shows a large operative region.

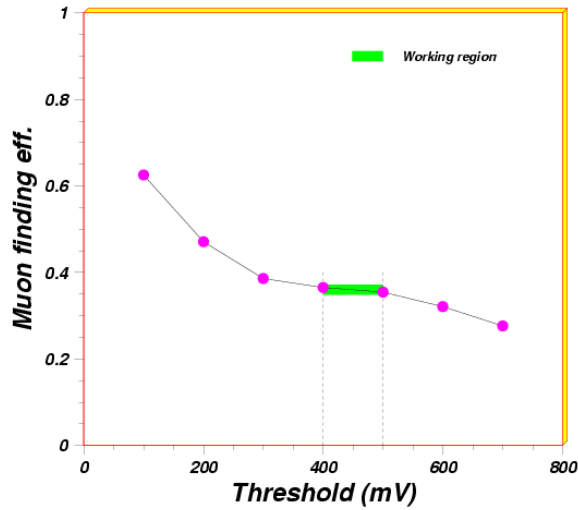


Figure 4.27: LV2 efficiency in muon detection measured for different HL V_{thr} values on the discriminators.

Chapter 5

Muon Lifetime Analysis

In the previous chapters we have provided a detailed introduction to the muon lifetime measurement performed with the FAST detector. It has been shown in particular how the full physics informations (particles entering into the target, pion and muon decays, electron tracks, trigger information, tag informations and z -counter hits) are converted into the *events* to be finally passed to the analysis, whose ultimate aim is to provide a muon lifetime histogram. From the point of view of the analysis, an event is a group of TDC data (coordinates and time information of the hits, plus control information, like triggers and event tags), generally coming from more than one TDC, that correspond to the same physical event triggered by a pion in the target and that include all the hits in the $30 \mu\text{s}$ time window for the TDC's. A fit procedure applied on the muon lifetime histogram provides the lifetime measurement, as one of the free parameters of the fit.

The present chapter will focus on these last two items: the analysis software, from data to histograms, and the fitting procedure applied on the muon lifetime histogram. This will be performed on a data sample corresponding to about 10^{10} muon decay events, from a collection period of about three weeks in 2006 (generally referred to as Run 2006).

The muon lifetime measurement - within its present statistical uncertainty - will be presented here. The next chapter will complete the measurement, with the detailed study of the systematic uncertainties.

5.1 Run 2006: Data Sample

A sample of 10^{10} muon decay events was collected in a short run of about three weeks between November and December 2006. This sample is the result of the first extensive data collection with the FAST detector, in running conditions very close to the ones required for the final data taking, except for the achieved trigger rate. The global

LV2 rate for the 2006 run was about 30 kHz. The LV2 trigger was used as selective trigger for the TDC's, in its nominal conditions: trigger on muon, 7×7 superpixel, muon coordinates transmission.

The achievable precision on the μ^+ lifetime from the global sample of Run 2006 is comparable to the present world average.

5.1.1 Sub-samples

The total data sample has been divided into 10 sub-samples of reduced statistics (see Table 5.1), for which the beam conditions and the experimental parameters were stable.

Run 2006: Data Samples		
Sample ID	Sample Name	N. events
1	01a	$2.068 \cdot 10^9$
2	01b	$1.070 \cdot 10^9$
3	02	$0.266 \cdot 10^9$
4	03	$0.886 \cdot 10^9$
5	04	$0.974 \cdot 10^9$
6	05	$0.562 \cdot 10^9$
7	06	$2.022 \cdot 10^9$
8	07	$1.565 \cdot 10^9$
9	08a	$0.928 \cdot 10^9$
10	08b	$0.390 \cdot 10^9$
Full Statistics (Run 2006)		$1.073 \cdot 10^{10}$

Table 5.1: Subsamples, with their statistics of muon decay events, corresponding to consecutive data taking periods for the total Run 2006. Stable experimental conditions are assumed in each subsample.

The advantage in this fragmentation, as we will show later, is an improved quality of the fit, mainly due to more accurate description of the background for each sample. We'll show later in the chapter how the complete fitting technique adopted for the muon lifetime measurement will involve both all the subsamples, treated separately, and the full statistics sample all together.

5.2 The Analysis Code: from Raw Data to Histograms

The full analysis procedure can be divided into three main blocks: the reading of the event, the processing of the event (i.e. the real analysis), and finally the filling of the histograms.

5.2.1 Event Reading and Event Structure

The event reading subroutine converts the raw data of the TDC's (already grouped into events by the event builder) to *hits information* and *control words*. In our jargon, hits are all the signals produced by particles in the target (coordinates and time), and control words mean all the information recorded in dedicated TDC channels, that does not correspond to hits from the target. The control words per TDC, attached to each event, are the following ones:

- Trigger information [$\times 2$]: LV1 trigger tag and LV2 trigger tag.
- Event tag information [$\times 2$]: tag1 and tag2 clocks. They are needed in the event building processes, as described in Chapter 3, Section 3.6.2.
- z -counter hits [$\times 2$]: 2 channels of each TDC are devoted to the z -counter hit (one for $z = 1$ to $z = 8$, the other for $z = 9$ to $z = 16$). A delayed coincidence between the z -hits and the LV1 trigger, with a fixed delay, different for each z counter signal (e.g. 0 ns for $z = 1$, 6 ns for $z = 2$, 12 ns for $z = 3$...) allows the proper codification of the 16 z information into 2 channels only per TDC.
- LV2 coordinates (pion or muon stopping location) [$\times 20$]: 20 TDC channels - in a (8,12) bits encoding for the x and y information - are devoted to record the coordinates provided by the LV2 trigger. Differently from all the other control words, common to all the triggered TDC's, the LV2 coordinates are registered only in the TDC that contains the stopping point.

5.2.2 Event Processing: Selection Cuts and Positron ID

Once the hits and the control words are available, the analysis process can start. It mainly consists of several selection cuts applied to the sample, and in the identification of the positron from the muon decay. The positron identification is the main task of the analysis, given that the muon coordinates are provided by the hardware, via the LV2 trigger system.

Table 5.2 lists the events selection applied on the sample, together with the efficiencies for every cut. 42 % of the LV2 triggered events pass all the required cuts

and the positron identification. These are the events going to fill the muon lifetime histograms.

Cut	Single cut efficiency	Global efficiency
LV2 trigger ($\pi \rightarrow \mu$ identified)	1.000	1.000
Number of hits	0.925	0.925
Number/Pattern of triggered TDCs	0.803	0.743
Muon found in LL data	0.994	0.739
Geometrical requirements for π^+ (i.e. match π^+ and μ^+ positions; superpixel inside the target)	0.906	0.669
Match of x_π and z_π	0.889	0.595
Electron identified	0.703	0.418

Table 5.2: Events selection efficiency for the Run 2006 data sample.

A description of the cuts listed in the above table will follow:

- At the very beginning, some cuts on the number of hits are applied on the original sample (*Number of hits* cut), to improve its general quality and eliminate pathological events i.e. events which don't have at least 3 hits in time with the trigger, which is the minimum required by the LV2 algorithm in the definition of a pion (Section 3.7.1).
- The LV2 information about the muon coordinates is then retrieved. It appears as control words in dedicated channels of one TDC, at a fixed time difference w.r.t. the LV1 trigger tag signal. In the muon location provided by the LV2 hardware there should be one LL hit. The analysis checks this; if this is not the case, the event is rejected (*Muon found in LL data* cut).
- A software algorithm applied on the in time hits mimics the LV2 hardware in finding the pion, and provides the (x_π, y_π) coordinates. Once the muon coordinates (x_μ, y_μ) (from the LV2 hardware) and the pion coordinates (x_π, y_π) (from the software algorithm) are available, further checks are performed, and other cuts are applied on the sample. From (x_π, y_π) , the superpixel is computed and the interested TDC's are identified. If the number and/or the pattern of the triggered TDC's (computed vs observed) do not coincide, the event is rejected (*Number/Pattern of triggered TDCs* cut).
- Also, the pion and muon coordinates should be compatible (i.e. same or adjacent pixel), and the superpixel should be entirely contained in the target (i.e. the pion cannot be in the 3 pixels thick border region of the target). If one of

these last two conditions is not fulfilled, the event is rejected (*Geometrical cut*). It should be noticed that the analysis algorithm for the pion coordinates determination, tested and already proven to be fully efficient (Section 4.11), applies now to LL data, while LV2 uses HL data. Some small discrepancies between software and hardware are thus expected.

- As a last check, the matching between the pion location and the recorded z -counter tag is required (*Match x_π/z_π cut*). This range requirement discards fake events, like e.g. a beam muon followed by a second HL signal, like an afterpulse.

For all the events passing the selection cuts described, the positron from the muon decay has to be identified. This is done using a set of 512 mask topologies in a 5×5 pixels matrix around the muon stopping point (i.e. inside the 7×7 superpixel centered on the pion, see Figure 3.15), generated considering all the possible geometrical patterns for electron tracks in the pixels matrix. The full set of electron patterns is reported in Appendix A.

An electron candidate is a cluster of simultaneous hits at any time in the full TDC window, excluding the first snapshot window (occupied by the pion track), which fulfils one of the allowed patterns. If more electron candidates are found for the same muon, the event is rejected. The definition of the positron based on predefined topologies, with an efficiency close to 70%, reduces the accidental background generated by particles from other pion or muon decays, and by other beam particles traversing the same detector region. It also allows detailed systematic studies of the signal and background for each individual topology, and eventually the rejection of those patterns dominated by background.

5.2.3 Lifetime Histograms

When one and only one positron per triggered event is found, its time (t_e) is defined as the average time of the hits belonging to its track, and a good muon decay event is identified. The time difference $t_e - t_\mu$, calculated for each good event, is used to fill the global lifetime histogram, shown in Figure 5.1. Another interesting global lifetime histogram is obtained by the absolute t_e distribution, without t_μ subtract, shown in Figure 5.2, which corresponds to the $t_e - t_\pi$ distribution (given our time reference, where $t_\pi = 0$, see Section 4.5.2).

The two global lifetime distributions, where *global* means that all the events passing the cuts in Table 5.2 contribute to the plots, are filled with the finest possible binning (1 bin = 1 tick), to keep the full time resolution. The two histograms ($t_e - t_\mu$ or $t_e - t_\pi$) are equivalent from what concerns the muon lifetime measurement. In other words, the main slope of the two exponential distributions is the same, provided that early times (i.e. earlier than about $10 \tau_\pi$), where extra muons can be produced by

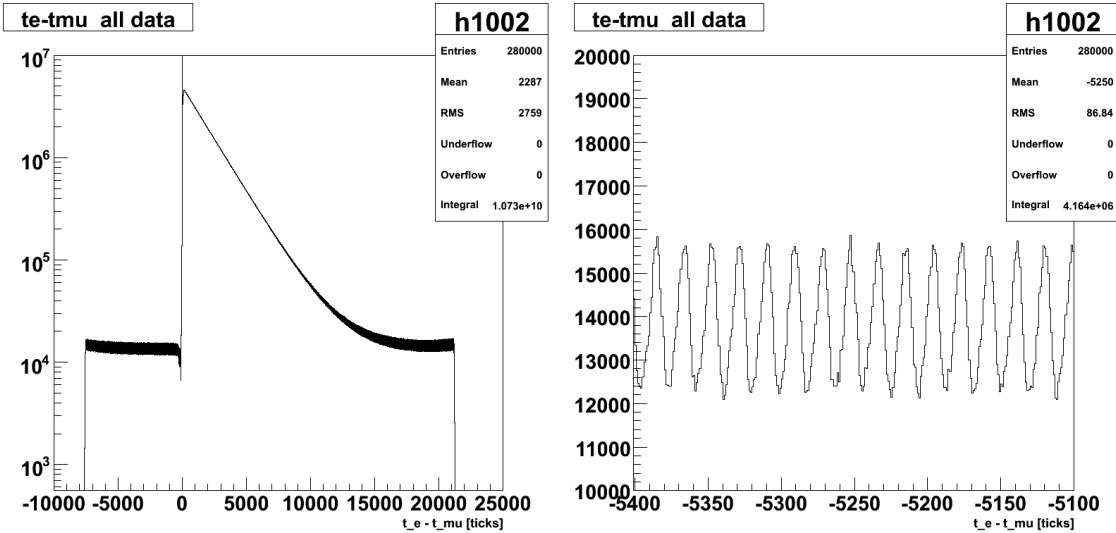


Figure 5.1: Muon lifetime histogram: $t_e - t_\mu$ distribution (in TDC ticks) for the full statistics of muon decay events from Run 2006 (left). The right plot is an enlarged view of the accidental background region at negative times.

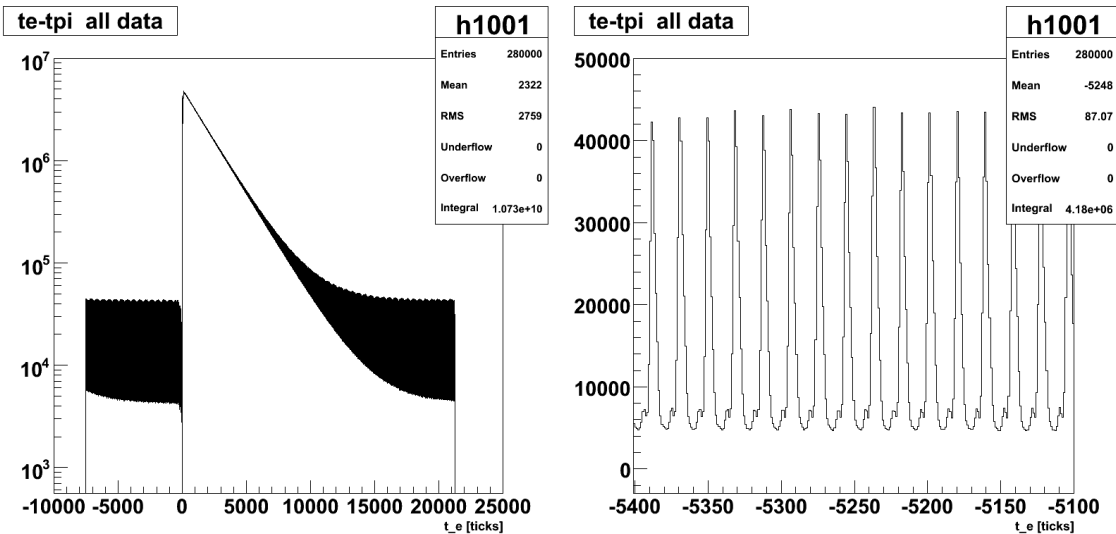


Figure 5.2: Muon lifetime histogram: $t_e - t_\pi$ distribution (in TDC ticks) for the full statistics of Run 2006 (left plot), together with an enlarged view on the accidental background region (right plot).

the pion beam particles, are disregarded. After these early times, the most striking difference among the $t_e - t_\mu$ or $t_e - t_\pi$ distribution is in the shape of the background. It

should be noticed that the two background plots of Figure 5.1 and 5.2 have different vertical scales. The background consists of flat accidental events, without any time structure (DC offset), as well as events where the decay electron is faked by beam particles from an RF bucket different from the one of the triggering pion, causing a periodic structure. This is true for both distributions, but, while $t_e - t_\pi$ has a clear structure for the background, the same distribution is smeared in case of $t_e - t_\mu$. This makes the distribution of $t_e - t_\pi$, Figure 5.2, the “golden” muon lifetime distribution, from which the lifetime will be extracted, via the fitting procedure. It provides in fact the most precise achievable background description.

Together with the global lifetime histograms used to extract the muon lifetime, many other sets of lifetime histograms are filled. The aim is to have separate lifetime measurements of reduced statistics for several parameters of the detector geometry, or decay topology. The idea is to profit at maximum of the granularity of the detector, to be able to identify and quote different sources of systematic errors. The following partial lifetime histograms ($t_e - t_\pi$ distributions) are separately filled in the analysis, and available for further systematic study:

- one lifetime plot for each x_π location, excluding the 3 pixels border region ($x_\pi = 4, 5 \dots 29$) [$\times 26$]
- one lifetime plot for each y_π location, excluding the 3 pixels border region ($y_\pi = 4, 5 \dots 44$) [$\times 42$]
- one lifetime plot for each position (1 to 16) of the pion inside the tube [$\times 16$] (See Figure A.1 in Appendix A)
- one lifetime plot for the pion stopping point in each tube [$\times 96$]
- one lifetime plot for each relative position of pion, electron and muon in the same or adjacent pixels (i.e.: π, μ, e in the same pixel; π, μ in the same pixel, e in an adjacent one; π, μ in different pixels, but e in the same pixel as μ ; π, μ, e in different pixels) [$\times 4$]
- one lifetime plot for each relative position of the muon w.r.t. to the pion, in the 3×3 pixels region around the pion [$\times 9$] (See Figure A.2 in Appendix A)
- one lifetime plot if there is only one muon candidate (LL hit in LV2 location), and another lifetime plot if more muon candidates are present [$\times 2$]
- one lifetime plot for each allowed topology of the decay electron [$\times 512$] (See Figures A.3 to A.10 in Appendix A)
- one lifetime plot for electrons ϕ distribution in 8 sectors around the muon location [$\times 8$] (See Figure A.11 in Appendix A)

Because of file handling reasons, not all the histograms listed above can have the 1 tick binning of the global lifetime distributions. A large binning (1 bin = 20 ticks) is applied for most of the specific lifetime histograms.

5.2.4 Control Histograms

Together with the previously described lifetime histograms, several other control histograms are produced by the analysis. They do not contain any lifetime information, but all the general information about the behavior of the target and the quality of the run. For example: the number of hits, the number of control words, the beam profiles, the TDC and LV2 operation monitoring histogram. Some control histograms have been already shown in the previous chapter (Figures 4.16 to 4.23, about the time distribution and the pixel occupancy).

5.2.5 FAST: An Online Analysis Experiment

The analysis in FAST (from raw data to histograms) is performed online. Given the high beam rate and the many informations collected for each event (hits and control words), it is not feasible to store the entire raw data volume on disks for later analysis. Only few histograms can be retained, and the original raw data are lost. This justifies, once more, the need to produce all the specific lifetime histograms - together with the main global ones - for a later study of the systematics, since it is impossible to reprocess the dataset for dedicated studies.

In Appendix A some more details on the online and offline analysis for FAST will be given.

5.3 Muon Lifetime Measurement: Fit Strategy

The muon lifetime (τ_μ) measurement is extracted from a binned maximum likelihood fit procedure to the lifetime histogram¹. The high precision requirements of the FAST experiment impose that all the details of the fitted distribution (statistical errors, correlations among parameters, stability of the fit, quality and robustness of the fit) must be carefully analysed. The study of the systematic uncertainty will be described in the next chapter, except for the part concerning the definition of the fitting function itself (Sections 5.4 and 5.9).

In the previous sections we have identified the $t_e - t_\pi$ distribution (Figure 5.2) as the proper muon lifetime histogram that has to be used for the fit. This choice has been justified in terms of the best achievable description of the background.

¹The fit is done using the standard minimization package `Minuit` in ROOT [57].

The fitting function has now to be determined. It must include both the signal (i.e. the real muon decays, with their exponential decay law) and the background.

The background will be studied on the pure background sample provided by the negative times events of the $t_e - t_\pi$ distribution, up to about $-8 \mu\text{s}$ before the pion. There are two principle ways to accurately describe the background:

- One can try to analyse and understand in detail its composition and time structure, and describe it by a proper function using the full time resolution of 1 TDC tick. This method will give confidence that the main features of the background are properly understood.
- One can smooth the periodic structure of the background, e.g. by rebinning the histogram, and then describe it by a simpler function. This leads to a loss of information, but without compromising the measurement: the lifetime information resides in the slope of the time distribution, which is unaffected by rebinning. Asymptotically, already the first moment of the distribution contains all relevant information and is a sufficient estimator of the muon lifetime.

It will be argued in this chapter that the latter method gives the optimum result for the muon lifetime at the current level of understanding. It is difficult to accurately describe the background in terms of a fitting function and arrive at a satisfactory fit quality, but the periodic structure of the background is understood as a function of the beam components and their arrival times. Therefore, the results of the former method will be described first.

The fitting function will be defined iteratively. A first version, defined on an a priori prediction of the data distribution, is initially used for the fit. It describes the exponential trend of the signal and uses as background description the one derived from the negative times region of the lifetime distribution, i.e. fixed shape. The fit is applied to each of the 10 subsamples (Table 5.1) separately, and - afterward - to the full statistics sample. The study of the residuals of the fit, and in particular its Fast Fourier Transform (FFT) analysis will show the limits of the fitting function, and will indicate ways to improve it. Finally, the best method for the analysis will be to rebin the lifetime histogram, using the RF beam period, and fit it with a simpler fitting function.

The details of the procedure adopted to extract the muon lifetime from the data sample will be given in the rest of the present chapter. It will be structured as follows:

- Section 5.4: The description of the predicted basic fitting function, in its first version, is given. It includes the signal, the background, obtained as a fixed shape background from the negative times region, plus a time dependent background component.

- Section 5.5: The description of the procedure to extract the background shape from the negative times lifetime distribution is detailed.
- Section 5.6: The fit on the negative times region is performed. This is done separately for each subsample, and the results are combined to extract the RF period for the background.
- Section 5.7: The positive time region of the lifetime histogram is fitted, separately for each subsample, with the fitting function defined in Section 5.4, and the background description from Section 5.5.
- Section 5.8: The full statistics sample is now considered, and the same fitting procedure of Section 5.7 is applied. The study of the residuals of this fit shows how to improve the fitting function.
- Section 5.9: A new fitting function, including the TDC non-linearity effects description and a pulsed background structure, evolving with time, is defined. The results of the fit on the full statistics sample are then presented.
- Section 5.10: The “smart rebin method” is applied on the histogram, to match the bin width with the RF period. This results in the best quality fit, and is then taken as the nominal fit method.
- Section 5.11 finally summarizes the results of the muon lifetime measurement, within its statistical uncertainty, obtained by the full statistics available for the Run 2006.

5.4 A Simple Fitting Function

The first fitting function used to describe the positive times distribution of the $t_e - t_\pi$ histogram is given by:

$$N(t) = B(t_{rel}) + S(t) + B'(t) \quad (5.1)$$

where:

$$t_{rel} = \text{mod}(t - t_0, T_{RF}) \quad (5.2)$$

$$S(t) = \frac{N_0}{\tau} e^{-t/\tau} \quad (5.3)$$

$$B'(t) = P_0 + P_2 \frac{N_0}{\tau} e^{t/\tau} . \quad (5.4)$$

$B(t_{rel})$, with t_{rel} defined by Eqn 5.2, represents the background function, as derived from the negative times region study, including an absolute time phase t_0 . It describes the periodic structure and the flat accidental contribution. It will be extensively detailed in the next Section 5.5.

$S(t)$ represents the positive times lifetime distribution (background subtracted), including the pure exponential law for the muon decay. τ is the muon lifetime, and N_0 represents the total number of signal events.

The last term $B'(t)$ in the fitting function of Eqn. 5.1 includes a DC residual background (P_0), accounting for possible differences in the accidental background rate for positive and negative decay times, and an exponentially growing term [37]. The latter is a small correction ($P_2 \sim 10^{-8}$) to the exponential trend in Eqn. 5.3, mainly contributing for large times (close to the end of the TDC time window), due to a particular type of overlapping events, that will be now described.

Superpositions of tracks from different events i.e. hits belonging to two or more $\pi^+ \rightarrow \mu^+ \rightarrow e^+$ chains, can either give rise to background, if the positron of the original μ^+ decay is not detected, or kill good events, because events with more than one possible electron track are rejected. Most of the backgrounds are flat combinatorial, and, as such, would be already included in the fitting function as flat offset. Some have the same $e^{-t/\tau}$ time dependence as the muon decay. For example the excess of electrons coming from a pion stopping in the superpixel, in the TDC time window before the considered one, i.e. for $t_\pi < -8 \mu s$, simply add to the signal. A remaining time dependent background component, with no $e^{-t/\tau}$ behavior, is left: it is due to events where the positron is not found and a pion from the beam fakes it. For clarity, if (π_1, μ_1, e_1) and (π_2, μ_2, e_2) are the two consecutive correct chains, the time dependent background $B'(t)$ is formed by events like (π_1, μ_1, π_2) , where π_2 fakes the non-identified e_1 . Such an event could be killed by the positron e_2 , if it appears within the usual time window and it is also reconstructed as a candidate positron. The probability of accepting a pion as a single fake positron depends on the arrival time of the pion in the TDC window: late beam pions (close to the limit of the TDC window) have a better chance of getting accepted as electrons, because their daughter muons and electrons occur preferably outside the considered TDC time window.

The rate (r_π) of these time dependent background events in the final muon lifetime plot is:

$$r_\pi \propto (1 - \epsilon_e)\epsilon_\pi(1 - n_{e2}\epsilon_e) \quad (5.5)$$

where $(1 - \epsilon_e)$ is the probability of losing the real positron e_1 , ϵ_π is the probability of accepting the pion π_2 as a positron, and n_{e2} is the fraction of positrons in the TDC time window from the π_2 decays. This latter term is the time dependent component:

$$n_{e2} = 1 - e^{-\frac{(t-t_{max})}{\tau}}, \quad (5.6)$$

where t_{max} is the end of the TDC window. Apart from proper normalisation factors, all absorbed in the P_2 factor of Eqn. 5.4, this results in a final $e^{+t/\tau}$ exponential term, to be added to the fitting function.

A “mirror component” of these special (π_1, μ_1, π_2) time dependent background events exists in the negative times region of the decay plot as well. The positrons from pions which arrived before the start of the TDC window ($t_\pi < -8 \mu s$), can fake real positrons. These background events would be (π_1, μ_1, e_2) , with e_2 belonging to a π_2 preceding the current time window. This background corresponds to an exponential increase of decay events at the beginning of the TDC window (large negative times), parametrizable with a $e^{-\frac{(t-t_{min})}{\tau}}$ trend. Such a component ($e^{-t/\tau}$, with a proper normalization constant) is relevant for the negative times region, but it does not affect the lifetime function for positive times.

5.5 Background Description, $B(t_{rel})$

Figure 5.3 shows the background distribution for negative times of the $t_e - t_\pi$ histogram, for one of the subsamples listed in Table 5.1, chosen as reference sample (sample *01a*); the global shape shown is indeed common to all the different samples.

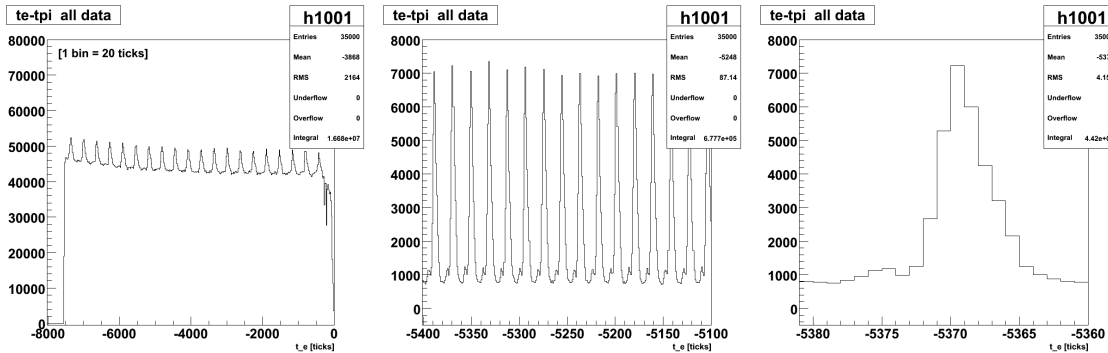


Figure 5.3: Negative times region for the $t_e - t_\pi$ distribution of sample *01a*. The plot on the left shows the entire negative times distribution (rebinning by a factor of 20); the other two histograms are enlarged views on the background structure (1 bin = 1 tick).

From the negative times distribution, especially from the rebinned one, the exponential decrease due to a contamination of electrons close to the end of the TDC time window, is visible. The proper description of the background, in the full negative times region of $[-7000, -1000]$ ticks, must then be divided into two parts: one to consider a flat plus an exponential distribution for the accidental events, the other to describe the shape and periodicity of the beam induced background.

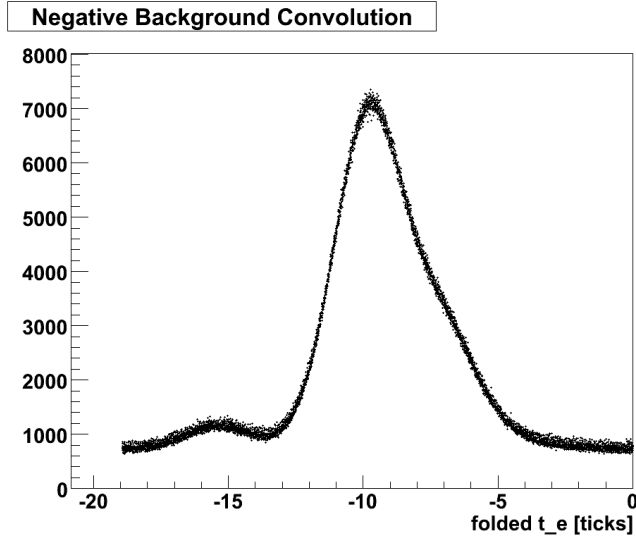


Figure 5.4: Time structure of the background (also referred as convolution of the negative background), obtained from the overlay of the data in the time window $[-7000, -1000]$ ticks, folded on top of each other with a period of 18.960051 ticks, see Section 5.6.1. Sample *01a* only is shown here.

As for the description and parametrization of the background shape, one single period (like in Figure 5.3, right histogram) would not allow a good sampling. However, profiting of the fact that the RF period ($19.75 \text{ ns} \sim 18.96 \text{ ticks}$) is not an integer multiple of the bin size (1 tick), each single RF period of the negative times distribution can be regarded as one separate sampling for the same background shape, every one with a slightly different phase. Overlaying these samplings, a detailed description of the general shape of the background is obtained, as shown in Figure 5.4.

This description depends on the exact value of the period T_{RF} used to build the convolution itself. As a first step, the period is extracted from a Fourier analysis (Fast Fourier Transform, FFT) of the data. We'll show later in Section 5.6.1 how the final T_{RF} value is obtained by a direct fit of the background data. The dependence of the muon lifetime on the choice of the exact value for T_{RF} will be included in the study of the systematic uncertainty (Chapter 6).

An attempt to parametrize the background shape of Figure 5.4 with three gaussian distributions is shown in Figure 5.5. Since the periodic background consists of events where the decay electron is faked by beam particles from another RF bucket, we expect this background to be formed by the three types of beam particles: the first peak are the muons, then electrons, and then pions (see the time of flight spectrum of the beam in Figure 3.2). This background should be dominated by the beam electrons. The reason is that pions and muons generally produce an additional decay

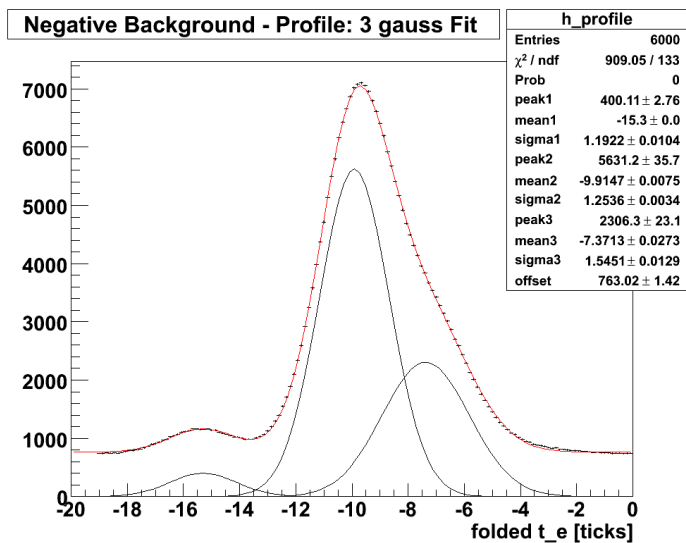


Figure 5.5: Time structure of the background (the profile histogram from the scatter plot of Figure 5.4 is used here), with a 3 gaussians fit. The three gaussian peaks correspond to beam muons (peak1, mean1, sigma1), electrons (peak2, mean2, sigma2) and pions (peak3, mean3, sigma3). The offset is also included in the fit.

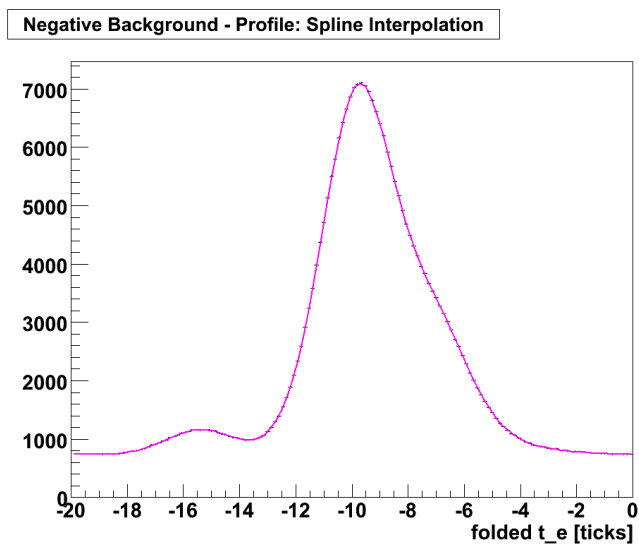


Figure 5.6: Time structure of the background (the profile histogram from the scatter plot of Figure 5.4 is used), with the interpolation spline function, obtained with 150 knots.

electron, which kills the event. The two peaks and one shoulder in Figure 5.5 reflect the beam composition: the time separation between the peaks is in good agreement with the TOF spectrum; the resolution of the peaks is dominated by the 1 tick time resolution of the FAST detector; the content of background particles strongly favours - as expected - the electrons component.

The description with the three gaussian distributions has the advantage of a clear interpretation in terms of particle types. In principle, it would also allow a parametrization of the time evolution of the particles content of the background. However, it is not sufficiently accurate to describe properly the background, as seen by the bad quality of the fit. The background description of choice is instead a spline function with 150 knots, as shown in Figure 5.6. A *spline function* is a piecewise polynomial function (cubic, in our case) defined on consecutive intervals limited by *knots*. When the knots are chosen equidistant, as in our case, the spline is said to be uniform. Clearly, the spline description of the background depends now not only on the T_{RF} period, but also on the number of knots. This has to be included in the systematics study.

To summarize: the best description of the background is provided by a periodic repetition, with period T_{RF} , of the spline function $B(t)$ obtained by the interpolation of the convoluted negative times data. By construction, this function includes structured, as well as accidental (i.e. flat) backgrounds. A global phase shift is needed (phase t_0) to exactly synchronize the $B(t)$ function with the data. We will call $B[\text{mod}(t - t_0, T_{RF})]$ the background description with the spline function, including the phase t_0 . For simplicity, it will be also be referred to as $B(t_{rel})$, with

$$t_{rel} = \text{mod}(t - t_0, T_{RF}). \quad (5.7)$$

For each of the available samples, a different $B(t_{rel})$ function is obtained. The procedure to obtain it, however, is identical for each sample.

5.6 Fit for the Negative Times Region

We have shown in the previous section how to obtain the background function $B(t_{rel})$ that has to be included in the final fitting function for the positive times region. Before moving to the muon lifetime fit, we use here the $B(t_{rel})$ function to fit the negative times region of the $t_e - t_\pi$ distribution. Such a fit will show how precisely the background can be described, and it will be used to derive the best value of the T_{RF} period.

Tables 5.3, 5.4 and Figure 5.7 summarize the results about the fit of the $t_e - t_\pi$ distribution in the interval $[-7000, -1000]$ ticks, for the chosen reference sample

01a. The function used to fit the entire negative times region is :

$$N_{neg}(t) = B(t_{rel}) + S_{neg}(t) + P_{neg}, \quad (5.8)$$

$$S_{neg}(t) = \frac{N_{neg}}{\tau} e^{-t/\tau}. \quad (5.9)$$

$B(t_{rel})$ is the shape of the background with T_{RF} periodicity, and t_{rel} defined in Eqn. 5.7. The $S_{neg}(t)$ function, identical to the signal function $S(t)$ (Eqn. 5.3), describes the exponential trend of the accidental background, with time constant τ . P_{neg} is the constant accidental background. Together with P_{neg} , N_{neg} , τ and the t_0 phase, also the T_{RF} value for the period - used to derive the convolution - is left as free parameter of the fit.

<i>Sample 01a</i>		<i>Fit: [-7000, -1000] ticks</i>
χ^2/ndf		6068.79/5995 = 1.01023
Prob(χ^2, ndf)		0.2491
Fitted Parameters		
Phase [ticks]	t_0	-6.0127 ± 0.0018
Period [ticks]	T_{RF}	18.960054 ± 0.000008
Offset	P_{neg}	-56.50 ± 1.52
Lifetime [ticks]	τ	1992.11 ± 66.84
Normalization	N_{neg}	$(10.41 \pm 1.31) \times 10^3$

Table 5.3: Results of the negative times fit for the sample 01a. The fit interval is $[-7000, -1000]$ ticks. The spline function for the negative times fit is obtained with 50 knots.

	t_0	T_{RF}	P_{neg}	τ	N_{neg}
t_0	1.000	-0.917	0.001	0.000	0.000
T_{RF}	-0.917	1.000	0.000	-0.001	-0.001
P_{neg}	0.001	0.000	1.000	-0.878	-0.906
τ	0.000	-0.001	-0.878	1.000	0.997
N_{neg}	0.000	-0.001	-0.906	0.997	1.000

Table 5.4: Correlation matrix for the parameters of the negative times fit for the reference sample 01a, for the fit results of Table 5.3.

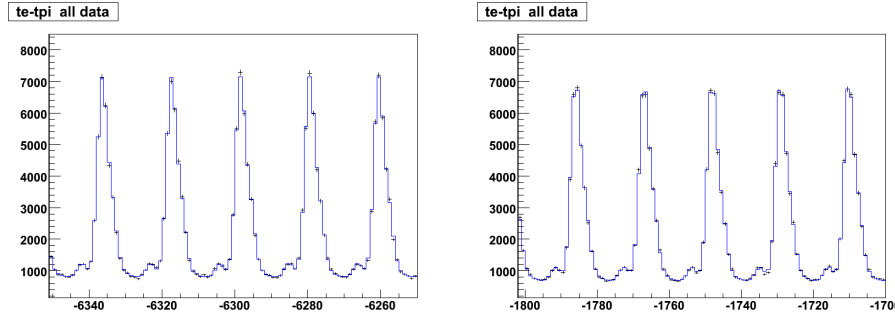


Figure 5.7: Examples of the negative times region fit, for the selected sample *01a*, in two different time regions. The points are the data (within statistical errors), the continuous line is the fitting function.

The quality of the fit of this procedure are shown in Table 5.5, for all data sample of 2006.

When the full statistics sample is joined, and the same procedure for the negative times fit is applied, the fidelity of the background description strongly deteriorates (last line of Table 5.5). This means that our approach to describe the background via the direct interpolation of the data is only valid for short enough run periods, where the parameters of the beam can be assumed to be stable. The details of the background composition depend indeed on several experimental conditions, like the beam line settings, possible instabilities in the proton beam etc.

This is also the reason for the differences in the achieved descriptions of the background among the different samples in terms of χ^2 . A better description of the background (i.e. higher P-values in the fit) corresponds to more stable beam conditions for the entire duration of the run. This result indicates that this method cannot be expected to give a high fidelity description of the background for the joint 2006 sample.

5.6.1 Period Determination

Among the free parameters of the fit in the region of negative times, the most relevant one is the period.

Figure 5.8 compares the different values of T_{RF} obtained from the negative fits of all the different samples, and defines its best estimate, as the weighted average value:

$$T_{RF} = [18.960051 \pm 0.000003] \text{ ticks} \quad (5.10)$$

This is the value that will be used as the period to obtain the convolution, from which we will describe the shape of the background, and derive the $B(t_{rel})$ function. The

Negative Times Fit $[-7000, -1000]$ ticks - All Samples				
sample ID	sample name	statistics	χ^2/ndf	Prob
1	<i>01a</i>	$1.34 \cdot 10^7$	1.0123	0.249
2	<i>01b</i>	$7.00 \cdot 10^6$	0.9865	0.774
3	<i>02</i>	$1.65 \cdot 10^6$	1.0084	0.321
4	<i>03</i>	$7.35 \cdot 10^6$	0.9935	0.651
5	<i>04</i>	$7.99 \cdot 10^6$	1.0101	0.288
6	<i>05</i>	$4.45 \cdot 10^6$	0.9919	0.681
7	<i>06</i>	$1.73 \cdot 10^7$	1.0425	0.011
8	<i>07</i>	$1.26 \cdot 10^7$	1.0187	0.154
9	<i>08a</i>	$7.47 \cdot 10^6$	1.0276	0.066
10	<i>08b</i>	$3.33 \cdot 10^6$	1.0127	0.242
full stat	Run2006	$8.25 \cdot 10^7$	1.1372	10^{-13}

Table 5.5: Quality of the negative times fit for all the subsamples of 2006 data collection. The statistics reported in the table corresponds to the number of events in the fitting interval region $[-7000, -1000]$ ticks. The last line is the fit quality when the fit is applied to the full statistics sample.

choice of adopting a unique value of T_{RF} for all the different samples is justified by the fact that the RF frequency of the accelerator is indeed not sample dependent. The influence of the exact T_{RF} value on the lifetime fit will be included as a systematic uncertainty.

If converted in time units (ns), the RF period determined from the analysis of the data is

$$T_{RF} = [19.750054 \pm 0.000003] \text{ ns}, \quad (5.11)$$

in agreement with the RF period of the accelerator (Table 3.1).

5.7 Muon Lifetime Fit on Separated Subsamples

We have now all the tools to perform the fit on the positive times region, and extract the muon lifetime value. The quality of the fit relies on a good description of the background. For this reason, the different samples are treated separately also in the muon lifetime fit procedure.

The five free parameters for the fit on the positive decay times region - see Eqn. 5.1 to 5.4 - are the initial phase t_0 for the background, which is the only free parameter for the background, the muon lifetime τ , the number of events N_0 , the residual offset P_0 , and the normalization factor P_2 for the positive exponential tail. The shape of the background is fixed by the spline interpolation; its period T_{RF} is fixed to the value of

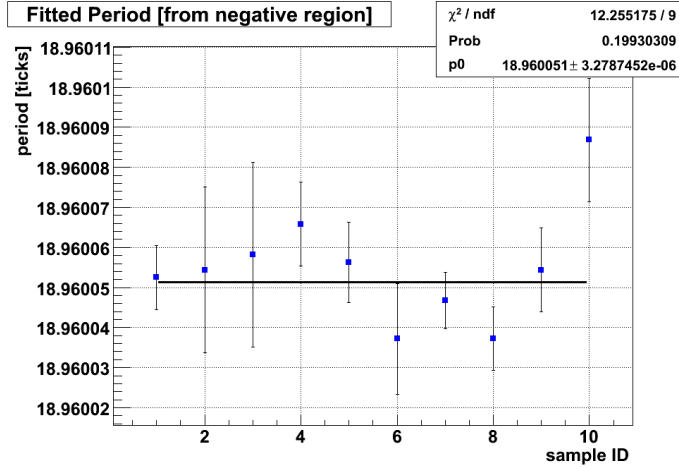


Figure 5.8: Fitted period (from the negative times fit) for all the available subsamples. The average T_{RF} period obtained corresponds to: $T_{RF} = [19.750054 \pm 0.000003]$ ns.

18.960051 ticks of Eqn. 5.10.

Table 5.6 reports - as an example - the detailed results of the muon lifetime fit for the reference sample *01a*, on the interval [600, 16000] ticks.

Table 5.7 lists the results obtained - under the same fitting conditions of the reference sample - for all the available subsamples. Figure 5.9 combines the different lifetime measurements coming from these fits. They result in the following value:

$$\tau_{\mu} = [2109.182 \pm 0.040] \text{ TDC tick}$$

The low probability values of the fits obtained for all the samples show the limitations of the fitting function used (Equations 5.1, 5.3 and 5.4) in reproducing the data. This is mainly due to the imperfect background shape description. Samples with low P-values in the negative fits of Table 5.5 (e.g. sample *06*) correspond to poor quality fits also in the positive regions. However, the opposite is not true: a bad quality fit in the positive region can correspond to a quite good background description in the negative sides (sample *03*, for example). This means that some structure on the data at positive times is not described by the fitting function used so far. A detailed study of the properties of the positive times distribution of the muon lifetime histogram is demanded, and a refinement of the fitting function needed. This will be done in the next Section 5.8.

<i>Sample 01a</i>		<i>Fit: [600, 16000] ticks</i>
χ^2/ndf		15982/15395 = 1.038
P-value = Prob(χ^2, ndf)		0.0005
Fitted Parameters		
Phase [ticks]	t_0	-5.9892 ± 0.0009
Offset	P_0	-64.89 ± 1.74
Lifetime [ticks]	τ	2109.140 ± 0.080
Normalization	N_0	$(2.03993 \pm 0.00006) \times 10^9$
Exp. Tail Norm.	P_2	$(4.89 \pm 1.57) \times 10^{-9}$

	t_0	P_0	τ	N_0	P_2
t_0	1.000	0.000	0.000	0.015	0.000
P_0	0.000	1.000	-0.671	-0.227	-0.870
τ	0.000	-0.671	1.000	-0.031	0.513
N_0	0.015	-0.227	-0.031	1.000	0.205
P_2	0.000	-0.870	0.513	0.205	1.000

Table 5.6: Results of the muon lifetime fit for the positive times region for the reference sample *01a*. The fitting function is the one given by Equations 5.1, 5.3 and 5.4; the background is derived by the spline approximation (150 knots) of the convolution of the negative times background (with fixed period T_{RF} from equation 5.10); the fit is performed in the [600, 16000] ticks time interval. The table at the bottom is the correlation matrix for the parameters of the fit on this particular sample *01a*. For any other sample the correlations among parameters are indeed very similar. There is a high anti-correlation between the fitted lifetime value and the normalization factors P_0 and P_2 .

5.7.1 Best Fitting Interval

The muon lifetime fit results presented so far refer to the fitting interval [600, 16000] ticks. The choice of this interval has been made looking at the stability of the parameters of the fit as a function of the start and end point of the fit. The best fit region is then defined as the largest interval where the fit is stable. We'll show later that, with an improved fitting function, the fitting region will be extended.

Figure 5.10 shows - for the reference sample *01a* - the evolution of the lifetime and the χ^2 of the fit, as a function of the starting point of the fit interval, from 200 to 3500 ticks (in steps of 100 ticks). For this scan, the stopping point of the fit is fixed to 16000 ticks. After the first 600 ticks the fit is stable and independent on the starting point of the fit region. The data for lower decay times (< 600 ticks) present structures that are not taken into account in the fit.

Muon Lifetime Fit [600, 16000] ticks - All Samples					
sample ID	sample name	statistics	χ^2/ndf	Prob	τ_μ [ticks]
1	01a	$1.57 \cdot 10^9$	1.0381	0.0005	2109.140 ± 0.080
2	01b	$8.14 \cdot 10^8$	1.0162	0.078	2109.057 ± 0.111
3	02	$2.03 \cdot 10^8$	1.0546	10^{-6}	2109.253 ± 0.223
4	03	$6.72 \cdot 10^8$	1.0378	0.0005	2109.075 ± 0.125
5	04	$7.39 \cdot 10^8$	1.0302	0.0043	2109.282 ± 0.119
6	05	$4.26 \cdot 10^8$	1.0081	0.238	2109.212 ± 0.156
7	06	$1.53 \cdot 10^9$	1.0605	10^{-8}	2109.209 ± 0.083
8	07	$1.19 \cdot 10^9$	1.0389	0.0004	2109.156 ± 0.094
9	08a	$7.04 \cdot 10^8$	1.0447	10^{-5}	2109.210 ± 0.122
10	08b	$2.96 \cdot 10^8$	1.0346	0.001	2109.329 ± 0.188
combined muon lifetime measurement					2109.182 ± 0.040

Table 5.7: Fit quality and fitted lifetime values for all the subsamples listed in Table 5.1, in the fit region [600, 16000] ticks. The same conditions for the fit described in Table 5.6 are applied, separately, for each sample. The statistics reported in this table correspond to the number of events in the fit region. The last line of the table is the combined measurement of the lifetime on all samples, obtained as the weighted average of the single samples measurements (see Figure 5.9).

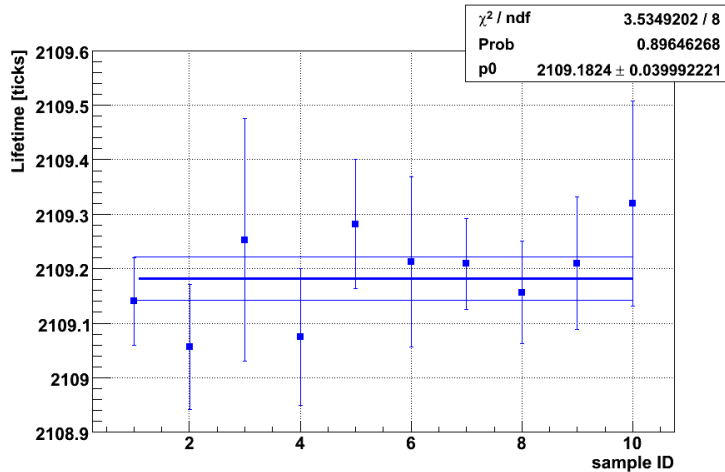


Figure 5.9: Muon lifetime results for all the subsamples fits of the Run 2006 (see Table 5.7). The horizontal lines represent the average measured value within one sigma deviation; the statistical precision achieved in the measurement is comparable with the world average accuracy.

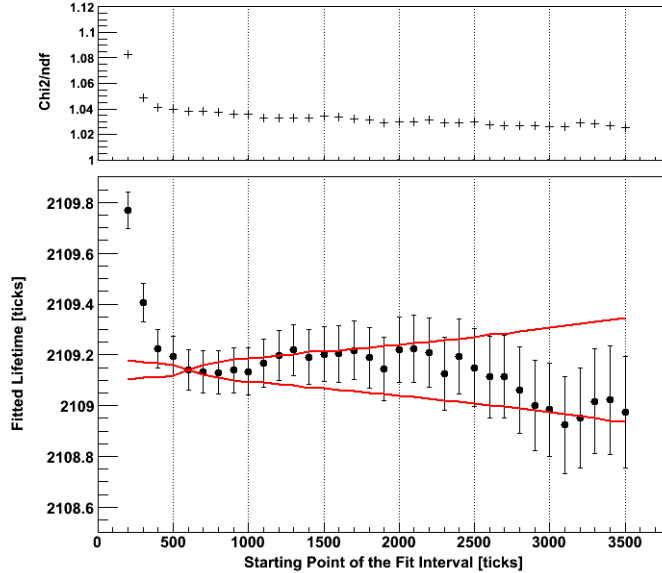


Figure 5.10: Stability of the lifetime and evolution of the χ^2 (top plot) as a function of the starting point of the fit, for the reference sample *01a* (fitting conditions described in Table 5.6). The stopping point for the fit is fixed at 16000 ticks. The red bands in the lifetime evolution plot represent the one sigma statistical deviation w.r.t. the reference point, expected from the results of fits on correlated subsets: $\sigma = \sqrt{|\sigma_i^2 - \sigma_{ref}^2|}$, where the reference point is the starting point of the fit at 600 ticks.

In Figure 5.11 the stability of the lifetime and the evolution of the χ^2 , versus the end point of the fitting region is studied, with the starting point of the interval fixed at 600 ticks. The end point of the fitting interval is changed from 13000 to 21000 ticks, in steps of 500 ticks.

The increase in the χ^2 for fits up to the highest times region indicates that, after about 16000 ticks, the fitting function fails in reproducing the data. This is the reason why the fit is stopped at 16000 ticks when the usual fitting function of Equations 5.1, 5.3 and 5.4 based on a fixed shape background is used.

5.8 Muon Lifetime Fit on the Full Sample

We consider now the full statistics sample (1.073×10^{10} muon lifetime events) and we apply the same fitting procedure described above, which led to the results of Table 5.7. In particular, we'll study the residuals of such a fit.

The exact fitting conditions for the full statistics sample are the following:

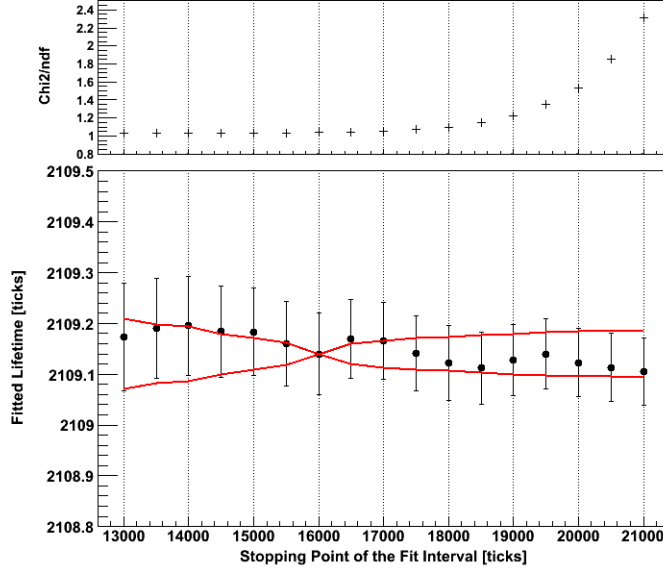


Figure 5.11: Stability of the lifetime and evolution of the χ^2 (top plot) as a function of the stopping point of the fit for the reference sample *01a* (fitting conditions described in Table 5.6). The starting point of the fit interval is fixed to 600 ticks. The red bands in the lifetime plot show the one sigma statistical deviation expected for correlated samples w.r.t. the reference point (fit [600,16000] ticks), $\sigma = \sqrt{|\sigma_i^2 - \sigma_{ref}^2|}$.

- fitting function in Equations 5.1 to 5.4;
- background description derived by the spline interpolation (with 150 knots) of the negative times data (interval for convolution: $[-7000, -1000]$ ticks), with T_{RF} fixed (Eqn. 5.10);
- free parameters of the fit: t_0 , τ , N_0 , P_0 , P_2 ;
- region for the fit: [600, 16000] ticks;

The results of the fit on the full sample are reported in Table 5.8. Figures 5.12 and 5.13 are respectively the pull and the residual of this fit. Figure 5.14 shows the stability of the measured lifetime value versus the start and stop point of the fit.

The following observations can be made from the histograms:

1. The fit quality is much worse than in any of the subsamples considered separately. It corresponds to a large ($\sim 10\%$) widening of the pull distribution,

<i>Full Statistics Sample (Run2006)</i>		<i>Fit: [600, 16000] ticks</i>
χ^2/ndf	19240.9/15395 = 1.24982	
Prob(χ^2, ndf)	0	
Fitted Parameters		
Phase [ticks]	t_0	-5.9800 ± 0.0003
Offset	P_0	-384.32 ± 4.08
Lifetime [ticks]	τ	2109.179 ± 0.036
Normalization	N_0	$(1.05240 \pm 0.00001) \times 10^{10}$
Exp. Tail Norm.	P_2	$(6.61 \pm 0.72) \times 10^{-9}$

	t_0	P_0	τ	N_0	P_2
t_0	1.000	0.000	0.000	0.013	0.000
P_0	0.000	1.000	-0.673	-0.235	-0.866
τ	0.000	-0.673	1.000	-0.023	0.513
N_0	0.013	-0.235	-0.023	1.000	0.210
P_2	0.000	-0.866	0.513	0.210	1.000

Table 5.8: Results of the muon lifetime fit (simple fitting function of Eqn. 5.1) for the full statistics sample Run 2006, in the interval [600, 16000] ticks.

although the central value is compatible with zero. This indicates the presence of structures not accounted for in the fitting function.

2. If we observe the residual outside the fitting region, a large tail at large times is visible. This is also confirmed by the χ^2 divergence at large times, already observed in the reference subsample (Fig. 5.11). Presumably this tail effect also affects the data in the fitting region.
3. As for the stability of the fit, the good results achieved for the single reference sample (Fig. 5.10 and 5.11) are not reproduced anymore when the full sample (about 5 times more statistics) is used. This confirms that different structures are hidden in different samples, and that the fitting function is inadequate for the fit.

A detailed study of the residual for the full statistics is mandatory, to improve the background understanding and the overall quality of the fit.

5.8.1 Fast Fourier Transform of the Residuals

We consider now the residuals of Figure 5.13, computed on the full range for the lifetime, and we analyse its Fourier transforms. The results are shown in Figures

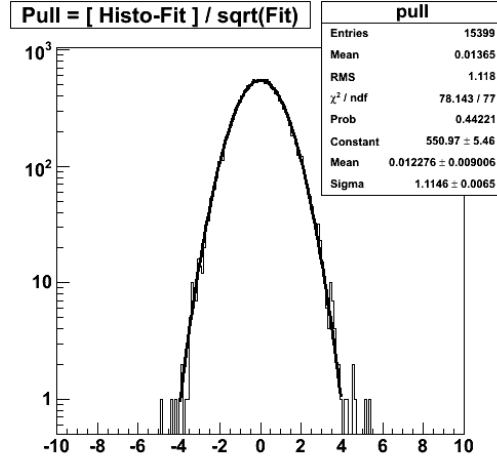


Figure 5.12: Pull of the muon lifetime fit of Table 5.8, on the full statistics sample, with the fitting interval [600, 16000] ticks.

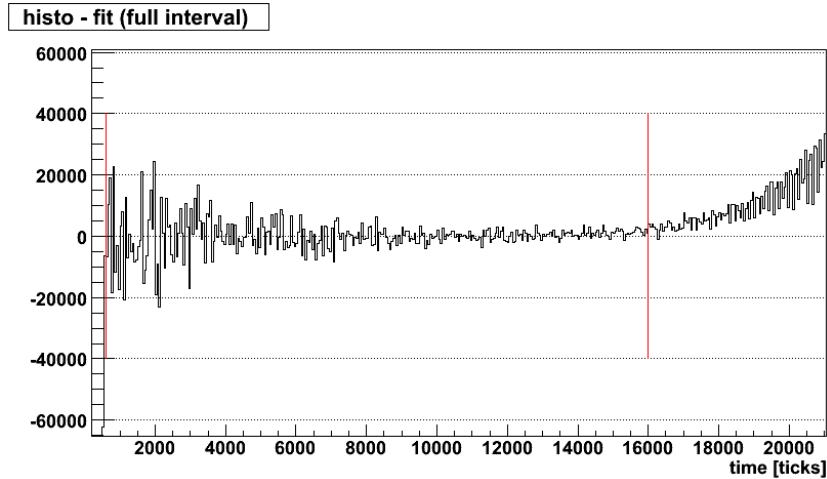


Figure 5.13: Residuals (fit subtracted from the data) for the muon lifetime fit on the Run 2006 sample. The two vertical lines show the fit region ([600, 16000] ticks) for the results presented. The fitting function is defined on the full interval, and the residual extracted up to 21000 ticks. A rebinning factor of 50 is applied to show the main features.

5.15 and 5.16, where the spectrum of the residual frequencies is shown on linear and logarithmic scale.

It is clear that there are 2 main frequencies (16/32 ticks and RF) and that they affect different parts of the lifetime spectrum. The 16/32 ticks structure is evident

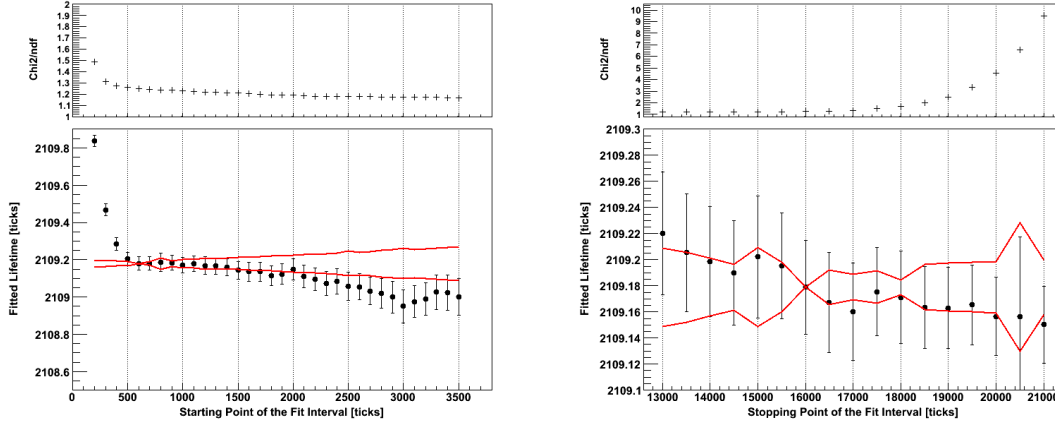


Figure 5.14: Fitted muon lifetime value versus the start point (left) and end point (right) of the fit, for the full statistics sample (simple fitting function of Eqn. 5.1). The red bands in the plots show the expected one sigma statistical deviation on correlated samples, w.r.t. the reference point (fit in [600, 16000] ticks). The fit is not stable after about 2000 ticks.

at small times, but strongly diminishes when we consider higher times. Vice-versa, the relative weight of the RF structure grows with increasing times, becoming the dominant structure at the end of the time window. We should notice that the last histogram in Figure 5.15 - totally dominated by the RF - is referred to a part of the spectrum so far excluded by the fit (it is the big deviation from zero already seen at large times in the residual plot of Figure 5.13). Its effects, however, also influence the data in the fitting region (see the FFT distribution on the [11000, 16000] ticks interval, where the RF peaks are already clearly visible).

A last important piece of information extracted by the Fourier analysis is that no μ SR effect is visible in the data. It should correspond to a period of about $T \sim 1000$ ticks (peak at very low frequencies, < 10 a.u.), where no structure is present.

5.8.2 Added structures in the data

We have thus identified the two main periodic structures in the data; we have now to interpret and parametrize them, to be able to include them properly in the fit.

The 32 ticks structure and the related 16 ticks one are connected with the TDC behavior: 32 ticks is the TDC clock. We explain the 32 ticks periodicity in the data as due to non linearity effects in the TDC conversion from coarse to fine ticks. Small non linearity effects in the TDC's, which indicates per mille level deviations in tick length over the 32 ticks main clock cycle, are also confirmed by dedicated laboratory tests.

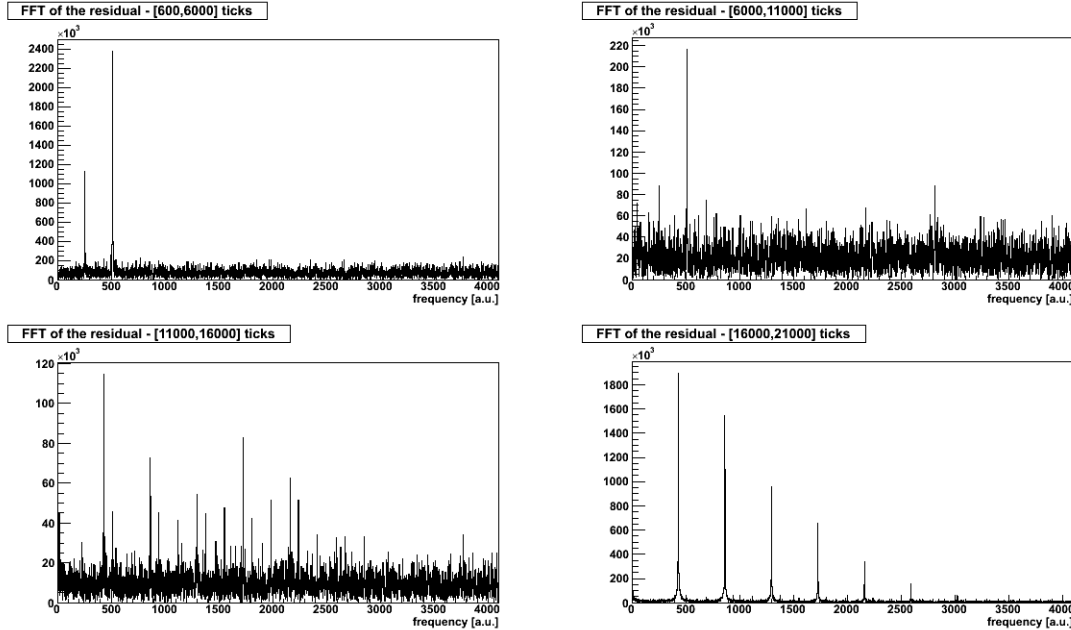


Figure 5.15: Fast Fourier Transform (FFT) of the residual from the full statistics sample fit (Table 5.8). The FFT is applied in four different time intervals: [600, 6000], [6000, 11000], [11000, 16000] and [16000, 21000] ticks. The x axis displays the frequency, in units (a.u.) of $1/8192$ tick $^{-1}$. The main peaks in the first histogram are located at $f = 256$ units ($T = 32$ ticks) and $f = 512$ units ($T = 16$ ticks). The structure which dominates the last histogram, at $f = 432$ units, and all its multiples, corresponding to a period of $T \sim 18.96$ ticks, is the RF beam structure. The two intermediate regions histograms present both structures (16/32 ticks and RF), but less pronounced.

Folding the residual with a 32 ticks period (in the same way as it is done for the convolution of the negative background), we obtain a description of the non linearity TDC effect, as shown in Figure 5.17. In the figure, the folded normalized residual (i.e.: [Data-Fit]/Fit) is shown. It is fitted by a function of two known periods, 32 and 16 ticks:

$$F_{tdc}(t) = p_0 \sin\left(\frac{2\pi t}{16} + p_1\right) + p_2 \sin\left(\frac{2\pi t}{32} + p_3\right), \quad (5.12)$$

where p_0 , p_1 , p_2 and p_3 are extracted from the fit (as shown in Figure 5.17). Any function describing time measurements coming from the TDC's must have a correction provided by this $F_{tdc}(t)$ function, i.e. has to be multiplied by a $[1 + F_{tdc}(t)]$ term.

Given the smallness of the multiplicative constants p_0 and p_2 in $F_{tdc}(t)$, it is clear why the peaks at 16 and 32 ticks periodicity appear only for high statistics region and

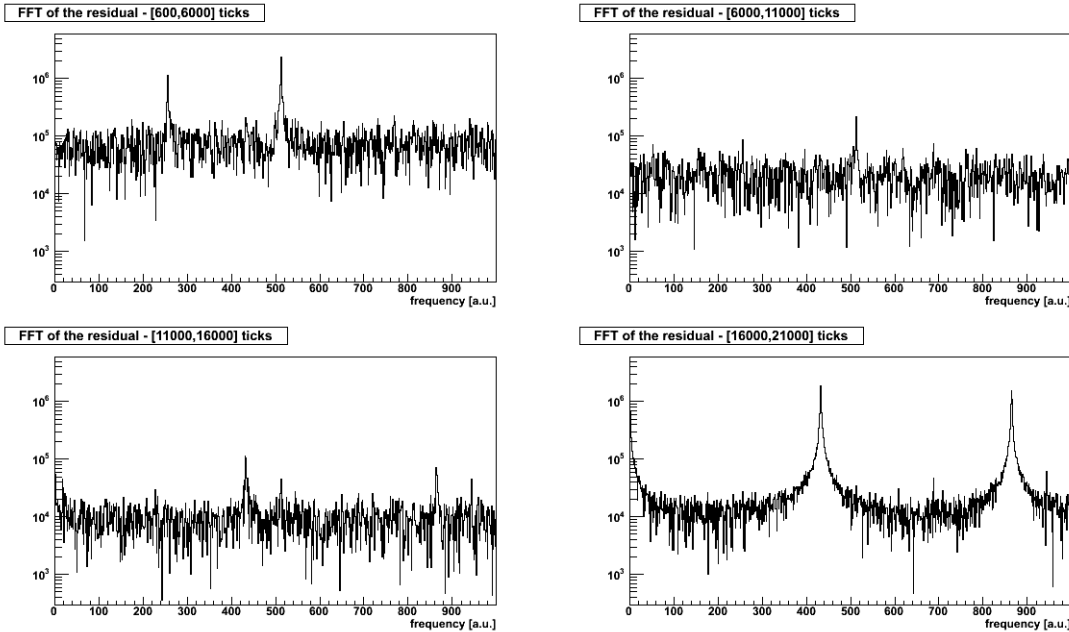


Figure 5.16: FFT of the residual from the fit of the full statistics sample, (see Figure 5.15), restricted to the most relevant zone of low frequencies, where the main structures are visible. All the 4 histograms have here the same (logarithmic) vertical scale, for a better direct comparison of the relative weights of the peaks.

are not visible in small statistics regions. The non linearity of the TDC's of course affects the full time window, but its effect becomes evident only when high statistics is considered. This argument justifies also the need to treat the full sample together, instead of fitting separately the subsamples.

Differently from the non linearity effects, the beam peak structure (RF) appears in the background dominated region (i.e. at large times). It is due to the already known effect of beam pions faking the electrons close to the end of the TDC window (see Section 5.4). So far, a continuous exponential growth - the $B'(t)$ term of Eqn. 5.4 - has been included in the fit to account for this effect. But the beam pion contamination should be considered instead as a growth of the pion contribution only, thus corresponding to a change in the background shape. By construction, the fitting function used so far, based on the periodic repetition of a fixed shape background, cannot reproduce this change in the particle contents for the peaks. To reproduce it, an additional function has been added to the fit. To build such a function, the same approach adopted so far is applied: a convolution (at T_{RF} period) of the residual in the interval [16000, 21000] ticks is performed, as shown in Figure 5.18. The result is a peak, corresponding to the pion contamination, plus some

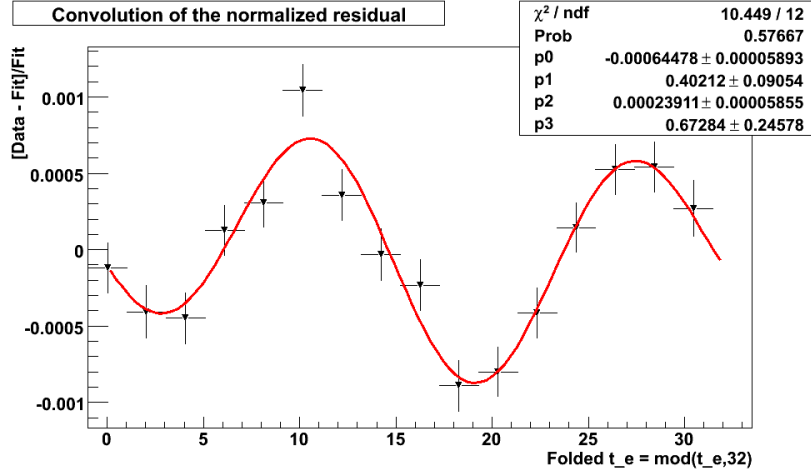


Figure 5.17: Convolution of the residual distribution of figure 5.13 on the interval [600, 16000] ticks, normalized to the fitting function, with a 32 ticks period ($\text{mod}(t_e, 32)$). The obtained distribution is fitted (red continuous line) with the function of Eqn. 5.12.

minor residual structures corresponding to the beam muons and electrons. The peak is parametrized with a function (f_{tail}) which is the sum of two gaussians. A time evolution on this parametrized f_{tail} shape must be allowed.

When applied to the data, the best description of the tail appears to be given by:

$$B''(t) = P_2 e^{+t/\tau} + P_\pi e^{+t/\tau} \times f_{tail}. \quad (5.13)$$

An exponentially growing amplitude ($P_\pi e^{+t/\tau}$) is assigned to the pion peak shape of Figure 5.18 to describe the pulsed tail component of the background. A continuous exponential term ($P_2 e^{+t/\tau}$), however, is also left in as an additional correction to reproduce the data.

5.9 Improved Fitting Function

The improved fitting function that includes the structures derived from the previous study of the residual is given by:

$$N(t) = [1 + F_{tdc}(t)] \times [B(t_{rel}) + S(t) + \tilde{B}''(t)]. \quad (5.14)$$

$F_{tdc}(t)$ is the non linearity TDC function of Equation 5.12; its parameters (constants and phases) are fixed to the values derived from the residuals (Figure 5.17).

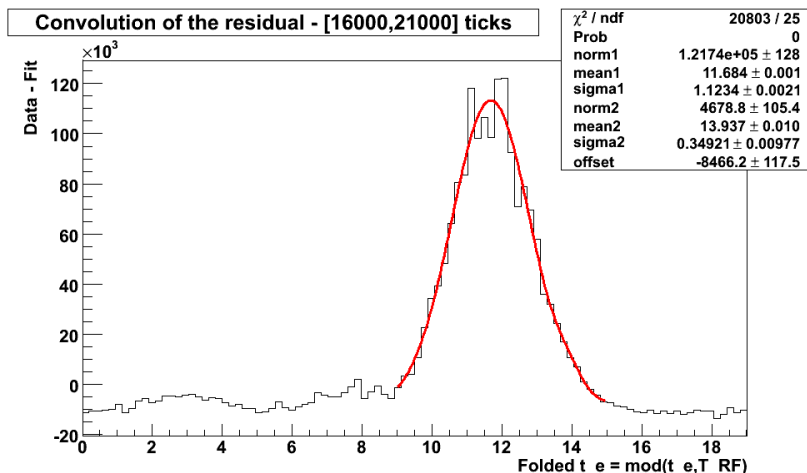


Figure 5.18: Convolution of the residual distribution of figure 5.13 on the interval [16000, 21000] ticks, with the period T_{RF} from equation 5.10 ($\text{mod}(t_e, T_{RF})$). The continuous line superimposed on the histogram is the description of the pion peak provided by the sum of two gaussian distributions. In the text, as well as in Equation 5.13, this function is generally referred as f_{tail} .

$B(t_{rel})$ represents the fixed shape background term, derived as usual by the spline interpolation of the negative times convolution ($[-7000, -1000]$ ticks interval for the convolution; spline interpolation described with 150 knots); as before, the period is fixed (Eqn. 5.10), and the phase t_0 is a free parameter of the fit. t_{rel} has been defined in Eqn. 5.7.

The signal function $S(t)$ for the exponential distribution is defined as usual:

$$S(t) = \frac{N_0}{\tau} e^{-t/\tau},$$

with τ and N_0 as free parameters of the fit (respectively lifetime and normalization factor).

The time dependent background $\tilde{B}''(t)$ includes the contributions of Eqn. 5.4 and the pion tail contamination term $B''(t)$ of Eqn. 5.13:

$$\tilde{B}''(t) = P_0 + \frac{N_0}{\tau} [P_2 e^{+t/\tau} + P_\pi e^{+t/\tau} \times f_{tail}] \quad (5.15)$$

P_0 is the residual accidental offset background, P_2 and P_π are two additional free parameters of the fit.

Summarizing, the improved fit on the full statistics sample, with the function of Eqn. 5.14, corresponds to a fit with six free parameters (t_0 , P_0 , τ , N_0 , P_2 and P_π),

and assumes two predefined functions: $F_{tdc}(t)$ and f_{tail} , both obtained by the study of the residual of the previous fit, with the basic fitting function.

5.9.1 Muon Lifetime Fit on the Full Sample with the Improved Fitting Function

Table 5.9 reports the details about the full statistics sample fit, with the improved fitting function defined in Equation 5.14. Its content, and in particular the χ^2 value, should be compared with the results of Table 5.8, where the same sample was fitted with the basic function, without the F_{tdc} and the pulsed tail terms.

The improvements in the χ^2 of the fit due to each one of the two added terms is summarized in Table 5.10, for two different fitting intervals ([600, 16000] ticks and [600, 20000] ticks). Table 5.10 shows that the largest improvement on the fit quality on the usual [600, 16000] ticks interval comes from the inclusion of the non linearity effect function. The pulsed tail term is a further improvement for the fit, and it is needed when we extend the fit to larger intervals, [600, 20000] ticks. Its effect is also visible in Figure 5.19, where the stability of the χ^2 versus the end point of the fit is represented, for both the basic and improved fitting function.

Figure 5.20 shows the pull and the residual of the fit with the improved fitting function, both for the [600, 16000] ticks interval (details of the fit are in Table 5.9) and for the [600, 20000] ticks interval (to be compared with the histograms in Figures 5.12 and 5.13). The obtained lifetime values for the two fits are

$$\tau_\mu = [2109.189 \pm 0.036] \text{ TDC tick}$$

for the [600, 16000] ticks fit range, and

$$\tau_\mu = [2109.187 \pm 0.030] \text{ TDC tick}$$

for the [600, 20000] ticks fit range. Notice the improvement in the statistical uncertainty when the bigger interval is considered.

The new fitting function of Equation 5.14 considerably improves the fit, still the pull presents some tiny structure ($\sigma_{pull} \sim 1.02$ when fit on [600, 16000] ticks; $\sigma_{pull} \sim 1.04$ when fit on [600, 20000] ticks). The FFT analysis on the residual (Figure 5.21) shows where the pull structure comes from: it is a remaining RF contribution, especially when the fit is extended up to 20000 ticks.

The limiting factor to a better description of the data with the method used so far comes from the imperfect description of the background, in particular of the pion

<i>Full Statistics Sample (Run2006)</i>		<i>Fit: [600, 16000] ticks</i>
χ^2/ndf	16017.3/15394 = 1.0405	
$\text{Prob}(\chi^2, \text{ndf})$	0.0002	
Fitted Parameters		
Phase [ticks]	t_0	-5.9757 ± 0.0004
Offset	P_0	-387.48 ± 4.08
Lifetime [ticks]	τ	2109.189 ± 0.036
Normalization	N_0	$(1.05241 \pm 0.00001) \times 10^{10}$
Tail Continuous Norm.	P_2	$(2.95 \pm 0.74) \times 10^{-9}$
Tail Pulsed Norm.	P_π	$(5.64 \pm 0.21) \times 10^{-8}$

	t_0	P_0	τ	N_0	P_2	P_π
t_0	1.000	-0.013	0.005	0.018	-0.076	0.423
P_0	-0.013	1.000	-0.673	-0.235	-0.846	-0.034
τ	0.005	-0.673	1.000	-0.023	0.502	0.016
N_0	0.018	-0.235	-0.023	1.000	0.204	0.013
P_2	-0.076	-0.846	0.502	0.204	1.000	-0.176
P_π	0.423	-0.034	0.016	0.013	-0.176	1.000

Table 5.9: Results of the muon lifetime fit - with the improved fitting function of Eqn. 5.14 - for the full statistics sample Run 2006, in the interval [600, 16000] ticks.

Fitting Function & Interval	χ^2	ndf	χ^2/ndf	σ_{pull}	
basic fitting function (Eqn. 5.1)	[600,16000]	19240.9	15395	1.2498	1.114
	[600,20000]	88905.4	19395	4.5839	1.4
added F_{tdc} term only	[600,16000]	16751.6	15395	1.088	1.040
	[600,20000]	86391.9	19395	4.454	1.299
added pulsed tail term only	[600,16000]	18504.9	15394	1.2021	1.096
	[600,20000]	23631.6	19394	1.2185	1.104
improved fitting function (Eqn. 5.14) (F_{tdc} and pulsed tail)	[600,16000]	16017.3	15394	1.0405	1.021
	[600,20000]	21130.5	19394	1.0895	1.044

Table 5.10: Achieved quality for the different fits on the full statistics sample, both in the usual [600, 16000] ticks interval, and in the wider [600, 20000] ticks.

contamination tail, the $B''(t)$ term. And in fact the description provided so far by Equation 5.13, with f_{tail} given by the two gaussians in Figure 5.18, is only a rough approximation of the changes in the background composition as a function of time. Ideally, the periodic background would be determined in large time windows of e.g. 1

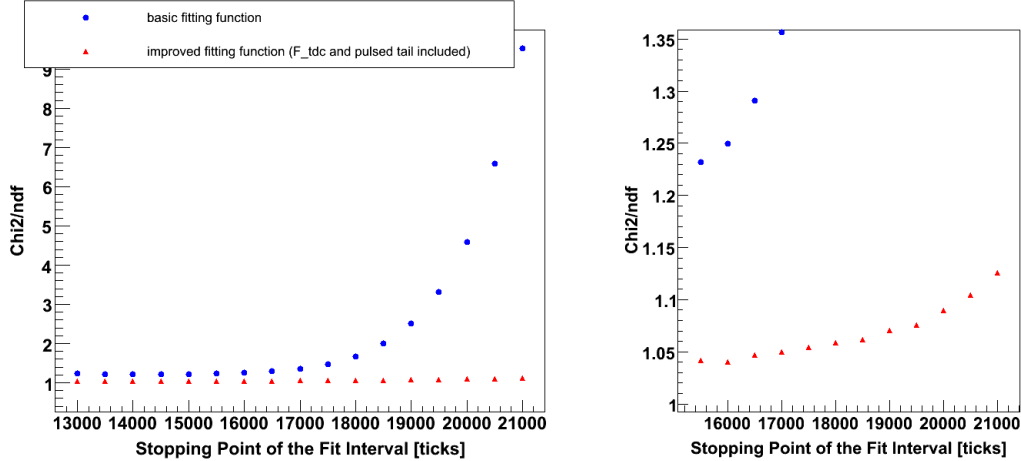


Figure 5.19: Reduced χ^2 of the fit as a function of the end point of the fit range. The results are referred to the full statistics sample, fitted both with the basic function of equations 5.1, 5.3 and 5.4 (blue dots) and with the improved function of equation 5.14 (red triangles), which includes the non linearity effects in the TDC's and the pulsed background description. The comparison among the two curves shows that the new fitting function allows to extend the fitting region up to the largest times. A zoomed view (right) shows, however, a trend in the χ^2 , also in case of the improved fitting function.

μs length by the convolution method. The parameters of the resulting function would then be interpreted as a function of time. This refinement requires, however, a large statistics sample, up to very long decay times and cannot be applied at the current level of statistics. Instead, the second principle method of smoothing the periodic background structure will be exploited in Section 5.10.

The fit performed here on the fine bin histogram, with a fitting function which includes a description of the periodic background as accurate as possible at the current level of statistics, will be used as an alternative analysis to check the consistency of the rebin method, and quote a systematic uncertainty deriving from the fit method itself.

5.10 Rebin Method

So far, the muon lifetime distribution has been fitted with a fitting function based on the attempt to include all the structures present in the data. It has been shown that the weak point in this approach is that it assumes that both the background shape and its evolution in time are precisely known.

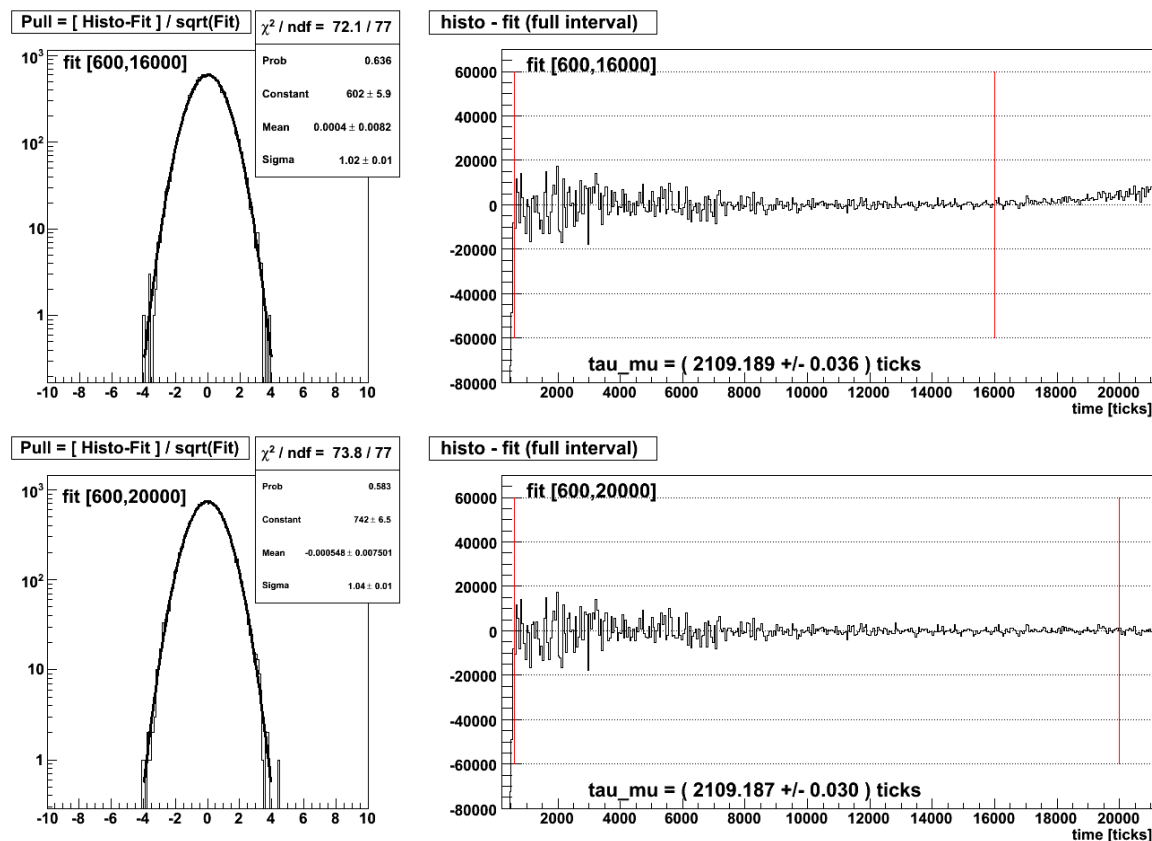


Figure 5.20: Pull (left) and rebinned residual (right) of the full statistics sample fit, performed with the improved function of Eqn. 5.14, on the usual [600, 16000] ticks interval (top) and on the extended region [600, 20000] ticks (bottom). On the residual plots the corresponding lifetime values obtained from the fits are reported.

A totally different approach to the fit - which overcomes this limitation - is to smooth out the periodic structure shape. The lifetime histogram is rebinned using the measured RF clock period (18.960051 ticks) as bin width. The period is not an exact multiple of the original bin size (1 tick). The procedure is thus not exactly a rebin, but a rebin combined with a sharing bin content procedure. The content of some original bins will have to be shared between adjacent final bins. To do that rigorously, a distribution of events inside a bin of 1 tick width must be known. Different approximations, such as constant, linear or quadratic functions of time have been tried, without effect on the fit result. By default, a uniform distribution is thus used to predict event migration.

The advantage of this method - in the following referred to as “smart rebin method” - is that it absorbs all RF periodicity structures in the new bin size. The

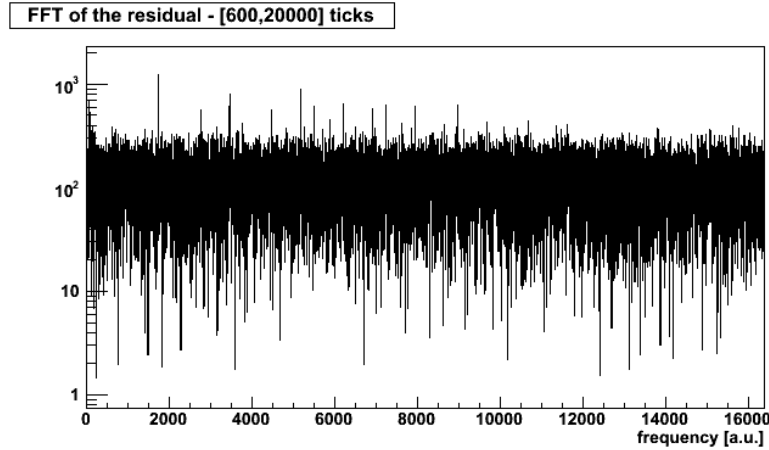


Figure 5.21: FFT of the residuals from the full statistics sample fit, performed with the improved function of Eqn. 5.14, on the [600, 20000] ticks interval. The unit frequency (a.u.) is $1/32768 \text{ tick}^{-1}$. A residual RF structure is still recognizable.

pulsed background terms in the fitting function (periodic spline and tail) are not needed anymore, and only the continuous ones have to be retained. The F_{tdc} structure (that has a different periodicity) is nevertheless still needed.

The fitting function, for the rebinned lifetime histogram will be:

$$N(t) = [1 + F_{tdc}(t)] \times \left[P_0 + \frac{N_0}{\tau} (e^{-t/\tau} + P_2 e^{t/\tau}) \right], \quad (5.16)$$

with the fixed expression of Eqn. 5.12 for the non linearity TDC effect $F_{tdc}(t)$, and P_0 , P_2 , N_0 and τ the free parameters for the fit. When the fit on the rebinned histogram is performed, the above function is numerically integrated on the bin size.

The “smart rebin method” does not require any precise description of the beam induced background structure. The information lost in rebinning only concerns details of the background time structure; there is no relevant information loss on the muon lifetime. The fit is simpler, robust, and of high quality. It is adopted as the nominal method for the muon lifetime fit, from which the final muon lifetime measurement will be extracted.

The systematic uncertainties related to the smart rebin method will be treated in the next chapter.

5.10.1 Muon Lifetime Fit on the Full Sample with the Rebin Method

Table 5.11 and Figure 5.22 report the results of the fit on the rebinned histogram of the full statistics sample for the Run 2006. The full range for the fit ([600, 20000] ticks) can be used. Since the histogram is rebinned, the real fitting region goes from 593.8 TDC ticks to 2008.9 TDC ticks. The total number of events in the fit range is 8.3×10^9 . The measured muon lifetime value is:

$$\tau_\mu = [2109.200 \pm 0.031] \text{ TDC tick}$$

The quality of the fit is shown in the pull and residual distributions shown in Figure 5.23. Mean and rms of the residual distribution are compatible with the expected values of zero and one. The residual as a function of time shows no obvious structure. The FFT on the residual in Figure 5.24 shows that no residual time structure remains, once the RF periodicity is absorbed in the smart rebin method.

The stability of the lifetime measurement versus the fitting interval region is shown in Figure 5.25. Compared to the result in Figure 5.14, obtained without the smart rebin, an improved region of stability is obtained.

<i>Full Statistics Sample (Run2006)</i>		<i>Fit: [600, 20000] ticks</i>
<i>Smart Rebin Method</i>		
χ^2/ndf	1030.65/1020 = 1.0104	
Prob(χ^2, ndf)	0.4014	
Fitted Parameters		
Offset	P_0	253135 ± 39
Exp. Tail Norm.	P_2	$(1.180 \pm 0.008) \times 10^{-8}$
Normalization	N_0	$(2.00104 \pm 0.00002) \times 10^{11}$
Lifetime [ticks]	τ	2109.200 ± 0.031

	P_0	P_2	N_0	τ
P_0	1.000	-0.714	-0.104	-0.498
P_2	-0.714	1.000	0.084	0.335
N_0	-0.104	0.084	1.000	-0.157
τ	-0.498	0.335	-0.157	1.000

Table 5.11: Results of the muon lifetime fit for the full statistics sample Run 2006, with the smart rebin method in the interval [600, 20000] ticks. The fitting function is the one given in Equation 5.16, integrated over the bin size.

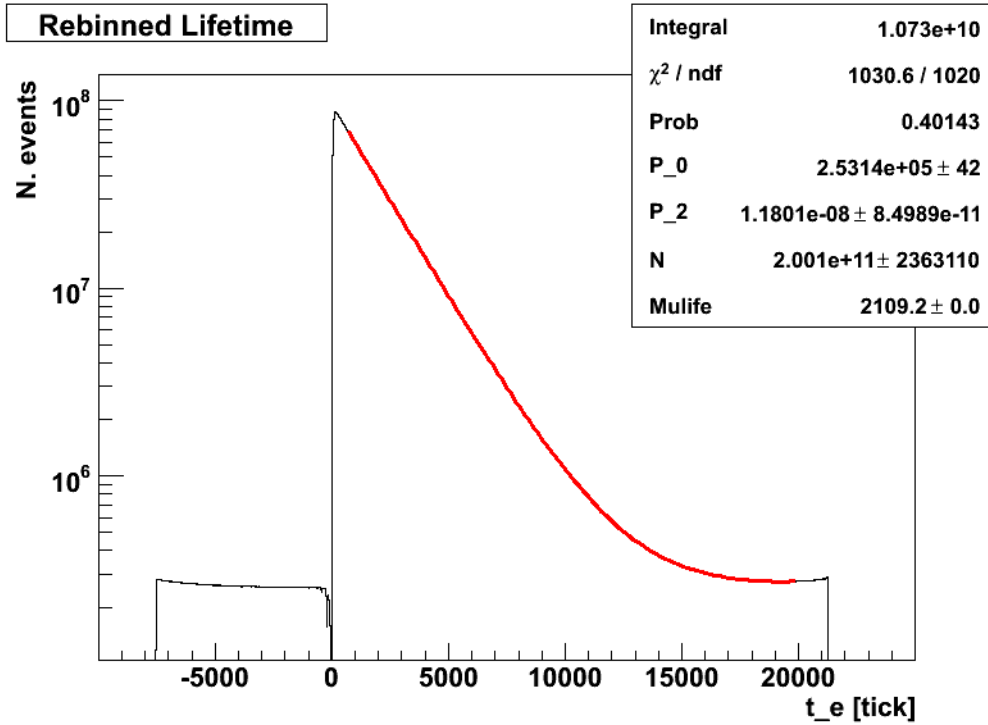


Figure 5.22: Muon lifetime fit on the rebinned histogram for the full statistics sample of Run 2006. The fitting function is given in Equation 5.16, the fit range is [600, 20000] ticks.

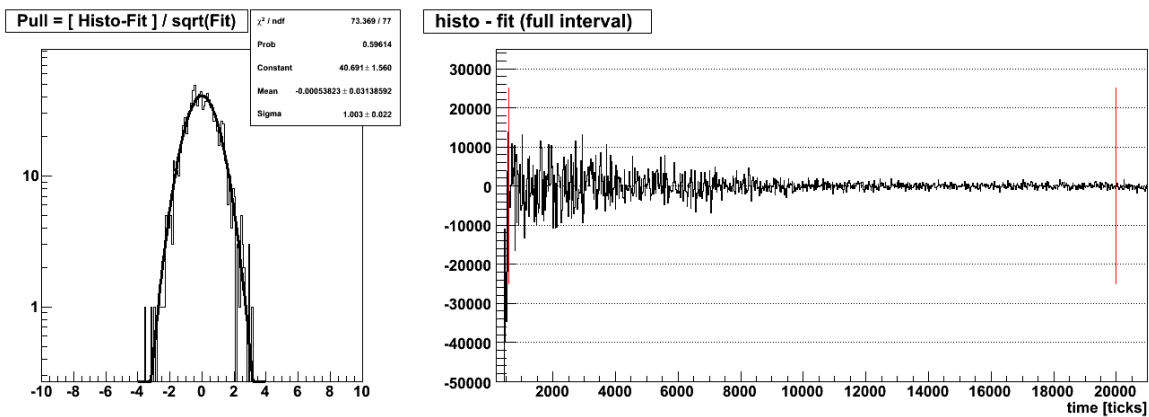


Figure 5.23: Pull (left) and rebinned residual (right) of the full statistics sample fit, performed with the smart rebin method, on the interval [600, 20000] ticks.

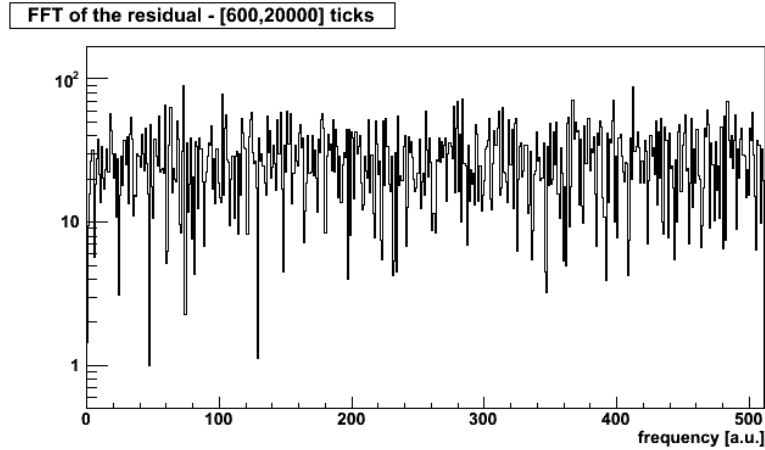


Figure 5.24: FFT of the residual from the full statistics sample fit, performed with the smart rebin method, on the [600, 20000] ticks interval. The unit frequency (a.u.) is $1/1024$ tick $^{-1}$. No residual structure is visible in the residuals of the rebinned histogram fit.

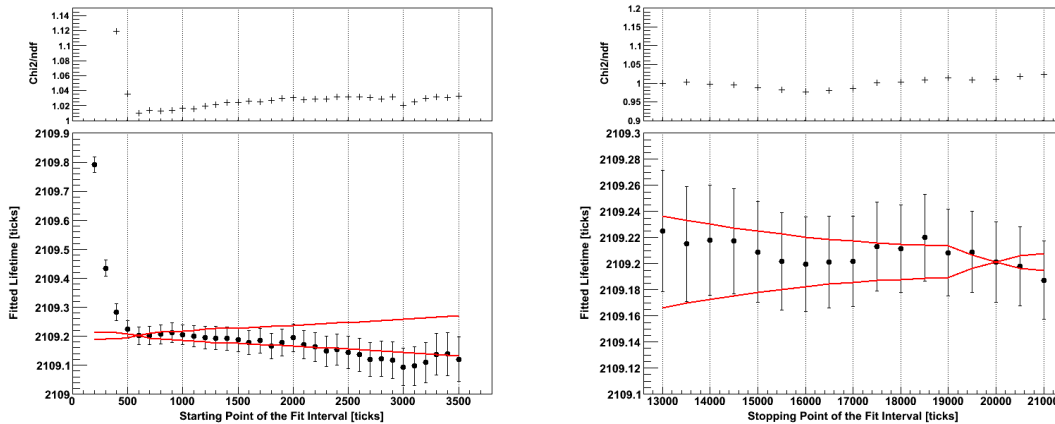


Figure 5.25: Fitted muon lifetime value versus the start point (left) and end point (right) of the fit, for the full statistics sample, with the smart rebin method. The red bands in the plots show the expected one sigma statistical deviation on correlated samples, w.r.t. the reference point (fit in [600, 20000] ticks).

5.11 Measurement of the Muon Lifetime: Conclusion

The muon lifetime value, extracted from the Run 2006 sample using the analysis described in the present chapter is :

$$\tau_{\mu} = [2109.200 \pm 0.031] \text{ TDC ticks}, \quad (5.17)$$

which corresponds to:

$$\tau_{\mu} = [2197.083 \pm 0.032] \text{ ns}$$

The excellent quality of the fit is shown by the $\text{Prob}(\chi^2) = 40 \%$. The quoted error on the measurement corresponds to 15 ppm, and describe the statistical uncertainty only. It is bigger than the one expected by the statistical power of the sample (~ 11 ppm), because of the large correlations between the lifetime and other parameters of the fit (see Table 5.11).

The statistical error is compatible to the one obtained, on the same sample, with the detailed description of the periodic structure. The difference between the two central values will be conservatively attributed to the systematics coming from the fitting method.

Chapter 6

Study of the Systematic Uncertainty

The systematic uncertainty associated with the presented measurement of the muon lifetime will be estimated in this chapter. Different classes of systematic errors can be identified; for each one, a contribution to the total systematic error will be quoted; finally the global systematic uncertainty will be assigned to the present lifetime measurement and compared with its statistical accuracy of 15 ppm.

The possible sources of systematic errors considered are related to the following items:

- geometry and uniformity of the target, Section 6.1;
- muon spin rotation (μ SR) and general anisotropy effects, Section 6.2;
- fit method, Section 6.3;
- choice of the lifetime estimator, Section 6.4;
- stability and rate dependence, Section 6.5;
- influence of the TDC performance, especially for what concerns the time smearing effect (Figure 4.25), Section 6.6;

6.1 Systematics Related to the Geometry

Several histograms are available among the online set of histograms (Section 5.2.3), to study the dependence of the lifetime τ_μ on the geometry of the target and quote the effects of possible non uniformities and inhomogeneities in the target.

Sets of lifetime histograms on different subsamples of the full statistics are available. In contrast with the full statistics histogram (1 bin = 1 tick), they are filled with a larger bin width (1 bin = 20 ticks). This does not allow to use the smart rebin method to extract the lifetime from the fit. The fit is thus performed using the fine bin fitting function, which already includes the corrections relative to the TDC non linearity and the pulsed background tail (Section 5.9). To fit histograms with a wide bin width, the fitting function is integrated over the bin. The background shape description is also adapted to the large bin width, with a recomputation of an effective period, and a new definition of the spline interpolation. A minimum number of 10^5 events per histogram is required, in order to avoid very low population positions in the target, due to the beam profile.

The systematics related to the fit method itself (fine binning vs rebinned histogram) will be treated later. Here only the comparison between the results of equivalent fits on different subsamples is considered. The aim is to verify if the subsamples are consistent among each other. Any inconsistency, larger than the expected statistical fluctuations, is considered to be of systematic origin. The *a priori* cut defined to distinguish between statistical fluctuations and systematic deviations is conservatively set to 3σ 's of the statistical error on the lifetime. The procedure adopted to quote the systematic uncertainties related to the target geometry is the following:

1. Fit all the histograms corresponding to the subsamples of the considered geometry (e.g. 96 lifetime histograms, one for every PSPM in the target) and compute their average.
2. Look if there are statistically incompatible points ($\Delta\tau_\mu > 3\sigma$) and obtain how much the average changes when those points are removed from the calculation of the average.
3. If the change in the averages is larger than the statistical deviation on the difference, we quote this variation as a signed systematic shift.

The procedure is repeated for every considered geometry. The results are given below.

6.1.1 Lifetime vs Pion Position (x_π and y_π)

The influence of the position of the $\pi^+ \rightarrow \mu^+ \rightarrow e^+$ decay chain in the target has been checked by measuring the lifetime as a function of the x and y coordinate of the pion stopping point. The results are shown in Figures 6.1 and 6.2, together with their pulls, expressed as the differences - in units of standard deviation - from the average value. The points are all statistically compatible. No evidence for a systematic effect beyond the expected statistical fluctuations is found.

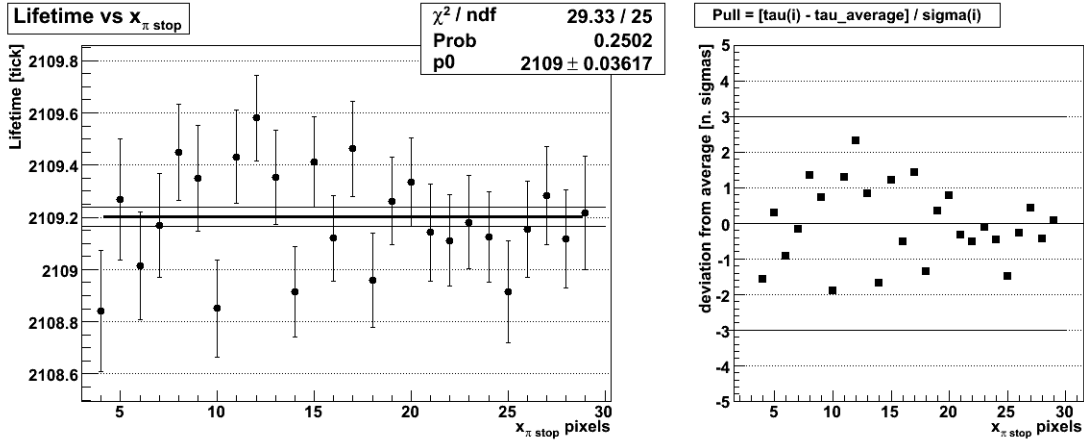


Figure 6.1: Left: Fitted lifetime values vs the x coordinate of the stopping pion in the target ($x = 4$ to 29); the fitted average, and the one sigma deviation (continuous lines in the graph) is also shown. Right: Pull of the distribution, i.e. deviation of each measurement (in units of standard deviations) from the average value. No points at distances larger than 3σ are found; no systematic effect is observed.

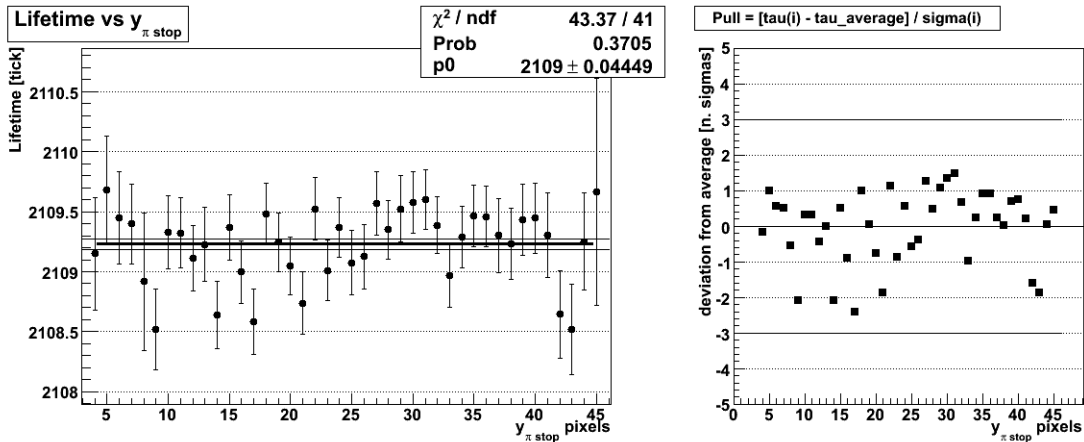


Figure 6.2: Left: Fitted lifetime values vs the y coordinate of the stopping pion in the target ($y = 4$ to 45); the continuous line represents the fitted average, within the one sigma deviation. Right: Deviation of each measurement (in units of standard deviations) from the average value. No systematic effect is observed.

6.1.2 Lifetime vs Position inside the PSPM

The dependence of the lifetime value on the position of the pion inside the photomultipliers, where different efficiencies are expected (see Section 4.6.1 and Figure 4.14)

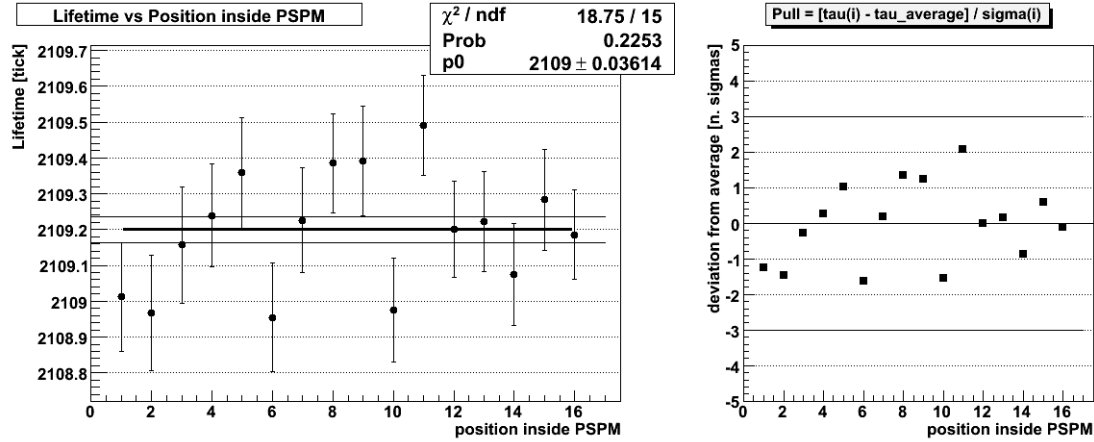


Figure 6.3: Left: Fitted lifetime values vs the position of the stopping pion pixel inside the PSPM (from 1 to 16, according to the numbering scheme of Figure A.1). Right: Pull of the distribution, i.e. difference from the average value in units of standard deviations. No evidence for a systematic effect is observed.

is also analysed. The results are reported in Figure 6.3, and show no evidence for a systematic effect.

Figure 6.4 explicitly shows the fitted lifetimes as a function of the average detection efficiency in the different pixels of the PSPM. No correlation between the efficiency and the lifetime is registered: a linear fit of the distribution (instead of the constant fit shown in the figure) does not improve the χ^2 of the measurement, and the fitted slope is compatible with zero.

6.1.3 Lifetime vs Target Geometry: PSPM, Chip, and TDC Structures

One lifetime histogram for every element of the hardware of the readout chain is available. The lifetime is measured separately for each PSPM (Figure 6.5), TDC chip (Figure 6.6) and TDC module (Figure 6.7).

Two PSPM's show a lifetime variation larger than 3σ 's. They are PSPM 12 and PSPM 49. There is no reason to suspect that their deviation is indeed of systematic origin and not due, instead, to statistical fluctuations. However, following our a priori definition of systematic error, we evaluate a systematic shift. The differences between the average lifetime values, with or without the two contributing tubes are $\Delta\tau_\mu^{(12)} = +0.018$ ticks and $\Delta\tau_\mu^{(49)} = +0.006$ ticks. Added in quadrature, the two numbers result in an estimate of the systematic uncertainty due to the position of the tubes in the target equal to $\Delta\tau_\mu = 0.019$ ticks, which corresponds to about one

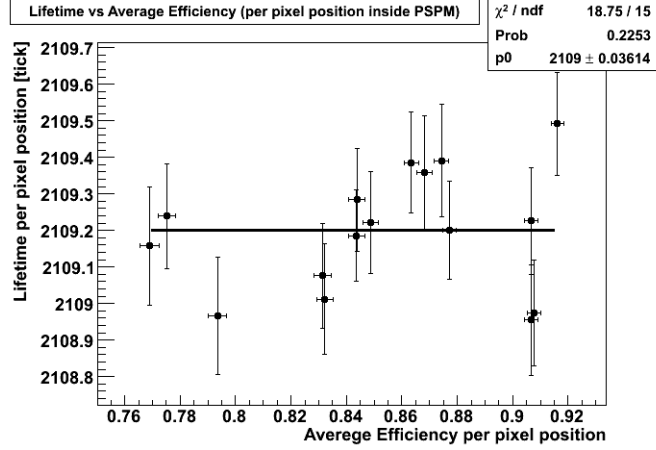


Figure 6.4: Fitted lifetime values for every position of the stopping pion pixel inside the PSPM, as a function of the average detection efficiency in that pixel. Results about the efficiency per pixel are in Figure 4.14, right. Any correlation of the lifetime with the efficiency is registered.

half the statistical error.

It has been proved from fits repeated on different fit ranges, with different fit functions, and different bin sizes, that the geometrical uncertainty related to the PSPM's scales with the total statistical error:

$$\sigma(\text{PSPM}) \sim 0.52 \times \sigma_{stat}.$$

When the full fit range [600, 20000] ticks is considered ($\sigma_{stat} = 0.031$ ticks), the systematic uncertainty associated with the PSPM's position in the target corresponds to $\Delta\tau_\mu = +0.016$ ticks = +7.6 ppm.

The same effect of the two PSPM's deviating from the average value is reflected also in the dependence of the lifetime versus the chip position, as shown in Figure 6.6. Since the geometrical effects come from the PSPM's, the chips and the TDC's are fully correlated, and the largest systematic uncertainty (from the PSPM's) is quoted as the systematic error due to the hardware non uniformity in the target.

The dependence of the lifetime measured for each tube versus the average tube efficiency (reported in Figure 4.14, left) is shown in Figure 6.8. No correlation among the two quantities is registered.

6.1.4 Geometrical Systematics: Summary

The influence of the target uniformity on the lifetime measurement has been studied. With the present statistical accuracy, the maximum systematic shift allowed by the

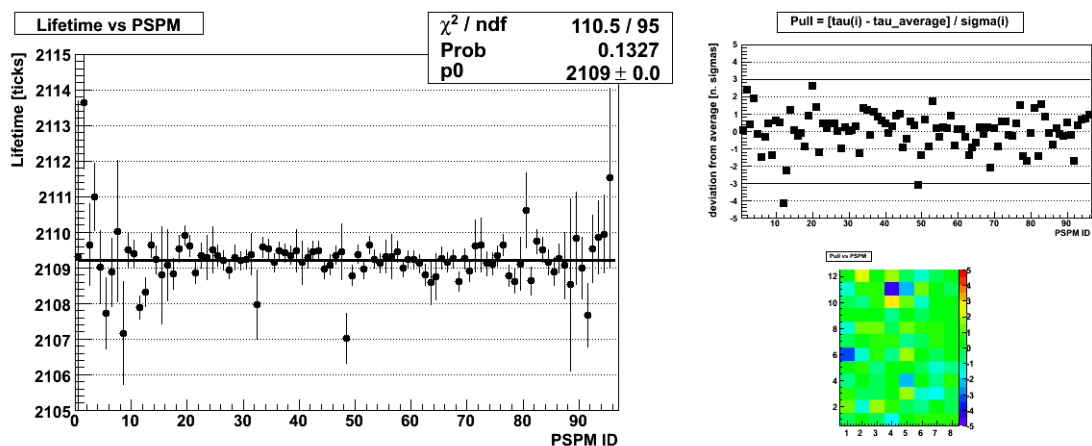


Figure 6.5: Fitted lifetime values, in tick units, vs the position of the PSPM in the target (according to the mapping of Figure 3.13). Also the pull (difference from the average value, in units of standard deviation) is shown on the right. The deviation from the average of each measurement is also graphically displayed, to show the position of the contributing tubes in the target. Two tubes (12 and 49) contribute to the systematic uncertainty, being $> 3 \sigma$'s away from the average value.

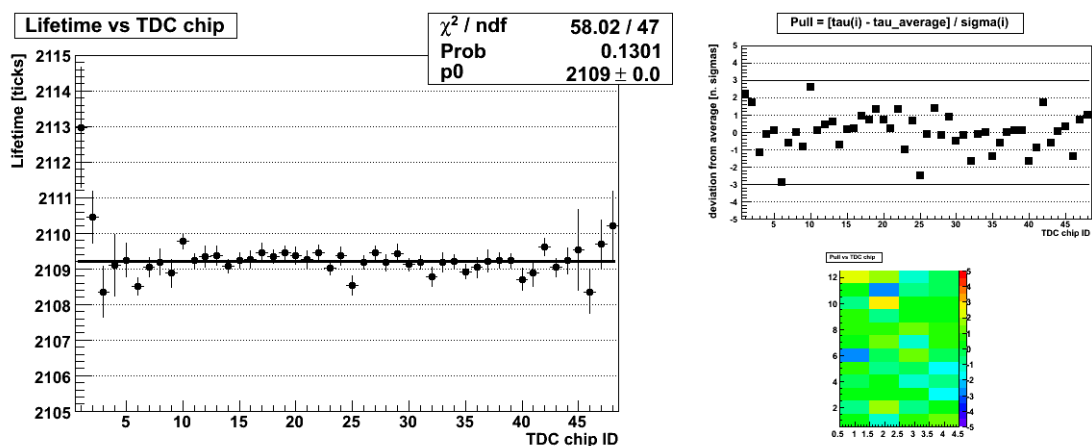


Figure 6.6: Fitted lifetime values vs the position of the TDC chip in the target. Also the pull (difference from the average value, in units of standard deviation) is shown.

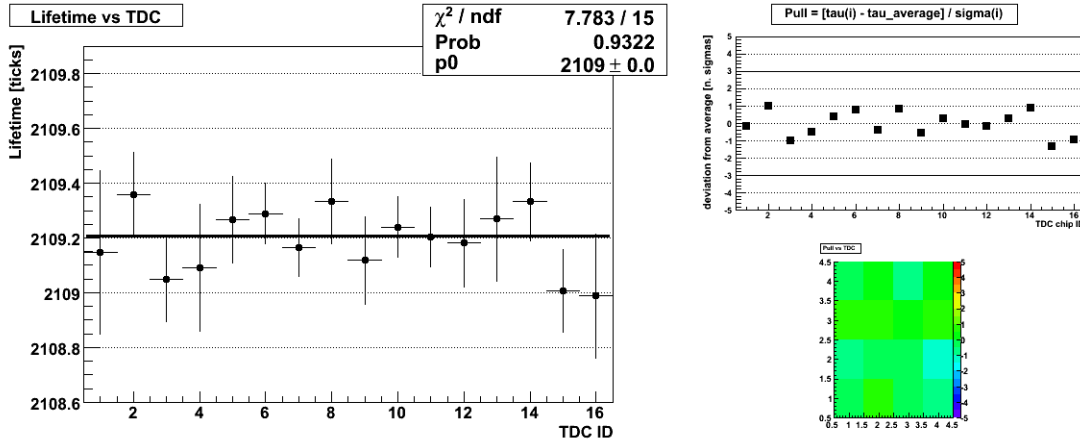


Figure 6.7: Fitted lifetime values vs the position of the TDC module in the target. Also the pull (difference from the average value, in units of standard deviation) is shown.

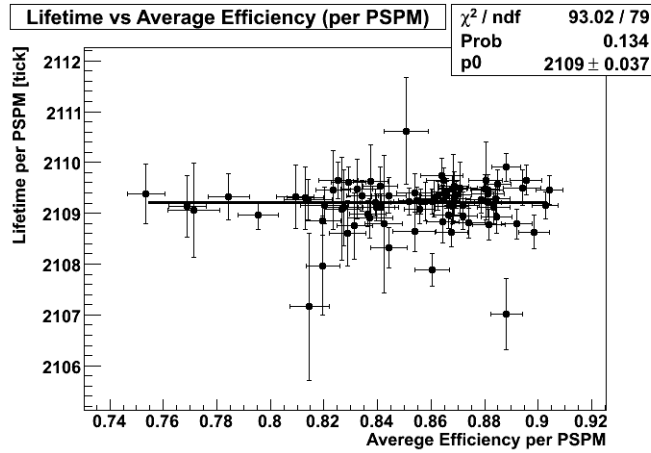


Figure 6.8: Fitted lifetime values for every PSPM, as a function of the average detection efficiency in the PSPM, as was derived in Figure 4.14, left. No correlation between the lifetime and the efficiency is registered.

data is:

$$\Delta\tau_\mu = +0.016 \text{ ticks} = +7.6 \text{ ppm}$$

It should be noticed that this contribution is dominated by one tube (PSPM 12), out of the 96 in the target, and it is presumably of statistical origin. It is likely to be reduced when a new data sample will be considered. All other geometric variables do not introduce any further systematic uncertainty.

6.2 Systematics Related to μ SR Effect and Isotropy

The effects that the precession of the muon spin in a magnetic field (muon spin rotation, μ SR) has on the FAST data and on the measurement of the muon lifetime will be described here. Before, a general introduction to the problem is given. Also other effects strongly connected with μ SR and related to an anisotropy of the decays in the target (i.e. the relative positions of π^+ , μ^+ , e^+) are considered.

6.2.1 μ SR: Possible Source of Systematic Error

The pion π^+ ($S_\pi = 0$; $\pi^+ \rightarrow \mu^+ \nu_\mu$) decays isotropically in its center of mass. The emerging μ^+ is a left-handed particle, with its spin antiparallel to the direction of its momentum.

When the μ^+ decay is considered, its V – A structure introduces a strong preference for the direction of the outgoing positron: the direction antiparallel to the parent muon momentum (in the pion rest frame) is strongly favored for the decay positrons [58]. This makes that the direction of the positron emitted in a μ^+ decay coincides, to a very good approximation, with the direction of the μ^+ spin (see Figure 6.9).

In the presence of a local magnetic field \vec{B} , the μ^+ spin (and the positron direction with it) precesses around an axis parallel to the field, with an angular precession frequency ω proportional to the intensity B of the field, [59]

$$\frac{\omega}{B} = 8.5 \times 10^8 \frac{\text{rad/s}}{\text{T}},$$

which corresponds to a frequency of 13.55 kHz per Gauss:

$$f_\mu = 13.55 \frac{\text{kHz}}{\text{G}} \times B. \quad (6.1)$$

If there is a preferential direction for the muon spin (polarized muons), the spin precession movement translates into a time dependent angular distribution of the decay positrons. If, in addition, there are anisotropies in the positrons detection

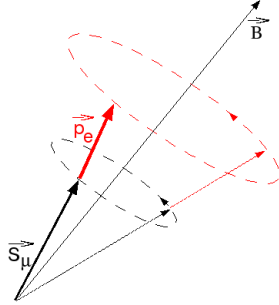


Figure 6.9: Sketch showing how the direction of the positron emerging from the μ^+ decay is correlated with the muon spin \vec{S}_μ . When a magnetic field is added, \vec{S}_μ undergoes a precession movement, which affects the angular distribution of the positrons as well.

efficiencies, a *time dependent efficiency* is produced, which could affect the lifetime distribution, on the time scale of the precession period. In this sense, the μ SR effects are one possible source of systematic error for the lifetime measurement, which has to be included in the systematics study.

It should be noticed however that the μ SR affects the lifetime measurement only if decays of polarized muons in a non isotropic detector are included. By construction, the FAST experiment minimizes both effects, so that the μ SR appears as a second order effect. FAST requires an isotropic μ^+ source, provided by the pion decay at rest in the target (explicitly required by the LV2 trigger), and the target is uniform, symmetric and with a large solid angle acceptance. Residual polarized muons (i.e. muons with a fixed spin direction) that could come from the beam are further suppressed by the range requirements combined with the z -counter informations (Section 3.3.6). Nevertheless, residual μ SR effects - due either to a small contamination of polarized beam muons, or to inefficiencies that could mimic their effects - cannot be neglected at the ppm level.

In the Earth magnetic field ($B \sim 0.5$ G) a precession period of about $150 \mu\text{s}$ is expected. It would be extremely difficult to identify its effects on the lifetime slope over the $20 \mu\text{s}$ observation period. A stronger local magnetic field is thus added ($B \sim 80$ G) - see Section 3.3.7 - to have a shorter precession period ($\sim 0.9 \mu\text{s}$) which can be identified in the lifetime spectrum and properly fitted with a suitable fitting function.

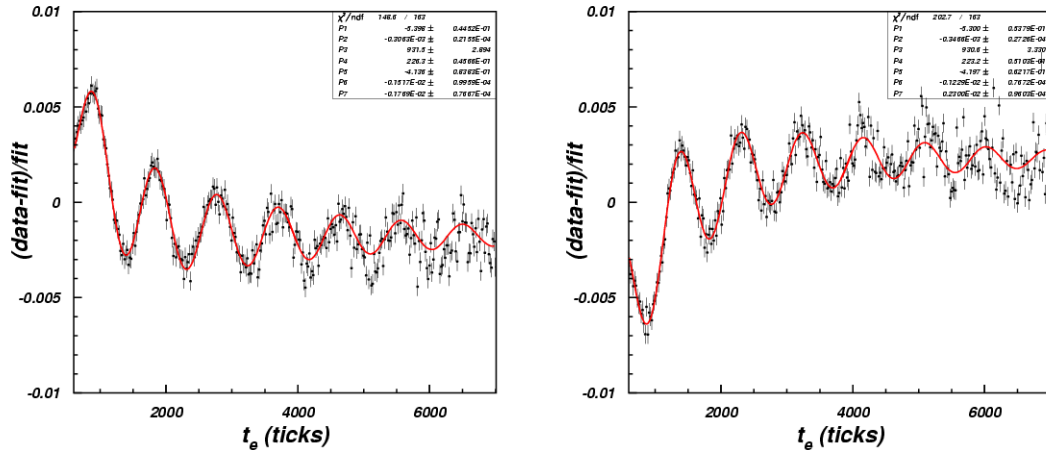


Figure 6.10: The muon spin rotation effect can be enhanced by selecting “ $\pi = \mu = e$ ” events (left) or “ $\pi = \mu \neq e$ ” events (right). The plots represent the residual of the lifetime fits on the two separate histograms. Both residuals are fitted with a periodic function (continuous red line) whose period (P_3) is left as free parameter. The samples have opposite phases and both are used to model the μ SR effect.

6.2.2 μ SR Effects in the Lifetime Measurement

Muon spin rotation effects, i.e. periodic structures with a period of approximately 0.9 μ s, are not visible in the global muon lifetime histogram. The Fourier analysis that has been used to recognize the RF structure of the beam induced background and the non linearity effects in the TDC’s (Sections 5.8.1 and 5.8.2) would have already shown this periodicity.

Nevertheless, the μ SR effects can be explicitly enhanced if special subsamples of data are considered. This is shown in Figure 6.10, where events are divided in two samples, selected among the events having the pion, the muon and the electron in the same pixel (left histogram), and the ones where the pion and the muon are in the same pixel, but the electron is not (right histogram). For the following, we’ll refer to the “ $\pi = \mu = e$ ” configuration, for events in which the muon is detected on the same pixel as the pion, and one hit of the electron track is found as well in that pixel; “ $\pi = \mu \neq e$ ” will be events in which the muon is in the same pixel as the pion, but no electron hits are found in the same pixel.

The fitted period (with excellent agreement from both samples) is 931 ticks, that corresponds to a magnetic field of about 76 G, consistent with the expected value. The time dependence of the position of the electron with respect to the muon (same

or different pixel) is a μ SR artifact. Let's consider the case where π^+ and μ^+ occupy the same pixel (" $\pi = \mu$ "): at the beginning, all muon spins point radially inward to the π^+ stop. The configuration in which e^+ is in the same pixel as μ^+ and π^+ is then highly probable. μ SR then rotates spins, and e^+ direction with it. After a rotation of 180° , muon spins point away from π^+ stop (especially for the forward-backward electrons), so that the " $\pi = \mu = e$ " configuration is disfavored, while the " $\pi = \mu \neq e$ " is enhanced. A continuous migration of events from one topology to the other (with μ SR periodicity) is thus expected. In the " $\pi \neq \mu$ " topology the same μ SR trend - although weaker - is observed, when the position of the electron w.r.t the muon is considered.

When the full sample is treated, the contributions from the various topologies compensate. A systematic uncertainty could derive anyhow if an imperfect compensation occurs. In order to test it, a periodic term - with the period fixed to 931 ticks, and the amplitude as a free parameter - has been included in the fitting function for the full statistics histogram. The resulting amplitude is compatible with zero. No systematic effect related to the μ SR effects is found.

A possible dependence of the fitted lifetime with the azimuthal angle of the electron track has been investigated. The electron angle is binned in eight regions (see Figure A.11), regardless of the relative position of muon and electron, and the corresponding histograms are filled. The residuals of their fits are shown in Figure 6.11 (left), together with their Fourier transforms (right). For comparison, the residual and Fourier transform are also provided for the full statistics sample (middle plot in the figures). For electrons emerging along the $\pm x$ and $\pm y$ (forward - backward, left - right) the expected contribution of μ SR with different phases is observed, but the total sample shows no effect. Good compensation from the subsamples is evident, and no systematic effect coming from this source is found at the current level of accuracy.

The dependence of the lifetime on the π^+ and μ^+ relative positions (according to the mapping in Figure A.2) is also considered. These topologies - which do not involve the positron position - are not strictly related to the μ SR effects. They are anyhow included here, as a general check of the isotropy of the target. The results are shown in Figure 6.12, and no systematics from the relative π^+/μ^+ position is found.

6.3 Systematics Related to the Fit Method

As shown in the previous chapter, the most accurate fit method used to provide the central value of the measured muon lifetime and its statistical uncertainty is the smart rebin method, applied on the full statistics sample on a range of [600, 20000] ticks.

After rebinning, the new bin width coincides with the periodicity of the beam

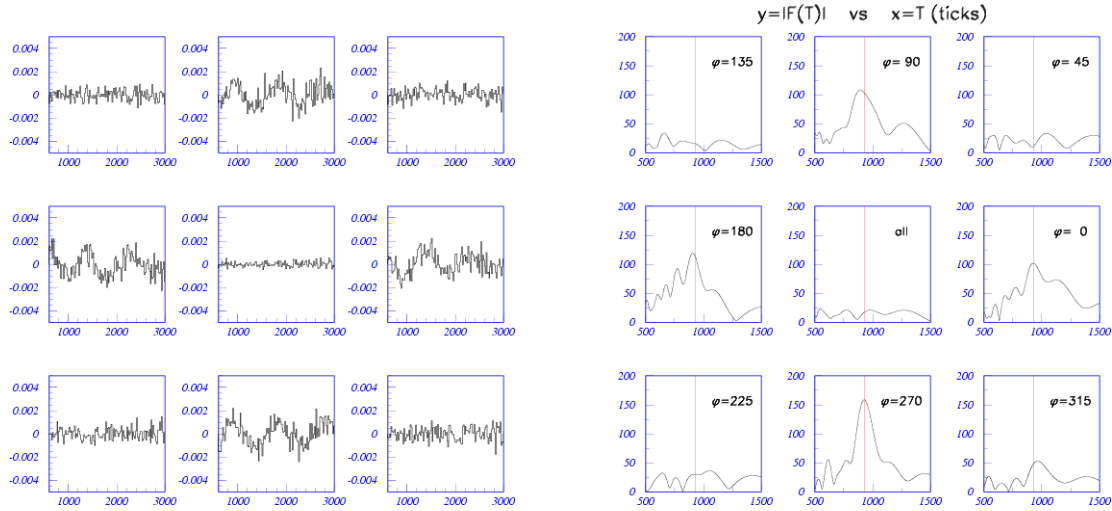


Figure 6.11: Left: Residuals $[(\text{data}-\text{fit})/\text{fit}]$ of the lifetime fits for the eight azimuthal directions of the electrons. The plot at the center is the residual for the full statistics sample. Some angles show a μSR effect as expected, but the total sample does not. Right: Fourier transform of the lifetime distributions for electrons emerging at different angles, and for the full statistics sample (central plot). While the μSR peak is visible for electrons leaving along the $\pm x$ and $\pm y$ directions, the total has no μSR contribution. No systematic effect is seen.

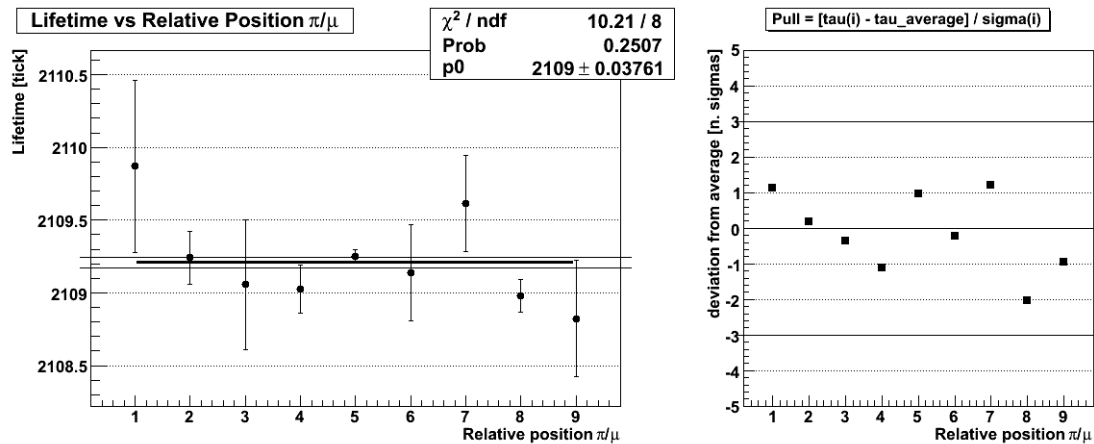


Figure 6.12: Fitted lifetime values vs the relative position of the muon w.r.t. the pion. The position mapping is shown in Figure A.2; position 5 corresponds to pion and muon in the same pixel. The pull (i.e. difference from the average value, in units of standard deviation) is shown on the right. No evidence of a systematic effect is observed.

induced background T_{RF} , see Eqn. 5.10. Since this is not an integer of the original bin size, the smart rebin implies an event migration correction. When the histogram is rebinned the original fitting function is integrated over the new bin width, according to a predefined number of integration steps. The fitting function has been defined in Sections 5.9 and 5.10, respectively for the non-rebinned and binned method; it includes the correction term for the non-linearity of the TDC's, and, in case of fine binning, the periodic background terms.

The systematic uncertainty related to the fit method will be considered in this section. Also cross checks that validate the procedure of the smart rebin (dependence on the exact value of the period which defines the bin width; on the number of integration steps; on the bin sharing algorithm) are considered.

6.3.1 Lifetime vs Bin Width

One of the largest contribution to the systematic uncertainty comes from the dependence of the fitted lifetime value on the bin width of the rebinned histogram, as shown in Figure 6.13. The evolution of the fitted lifetime with the bin size is observed. This is related to the required precision in the description for the background, that reduces with larger bin size. The systematic shift is quoted as the difference between the result of the fit from the non-rebinned histogram (bin width = 1 TDC tick, Section 5.9.1) and the rebinned one (bin width = T_{RF} value, Section 5.10.1, red point in the figure). This covers the fitted lifetimes for all possible values of bin width. For the comparison, the fits on the reduced fitting interval of [600, 16000] ticks are considered, since an acceptable description of the fine bin distribution up to 20000 ticks is not achievable. Also, the interval for the non-rebinned histogram is tuned to exactly match the same fit range used for the rebinned function. Details are in Table 6.1.

Fit Method	Bin Width	Measured τ_μ [ticks]	Fit Range [ticks]
non rebinned histo (§5.9.1)	1 tick	2109.188 ± 0.036	[594, 16008]
smart rebin method (§5.10.1)	T_{RF}	2109.199 ± 0.037	[600, 16000]

$\Delta\tau_\mu = -0.011$ ticks $\Rightarrow \Delta\tau_\mu/\tau_\mu = -5.2$ ppm.

Table 6.1: Systematic lifetime shift (5.2 ppm) associated with the fit method, quoted from the comparison of the fits obtained by the rebinned (nominal) and non-rebinned histogram.

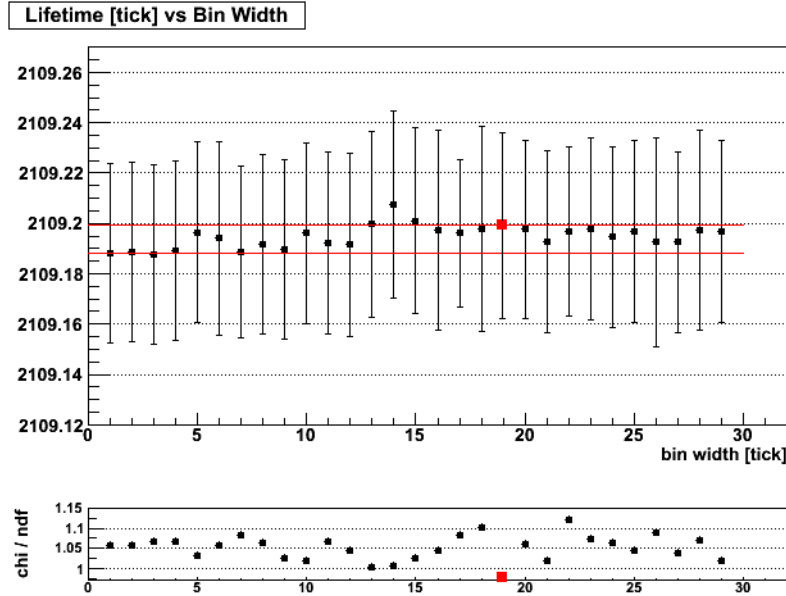


Figure 6.13: Fitted lifetime value as a function of the bin width. The fit is performed on the full statistics sample, in the fit range $[600, 16000]$ ticks. The red point corresponds to the smart rebin fit (bin width = T_{RF} ; uniform bin sharing algorithm). The two red solid horizontal lines show the difference (0.011 ticks) among the non rebinned (Section 5.9.1) and the smartly rebinned (Section 5.10.1) fits; this difference is quoted as the systematics related to the fit method. The bottom plot is the reduced χ^2 of the fits, as a function of the bin width, showing that when the smart rebin method is applied, the best quality of the fit is achieved.

6.3.2 Lifetime vs T_{RF} Value and Phase

The smart rebin method is based on the exact knowledge of the periodicity of the background T_{RF} , which provides the bin width of the rebinned histogram. This quantity is known with high precision ($T_{RF} = [18.960051 \pm 0.000003]$ ticks, Eqn. 5.10) from the study of the background at negative times. The dependence of the fitted lifetime value on the T_{RF} value (i.e. the lifetime vs the exact bin width adopted in the smart rebin method) has been studied. The T_{RF} value has been changed within $\pm 20 \sigma$'s away from the nominal value, with no significant change in the fitted lifetime value ($\Delta\tau_\mu < 0.1$ ppm). The value of the period for the background is so precisely known and sufficiently large with respect to the original bin size, that its influence on the smart rebin method is negligible.

To further validate the method, the sensitivity to the phase of the periodic beam background has been estimated, by varying this parameter in one full T_{RF} period. No effect on the lifetime is seen, with $\Delta\tau_\mu < 0.1$ ppm.

6.3.3 Lifetime vs Bin Sharing Algorithm

Different bin event migration algorithms have been tried, to prove that the bin sharing procedure does not produce any bias in the measurement. By default, a uniform distribution inside the bin is assumed. Also linear and quadratic distributions have been tested. Their coefficients are defined on the basis of the derivatives of the histogram in the split bin and the two neighbor ones. The difference in the fitted lifetime values (see Table 6.2) are well below 0.1 ppm, and so negligible.

Bin Sharing Algorithm	Fitted Lifetime Value [ticks]
uniform	[2109.19989 ± 0.03101]
linear	[2109.19999 ± 0.03100]
quadratic	[2109.19997 ± 0.03100]

Table 6.2: Fitted lifetime values versus different event migration algorithms. The fit is made on the full statistics sample, performed with the smart rebin method, on the interval [600, 20000] ticks.

6.3.4 Lifetime vs Integration Steps

When the histogram is rebinned, the fitting function is numerically integrated over every bin, according to a fixed number of integration steps inside the bin. The fit has been repeated changing the number of divisions per bin, from 10 to 150; 20 divisions is the default. No relevant effect on the lifetime is present, with $\Delta\tau_\mu < 0.02$ ppm.

6.3.5 T_{RF} and Number of Knots

The non-rebinned fitting function method - where a detailed description of the background shape and evolution is attempted (see Section 5.9) - is not used as the nominal method for the fit, because it suffers from systematic uncertainties in the background description. It has been used nevertheless to quote the systematics related to the fitting method itself. It relies on a fixed shape background description, which is based on a fixed T_{RF} value for its periodicity (extracted by the negative times study) and on a fixed number of knots used to derive the spline description of its shape (optimized to minimize the χ^2 of the fit). The dependence of the lifetime on both choices (T_{RF} value and number of knots) is now considered. This study is not meant to add a further systematic uncertainty to the measurement, but to identify and describe some of the contributions to the already quoted systematics related to the fit method (Table 6.1), that depends on the imperfect description of the background.

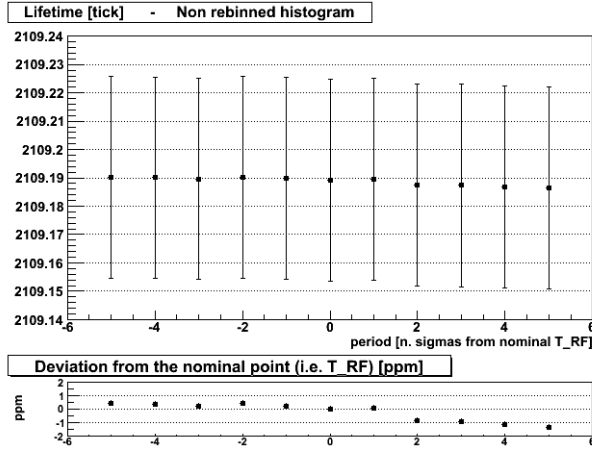


Figure 6.14: Fitted lifetime value as a function of T_{RF} period, measured in terms of number of standard deviation from the nominal value (Eqn. 5.10). The fit is performed on the full statistics sample, in the range $[600, 16000]$ ticks, for the non-rebinned histogram, with the fitting function described in Section 5.9. The plot on the bottom shows the deviation (in ppm units) of the fitted lifetime w.r.t. the value obtained by the fit in the nominal conditions (i.e. period = T_{RF}).

Figure 6.14 is the evolution of the lifetime versus the background period (in the range $\pm 5 \sigma$'s from the nominal value). Deviations up to 1.7 ppm are observed. Figure 6.15 shows the lifetime as a function of the number of knots for the spline. A sufficiently large number of knots (> 125 , in the figure) is needed for the lifetime to be stable, but deviations up to 1 ppm are still observed in the lifetime even when the stability is reached.

These results confirm that a large fraction of the lifetime shift observed between the two methods is indeed due to the insufficient understanding of the periodic background, which however has no influence on the result obtained with the smart rebinning method.

6.3.6 Fit Method Systematics: Summary

The systematic shift related to the fit method thus corresponds to

$$\Delta\tau_{\mu} = -0.011 \text{ ticks} = -5.2 \text{ ppm},$$

conservatively obtained as the deviation of the lifetime derived by the non-rebinned histogram from the one obtained with the nominal fit method. The main contribution to this uncertainty comes from the imperfect description of the background available

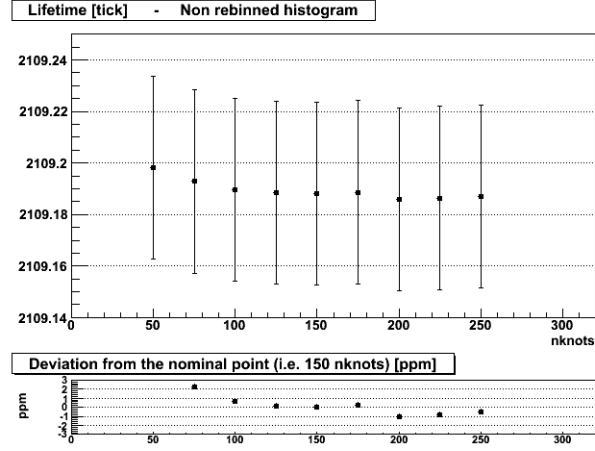


Figure 6.15: Fitted lifetime value as a function of the number of knots used to derive the spline description for the shape of the background (default is $\text{nknots} = 150$). The fit is applied on the full statistics sample, in the range $[600, 16000]$ ticks, for the non-rebinned histogram, with the function described in Section 5.9. The bottom plot is the deviation (in ppm units) of the fitted lifetime w.r.t. the value obtained by the nominal fit (i.e. 150 knots).

with the non-rebinned function fit. This does not have a big relevance for the present measurement, still dominated by the statistical uncertainty, but it will be a major issue for the final precision analysis. A better modelisation of the background and its evolution is needed to reduce the uncertainty related to the fit method.

6.4 Lifetime Estimator

The nominal analysis uses the distribution of the electron time referred to the beam pion, $t_e - t_\pi$. An alternative distribution, referring the electron time to the muon stop time, $t_e - t_\mu$, is available. The distributions are sensitive to different systematic effects. Referring the electron to the beam pion makes the distribution independent of the muon time, while taking the muon stop time as the reference makes the analysis less sensitive to the shape of the background coming from beam particles.

The differences in the two descriptions come essentially from the imperfect modelisation of the backgrounds, which are different in the two cases. As we have shown before, the background description uncertainty is already included in the fit method systematics. However, since the $t_e - t_\mu$ distribution uses an estimator that is different from the one adopted for the computation of any other systematic effect, it provides

an independent lifetime measurement: the difference of the fitted lifetime values between the $t_e - t_\mu$ distribution and $t_e - t_\pi$ distribution is taken as the uncertainty associated to the analysis strategy in the choice of the estimator for the lifetime. It amounts to:

$$\Delta\tau_\mu = +0.0037 \text{ ticks} = +1.8 \text{ ppm.}$$

It should be noticed however that the current version of the analysis - focused on the $t_e - t_\pi$ histograms - does not provide ways to cross-check the robustness of the $t_e - t_\mu$ fit, which thus is not at the same level of accuracy as the nominal one. It is likely that this shift will decrease in the future upgrade of the experiment.

6.5 Stability of the Measurement

The time stability of the measurement is an important requirement for a high precision measurement. To check this, the full data set has been divided in 89 subsets of similar size (about 1.2×10^8 events) and similar duration (~ 4 hours). The nominal fitting procedure is applied to every subset, and the stability checked. The result is shown in Figure 6.16. It confirms the good time stability of the measurement, within the statistical uncertainty of 15 ppm. The good uniformity of the total sample is also shown in Figure 6.17, where the distribution of the reduced χ^2 and the probabilities of all the fits are shown.

6.5.1 Clock Stability

The stability of the Rb clock used to drive the TDC's has been tested, before and after the data taking, with an equivalent clock. Its behavior during the data taking can be checked using the RF frequency of the accelerator. The full Fourier transform of the negative time region of the data is used. The value of the beam period can be obtained for each subsample. Figure 6.18 displays the stability of the period. The clock is found stable within 0.5 ppm.

6.5.2 Beam Rate Dependence

Although the bulk of the data taking was performed at a fixed trigger rate of 30 kHz with LV2 trigger, there is some small spread (from 29 to 34 kHz, within 5% of the average) that can be used to investigate the influence of the trigger rate. In addition there is a small sample (4×10^8 events) recorded at 42 kHz. Both have been used to study the evolution of the measured lifetime with the trigger rate, which is presented in Figure 6.19. No systematic effect is observed in the limited rate interval available.

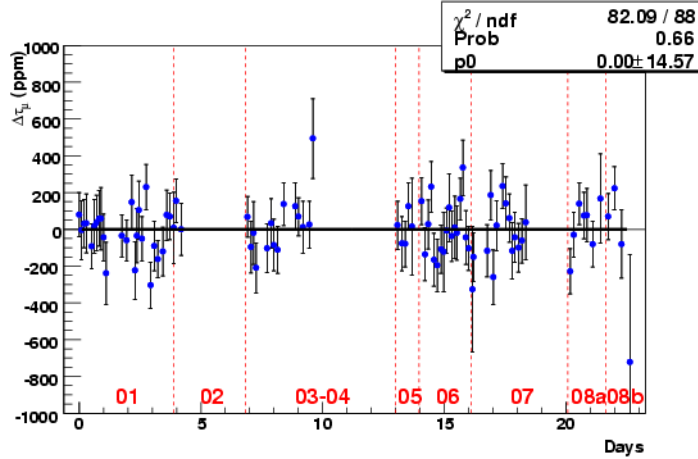


Figure 6.16: Time stability of the muon lifetime measurement for the Run 2006 data taking. Each point in the plot represents - for one subsample of the full data set ($\sim 1.2 \times 10^8$ events) - the deviation of the fitted lifetime value (in ppm units) from the average value (solid black line). The fit is a smart rebin fit on the interval [600, 20000] ticks, performed separately on every subsample. The red vertical dashed lines group the samples according to the notation of Table 5.1.

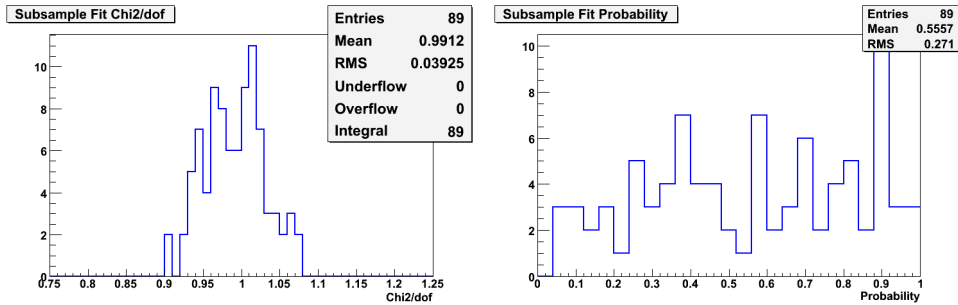


Figure 6.17: Reduced χ^2 (left) and fit probability (right) distributions from the fits on the subsets represented in Figure 6.16. A good fit quality is achieved for every subset (average $\chi^2/\text{ndf} = 0.99$).

This potential source of systematics, which influences pile-up and background will have to be investigated more, as the accuracy of the result increases.

6.6 Influence of the Time Smearing

It has been shown in Section 4.10 that the 2006 data taking rate was limited by the time smearing problem (Figure 4.25) occurring in the TDC's, due to the loss

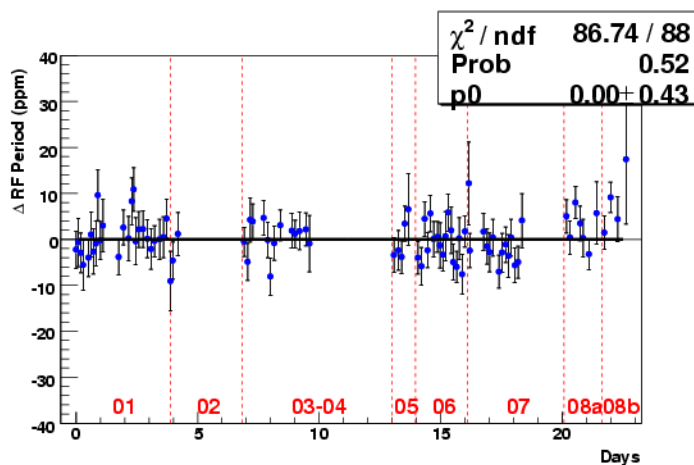


Figure 6.18: RF period of the beam, as measured from the Fourier transform, for the subsets of the Run 2006 data taking, referred to the nominal T_{RF} value (Eqn. 5.10). The obtained values are stable within 0.5 ppm, and no systematic trend is observed.

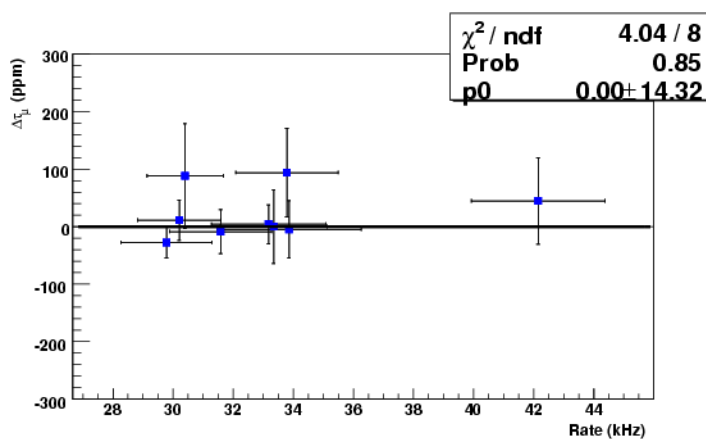


Figure 6.19: Muon lifetime measured as a function of the LV2 trigger rate, referred to the nominal lifetime value.

of synchronization of the four chips inside the same TDC. The data affected by this problem are excluded from the analysis, with a real time procedure which checks their quality and decides if the data have to be rejected or retained. However, to eliminate the possibility of a residual contribution of bad timing events to the data sample from which the muon lifetime measurement is extracted, the bad runs have been separately studied. A lifetime value was measured using those data. The obtained value of the lifetime for the bad samples is compatible with the nominal one, with a time difference of $\Delta\tau_\mu = 15 \pm 60$ ppm. Moreover, there is no geometrical structure associated to the

bad runs, although the probability of time distortion is higher for some TDC's. There is thus no evidence for any systematic effect.

6.7 Systematic Uncertainty: Summary

The systematic uncertainties of the muon lifetime measurements have been studied. They have been quoted as the *signed* shifts $\Delta\tau_\mu$ between the lifetime value obtained taking into account the source of systematic uncertainty, and the one derived by the nominal fit. Table 6.3 summarizes the results.

Source of systematic	$\Delta\tau_\mu$ [ticks]	$\Delta\tau_\mu$ [ppm]
Homogeneity of the Target	+0.016	+7.6
Fit Method	-0.011	-5.2
Lifetime Estimator (i.e. $t_e - t_\mu$ vs $t_e - t_\pi$)	+0.004	+1.8
μ SR and Isotropy of the Target	-	< 1
Time Stability (i.e. clock)	-	< 1
Beam Rate	-	< 1
TDC performance (i.e. time smearing)	-	< 1
TOTAL	± 0.0137	± 6.5

Table 6.3: Systematic shifts in the muon lifetime measurement from the Run 2006 data taking. The two dominant contributions come from the homogeneity of the target and the fit method. The determination of the systematic errors is limited by the statistics of each measurement. The measured value of the lifetime (used in the table to quote the systematics in ppm units) is $\tau_\mu = [2109.200 \pm 0.031]$ ticks, as from Eqn. 5.17.

The total systematic uncertainty associated to the measurement corresponds to ± 6.5 ppm, calculated by adding in quadrature the contributions of the same sign, then averaging the absolute values of the positive and negative errors, in order to obtain a symmetric total error. The two dominant contributions to the final systematic uncertainty come from the homogeneity of the target (two PSPM's only) and the fit method.

The determination of the systematic errors is indeed limited by the statistics that could be used to quote them, but there is no evidence of systematic biases to the lifetime measurement. At present the muon lifetime measurement from FAST is dominated by the statistical uncertainty.

The final measured value of the muon lifetime, including statistical and systematic errors, is:

$$\tau_\mu = [2109.200 \pm 0.031 \text{ (stat)} \pm 0.014 \text{ (syst)}] \text{ TDC ticks}$$

$$\tau_\mu = [2197.083 \pm 0.032 \text{ (stat)} \pm 0.015 \text{ (syst)}] \text{ ns}$$

Chapter 7

Conclusion

The first precise measurement of the positive muon lifetime with the FAST experiment - to a precision comparable with the current world average - has been performed. A data sample of 1.073×10^{10} muon decays has been collected in December 2006 during about 3 weeks of data taking, at an average LV2 trigger rate of 30 kHz, corresponding approximatively to 160 kHz beam rate.

The analysis performed on the sample has been presented in this work. Also the experimental details and performance of the FAST detector have been described.

The measured muon lifetime, including both the statistical and systematical uncertainties, is:

$$\tau_{\mu}^{\text{FAST}} = [2197.083 \pm 0.032 \text{ (stat)} \pm 0.015 \text{ (syst)}] \text{ ns} \quad (7.1)$$

The obtained value is compatible with the current world average, and corresponds to a relative precision of 16 ppm. (The precision of the current world average value amounts to 18 ppm). The uncertainty of the presented muon lifetime measurement is dominated by statistics; there is no evidence of large systematic effects, up to the level of sensitivity indicated by the systematic error. The accuracy in the determination of the systematic uncertainty is limited by the statistical power of the sample. It is expected that both uncertainties will be decreased in future, with larger data samples.

Figure B.5 compares the FAST result with the past measurements of the muon lifetime. It also includes the recent 11 ppm measurement reported by the MuLan collaboration [41]. All the results combined together lead to a significant improvement in the current precision on the muon lifetime:

$$\tau_{\mu}^{\text{w.a.}} = [2197.034 \pm 0.018] \text{ ns} \quad (7.2)$$

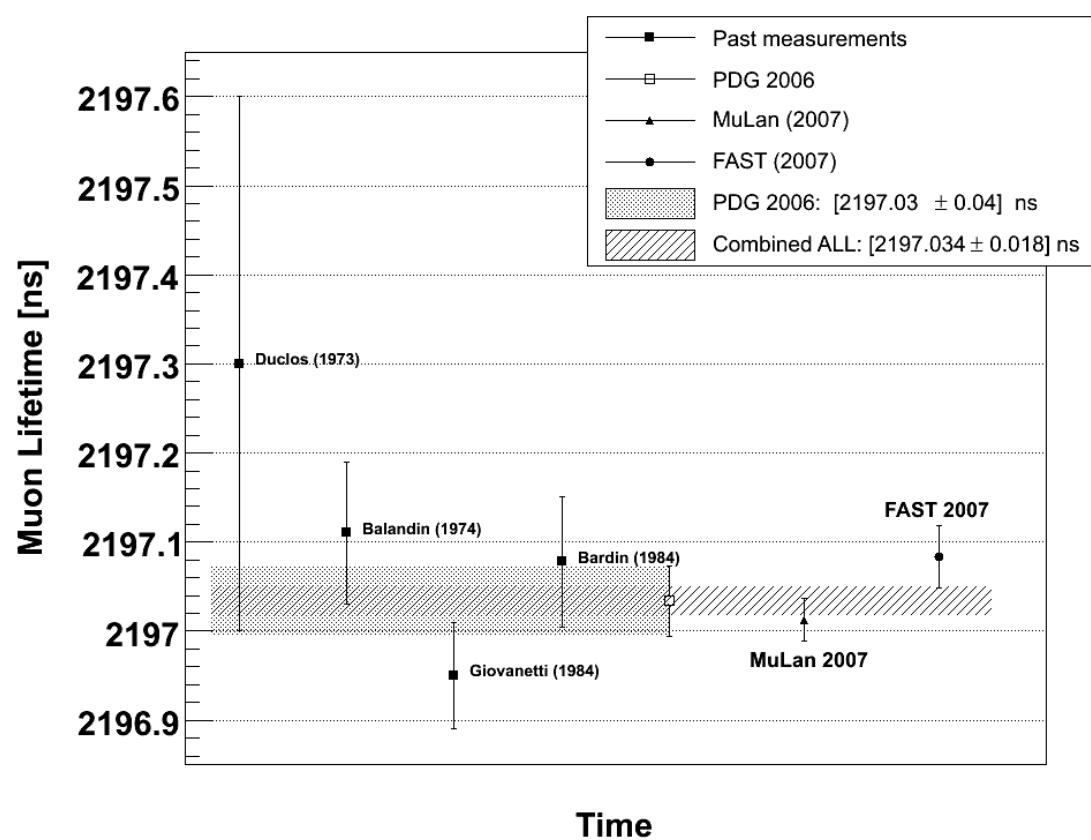


Figure 7.1: Available measurements of the positive muon lifetime, including the recent results from MuLan and FAST. The improved world average value is : $\tau_{\mu} = (2197.034 \pm 0.018) \text{ ns}$ (8.2 ppm).

The value for the Fermi coupling constant G_F , obtained from the FAST measurement of the muon lifetime (Eqn. 7.1) is:

$$G_F^{\text{FAST}} = [1.166353 \pm 0.000009] \times 10^{-5} \text{ GeV}^{-2}.$$

The value derived from the world average value (Eqn. 7.2) is

$$G_F^{\text{w.a.}} = [1.166366 \pm 0.000005] \times 10^{-5} \text{ GeV}^{-2},$$

which corresponds to a relative precision on G_F equal to 4.3 ppm. G_F has been derived - as defined in Chapter 1 - without including the weak corrections. At such a level of precision, however, the influence of the W propagator mass is still not appreciable.

7.1 Future prospects for the FAST experiment

The final goal of the FAST experiment is the determination of the Fermi coupling constant G_F at the level of 1 ppm (i.e. 2 ppm precision on τ_μ). This requires a final data sample of a few 10^{11} muon decay events.

The detector has proven to be reliable and the feasibility of the measurement has been largely established by the 2006 run. An increased trigger rate, however, will be needed to achieve the desired statistics, for the upcoming longer data collection period of 2007 and 2008. The DAQ hardware has to be upgraded and the TDC time smearing problem solved. An improved accuracy in the description of the background will be needed to reduce the systematic uncertainty. In particular this involves a proper parametrization of the time evolution in the composition of the beam induced background. Also the idea of a clock frequency multiple of the RF frequency could be considered. To understand the effects of pile-up and background level, measurements at different rates, in a range larger than the one already considered, will be needed. To assess the systematics of the μSR for the expected higher statistics, the magnetic field will be varied.

Appendix A

Additional Information about the Analysis

The description of the analysis procedure and histogram filling given in Chapter 5, can be completed with some technical details not treated so far.

Section A.1 provides the full list of patterns allowed for positrons emerging from the muon decays. Also the mappings adopted for special geometries of some of the specific lifetime histograms are given. A comment on the online and offline characteristics of the analysis for FAST is given in Section A.2. Some considerations about the blinding procedure of the analysis - not applied on the data sample whose result has been presented in this work, but foreseen for the future data taking - are added in Section A.3.

A.1 Numbering Schemes and Electron Patterns

In Figures A.1 and A.2 are shown the numbering schemes for the position of the pion inside the photomultiplier (1 to 16) and for the muon position relative to the pion (1 to 9). Figures from A.3 to A.10 are all the generated allowed patterns for positrons. Figure A.11 is the numbering for the binned ϕ sectors of the positron directions. For every one of the above geometries a separate lifetime histogram is filled in the analysis stage.

A.2 Online and Offline Analysis

The very high data rate of the FAST detector makes impractical the storage of all the events for a posterior analysis (because of disk space and also disk writing speed). Furthermore, the reading and reprocessing time for these events would require longer

13	14	15	16
9	10	11	12
5	6	7	8
1	2	3	4

Figure A.1: Numbering scheme for the pixel position of the pion inside the PSPM.

7	8	9
4	5 _(π)	6
1	2	3

Figure A.2: Numbering scheme for the relative position of the muon w.r.t to the pion.

than a new data taking period for the same number of events. This is the reason why the FAST analysis is performed completely online. All data are analysed in real time, the full set of lifetime and control histograms is produced, and it is continuously updated to the total collected statistics. Periodically the histograms are stored on disks, so that not only the results of the full statistics, but also their time evolution is accessible. The histograms contain indeed all the required information for the lifetime measurement and the study of the systematic errors.

Among the original data, only a pre-scaled fraction, in the range of 1% to 10% depending on the rate, is stored for offline analysis. This is useful to study some specific aspects of the systematic errors, but also to constantly monitor the data quality during the run. This is done via the monitoring program, based on an offline version of the same analysis code that performs the online analysis, but with dedicated control histograms and no lifetime plots.

A.2.1 Monitoring Program

When a certain amount of data (typically 10^5 events) is written on disk, a set of control histograms is produced by the offline version of the analysis program. The histograms contain information on critical quantities of the system (timing, multiplicities, TDC

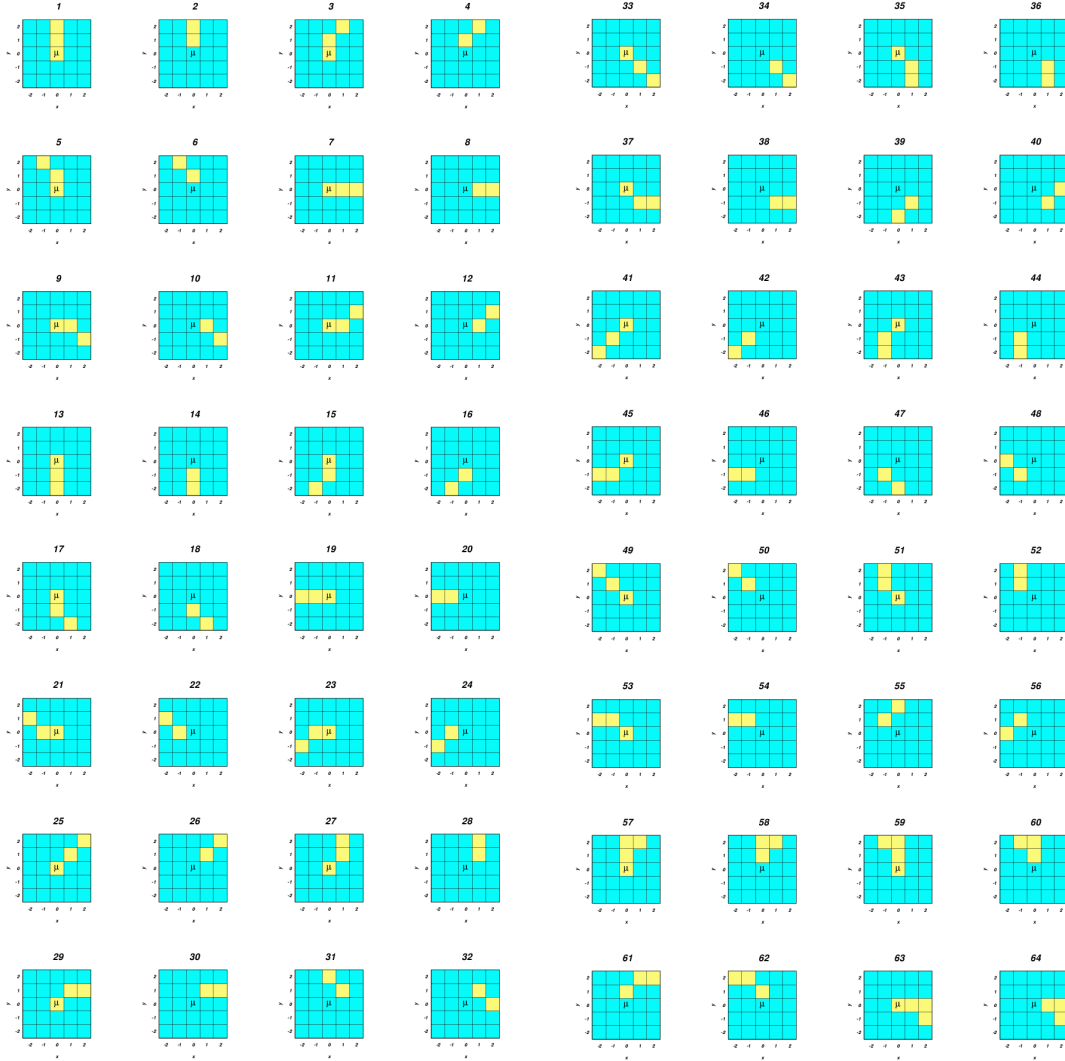


Figure A.3: Positron patterns (from 1 to 64).

operation and LV2 functionality). A subset of these histograms is used to validate the corresponding data sample by comparing it with a reference run. In addition, the monitoring program requests every minute a data record from the Slow Control program, which contains beam rates, the accelerator current and rates from all stages of the DAQ program.

A web-based interface allows remote, platform-independent, access to the monitor information. A snapshot of the graphical interface is shown in Fig. A.12. The displayed information is periodically refreshed to show the latest control histograms as well as time evolutions of the rates. The overall status is also displayed, notified



Figure A.4: Positron patterns (from 65 to 128).

and stored for later offline analysis.

A.3 Blind Analysis

To avoid any possible bias in the muon lifetime measurement, a blinding procedure is foreseen for the analysis on the incoming new data samples (with improved statistical power).

It will be introduced as follows. At the level of the event building, the TDC times

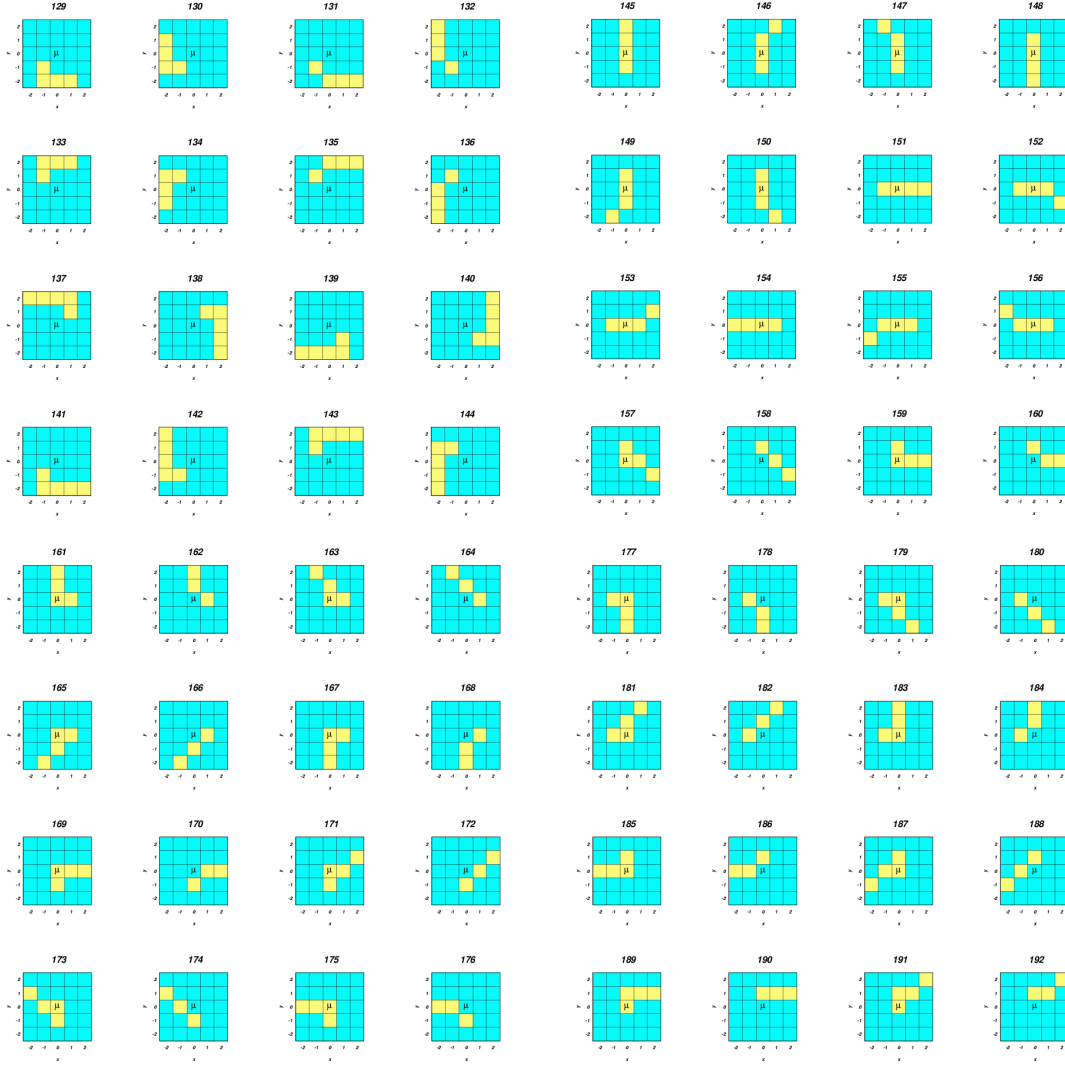


Figure A.5: Positron patterns (from 129 to 192).

are first smeared, and then rescaled by a blind factor. The blind factor is generated at the beginning of the data taking, according to a gaussian distribution with a 50 ppm width around 1. The smearing of the TDC data is needed because they are integer numbers, as thus they would generate beatings once rescaled by the blind factor. Possible smearing algorithms have been tried (flat, gaussian, exponential) and no significant differences among them is found. The flat distribution is then used for the smearing.

Although our simulations show that the true measured lifetime can finally be retrieved from these data - once the blind factor is revealed - we conservatively store

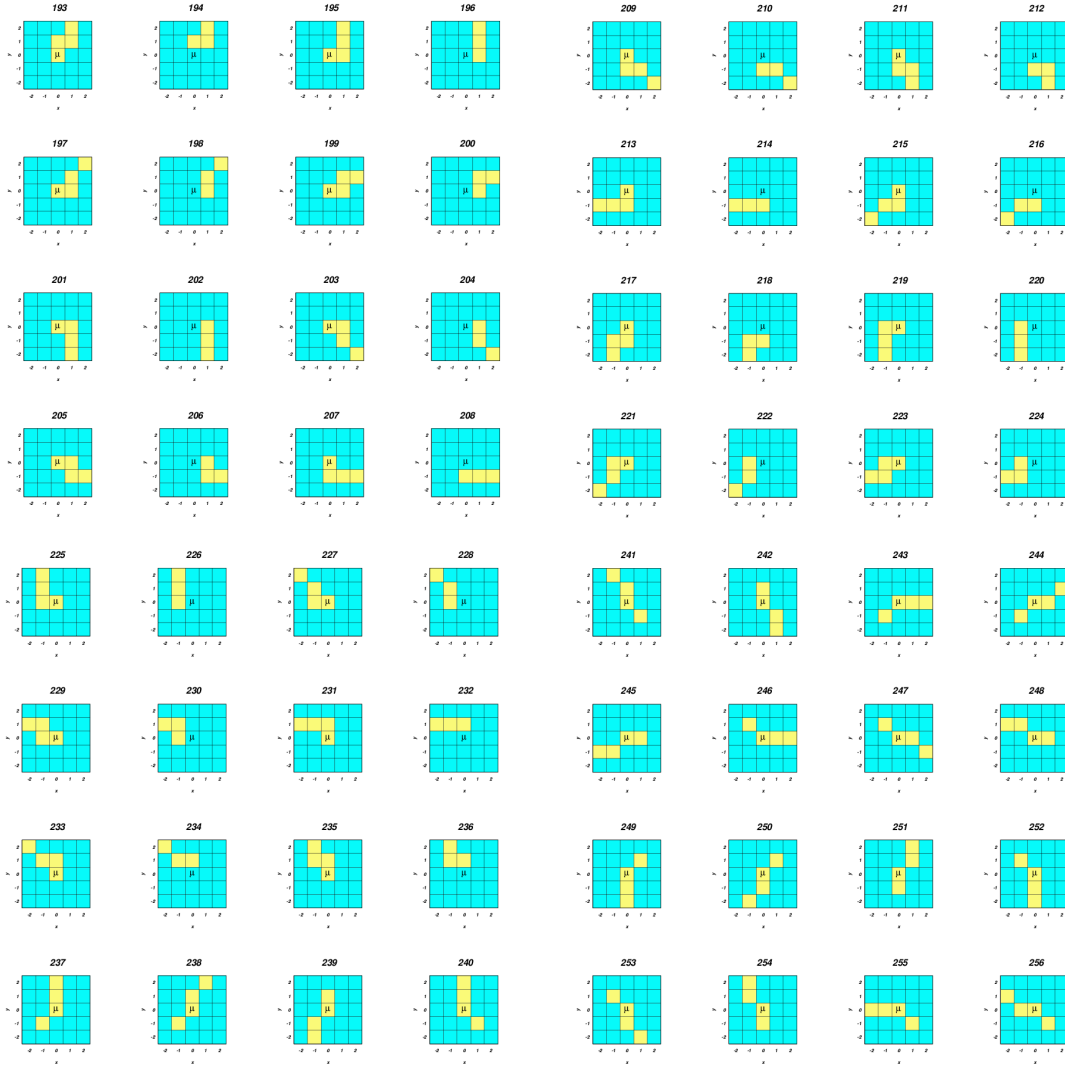


Figure A.6: Positron patterns (from 193 to 256).

also the set of unadjusted histograms, but encrypted. The encryption of the unadjusted (not blind) histograms, as well as the generation of the blind factor is done using a secret sharing technique. Four keys at least (every member of the collaboration possesses one) are needed to unblind the analysis, revealing the blind factor and decrypting the unadjusted histograms.



Figure A.7: Positron patterns (from 257 to 320).

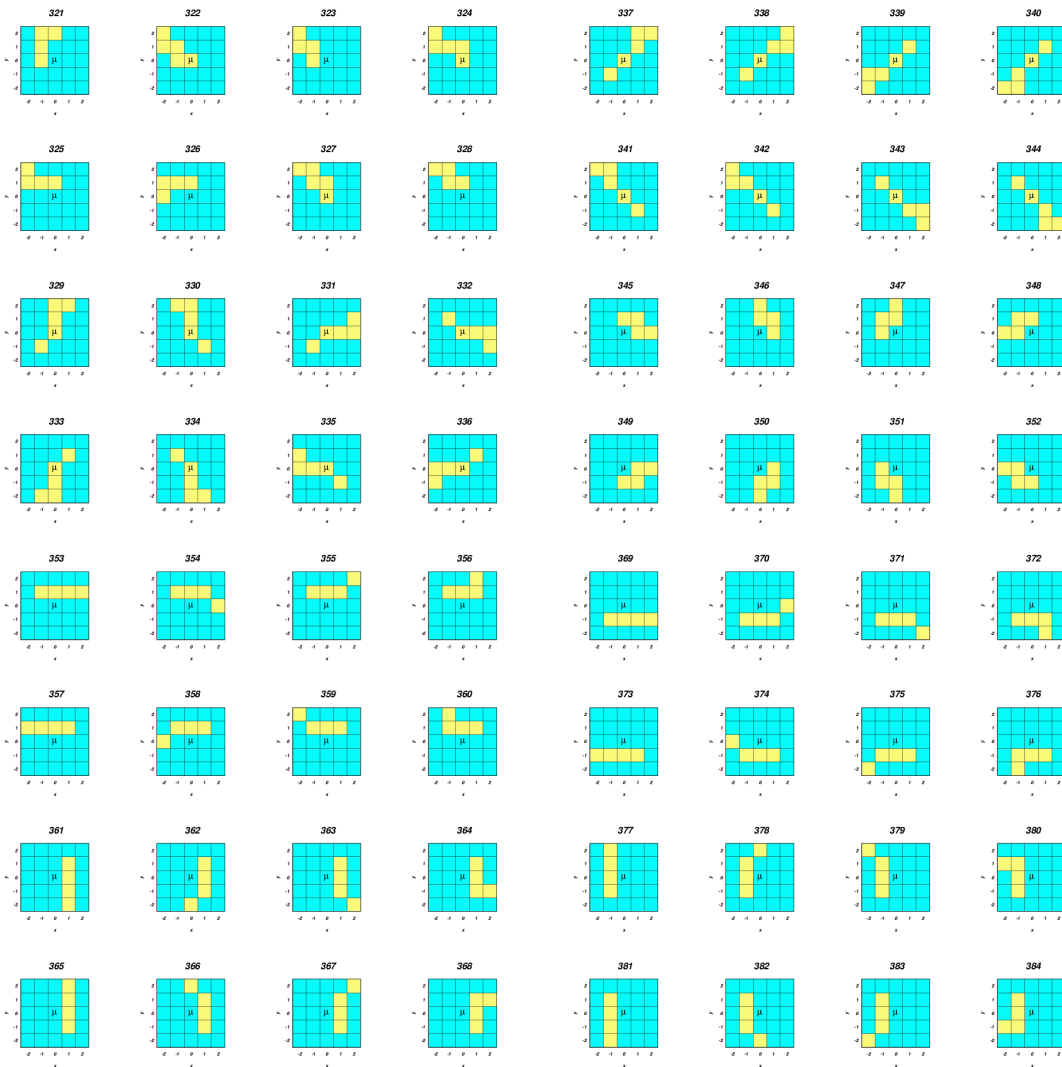


Figure A.8: Positron patterns (from 321 to 384).



Figure A.9: Positron patterns (from 385 to 448).



Figure A.10: Positron patterns (from 449 to 512).

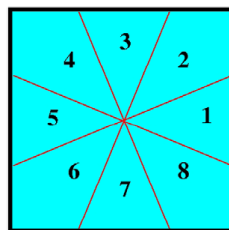


Figure A.11: Numbering scheme for the positron sectors (above patterns are grouped together according to their orientation in the azimuthal ϕ direction).

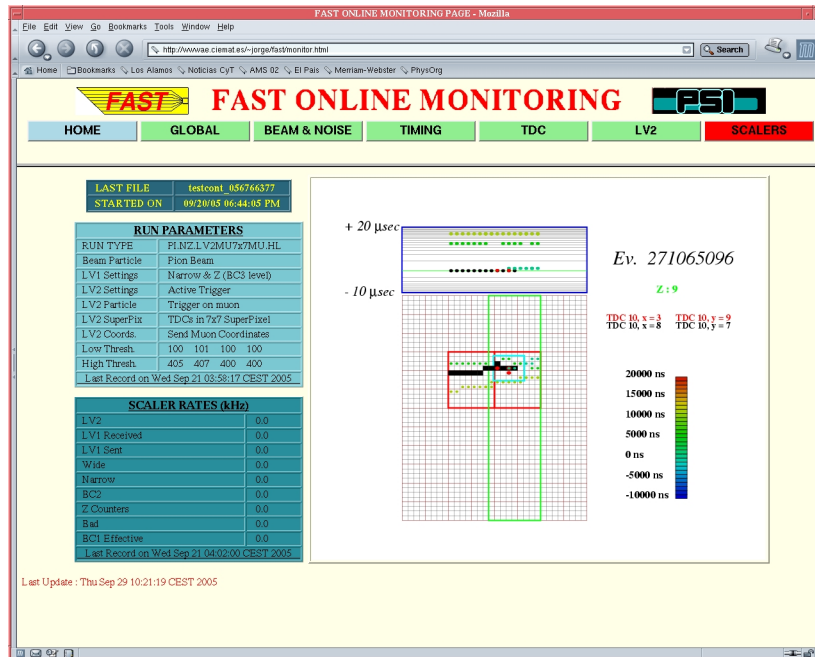


Figure A.12: Snapshot of the front page of the FAST monitoring program web-based graphical interface. In addition to the run conditions included on the tables, an event display with the geometrical and temporal information of the data hits is shown.

Appendix B

Résumé (French Summary)

B.1 Introduction

La constante de couplage de Fermi G_F joue un rôle clé dans les mesures de précision des interactions électrofaibles du Modèle Standard. Avec la constante de couplage électromagnétique (α) et la masse du boson Z (M_Z), G_F est une des quantités les mieux mesurées de la physique électrofaible. Elle rentre donc comme un des paramètres dans tous les calculs [15].

Actuellement, G_F est loin d'être le facteur limitant dans les "fit" électrofaibles. Les incertitudes sur d'autres paramètres, principalement les masses du W et du boson de Higgs, doivent être fortement améliorées, de deux ou trois ordres de grandeur, avant que la précision sur G_F ne commence à avoir de l'importance sur les prévisions du Modèle Standard.

Néanmoins, la précision sur G_F ne dépend que des limites expérimentales, et peut être améliorée d'un ordre de grandeur avec une mesure de précision du temps de vie du muon, τ_μ .

La détermination la plus précise de G_F est calculée à partir du temps de vie du muon, selon la formule suivante:

$$\frac{1}{\tau_\mu} = \Gamma_\mu = \frac{G_F^2 m_\mu^5}{192\pi^3} (1 + \Delta q), \quad (\text{B.1})$$

où Δq inclut les corrections d'ordre supérieur, dans la QED et la QCD.

Avant 1999, l'incertitude sur G_F était de 17 ppm (parties par million), dont 9 ppm d'origine expérimentale, et 15 ppm théorique. L'incertitude théorique était dominée par l'évaluation des corrections radiatives au deuxième ordre, qui n'étaient pas encore calculées. Récemment, les calculs complets des corrections à deux boucles ont été faites, ce qui a réduit l'incertitude théorique sur G_F à 0.3 ppm [17, 18, 19]. Maintenant

que l'erreur théorique est nettement réduite, d'autres améliorations sur la connaissance de G_F doivent arriver du côté expérimental, avec une mesure très précise de τ_μ .

Aujourd'hui la valeur connue de τ_μ est [12]:

$$\tau_\mu = (2197.03 \pm 0.04) \text{ ns}, \quad (\text{B.2})$$

correspondant à 18 ppm, ce qui donne l'incertitude de 9 ppm sur G_F : $\frac{\delta G_F}{G_F} = \frac{1}{2} \frac{\delta \tau_\mu}{\tau_\mu}$. Cette valeur a été obtenue par des expériences qui datent déjà de plus de vingt ans.

B.2 L'Expérience FAST

Le but de l'expérience FAST au laboratoire Paul Scherrer Institute (PSI) est la mesure du temps de vie du muon, τ_μ , avec une précision de 2 ppm (~ 4 ps). En considérant toutes les incertitudes expérimentales et théoriques, ceci correspondra à une mesure de G_F à la précision de 1 ppm, soit une amélioration d'un ordre de grandeur par rapport à la moyenne mondiale.

Du point de vue purement statistique, 2.5×10^{11} événements de désintégration de l'anti-muon (μ^+) sont nécessaires pour réaliser la précision prévue. Afin d'éviter les effets sur la mesure de τ_μ dus à la capture des muons par des noyaux de la cible, des muons de charge positive sont utilisées pour la mesure. Chaque événement de désintégration doit correspondre à une période d'observation d'approximativement 20 μs , soit environ 10 fois τ_μ . Afin de rester dans un intervalle de temps raisonnable pour la prise des données, plusieurs événements doivent se produire dans la même fenêtre et le détecteur doit être capable de les distinguer.

FAST utilise un faisceau de pions chargés π^+ en courant continu ($p = 170$ MeV/c), sur une cible de scintillateur à grande granularité, lue par plusieurs photomultiplicateurs multicanaux (Position Sensitive PhotoMultiplier, PSPM). La cible sert aussi bien comme matériel d'arrêt pour les π^+ et les μ^+ issus de leurs désintégrations ($\pi^+ \rightarrow \mu^+ \nu_\mu$), que comme détecteur pour les positrons e^+ issus de la désintégration des muons ($\mu^+ \rightarrow e^+ \bar{\nu}_\mu \nu_e$). Un schéma du dispositif expérimental est montrée en Figure B.1.

Les trajectoires et les temps de chaque particule de la chaîne complète $\pi^+ \rightarrow \mu^+ \rightarrow e^+$ sont mesurés. En particulier, la différence de temps entre le positron et le muon est enregistrée pour chaque événement. La mesure des temps est effectuée par 16 TDC (Time to Digital Converter) CAEN V767 de haute performance, pilotés par une horloge au rubidium, cadencée à 30 MHz et ayant une grande stabilité temporelle ($\Delta t/t \sim 2 \times 10^{-10}$). Les TDC possèdent un "buffer" interne circulaire et ont la possibilité de retenir les coups dans une fenêtre temporelle autour du signal de déclenchement. La largeur et la position de la fenêtre relativement au déclenchement

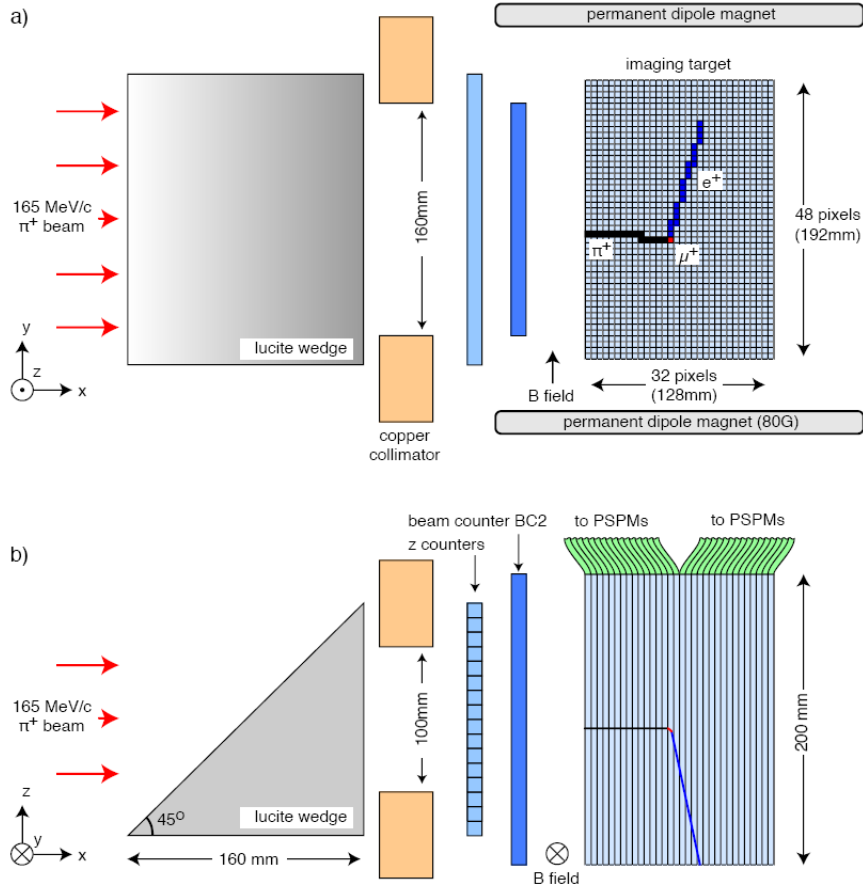


Figure B.1: Vue schématique de la cible FAST, vue du haut (a) et vue de côté (b), illustrant le concept général de l'expérience. Un pion est arrêté dans la cible et la chaîne $\pi^+ \rightarrow \mu^+ \rightarrow e^+$ est observée.

sont des paramètres programmables. Dans notre cas le déclenchement est fourni par le pion entrant dans la cible et la fenêtre de temps des TDC's est $[-10 \mu\text{s}, +20 \mu\text{s}]$ par rapport au déclenchement.

La cible FAST (Fiber Active Scintillator Target) est un bloc de scintillateur, divisé en 1536 (32×48) pixels, pour une dimension totale de $x \times y \times z = 128 \text{ mm} \times 192 \text{ mm} \times 200 \text{ mm}$. Chaque pixel est une barrette de scintillateur plastique Bicron BC400, de dimension $4 \text{ mm} \times 4 \text{ mm} \times 200 \text{ mm}$, dans laquelle deux fibres à décalage de longueur d'onde (WaveLength Shifting Fibers, WLSF, Bicron BCF-92MC) sont insérées. Leur rôle est de collecter et de guider la lumière jusqu'aux photomultiplicateurs. Une couche de peinture diffusante et réfléchissante blanche (Bicron BC-620) est appliquée sur chaque barrette, pour améliorer la collection de photons et pour éviter la diaphonie entre les canaux.

Pour obtenir une distribution uniforme des points d'arrêt des pions dans la cible, un large faisceau est utilisé, avec un absorbeur en plexiglas ayant la forme d'une cale, placé devant la cible. La cale fournit un gradient vertical dans l'épaisseur de l'absorbeur, de sorte que les pions pénètrent à différentes profondeurs dans la cible, selon leur position verticale d'entrée. Cette position est mesurée par un "z-hodoscope" horizontal placé devant la cible. La Figure B.2 montre une photo de la cible; on voit également la cale et le z-hodoscope horizontal.

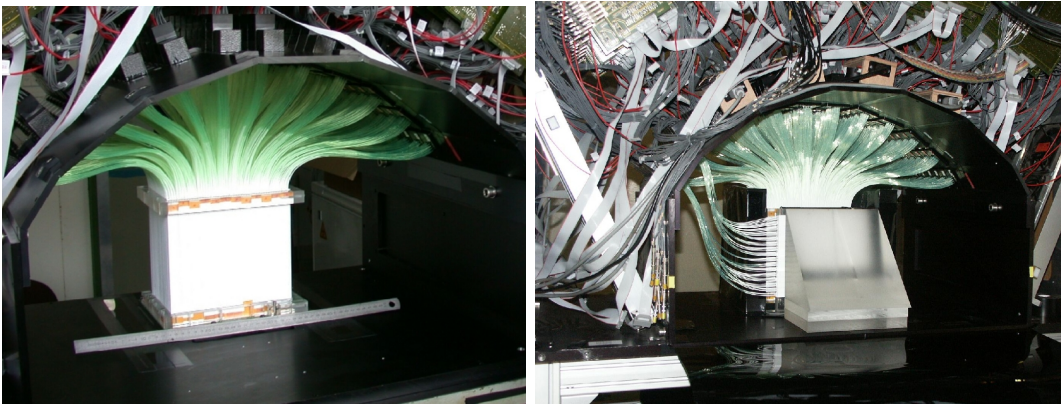


Figure B.2: Photographies de la cible FAST (à gauche) et du dispositif expérimental, incluant la cale, le z-hodoscope horizontal et l'aimant permanent (à droite).

Pour évaluer les erreurs systématiques dues aux effets résiduels de rotation du spin du muon (μ SR), un champ magnétique transversal faible et homogène d'environ 80 G est constamment maintenu dans la région de la cible. Le champ magnétique est fourni par un aimant permanent, se composant de deux plaques de ferrite magnétisée, placées des deux côtés de la cible.

Aucune mesure de l'intensité des signaux est prévue dans FAST, où seulement le temps des coups est enregistré avec les modules TDC. La discrimination entre les particules au minimum de ionisation (c.-à-d. les positrons) et les particules au point d'arrêt (π^+ ou μ^+) est faite par des discriminateurs à double seuil. Les signaux de bas seuil (LL) sont envoyés aux TDC, tandis que les signaux qui dépassent le seuil élevé (HL) sont envoyés au système de déclenchement de niveau deux (LV2).

Le trigger de premier niveau (LV1) est basé sur une coïncidence des scintillateurs du faisceau avec le signal radio-fréquence (RF) de l'accélérateur. Pour atteindre la précision de 2 ppm sur τ_μ , un grand échantillon de données doit être traité, ce qui implique un taux élevé de déclenchement, si on veut maintenir la durée de la prise des données dans des limites raisonnables. Un système de déclenchement de niveau deux (LV2) a été conçu et installé pour réduire le flux de données que le système d'acquisition (DAQ) doit traiter. De cette manière, le détecteur peut travailler avec

un faisceau à quelques centaines de kHz (maximum 1 MHz), et une durée de prise des données de quelques mois. Le LV2 effectue l'identification du point d'arrêt du pion et la détection du muon et transmet ses informations aux TDC. Finalement, il fournit le signal de déclenchement à ces modules TDC qui contiennent au moins un pixel de la matrice de pixels 7×7 autour du point d'arrêt du pion ("superpixel"). Toute l'information appropriée sur les temps est contenue dans cette région, donc seuls les TDC qui contiennent le superpixel doivent être lus par le DAQ.

Le programme d'analyse qui reçoit les événements du DAQ doit identifier, entre tous les coups enregistrés dans le TDC's, ceux qui correspondent aux particules dans la chaîne $\pi^+ \rightarrow \mu^+ \rightarrow e^+$. Il utilise les coordonnées du muon données par le LV2, qui a un accès unique aux données HL des discriminateurs et qui fournit donc une identification propre de la trace du pion et du muon. La tâche principale pour l'analyse est alors l'identification du positron venant de la désintégration du muon. Ceci est fait en utilisant un ensemble de 512 topologies prédéfinies pour la position du positron par rapport au muon, dans une matrice de 5×5 pixels autour du point d'arrêt du muon. Si plusieurs candidats sont trouvés pour le positron, l'événement est rejeté. Cette approche réduit le fond accidentel provenant des autres particules du faisceau, qui traversent la même région du détecteur. La même approche permet aussi des études systématiques détaillées du signal et du fond pour chaque topologie individuelle.

Le taux de données très élevé pour le détecteur FAST rend impraticable le stockage de tous les événements pour leur analyse hors ligne. En outre, la lecture et l'analyse de ces événements exigeraient plus de temps qu'une nouvelle prise de données pour le même nombre d'événements. La solution adoptée est d'analyser entièrement toutes les données en ligne, et de stocker l'ensemble des histogrammes du temps de vie, avec la statistique complète. Seule une fraction pré-établie des données brutes est sauvegardée (entre 1% à 10%, selon le taux de faisceau). Les histogrammes contiennent toute l'information exigée pour la mesure du temps de vie et l'étude des erreurs systématiques.

B.3 Échantillon de Données

L'échantillon de données utilisé pour l'analyse présentée dans ce travail a été enregistré en décembre 2006, sur une durée d'environ trois semaines, à un taux moyen de déclenchement de niveau deux de 30 kHz. Il contient 1.073×10^{10} événements de désintégrations de muons. La Figure B.3 montre la distribution totale du temps de vie.

Les entrées avec des valeurs négatives de temps de désintégrations permettent une description précise du bruit de fond. Le bruit de fond se compose de deux types d'événements. L'un consiste en des événements accidentels plats, qui n'ont pas de structure temporelle. L'autre vient des particules du faisceau provenant d'un paquet

différent de celui du pion, qui sont vues par le détecteur comme des positrons. Cette composante a une structure périodique, à la fréquence RF du faisceau.

Les événements dans la région positive des temps sont employés pour la mesure du temps de vie du muon.

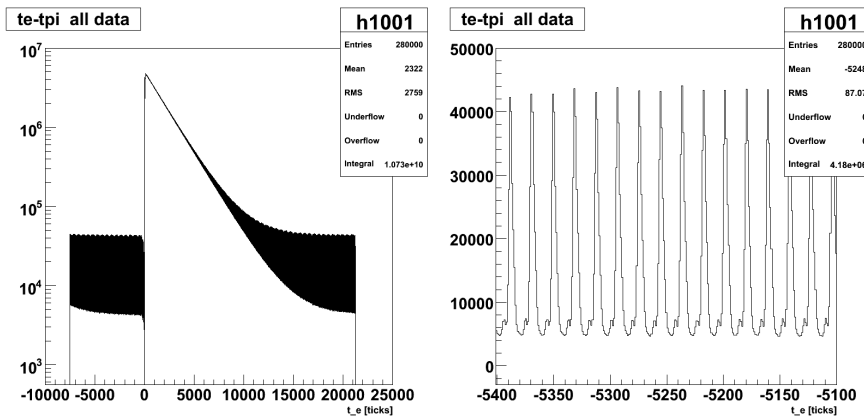


Figure B.3: Histogramme du temps de vie du muon, avec la statistique totale de la prise de données en 2006. Le temps t_e du positron est mesuré en coups de TDC (1 coup de TDC = 1.046666666 ns). La fenêtre temporelle du TDC, approximativement $[-10 \mu\text{s}, 20 \mu\text{s}]$, est visible. A droite une vue agrandie sur la région du fond accidentel, qui montre la structure RF du faisceau.

B.4 La Méthode d'Ajustement

La mesure du temps de vie du muon est effectuée - à partir de l'histogramme en Figure B.3 - en trois étapes. D'abord, la période du faisceau (RF) est obtenue, avec une précision élevée, par l'étude de la région négative. Puis, l'histogramme est "rebinné", en utilisant comme nouvelle largeur la période RF mesurée. Enfin un ajustement sur l'histogramme ainsi obtenu est effectué, avec τ_μ comme l'un des paramètres libres. La taille du bin est choisie de cette façon afin de réduire au minimum l'influence de la structure périodique du fond dans la mesure du temps de vie. Une étude détaillée de la forme du bruit de fond et de son évolution temporelle a montré en effet que la qualité de l'ajustement dépend fortement de la forme choisie pour la modélisation du fond. Quand la taille des bins coïncide avec la période de faisceau, la structure périodique est lissée et la description des données devient beaucoup plus simple et robuste.

La fonction qui décrit la distribution est

$$Data(t_e) = f_{TDC}(t_e) \times \left[P_0 + \frac{N_0}{\tau_\mu} (e^{-t_e/\tau_\mu} + P_2 e^{t_e/\tau_\mu}) \right] \quad (\text{B.3})$$

où t_e est le temps de l'électron par rapport au temps du pion du faisceau; τ_μ , P_0 , N_0 et P_2 sont les paramètres libres pour l'ajustement. P_0 est le composant accidentel du fond; N_0 dans la normalisation est le nombre d'événements. Le terme P_2 rend compte d'une terme de fond qui évolue avec le temps, avec une augmentation exponentielle. Il est dû aux événements où le positron n'est pas trouvé, mais un pion est détecté à sa place. Si (π_1, μ_1, e_1) et (π_2, μ_2, e_2) sont les deux chaînes correctes consécutives, le fond qui dépend du temps, décrit par le terme $P_2 e^{t_e/\tau_\mu}$, est constitué par des événements comme (π_1, μ_1, π_2) , où π_2 est mesuré à la place de e_1 . Un tel événement pourrait être rejeté par le positron e_2 , s'il apparaît dans la fenêtre habituelle de temps et il est également reconstruit comme un candidat positron. La probabilité d'accepter un pion à la place d'un positron dépend donc du moment dans lequel le pion arrive par rapport à la fenêtre temporelle du TDC: les pions près de la limite de la fenêtre du TDC ont en fait une meilleure chance d'être acceptés comme électrons, parce que leurs muons et positrons apparaissent de préférence à l'extérieur de la fenêtre de temps considérée par le TDC.

La composante miroir de ce type d'événements existe aussi bien dans la région de temps négative. Les événements du fond seraient, cette fois, de la forme (π_1, μ_1, e_2) , avec π_2 appartenant à la fenêtre de temps précédente. Ceci correspond à une augmentation exponentielle des événements de désintégration au début de la fenêtre de TDC.

Le terme f_{TDC} dans la fonction d'ajustement (Eq. B.3) décrit l'effet de la non-linéarité dans le comportement des TDC, qui a été reproduit aussi par des mesures en laboratoire. Il correspond à deux termes, un avec une période de 16 coups de TDC, et l'autre avec une période de 32 coups de TDC. La forme exacte pour la correction f_{TDC} est obtenue par l'étude des résidus de l'ajustement, en les superposant par période de 32 coups de TDC, ce qui correspond à la période de l'horloge qui pilote les TDC.

B.5 Résultat de l'Ajustement

Un ajustement d'un maximum de vraisemblance "binné" est effectué sur l'histogramme obtenu précédemment. La région utilisée pour cet ajustement est [600, 20000] coups des TDC, afin d'éviter des inefficacités dans la région des petits temps et d'avoir un intervalle suffisamment long. Le résultat de l'ajustement est montré en Figure B.4. Les queues exponentielles décrites ci-dessus aux bords de la fenêtre temporelle du TDC sont aussi visibles.

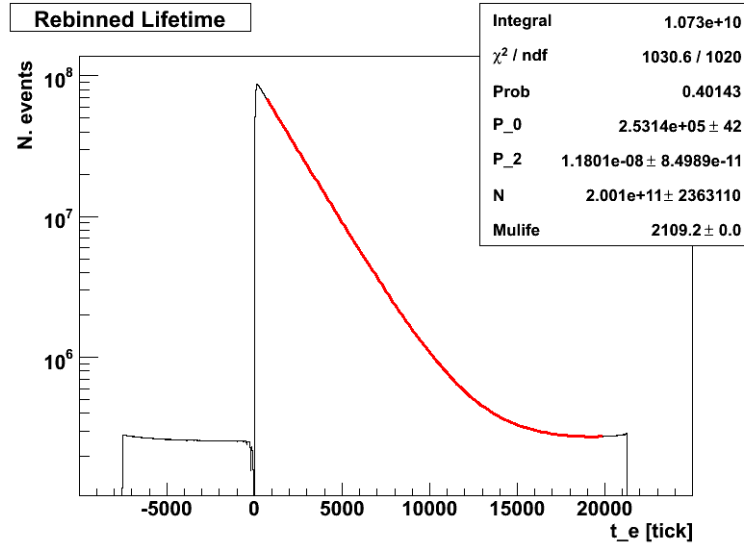


Figure B.4: Ajustement du temps de vie du muon sur l’histogramme rebinné, pour l’échantillon de statistique totale de la prise de données en 2006. La fonction utilisée est donnée dans l’équation B.3, l’intervalle d’ajustement est [600, 20000] coups.

Le résultat pour le temps de vie du muon est

$$\tau_\mu = (2109.200 \pm 0.031) \text{ coups de TDC}, \quad (\text{B.4})$$

et correspond à un χ^2 réduit $\chi^2/\text{ndof} = 1.01$ pour 1020 degrés de liberté, i.e. une probabilité de 40.1%. Les résidus de l’ajustement, définis comme $(\text{data} - \text{fit})/\sqrt{\text{fit}}$ sont distribués sous forme d’une gaussienne, avec pour valeur centrale $x_0 = (-0.001 \pm 0.031)$ coups, et pour largeur $\sigma = (1.003 \pm 0.022)$ coups. La transformée de Fourier des résidus est calculée. Il n’y a aucune contribution restante des fréquences associées au faisceau (RF) ou à la non-linéarité du TDC.

B.6 Évaluation des Incertitudes Systématiques

Les sources possibles d’incertitudes systématiques sur la mesure du temps de vie du muon ont été identifiées et leur influence sur la valeur du temps de vie mesuré a été évaluée. L’erreur systématique est définie comme la différence entre la valeur mesurée en prenant en considération la source d’incertitude systématique et la valeur obtenue par l’ajustement nominal.

La Table B.1 récapitule les résultats obtenus. Il n’y a aucune évidence de grandes erreurs systématiques, au niveau de la sensibilité statistique. Les sources principales

d'incertitudes systématiques sont:

- l'inhomogénéité de la cible i.e. l'influence de la position de la chaîne de désintégration $\pi^+ \rightarrow \mu^+ \rightarrow e^+$;
- la méthode d'ajustement, évaluée en comparant la mesure faite avec la méthode de l'histogramme rebinné (Section B.4) et une mesure indépendante, qui utilise l'histogramme original;
- la stratégie d'analyse. L'analyse nominale utilise la distribution des temps du positron t_e rapportée au pion de faisceau. Une distribution alternative utilise le temps du positron par rapport au temps d'arrêt du muon ($t_e - t_\mu$). La différence des valeurs de temps de vie obtenues est prise comme incertitude liée à la stratégie d'analyse.

Les effets de μ SR ne sont pas visibles dans l'histogramme global de temps de vie du muon. Néanmoins, ils peuvent être artificiellement augmentés si des sous-échantillons spéciaux de données sont considérés, par exemple les événements dans lesquels le positron est détecté dans le même pixel que le pion et le muon. Quand l'échantillon total est traité, les contributions des diverses topologies compensent. Aucun effet systématique lié aux effets de μ SR n'est trouvé.

La stabilité en temps de la mesure a été vérifiée, en divisant l'échantillon total en plusieurs sous-échantillons, de même taille et de même durée. L'horloge pilotant les TDC est stable à moins de 0.5 ppm. La dépendance du temps de vie avec le taux des déclenchements a été étudiée aussi, dans le petit intervalle de taux disponibles, et aucun effet n'a été trouvé.

Source	$\Delta\tau_\mu$ [ticks]	$\Delta\tau_\mu$ [ppm]
Homogénéité de la cible	+0.016	+7.6
Méthode d'ajustement	-0.011	-5.2
Stratégie d'analyse (c.-à-d. $t_e - t_\mu$ vs $t_e - t_\pi$)	+0.004	+1.8
μ SR et isotropie de la cible	-	< 1
Stabilité temporelle (c.-à-d. horloge)	-	< 1
Taux de faisceau	-	< 1
TOTAL	± 0.0137	± 6.5

Table B.1: Incertitudes systématiques dans la mesure du temps de vie du muon pour la prise de données 2006. Les deux contributions principales viennent de l'inhomogénéité de la cible et de la méthode d'ajustement. La détermination des erreurs systématiques est limitée par la statistique.

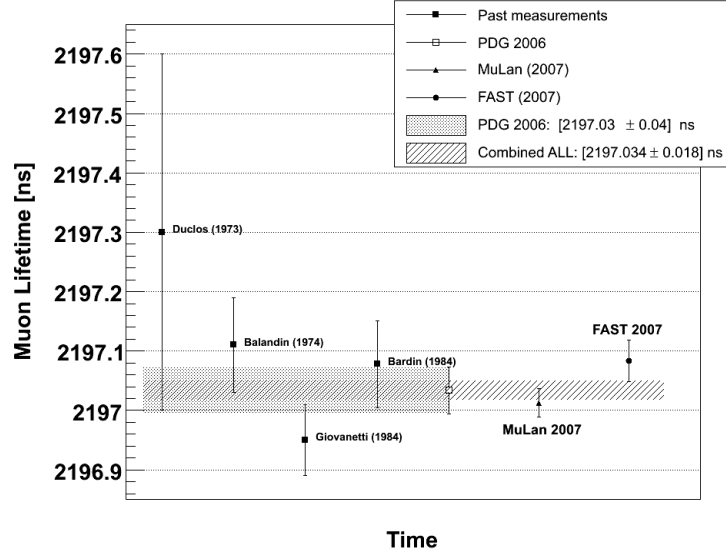


Figure B.5: Mesures existantes du temps de vie de l'anti-muon μ^+ , y compris les résultats récents de MuLan et de FAST. La nouvelle valeur moyenne est: $\tau_\mu = (2197.034 \pm 0.018)$ ns (8.2 ppm).

B.7 Résultats et Conclusions

La valeur mesurée pour le temps de vie du μ^+ par le détecteur FAST, avec l'échantillon de données du run 2006 (environ 10^{10} évènements) est:

$$\tau_\mu = 2109.200 \pm 0.031 (sta) \pm 0.014 (sys) \text{ coups de TDC} \quad (\text{B.5})$$

$$\tau_\mu = 2197.083 \pm 0.032 (sta) \pm 0.015 (sys) \text{ ns} \quad (\text{B.6})$$

La mesure inclut les incertitudes statistiques et systématiques. La valeur obtenue, qui correspond à une précision totale relative de 16 ppm, est compatible avec la moyenne mondiale (Eqn. B.2).

La mesure est dominée par l'incertitude statistique qui est également le facteur limitant dans la détermination des erreurs systématiques. Il n'y a aucune évidence de grandes erreurs systématiques, au niveau de sensibilité actuel.

La Figure B.5 compare le résultat de FAST aux autres mesures existantes. Elle inclut également la mesure récente rapportée par la collaboration MuLan, à la précision de 11 ppm. Tous les résultats combinés mènent à une amélioration significative (un facteur 2) de la précision sur le temps de vie du muon, et sur la valeur de la constante de Fermi G_F .

La constante de Fermi mesurée par FAST correspond à:

$$G_F^{\text{FAST}} = [1.166353 \pm 0.000009] \times 10^{-5} \text{ GeV}^{-2}, \quad (\text{B.7})$$

et la nouvelle moyenne mondiale (qui tient compte de toutes les mesures existantes) est

$$G_F = [1.166366 \pm 0.000005] \times 10^{-5} \text{ GeV}^{-2}. \quad (\text{B.8})$$

Bibliography

- [1] S.H.Neddermeyer and C.D.Anderson, *Phys. Rev.* 51, 884 (1937)
- [2] J.C.Street and E.C.Stevenson, *Phys. Rev.* 52, 1003 (1937)
- [3] H. Yukawa, *Proc. Phys. Math. Soc. Japan* 17, 48 (1935)
- [4] M.Conversi, E.Pancini, O.Piccioni, *Phys. Rev.* 71, 209 (1947)
- [5] C.M.G.Lattes, H.Muirhead, G.P.S.Occhialini, C.F.Powell, *Nature* 159, 694 (1947)
- [6] C.D. Anderson, *Phys. Rev.* 43, 491 (1933)
- [7] M.Gell-Mann and E.P.Rosenbaum, “Elementary Particles”, *Scientific American* (1957)
- [8] E.Gardner and C.M.G.Lattes, *Science* 107, 270 (1948)
- [9] G.Belanger - Notes pour le cour “Le Modèle standard” dans le cadre du 3eme cycle de la physique en Suisse romande.
- [10] C.Quigg - “Gauge theories of the Strong, Weak and Electromagnetic Interactions”, The Benjamin/Cummings Publishing Company, 1983
- [11] C.Quigg - 2003 CERN-CLAF School of High-Energy Physics, hep-ph/0404228
- [12] W-M Yao *et al* 2006 *J. Phys. G: Nucl. Part. Phys.* 33 1 (2006 edition of *Review of Particle Physics*)
- [13] G.Gabrielse *et al* *Phys. Rev. Lett.* 97, 030802 (2006)
- [14] ALEPH, DELPHI, L3, OPAL, SLD and the LEP-EWWG, *Phys. Rept* 427, 257 (2006) hep-ex/0509008
- [15] LEP-EWWG, <http://www.cern.ch/LEPEWWG>

- [16] J.Ellis and R.Peccei, CERN report 86-02 vol.1 (1986)
- [17] T.Ritbergen and R.G.Stuart, *Phys. Rev. Lett.* 82, 488 (1999)
- [18] T.Ritbergen and R.G.Stuart, *Nucl. Phys. B* 564, 343 (2000)
- [19] T.Ritbergen and R.G.Stuart, *Phys. Lett. B* 437, 201 (1998)
- [20] M.Roos and A.Sirlin, *Nucl. Phys. B* 29, 269 (1971)
- [21] T.Kinoshita and A.Sirlin, *Phys. Rev.* 113, 1652 (1959)
- [22] S.M.Berman, *Phys. Rev.* 112, 267 (1958)
- [23] J.P.Derendinger, “Théorie quantique des champs”, Presses polytechniques et universitaires romandes (2001)
- [24] J.Lesgourgues, S.Pastor, *Phys. Rept.* 429, (2006) astro-ph/0603494v2
- [25] A.Czarnecki, G.P.Lapage, W.J.Marciano, *Phys.Rev. D* 61 073001 (2000) hep-ph/9908439
- [26] A.Sirlin, *Rev. Mod. Phys* 50, 573 (1978)
- [27] D.A.Ross, M.Veltman *Nucl. Phys. B* 95, 135 (1977)
- [28] F.Abe *et al.* [CDF Collaboration], *Phys. Rev. Lett.* 73, 225 (1994)
- [29] M.W.Grunewald, “Precision Tests of the Standard Model”, hep-ex/0511018
- [30] A.B.Arbuzova *et al.*, *Computer Physics Communications* 174, 728 (2006) hep-ph/0507146
- [31] L.Malgeri, FAST internal note (FAST 2007/01), March 2007 (available on FAST server: <http://www.cern.ch/fast>)
- [32] G.Bardin *et al.*, *Phys. Lett. B* 137, 135 (1984)
- [33] K.L.Giovanetti *et al.*, *Phys. Rev. D* 29, 343 (1984)
- [34] M.P.Balandin *et al.*, *JETP* 40, 811 (1974)
- [35] J.Duclos *et al.*, *Phys. Lett. B* 47, 491 (1973)
- [36] FAST Collaboration, F. R. Cavallo *et al.*, “Precision measurement of the μ^+ Lifetime (G_F) with the FAST detector”, PSI Proposal R-99-06.1 (1999)

- [37] FAST Collaboration, T. Case *et al.*, “Study of Systematic Errors in the Measurement of the μ^+ Lifetime (G_F) with the FAST detector”, Addendum to PSI Proposal R-99-06.1 (1999)
- [38] MuLan Collaboration, R.M.Carey *et al.*, “Precision Measurement of the Positive Muon Lifetime Using a Pulsed Muon Beam and the μ Lan Detector”, PSI Proposal R-97-05 (1999)
- [39] D. Tomono *et al*, *Nucl. Instrum. Meth. A* 503, 283 (2003).
- [40] D. Tomono *et al*, *Nucl. Phys. B (Proc. Suppl.)* 149, 341 (2005)
- [41] D.B. Chitwood *et al.*, Submitted to *Phys. Rev. Lett.* arXiv:hep-ex/0704.1981 (2007)
- [42] “Paul Scherrer institute Accelerator Facilities” Users’ Guide (1994)
<http://www.psi.ch>
- [43] <http://www.detectors.saint-gobain.com/Media/Documents/S00000000000000001004/SGC%20BC400-404-408-412-416%20Data%20Sheet%200105.pdf>
- [44] http://www.detectors.saint-gobain.com/Data/Element/Product/product.asp?ele_ch_id=P00000000000000001909
- [45] <http://www.detectors.saint-gobain.com/Media/Documents/S00000000000000001004/SGC%20BC600%20Data%20Sheet%200105.pdf>
- [46] <http://www.detectors.saint-gobain.com/Media/Documents/S00000000000000001004/SGC%20BC620%20data%20sheet%200105.pdf>
- [47] http://sales.hamamatsu.com/assets/pdf/parts_H/H6568_series.pdf
- [48] M.Negrazus and D.George, *Cheap, good, fast: How a permanent magnet array was used to provide a detector magnetic field for FAST*, PSI Scientific and Technical Report 2004 - Volume VI
- [49] CAEN, “Mod. V756 - 128 Channel General Purpose Multihit TDC Technical Information Manual”, Version 4 (2003)
- [50] J. Christiansen, “32 Channel general purpose Time to Digital Converter”, CERN/ECP-MIC.
- [51] http://www.ces.ch/products/links/pvic_8026.html
- [52] Y.Gu and R.L.Grossman, *Computer Networks (Elsevier)* 51, 7 (2007)

- [53] L.Malgeri and J.Kirkby, FAST internal note (FAST 2003/05), March 2003 (available on FAST server: <http://www.cern.ch/fast>)
- [54] G.Martinez *et al.*, *Nuclear Science Symposium Conference Record*, 2004 IEEE, 10.1109/NSSMIC.2004.1462574
- [55] <http://midas.psi.ch/mscb>
- [56] J.Kirkby, FAST internal note (FAST 2004/01), January 2004 (available on FAST server: <http://www.cern.ch/fast>)
- [57] F.James, Fortran MINUIT Reference Manual, <http://wwwasdoc.web.cern.ch/wwwasdoc/minuit/minmain.html>
- [58] J.I.Friedman and V.L.Telegdi, *Phys. Rev.* 106, 1290 (1957)
- [59] J.Brewer *et al.*, *Muon Physics*, Academic Press New York 1975, Vol.III

Acknowledgments

It is always a nice feeling - when you feel you're about to turn a page - to stop for a while and thank all the ones that helped, in a way or another, to reach the end of that page.

A sincere big thank goes to all the members of the FAST collaboration, the ones who made possible this thesis work, with their ideas, their hard work, their help and support, their encouragement and patience in answering all my questions, always in a friendly and nice working atmosphere. Thanks in particular to Martin Pohl, for the opportunity he gave me with this work, for his guidance, especially in my first steps in the experiment, the confidence that he has always demonstrated, and also the time and attention spent reading the drafts of this thesis. Thanks to Konrad Deiters, always available at PSI for any prompt intervention that the experiment often needed, and always caring about my progresses. Also, thanks to the Deiters (the whole family!) for the warm atmosphere of the several evenings spent together during my stays at PSI. Thanks to Gustavo Martinez, because of the LV2 of course, but - even more - for having often shared time (especially when Xmas was approaching), debugging phases and tests in the control room, and many dinners spent talking about everything except FAST. Thanks to Luca Malgeri, without whom I simply could not have done this work: thanks for all the teachings, all the answers, the infinite patience, the simplicity which made me understand (or at least believe to understand!) the most difficult topics, the neverending support and the many advices, also in matter of future.

Thanks to Jean-Jacques Blaising, Alain Blondel and Francesco Navarria for having accepted with enthusiasm to join the thesis committee.

Thanks to the whole mechanical engineering group at the DPNC, and in particular to Florian Masciocchi, Manfred Willenbrock and Philippe Bouvier, for the essential support in the construction of the FAST target. Thanks to the many staggers that helped in those phases, Hanneke and Diego in particular. A big thank to Philipp Azzarello, who spent time and resources helping to develop the best way to glue the fibers into the bars. And my excuses to the AMS group, in particular to the ones working in the clean room, for the glue spots left everywhere, despite the attempts to avoid it!

Thanks to the electronics engineering group at the DPNC, Pierre Bene, Jean-Pierre Richeux et al., for the LED mask and the availability in every FAST request of special or strange cable or connector.

Thanks to Peggy Argentin and Catherine Blanchard, irreplaceable help in all the bureaucratic challenges that the university imposes us; and many thanks to Yann, fundamental help in all the other challenges that informatics imposes as well, who saved me (and my files!) more than once.

Thanks to all the ones - at the university - who made the life nicer in these years, sharing lunch times, coffee breaks, or simply a few words and smiles in the corridors. And many more thanks to the ones who shared a bigger part of my life in these times, who became - and will remain - good friends. Thanks to Mercedes, Sofia & Joao, Anna, Till, Audrey et Olivier (entre outre, merci pour tous les documents en français qui sont sortis de mon ordinateur, y compris le résumé de la thèse, mais pas cette phrase qui a donc le droit d'être pleine d'erreurs!), Shulamit, Sonia, Simone, Silvia, Daniel, Arno, Mario and all the rest of the DPNC. A special thought is for my office mates, starting from Pablo, Bertrand and Patrick (I will never forget the frightening "air conditioning cage", and the day when I entered the office and found a nice squared rearrangements of the tables!), and finishing with Rikard, Hayk, Jean-Sebastien and Vassil, who shared space, telephones, good and also bad moods...

Thanks to Catherine Leluc, Monica, Cyril, Nicolas M., Nicolas B., Mercedes, Luigi and François for the nice ambience we had in the Physique Generale exercises sessions. And thanks - much more - to Catherine Leluc for her assistance in the 3eme cycle exams, including a long train travel.

Thanks to Genevieve Belanger and Antonio Pich (even if they don't even know who I am), and to Martin Pohl, again, the ones responsible for my (little) knowledge of the Standard Model.

Un caro pensiero, ricco di stima e affetto, va al Prof. Roberto Bonetti, alla disponibilità, alla correttezza e all'umanità con cui mi ha insegnato la curiosità, la pazienza e il rigore necessari alla fisica sperimentale.

Il grazie più grande é per Mamma e Papà, da cui ho imparato molto, forse tutto. E al resto della mia bella famiglia. Mi piace pensare che uno degli insegnamenti più belli che da voi ho ricevuto é il significato del termine *per sempre*. Un bacio speciale al mio piccolo Pietro, che ci ha reso tutti così felici e orgogliosi, e alla mia "piccola" Arianna, che - anche se grande - resterà sempre la mia piccola.

Infine, grazie, con tutto il cuore, a Mauro, e di certo non solo per l'appoggio, l'incoraggiamento e l'aiuto concreto, ma soprattutto perchè a lui - usando parole purtroppo non mie - é toccato il compito più difficile, quello di volermi bene tutti i giorni!

